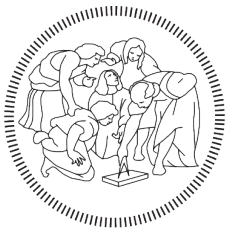

POLITECNICO
MILANO 1863

School of Civil, Environmental and Land Management Engineering
Master of Science in Civil Engineering - Structures

Modelling and assessment of aeolian vibrations of overhead transmission line conductors: theory and implementation

Author:
Chiara Gazzola
854771

Advisor:
Prof. Luca Martinelli
Coadvisor:
Ing. Francesco Foti

Academic Year 2016-2017

"*Once you stop learning, you start dying.*"

A. Einstein

Abstract

A somewhat new approach for the modelling of the aeolian vibration response of a conductor equipped with Stockbridge dampers, based on the concept of dynamic substructuring, is developed. The conductor mechanical model is based on the free vibration equation of motion of a pre-tensioned Euler Bernoulli beam; the Stockbridge damper dynamic behaviour is described through a linear model. Each arm of the damper is treated as a cantilever beam with a lumped tip mass, the clamp is considered as fixed and the imposed clamp displacement and rotation are accounted for through inertia forces applied in correspondence of the centroid of the damper masses. The hysteretic damping of the messenger cable is taken into account through two distinct modal damping parameters, in this way the frequency and the amplitude of the two peaks of the damper response are correctly reproduced.
The natural frequencies and the modal shapes are computed starting from the impedance matrix of the overall system cable-plus-dampers. Dampers are treated as substructures connected to the principal system, represented by the conductor, in turn subdivided into a number of elements, depending on the loading conditions and on the number of devices connected to it. In this way the modal shapes and the response of the system at an arbitrary excitation frequency include the distortional effect due to the presence of dampers.
For each natural frequencies, the Energy Balance Method is used to predict the steady-state aeolian vibration of the conductor and conductor-plus-dampers system.
The proposed procedure allows to significantly reduce the computational effort with respect to other numerical approaches, such as the Finite Element Method, which requires a very refined mesh to capture the cable higher modes, the ones excited by aeolian vibration. Furthermore, the impedance of each substructures can be derived in the domain that is most appropriate, for instance experimentally obtained substructures can be combined with numerical models.

Sommario

Un approccio innovativo per la modellazione della risposta alle vibrazioni eoliche di un cavo protetto da smorzatori Stockbridge, basata sul concetto di sottostrutturazione dinamica, é illustrato nella presente tesi. Il modello meccanico del cavo è sviluppato partendo dall'equazione del moto delle vibrazioni libere di una trave di Eulero-Bernoulli pretesata; il comportamento dinamico dello smorzatore Stockbridge è descritto attraverso un modello lineare. Ogni braccio dello smorzatore è modellato come una mensola, dotata di una massa concentrata in corrispondenza dell'estremo libero; il vincolo di incastro è considerato come fisso e lo spostamento e rotazione imposti al vincolo vengono tenuti in conto attraverso forze di inerzia generalizzate, applicate in corrispondenza del baricentro delle masse dello smorzatore. Lo smorzamento isteretico del cavo *messenger* è introdotto nel modello attraverso due distinti parametri modali di smorzamento; in questo modo la frequenza e l'ampiezza dei due picchi della risposta dello smorzatore sono riprodotti correttamente.
Le frequenze naturali e le forme modali sono calcolate partendo dalla definizione della matrice di impedenza del sistema cavo-più-smorzatori. Gli smorzatori sono trattati come sottostrutture collegate al sistema principale, rappresentato dal cavo, a sua volta suddiviso in un numero di elementi, in dipendenza dalle condizioni di carico e dal numero di dispositivi ad esso collegati. In questo modo le forme modali e la risposta del sistema per un'arbitraria frequenza di eccitazione includono l'effetto distorsionale dovuto alla presenza degli smorzatori.
In corrispondenza di ogni frequenza naturale, il livello di vibrazione a regime del cavo e del sistema cavo-più-smorzatori è determinato applicando il metodo del bilancio di energia (*Energy Balance Method*).
La procedura proposta permette di ridurre significativamente l'onere computazionale, rispetto ad altri approcci numerici, quale ad esempio il Metodo degli Elementi Finiti, che richiede una mesh molto fitta per cogliere i modi più alti del cavo, quelli eccitati dalle vibrazioni eoliche. Inoltre, l'impedenza di ogni sottostruttura può essere ricavata nel dominio più appropriato, ad esempio impedenze determinate sperimentalmente possono essere assemblate all'interno del modello numerico.

Acknowledgements

I would like to thank Prof. Luca Martinelli for enabling me to work on this project and for giving me useful methodological suggestions.

I would also like to thank Ing. Francesco Foti for supporting me during this work; his patience and kindness in understanding and answering all my questions were a great help and I learned a lot from them.

Thanks to my parents who never give up believing in me and without the support of whom I would not be here today.

After five years it is time to conclude this chapter, full of great encounters and everlasting memories. Every step along the way was a true opportunity to grow, and I would like to thank all the people who walked by my side even for a little while and all the friends that let me realize that things do not work only in the way I am used to.

Contents

List of Figures

List of Tables

Chapter 1

Introduction

1.1 Problem

The present study focuses on *aeolian vibration* of overhead electrical transmission lines. Aeolian vibration is the name associated, in the field of transmission lines engineering, to *Vortex Induced Vibrations* (VIV); vibration is caused by the alternate shedding of Karman vortices from the top and bottom of the line's conductor. These vortices change between clockwise and counter-clockwise rotation direction, producing harmonically varying lift forces on the cable, perpendicularly to the mean fluid velocity (EPRI, 2006). A condition of resonance is established when the frequency of the periodic lift force matches a natural frequency of the conductor, resulting in a significant level of vibration for the line.
Aeolian vibration is an "every day" vibration, since it can occurs at every wind speed between 1 to 7 m/s. It takes place mainly in the vertical plane of the cable; it is characterized by high vibration frequencies, in the approximate range of 3-150 Hz, and by vibration amplitude of the order of one conductor diameter (EPRI, 2006).
This small-amplitude vibration produces alternating bending stresses and, if left uncontrolled, may result in the fatigue failure of both the conductor and the support equipment. Fatigue of cable strands can occur at points where motion of the cable is constrained against transverse vibrations, such as suspension clamps and interconnected equipments clamps.

Aeolian vibration can be controlled by dampers. The most popular type of transmission line damping device is the Stockbridge damper, patented in 1925 by George H. Stockbridge (Stockbridge, 1925). This mechanical system is composed by a short metallic strand, usually referred to as *messenger cable*, and two shaped counterweights rigidly attached at its extremities; it is clamped to the conductor and reduces the conductor vibration through the motion of the masses and the hysteretic damping of the messenger wire. It behaves basically as a *tuned mass vibration adsorber* (Den Hartog, 1985): by properly choosing the parameters of the damper, such as the mass of the blocks, the length and the stiffness of the messenger cable, the impedance of the damper coincides

with that of the conductor. In this way, the device is able to dissipate most of the energy imparted by the wind to the conductor. Unlike linear *Tuned Mass Dampers*, the nonlinearity of the device, caused by the hysteretic damping behaviour of the messenger cable, implies that the resonant frequencies of the damper vary with the amplitude of vibration of the damper clamp. This makes the Stockbridge damper effective over a wider range of vibration frequencies (*self-tuning effect*).
The effectiveness of a Stockbridge-type damper is critically linked to its location on the conductor span (Ervik et al., 1986): if a damper or a system of dampers works satisfactorily, they manage to reduce the conductor vibration at all location in the span to a safe value, whereas, the distortion of the conductor waveform of an unsuitable damper or a damper collocated in an unsuitable position, can lead to an increase in strain in the conductor at the damper clamp and/or at the span end.

The aeolian vibration response of the cable-plus-dampers system is commonly analyzed by applying the Energy Balance Method, that is, the vibration level is evaluated through the balance between the energy imparted by the wind and the energy dissipated by both the conductor itself and the added dampers. Despite all the approximations involved in the method, it represents an useful tool to study the complex structure-flow interaction phenomenon of aeolian vibration.

1.2 Motivation

The first natural frequency of a typical overhead transmission line conductor is of the order or 0.1 Hz (Hagedorn (1987) and Wolf et al. (2018)). Therefore, the range of 10-50 Hz, over which aeolian vibration is generally analyzed, approximately corresponds to the interval from the 100th to 500th eigenfrequency of the cable. This means that almost certainly the vortex shedding frequency matches a natural frequency of the cable and transmission lines exposed to low to moderate wind are persistently subjected to aeolian vibration. The latter is one of the most important problems in transmission lines, since it represents the major cause of fatigue failures of conductors strands or of items associated with the support use and protection of the conductor. This failure could lead to power interruption, thus to economic losses and people discomfort and can causes serious injuries. For these reasons the assessment of aeolian vibration severity is one of the major concerns in both the design of new lines and in the upgrade or retrofit of the existing ones.
Claren and Diana (1969) and Diana and Falco (1971) are among the first authors to initiate the understanding of the performance of a transmission line, developing a mathematical model for the single conductor. Many researchers, in the subsequent years, propose different models of the conductor, dampers and conductor-plus-dampers system. Most of the recent ones are based on the Finite Element Method (see. e.g Barry (2010), Dos Santos (2015), Barbieri et al. (2017)), which has however the drawback of being computationally demanding, since, aeolian vibration typically excites the higher modes of the cable, characterized by very small wavelengths. In fact, the conductor span

is usually of the order of 300 m to 1000 m and, considering the interval from the 100th to 500th eigenfrequency of the cable, the percentage ratio between the wavelength and the conductor span is of the order of 1.5-0.3%.
Although the Energy Balance Method is widely used, the literature on the subject is quite poor. Thus, futher research is necessary to develop a comprehensive model able to take into account all the aspects related to the mechanical behaviour of conductor, dampers and conductor-dampers interaction and to effectively reduce the process of trial and error often needed to design the optimal number and position of damping devices, in order to guarantee a safe level of vibration along the entire conductor span.

1.3 Objectives

The following objectives are pursued in this thesis:

- state of the art review of the phenomena of aeolian vibration of overhead transmission line;
- development of a mechanical model for the single conductor, based on the concept of dynamic substructuring, which allows to represent the high modes of the cable with a very limited number of elements. The proposed model is based on a beam-like description of the conductor, since the cable flexural stiffness is taken into account.
- Definition of a linear model for the general case of an asymmetric Stockbridge-type damper, able to take into account of the rocking contribution in term of impedance and energy dissipation.
- Development of an *ad hoc* Matlab code to perform modal analysis of the conductor and conductor-plus-dampers system, which allows to define the distortional effect of dampers on the conductor modal shapes.
- Implementation of the Energy Balance Principle to determine the level of vibration for the case of single conductor and conductor equipped with dampers. Analysis of the influence of parameters like axial tension, level of turbulence, damper configuration on the level of vibration.

1.4 Thesis overview

The present thesis in arranged in seven different chapters. After this introduction about the general contents of the document, in chapter 2 the state of the art is presented. The phenomenon of aeolian vibration is disussed along with the mechanical behaviour and the possible modelling choices of single conductor, Stockbridge-type dampers and conductor-plus-dampers system. Finally, the Energy Balance Method, the most popular approach used to predict the staedy-state aeolian vibration of transmission lines, is illustrated.
Chapter 3 deals with the model proposed to describe the conductor behaviour, also

proposing a solution to model a slack cable, apt to analyze for instance the messenger wire of the Stockbridge damper, which is usually not pre-tensioned. Some benchmarks are reported to validate the model.
The Stockbridge damper model is proposed in chapter 4. The undamped equations of motion and the generalized forces acting at the damper clamp are derived for the most general case of an asymmetric damper. Then, in order to compare the impedance functions with some available experimental and numerical data, the hysteretic damping model is introduced for a symmetric damper subjected only to a vertical translation of the clamp.
Chapter 5 describes the implementation of the procedure for the computation of the natural frequencies and modal shapes for cable-plus-dampers system. An example, whose analytical solution is known, is proposed to validate the code.
Chapter 6 deals with the Energy Balance Principle, used in the present work to determine the steady-state aeolian vibration of the single conductor and of the conductor equipped with dampers. The computation and implementation of the power imparted by the wind, the power dissipated by the conductor self-damping and the power dissipated by dampers are illustrated, along with some case studies.
In the last chapter 7, the conclusions of the study are drawn and some hints for future developments are proposed.

Chapter 2

State of the art

In this chapter, existing literature about wind-induced vibrations, conductor modelling and vibration damping devices is discussed. Due to the focus on Stockbridge dampers and aeolian vibrations, related literature is investigated in more detail. In section 2.1 a brief description of the most common types of wind-induced vibrations of transmission line conductors is presented, then section 2.2 is focused on the description of the phenomenon of aeolian vibrations. The basic characteristics, the mechanics and the possible modelling of conductors are adressed in section 2.3; the dynamics and the modelling of the Stockbridge dampers is described in section 2.4. The dynamic interactions between cable and dampers are discussed in section 2.5. Finally, section 2.6 deals with the Energy Balance Method, the most popular approach used to predict the steady-state aeolian vibration of the conductor-plus-dampers system.

2.1 Wind-induced vibrations

The types of motion that derive their energy from wind forces applied to conductors are referred to as *wind-induced vibrations*. Three different categories of cyclic conductor motion can be recognized (EPRI (2006), Ervik et al. (1986)):

- *aeolian vibrations*, for single and bundled conductors,
- *galloping*, for single and bundled conductors and
- *subspan oscillations*, for bundled conductors only.

Aeolian vibrations is the name associated, in the field of transmission lines engineering, to *Vortex Induced Vibrations* (VIV); they are due to vortex shedding of the conductor and are one of the major cause of fatigue failures of conductors. Aeolian vibrations occur for low to mean wind speed up to about 10 m/s; they are observed in 3-150 Hz frequency range and have peak-to-peak amplitudes of up to one conductor diameter (see e.g. EPRI (2006), Barry et al. (2014), Barbieri and Barbieri (2011)).
In section 2.2 a detailed description of this phenomenon is presented.

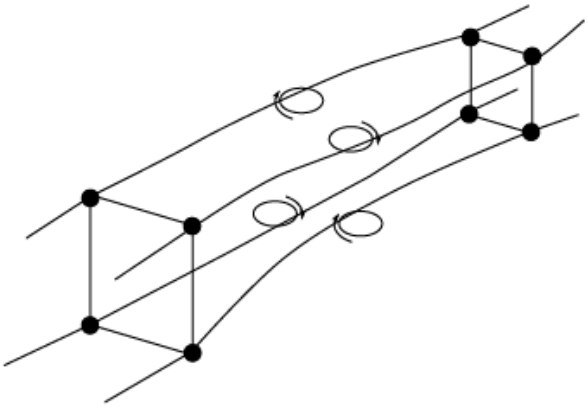

Figure 2.1: Typical subspan oscillation shape for a quad bundle (EPRI, 2006).

Galloping is characterized by low frequencies and high amplitudes of vibration (up to several times the sag of the cable), occurring mainly in the cross-wind direction. It is a vertical oscillation of the conductor span in one or a few loops, but it usually incorporates other less visible twisting, lateral and longitudinal motions. Galloping is usually caused by moderately strong, steady crosswinds (wind velocity over 15 m/s) and it is a form of instability due to the unstable shape assumed by the conductors when they are covered with ice. Vibrations due to galloping are associated to relevant changes in the cable axial force, inducing severe dynamic loads at the suports (EPRI (2006), Foti and Martinelli (2016b), CIGRE (2007)).
Subspan oscillations occur for bundled conductors and it is caused by the wake produced by the windward conductor on the leeward one. For this reason this phenomenon is referred to as *wake induced oscillations*. They are characterized by intermediate frequency of the order of a few Hz and amplitude of the order of the conductor spacing in the bundle. The motion occurs in moderate to strong winds, usually in the range from 7 to 18 m/s (EPRI, 2006).
Figure 2.1 shows the typical oscillation shape for a quad bundle: the single sub-conductor motion is elliptical and is the result of the combination of an essentially horizontal mode of vibration of the bundle with an essential vertical one. Figure 2.2 shows the three main types of power line vibration. Figure 2.3 represents a typical wind speed statistical distribution, from which it can be easily assess that aeolian vibrations can be classified as a frequent phenomenon, while galloping and subspan oscillations are relatively rare phenomena.

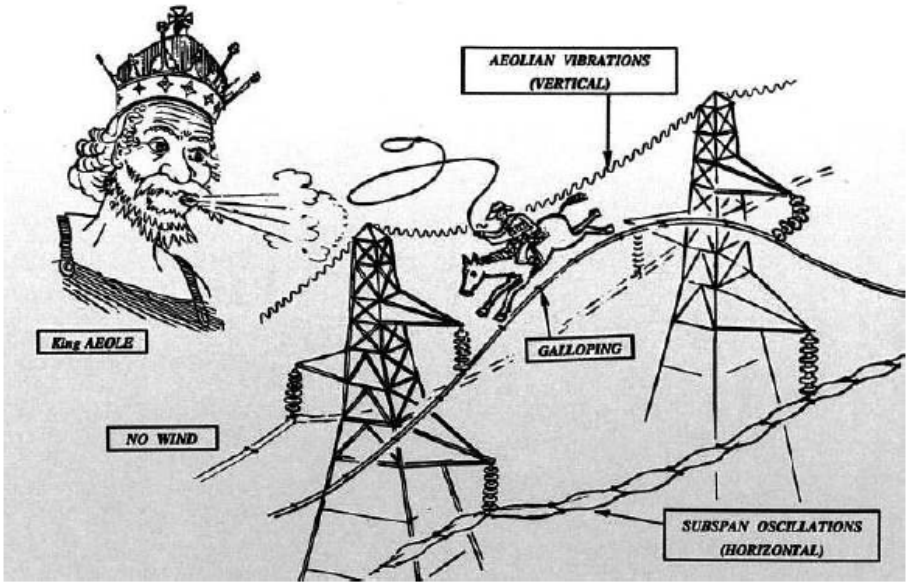

Figure 2.2: The three main type of power line vibration (EPRI, 2006).

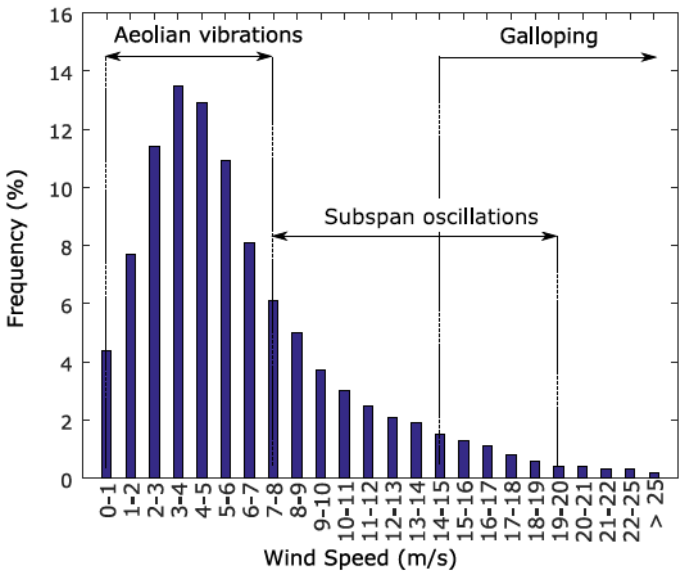

Figure 2.3: Typical wind speed statistical distribution, adapted from (EPRI, 2006).

2.2 Aeolian vibrations

Aeolian vibrations are one of the most important problem in transmission lines because they represents the major cause of fatigue failure of conductor strands or of items associated with the support, use and protection of the conductor. They occur when a smooth wind flow of 1 to 7 m/s interacts with a conductor, they are characterized by vibration frequencies in the approximate range of 3-150 Hz and vibration amplitude can be, at maximum, about one conductor diameter.
Aeolian vibrations are caused by vortex shedding from the conductors. Vortex shedding uccurs in bluff body or when there is flow or boundary layer separation, which produce vorticity, and, as a consequence, oscillating vortices arise behind the object. The various regime of flows can be determined by the Reynolds number (see e.g. EPRI (2006),Vecchiarelli (1997), Lienhard (1966)):

$$Re = \frac{V \cdot D}{\nu}, \tag{2.1}$$

where D represents the cylinder diameter, V the wind velocity and ν the kinematic viscosity of the fluid (EPRI (2006), Vecchiarelli (1997), Ervik et al. (1986), Lienhard (1966)). The various flow regimes as a function of the Reynolds number are represented in Figure 2.4.

Vortex shedding generates alternating forces that act fundamentally in the transverse direction of the flow (*lift forces*) and the frequencies of the vortex shedding are approximately given by the Strouhal formula (see e.g. EPRI (2006), Hagedorn (1987), Ervik et al. (1986)):

$$f_{VS} = S \cdot \frac{V}{D}, \tag{2.2}$$

where S is the Strouhal number (S=0.18-0.22), V is the wind velocity and D is the conductor diameter. Thus, the lowest frequencies will be found for large conductor diameters and low wind velocities, instead the highest frequencies are found for small conductor diameters and relatively high wind velocities.
When the body is fixed the lift forces are generally out of phase or unsynchronized, hence the net lift force is extremely small. Vortex shedding in the case of a vibrating conductor produces aeolian vibration: the motion of the conductor in the transverse direction may be initiated when the velocity of the flow is such that the vortex-shedding frequency is close to the natural vibration frequency f_n of the conductor. The conductor motion can subsequently (Vecchiarelli, 1997):

- increase the strenght of the shed vortices, hence the magnitude of the vortex-induced lift forces along the conductor are amplified;
- enhance the spanwise correlation of vortex shedding: vortex-induced lift forces act in phase and become synchronized.
- f_{VS} is changed to equal or almost equal f_n, consequently the Strouhal law is violated and the conductor takes control over the shedding phenomenon. Shedding

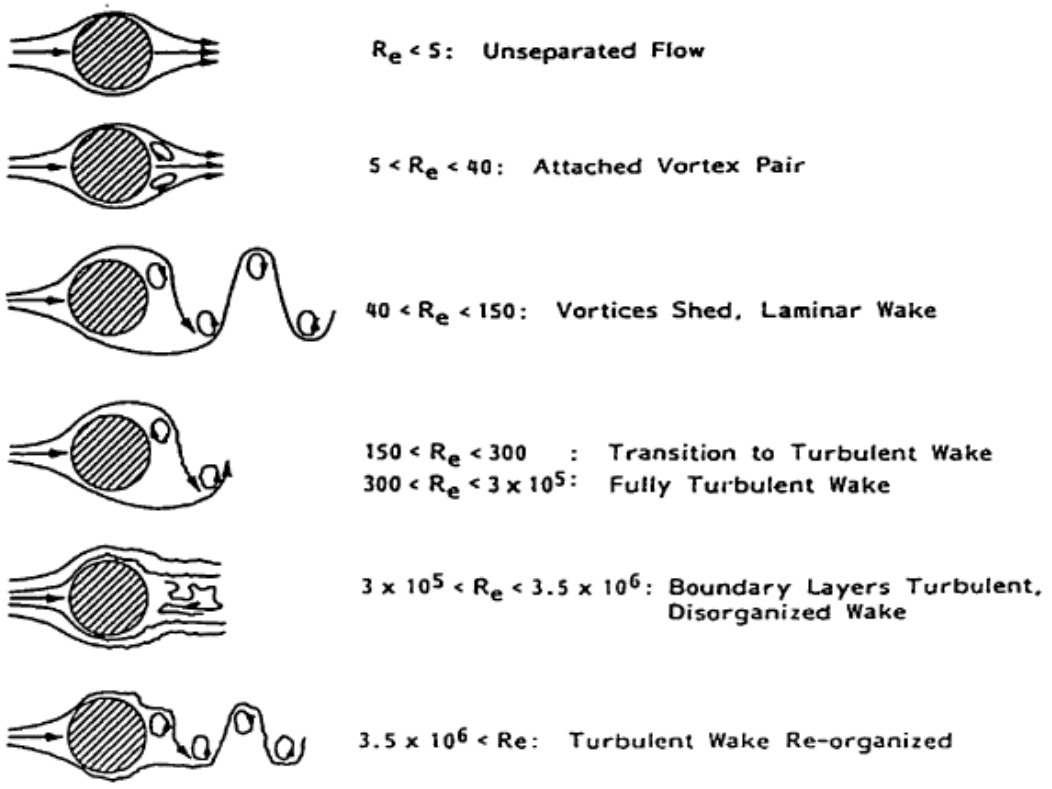

Figure 2.4: Vortex shedding with respect to Reynolds number variation for the particular case of a stationary circular cylinder (Lienhard, 1966).

frequency remains anchored to the natural one in a velocity range, denoted as *lock-in* range. The conductor is then in resonance and stays in resonance for wind speed as large as 130 % of the onset velocity.

As a consequence of these effects, the conductor can experience a significant level of vibration.
A study from (Diana and Falco, 1971), concluded that the lift force that acts during the vibration of the conductor (considered as a rigid cylinder in a uniform flow) is harmonic in time, as well as the conductor displacement in steady-state condition. The magnitude of the lift force can be defined as:

$$F_L = \frac{1}{2} \cdot \rho \cdot C_l \cdot D \cdot L \cdot V^2, \tag{2.3}$$

where D is the conductor diameter, L is the span length of the conductor, C_l is the lift coefficient, ρ represents the density of the fluid and V the wind velocity. A maximum lift coefficient of 0.55 was measured on a cylinder which showed a maximum normalized vibration of 0.55D peak to peak. The cylinders with maximum vibration amplitudes above and below this value experienced lift coefficient in between the value of 0.28 and 0.33 (Barry (2010), Dos Santos (2015)).

The main factors affecting aeolian vibrations are the span length, the tension and the type of terrain: aeolian vibration is most severe when the conductor tension is high, the span is long and the terrain is smooth with low-to-moderate steady wind. (EPRI (2006) Kasap (2012)). The roughness of the terrain determines the level of the wind turbulence, in particular increasing the terrain roughness, the turbulence level increases. Important wind velocity fluctuations, due to turbulence, cause the loss of synchronization between conductor vibration and vortex shedding, because the wind continuously changes and the phenomenon is always in transient conditions. This has the effect of reducing the power imparted to the conductor by the wind, and so also the vibration level is usually reduced.

Conductor vibration causes localized bending which, in dependence of its level, can cause fatigue failures of the conductor strands at the suspension clamps or at the clamps of dampers and other devices installed on the conductor (EPRI (2006), Ervik et al. (1986)).

2.3 Conductors

The conductor of an overhead power line is considered to be the most important component of the overhead line, since its function is to transfer electric power, and its contribution toward the total cost of the line is up to 40 % (EPRI, 2006). As a consequence, great attention has to be paid to the selection of a proper conductor configuration to meet load requirements.
The following section focuses on the basic properties and different possible dynamic modelling of conductors.

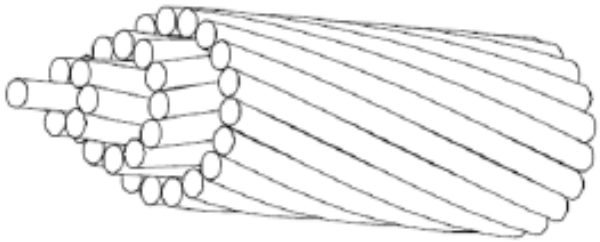

Figure 2.5: Structure of a typical conductor (EPRI, 2006).

2.3.1 Types and basic properties of conductors

Conductors are stranded cables. The most widely used form of conductor is that of layers of round wires stranded, first, around a so-called core, which can be of the same material or different, and then around each other. In order to keep the integrity of this construction, the stranding takes place in alternating directions from layer to layer, as can be seen from Figure 2.5.

Most of the conductor design requirements concern mechanical constraints. The electrical aspects are usually restricted to current density, electrical resistance, and the associated power loss and voltage gradient, which are tackled by adding area and adjusting the outside diameter or using multiconductor bundles on the line. Overhead conductors can be realized with different combination of materials, resulting in different strenght-to-weight ratio, which is the main mechanical criterion used to select the proper conductor for every specific application. The most used types of conductor are listed in the following (EPRI, 2006):

- *All Aluminum Conductor* (AAC) or *Aluminum Stranded Conductor* (ASC) are constructed from commercially pure aluminum. Due to their relative low strenght-to-weight ratio, they are suitable for short spans in distribution networks, and for areas where ice and winds loads are limited.
- *All Aluminum Alloy Conductor* (AAAC) or *Aluminum Alloy Stranded Conductor* (AASC) are composed by an aluminum-magnesium alloy, ensuring a higher strenght with respect to the previous item.
- To obtain a better strenght-to-weight ratio, a strenght member has to be added to the conductor:
  - *Aluminum Conductor Alloy Renforced* (ACAR) has an aluminum alloy core.
  - *Aluminum Conductor Steel Reinforced* (ACSR) and *Aluminum Alloy Conductor Steel Reinforced* (AACSR) have a core with steel wires, which ensure a higher strenght-to-weight ratios with respect to aluminum alloys. ACSR is the most commonly used conductor type.

Figure 2.6 shows the types of conductors used for different span characteristics.

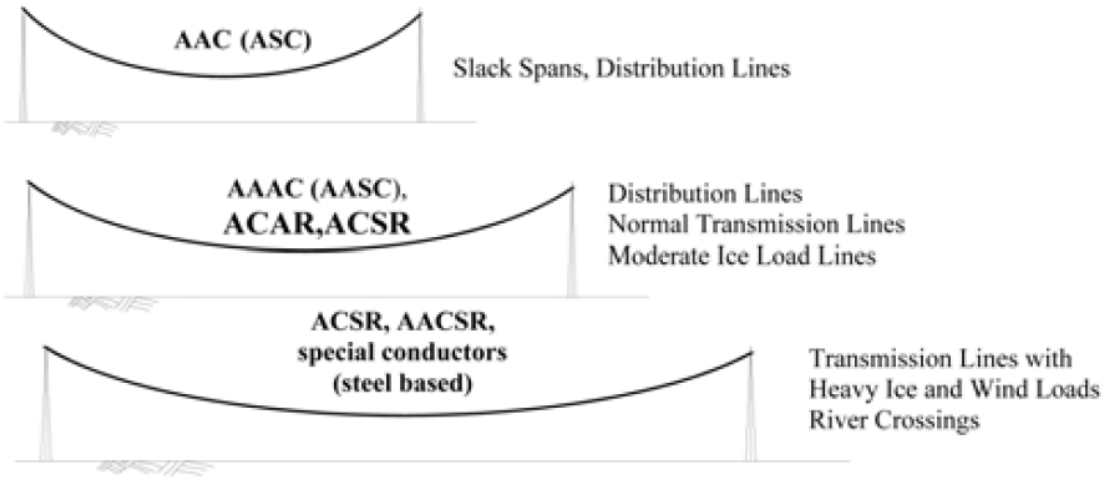

Figure 2.6: Typical use of bare conductors (EPRI, 2006).

Special conductors with different arrangement of wires are used for special situations: e.g. conductors with high steel content for very long spans, conductor with shaped aluminum wires or self-damping conductor (McCulloch et al., 1980). Figure 2.7 represents the cross sections of special conductors.

2.3.2 Inner conductor mechanics

As pointed out in chapter 1, it is well known that aeolian vibrations lead to conductor fatigue. In particular, the fatigue mechanism of vibrating conductors is a highly localized phenomenon called *fretting fatigue*: it occurs on the outer surface of the wires because of the cyclic microslip induced by the conductor motion (EPRI (2006), Vecchiarelli (1997), Dos Santos (2015)).
Fatigue of conductor strands occurs at points where the motion of the conductor is constrained against transverse vibration, such as support locations and damper clamps. Failure occurs as minute cracks resulting from fretting and cyclic strain variation propagate through individual conductor strands. Crack initiation and crack growth depend upon (EPRI, 2006):

- contact stresses between strands in the vicinity of the clamp,
- macroscopic stresses (or strains) in the individual wires of the conductor.

Figure 2.8 shows an example of fatigue failure of conductor strands in correspondence of the suspension clamp.

An in-depth knowledge and modeling of the conductor inner mechanics is necessary to end up with a quantitative approach to conductor fatigue, to describe properly conductor self-damping and thus to model the dynamic behaviour of Stockbridge dampers (adressed in section 2.4).

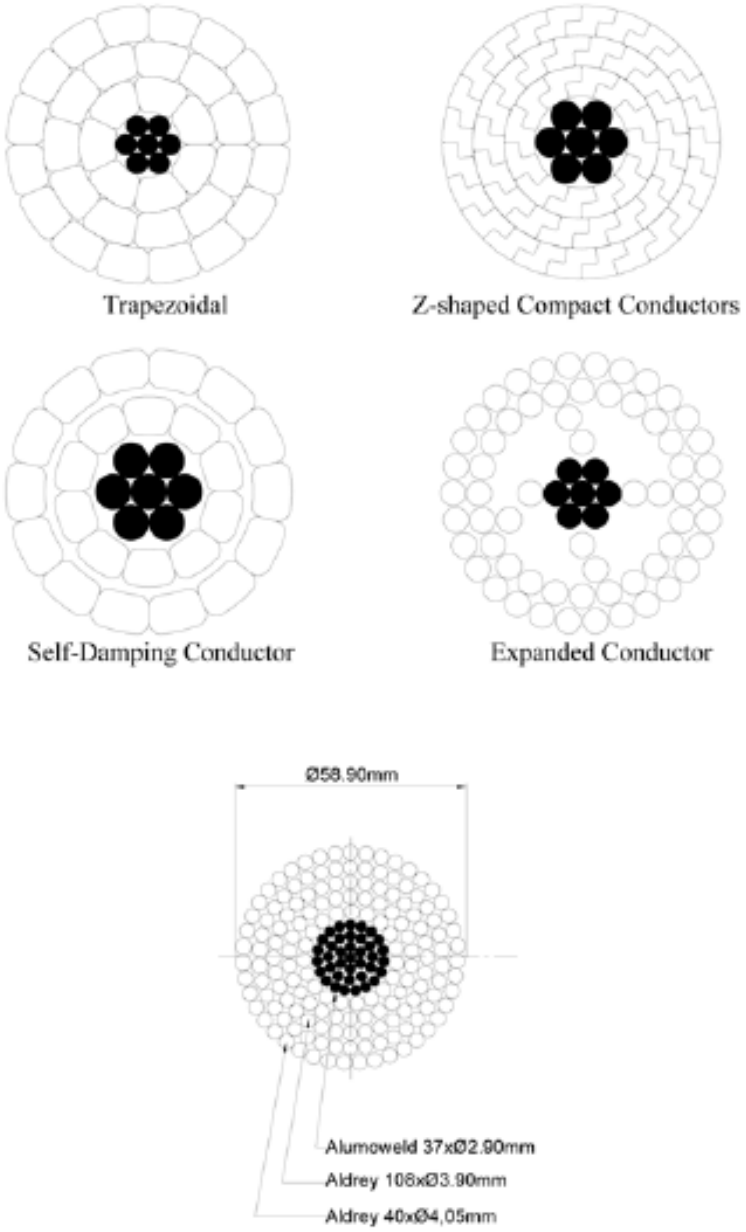

Figure 2.7: Cross sections of special conductors (EPRI, 2006).

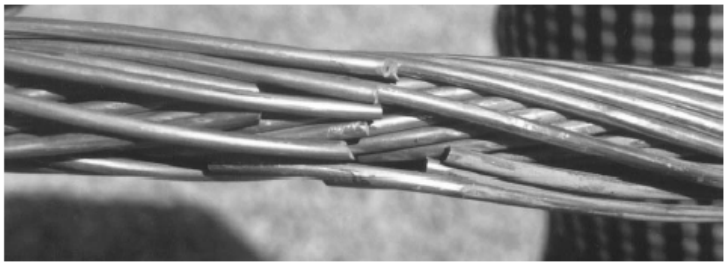

Figure 2.8: Fatigue failure of conductor strands at the suspension clamp (Kasap, 2012).

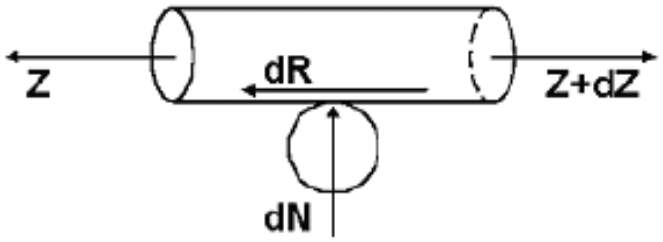

Figure 2.9: Axial force equilibrium of a differential wire element (EPRI, 2006).

Bending Stiffness

When a conductor is bent, the movement of its wires is prevented by friction forces, acting on the internal contact surfaces between the wires belonging to adjacent layers. This situation can be described in a first approximation by the axial force equilibrium of a differential wire element, as depicted in Figure 2.9. Initially, the friction forces R (caused by the interlayer compression forces N, which themselves are caused by the wire tension force Z) are large enough to prevent any relative sliding between the wires; this limit kinematic condition is referred to as the *full-stick* state of the strand (Foti and Martinelli, 2018). The corresponding bending stiffness is called EI_{max} and can be computed assuming that all wires act together as a solid. The most simple expression for the maximum value of the bending stiffness is the one reported in (EPRI, 2006):

$$EI_{max} = \sum (E_i \cdot I_i), \tag{2.4}$$

where I_i and E_i are respectively the moment of inertia and Young's modulus of wire i. The moment of inertia I_i relative to the neutral axis of the conductor, for each wire is given by (EPRI, 2006):

$$I_i = I_{0i} + A_i \cdot d_i^2, \tag{2.5}$$

where I_{0i} is the moment of inertia of wire i relative to its own axis, A_i is the area of the wire and d_i is the distance from the wire's neutral axis to the conductor's neutral axis.

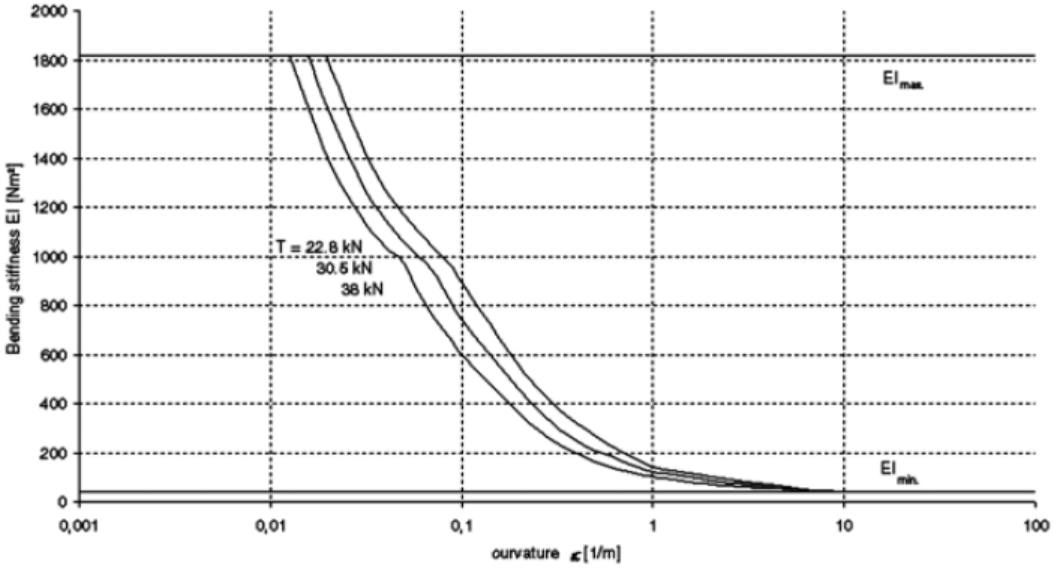

Figure 2.10: Bending stiffness EI of ACSR Cardinal as a function of the conductor curvature χ with the tension T as parameter (EPRI, 2006).

EI_{max} corresponds to the maximum attainable value of stiffness for the conductor.
By incresing the value of the bending curvature, the wires progressively start to slip up to the situation for which all the wires are in the slipping state and their bending strain develops as though they bend around their own neutral axis. This condition is referred to as *full-slip* state (Foti and Martinelli, 2018) and the corresponding bending stiffness is called EI_{min} and is computed assuming that all the wires act independently of one another. The most simple expression for the minimum value of the bending stiffness is the one reported in (EPRI, 2006):

$$EI_{min} = \sum (E_i \cdot I_{0i}), \tag{2.6}$$

EI_{min} corresponds to the lowest theoretical value of stiffness for the conductor.
Different expressions for EI_{max} and EI_{min}, based on more refined mechanical models of the strand have been also reported in the literature (see e.g. Foti and Martinelli (2016c), Foti and Martinelli (2016a) and the review papers Cardou (2006), Cardou and Jolicoeur (1997), Spak et al. (2013)). In spite of their simplicity, however, Equation 2.6 and Equation 2.4 give a good estimate of the upper and lower theoretical bounds of the bending stiffness.
In between the two extreme values of the bending stiffness a more or less smooth transition takes place (Figure 2.10). The generally adopted stiffness value ranges from 30 to 50 % of the cable maximum stiffness value EI_{max} and it is generally assumed constant with frequency and along the span (CIGRE, 2005).

Conductor Self-Damping

As pointed out in section 2.3.2, when the conductor is bent the strands of the conductor tend to slip against each other and frictional force is induced. This frictional micro-slip is the main source of conductor self-damping, i.e. the capacity of the conductor to dissipate energy internally while vibrating.
One of the most important parameters influencing the conductor self-damping is the conductor tension: when the tension is increased, the strands tend to lock and the slippage is reduced, hence the conductor self-damping is reduced too. In particular, if the ratio between tension and cable unit weight H/w exceeds certain limit value, aeolian vibrations can cause serious conductor damage. This limit H/w value is generally exceeded on transmission lines and then it is enstablished practise to protect conductors with suitable dampers (CIGRE, 2005).
The methods to measure the self-damping of cables are essentially two, the *Power method* (PM) and the *Inverse Standing Wave Ratio method* (ISWR); they are widely described in *IEEE 563-1978 Guide on conductor self-damping measurements.*
Data measured in the laboratory span are generally expressed empirically through a power law, described in section 2.6.

2.3.3 Mathematical model of the conductor

(Claren and Diana, 1969) are among the first authors to develop a mathematical model for a single conductor. They modelled the conductor as a tensioned Euler-Bernoulli beam, assuming a constant flexural rigidity and tension along the cable and ignoring damping. The equation of motion can be written has:

$$EI\frac{\partial^4\omega}{\partial x^4} - T\frac{\partial^2\omega}{\partial x^2} = -m\frac{\partial^2\omega}{\partial t^2}, \tag{2.7}$$

where EI denotes the cable flexural rigidity, m is the mass per unit length and ω is the transverse displacement. The natural frequencies and vibration modes for the *Taut Beam* (TB) model can be expressed in the following way (Claren and Diana, 1969):

$$f_{n,TB} = \frac{1}{2\pi}\cdot\sqrt{\left(\frac{n\pi}{L}\right)^2\cdot\frac{T}{m}\cdot\left(1+\left(\frac{n\pi}{L}\right)^2\cdot\frac{EI}{T}\right)} \tag{2.8}$$

and

$$y_{n,TB(x)} = A_n\cdot Sh(z_n x) + B_n\cdot Ch(z_n x) + C_n\cdot sin(a_n x) + D_n\cdot cos(a_n x), \tag{2.9}$$

where

$$z_n = \sqrt{\frac{T}{EI} + \sqrt{\frac{T^2}{(2EI)^2} + m\frac{(2\pi f_{n,TB})^2}{EI}}}, \quad a_n = \sqrt{-\frac{T}{EI} + \sqrt{\frac{T^2}{(2EI)^2} + m\frac{(2\pi f_{n,TB})^2}{EI}}}. \tag{2.10}$$

It can be observed that the modelling of the conductor as a tensioned beam is more realistic than the *Taut String* model. On the other hand the latter is easier to deal with, because it doescn't imply the evaluation of the flexural stiffness *EI* of the beam model, that, as pointed out in section 2.3.2, depends on the relative sliding of the wires forming the cable and can be difficult to estimate.
According to the *Taut String* model natural frequencies and vibration modes can be computed with the following expressions (Claren and Diana, 1969) :

$$f_{n,TS} = \frac{n}{2L} \cdot \sqrt{\frac{T}{m}} \tag{2.11}$$

and

$$y_{n,TS}(x) = A_n \cdot sin\left(\frac{2\pi}{\lambda_n} \cdot x\right). \tag{2.12}$$

The shape of the vibration modes depends on the span end conditions, and this is, in turn, fundamental to the correct evaluation of the strains and stresses at the span extremities. If the end conditions are hinges, the shape of the vibration modes is the same as for the taut string (Figure 2.11), and the maximum bending strain of the conductor is found at the antinode (EPRI, 2006).

If the span extremities are fitted with fixed constraints, the vibration mode shape is as in Figure 2.12 and the maximum bending strain is found at the span extremities (EPRI, 2006).

The most common approach to model the single conductor is to treat it as an axially loaded Euler-Bernoulli beam, considering the following aspects:

- the static configuration of a conductor is represented by a catenary, and the tensile load is not constant along the span. For this reason the frequency and the related shape of the first vibration mode is different from the one of Figure 2.11. However, the cable length l is usually in the order of 300-1000 m, while the cable's sag is small, in general a few percent of the span (3-5%). Moreover, aeolian vibration does not excite the first conductor modes (section 2.2), hence the sag can be disregarded and the cable can be modelled as a straight flexible continuous system (Hagedorn (1987), EPRI (2006))

- The cable bending stiffness is small but essential in order to calculate bending strain (Hagedorn (1987), EPRI (2006)).

- Considering the cable bending stiffness is necessary for an other reason. In the more general situation dampers execute a rototranslative motion, exerting on the cable not only a concentrated force, but also a moment. The latter can be taken into account only if the stiffness of the cable is considered (Hagedorn (1982), EPRI (2006)).

- The cable bending stiffness has however only negligible influence on the eigenfrequencies and eigenmodes of the free cable vibrations, which are almost exactly those of a string without bending stiffness (Hagedorn (1987), EPRI (2006)).

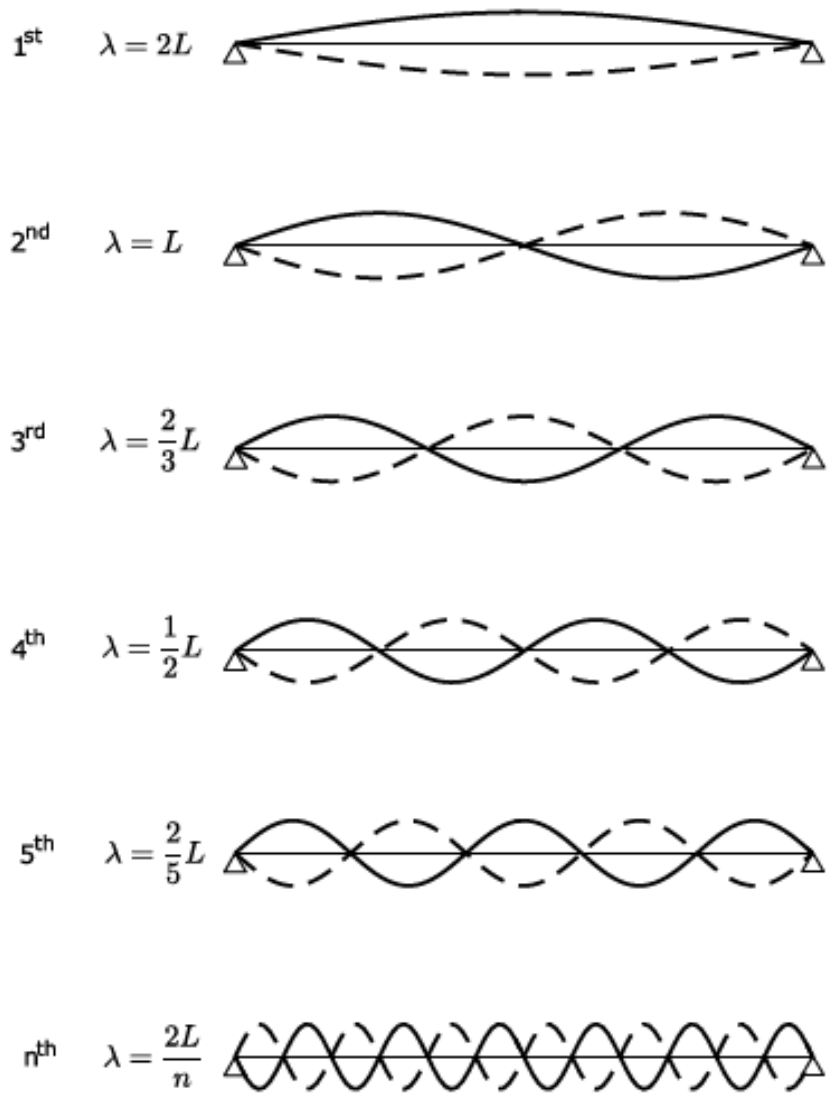

Figure 2.11: Vibration modes for the *Taut String* model (EPRI, 2006).

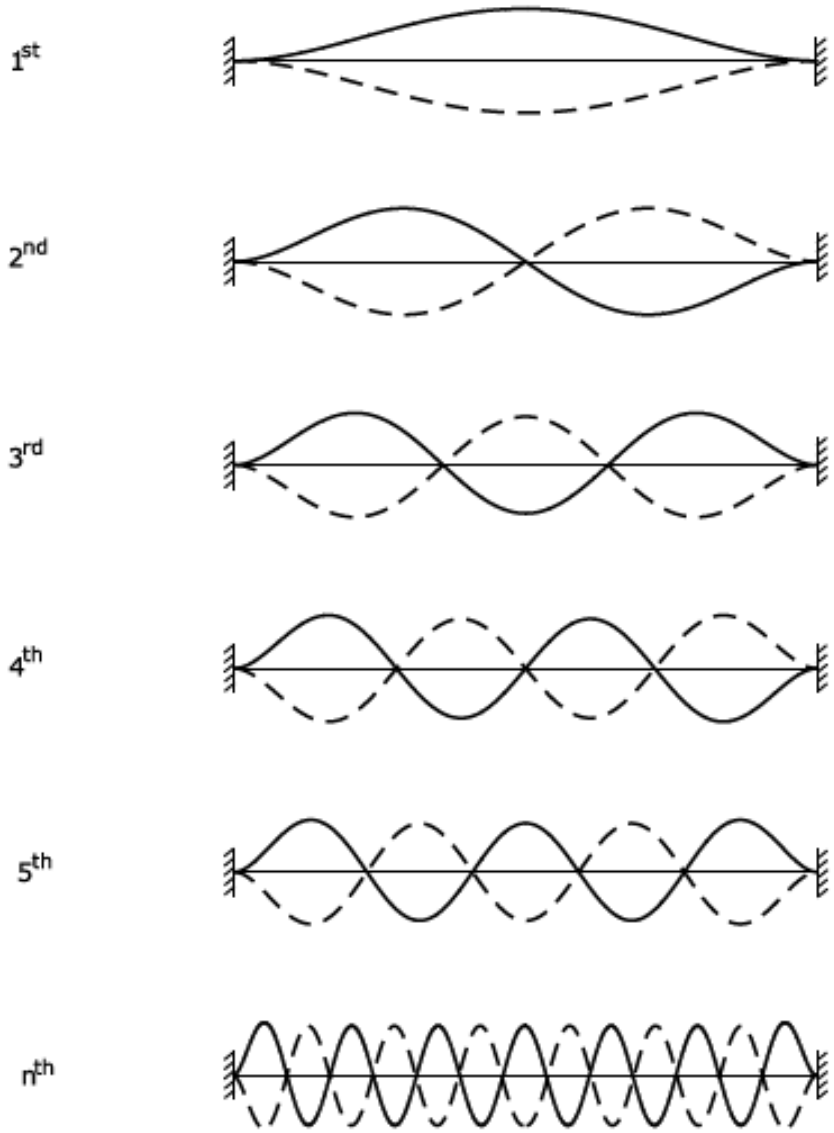

Figure 2.12: Vibration modes for the *Taut Beam* model (EPRI, 2006).

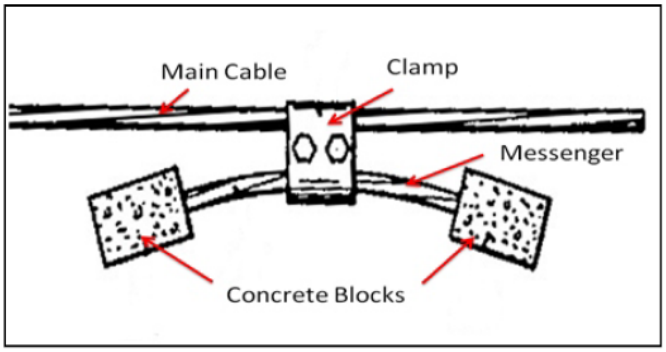

Figure 2.13: Stockbridge's original concrete block design (Kasap, 2012).

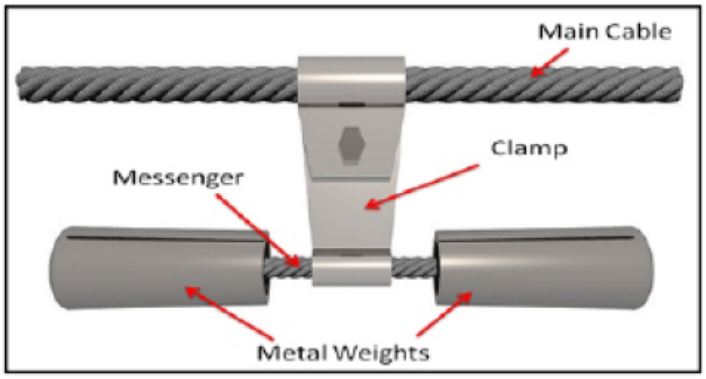

Figure 2.14: Vibration damper of Stockbridge type (Buscemi, 2016).

2.4 Stockbridge dampers

The objective of vibration dampers is to reduce aeolian conductor vibrations through the dissipation of some of the energy which is transferred from the wind to the conductor. The Stockbridge damper was invented in 1925 by George Stockbridge and is the most common type of transmission line damper (EPRI (2006), Canales et al. (2008)).
In general, the Stockbridge damper is composed by a short metallic strand called the *messenger cable*, and two shaped masses rigidly attached at its extremities. The connection between the damper and the main conductor is ensured by means of a rigid clamp. The first Stockbridge damper as patented by George Stockbridge (Stockbridge, 1925) had a concrete block at each end of the messenger as shown in Figure 2.13; Figure 2.14 shows a modern vibration damper with metal weights.

When the device is actuated through a clamp motion, the messenger cable flexes, because it is not stiff enough to force the masses to accurately follow the motion of the cable clamp. During the flexural vibrations of the messenger cable, the wires of the strands undergo internal sliding in presence of friction, hence providing energy dissipation due

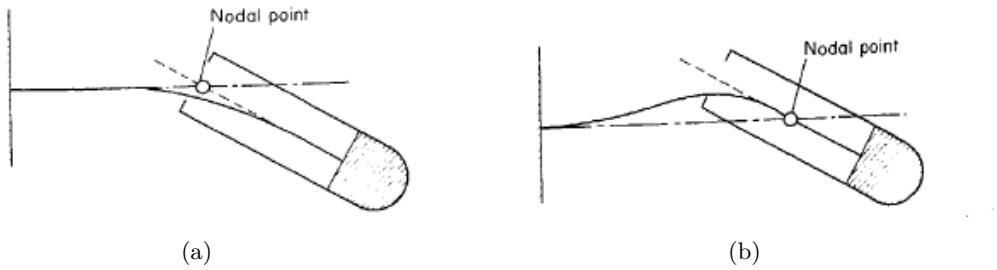

Figure 2.15: (a) First natural mode of vibration of symmetrical Stockbridge damper. (b) Second natural mode of vibration of symmetrical Stockbridge damper (Wagner et al., 1973).

to the same mechanism described for the conductor in section 2.3.2. Owing to this dissipative phenomenon, the messenger cable shows a hysteretic behaviour characterized by a non-linear dynamic response: the structural damping and the dynamic stiffness of the messenger cable are function of the amplitude of vibration of the support motion (see e.g. EPRI (2006), Foti and Martinelli (2018)).
Basically, the Stockbridge damper behaves as a *tuned mass vibration adsorber* (Den Hartog (1985), Buscemi (2016), Kasap (2012), Langlois and Legeron (2014a)): by properly choosing the parameters of the damper, such as the mass of the blocks, the length and the stiffness of the messenger cable, the impedance of the damper coincides with that of the conductor. In this way, the energy imparted to the conductor from the wind is greatly dissipated by the Stockbridge damper.
The two sides of the messenger cables behave basically as cantilevers with lumped masses at their ends subjected to a prescribed support motion.
A Stockbridge damper is said to be symmetrical or 2-R (two resonances) damper if the weights and messenger cables are identical on both sides of the clamp; this type of damper possesses two natural modes of vibration, when clamp motion is restricted to the vertical direction (Figure 2.15). In the first mode of vibration the outer ends of the two weights are the points of maximum motion and the nodal point corresponds to the attachment point of the weight with the messenger cable. The second mode describes a rotation of the weights about their own center of gravity.
Claren and Diana in 1968 designed an asymmetric Stockbridge damper, known as 4-R (four resonaces) Stockbridge damper, with two different masses, different moment of inertia and different lengths of the messenger cable (Figure 2.16). The 4-R Stockbridge damper is a four-resonance system; the four resonance frequencies are evenly distributed in the frequency range of interest for aeolian vibration in order to flatten the damper response curve and broaden the frequency range of conductor vibration that can be covered with a specific damper size (Claren and Diana, 1969) (Figure 2.17).

The Stockbridge damper behaviour is nonlinear and this is due to the hysteretic behaviour of the messenger cable; this means that the resonant frequencies of the damper vary with the amplitude of vibration of the damper clamp. The great efficiency of the

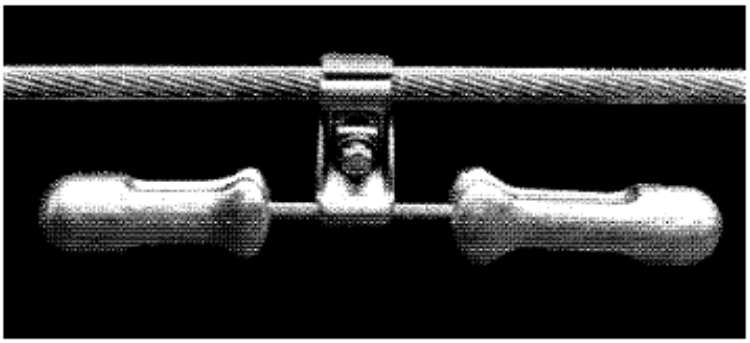

Figure 2.16: Asymmetrical Stockbridge-type damper (EPRI, 2006).

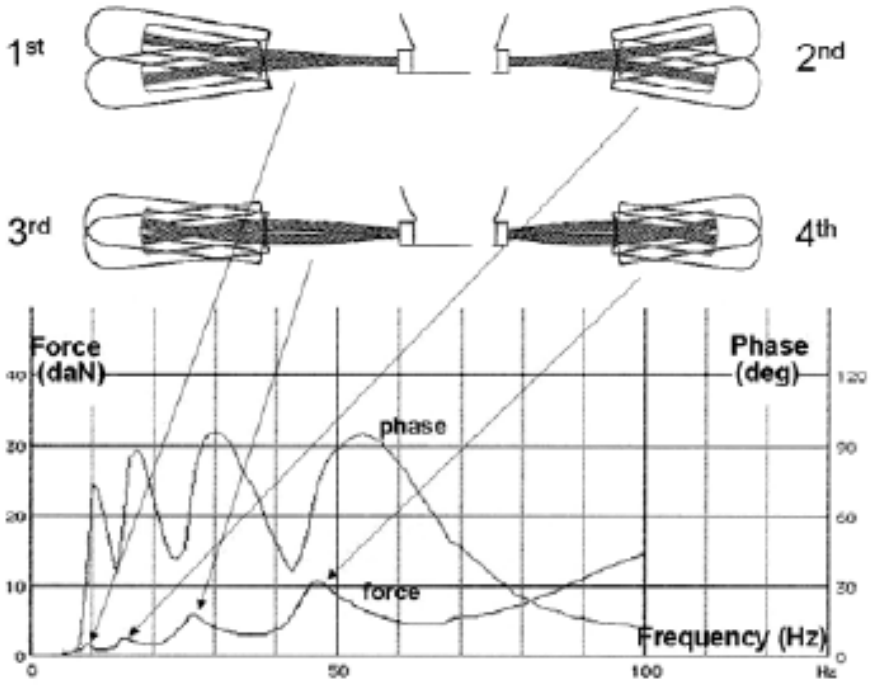

Figure 2.17: Typical response of a 4-R Stockbridge-type damper (EPRI, 2006).

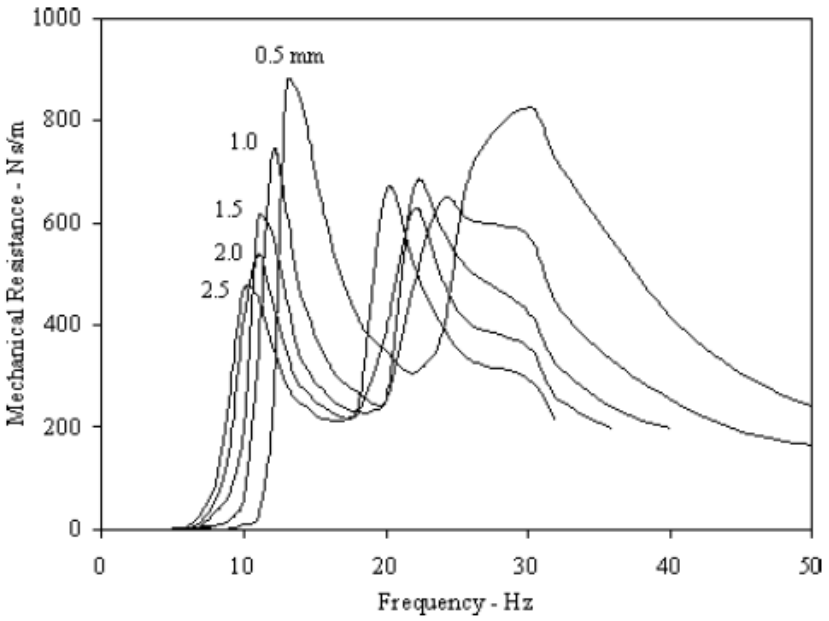

Figure 2.18: Mechanical impedance of a 2-R Stockbridge damper (EPRI, 2006).

Stockbridge damper is due to this nonlinear behaviour that make the damper self-tuning (EPRI, 2006). When the excitation frequency from the wind falls at one of the resonant peaks for small damper clamp amplitude, where damping may be small, the amplitude of the span increases. The damper clamp amplitude increases with it, shifting the frequency of the resonant peak away from the excitation frequency. The shift continues until a damper amplitude is reached where the damping efficiency is high enough to prevent further increase. Figure 2.18 represents the mechanical impedance as a function of the clamp vibration amplitude of a 2-R Stockbridge damper, showing its typical nonlinear behaviour.

Laboratory tests of Stockbridge dampers are performed according to the *IEEE Guide for Laboratory Measurement of the Power Dissipation Characteristics of Aeolian Vibration Dampers for Single Conductors*. Four standard experimental methods can be used for measuring the energy dissipated by Stockbridge-type damper. Three of them, called *basic methods* are perfomed in the laboratory test span and measure directly the energy losses due to both the conductor and the damper, which is clamped on the cable. They are the *Inverse Standing Wave Ratio* (ISWR) test, *Power test* and *Decay test*. The fourth test procedure, called *direct method* is the *Forced Response test* and is the least expensive of the four methods. In the *Forced Response test* a damper is mounted on a shaker, which provide a harmonic motion of the damper clamp in the vertical direction. A load cell measures the force trasmitted to the damper and a velocity trasducer or an

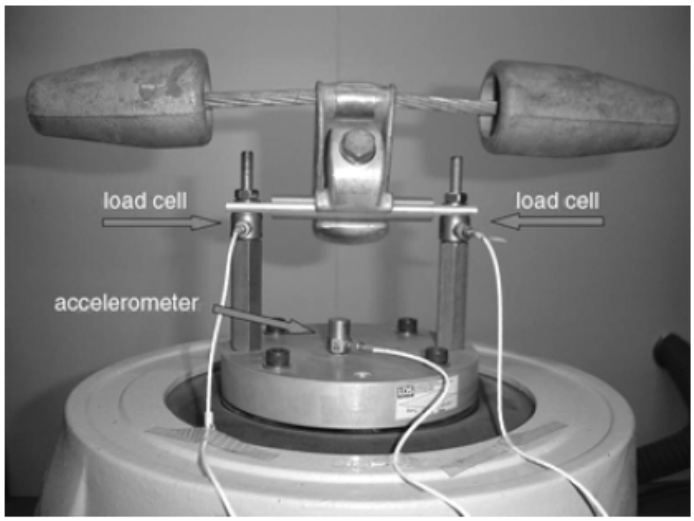

Figure 2.19: Shaker setup for the damper characteristic test (EPRI, 2006).

accelerometer is employed to determine the velocity of the damper clamp. Figure 2.19 shows the shaker setup for the damper characteristic test. The aeolian vibration amplitudes on the real span are computed through software, generally based on the Energy Balance Principle.
Due to the aforementioned nonlinearity, the damper can be tested for different values of imposed displacements or imposed velocities. In fact, the test can be performed such that the displacement amplitude or velocity amplitude of the damper clamp is fixed; in the second case the clamp displacement amplitude decreases inversely as the vibration frequency increases (Vecchiarelli (1997), Diana et al. (2003a), EPRI (2006)).
Basic methods allow to define the behaviour of the whole system cable-plus-damper, taking into account the variation of the loop lengths and shapes due to the presence of damper. On the other hand, these types of test are very expensive and cannot be used to get the behaviour of the damper alone. Testing the damper on the shaker (*Forced Response test*) is easier and cheaper than on the span, but the shaker only imposes a vertical motion to the damper clamp, while on the test span and in service the clamp rotates and traslates. (Diana et al., 2003a) demonstrates that the clamp rocking provides a contribution to the energy dissipation which is not negligible, especially when the damper is close to a node of the cable deflected shape.

2.4.1 Modelling of the Stockbridge type damper

Stockbridge-type damper has an apparently simple structure, but its modelling is not so straightforward. This is mainly due to the fact that the system response is nonlinear because the messenger cable has a hysteretic behaviour (see e.g. Sauter (2003), Hagedorn and Sauter (2002)), hence the cable dynamic stiffness and damping depend upon the

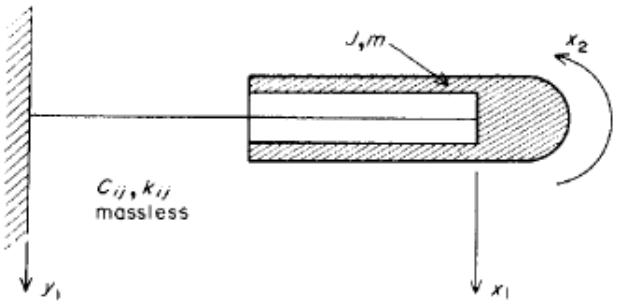

Figure 2.20: Equivalent two degrees of freedom linear system (Wagner et al., 1973).

amplitude of cable deflection. Furthermore there is a large scatter in the dynamic characteristics of the same cable type produced by different manufacturers, hence the tests provide dynamic characteristics that don't reflect exactly the behaviour of the damper in service.
Many authors try to model the Stockbridge damper behaviour with different approaches. Even if, as repeatedly stressed, Stockbridge damper response is nonlinear, many attempts to model it as a linear system can be found in literature.
(Wagner et al., 1973) analyzes the behaviour of a symmetric Stockbridge damper making reference to the two-degrees of freedom linear system shown in Figure 2.20. Exploiting symmetry, the authors model the damper as a cantilever beam (the messenger cable) with a concentrated rigid mass at the tip (damper weight) and subjected to a base motion (only the vertical motion of the clamp is considered); the mass of the messenger cable is neglected, being very small compared to the damper's mass. The two degrees of freedom coincide with the translation and rotation of the damper's mass (x_1 and x_2 in Figure 2.20). The damping of the system is considered purely hysteretic and it is introduced in the equations of motion as a damper coefficient matrix, whose terms are proportional to the corresponding ones of the stiffness matrix, through a hysteretic damping coefficient.
(Hagedorn, 1982) examines the dynamic behaviour of asymmetric dampers characterized by (2x2) complex impedance matrices; such dampers transmit not only a concentrated force but also a moment to the cable. The author concludes that the moment may strongly affect the local bending strains near the damper clamp. The damper impedance matrix is evaluated experimentally and the Stockbridge damper is considered as a linear system. In fact, Hagedorn pointed out that, due to the damper nonlinearity, it would be necessary to measure damper impedance curves for different amplitudes via equivalent linearization and to consider amplitude-dependent impedances in all the calculations. However, the changes in the impedance curves from one Stockbridge damper to another of the same type due to fabrication tolerances are of the same order as the change in the impedance with the amplitude in one and the same damper. For this reason, the author uses an average impedance curve for each damper type (which does not depend on the amplitude) for the development of his model.

Another investigation on the assessment of the dynamics of Stockbridge damper is conducted by (Markiewicz, 1995). In his paper he presents a method and a computational model for the evaluation of the optimum dynamic characteristics of Stockbridge dampers to be mounted near tension insulator assemblies (dead-end span). He points out that the optimum damper impedance required for dead-end spans differs significantly from the optimum impedance of the damper designed to protect conductor near suspension clamps (suspension span). This is due to the dynamic interaction between the tension system and the damper itself, which cannot be neglected for vibration frequencies close to resonance frequencies of the tension system.
As already mentioned, (Diana et al., 2003a) report the results of an experimental campaign with a modified dynamometric Stockbridge damper clamped to a laboratory test span. The aim of the paper is to get the force and torque exerted between the cable and dermine their contribution to the global energy loss. It turns out that the role of rocking on the global energy losses is remarkable only if the damper is clamped very close to a nodal position of the cable's deflected shape.
(Diana et al., 2003b) deals with a methodology to evaluate the (2x2) mechanical impedance matrix of a non symmetric Stockbridge-type damper, based on damper translational tests on a shaker and on a 6 d.o.f. linear model of the damper itself. The damper is assumed rigidly clamped on the cable and its motion in a plane; the messenger cable is modelled as an Euler-Bernulli beam and the damper masses are considered as rigid. 6 d.o.f. are considered, i.e. the translation and rotation of each mass and the translation and rotation of the damper clamp. The hysteretic damping is considered as a damping matrix proportional to the stiffness matrix through the hysteretic damping coefficient. The model considered is linear: it represent the damper linearized dynamic behaviour for each damper clamp translation velocity considered in the experimental test. The authors pointed out that to capture the real nonlinear behaviour of the damper it is necessary to introduce a rheological model, but the identification procedure of the related parameters is quite cumbersome and could be a possible source of errors.
(Hagedorn and Sauter, 2002) develop a nonlinear model for the Stockbridge damper, representing the messenger cable with a single distributed Jenkin element to simulate the damper impedance based on data obtained from a simple experiment carried out with a piece of damper cable. The local mechanical properties of the wire cable are experimentally identified in time domain, in particular, the moment-curvature relation is determined at every location of the wire cable subjected to dynamic flexural deformations.
(Barbieri et al., 2007) propose a linear model for the Stockbridge damper. The messenger cable is modelled using the Euler-Bernoulli beam finite element and to take into account the cable hyteretic damping, it is considered a complex flexural stiffness ($EI = EI_0(1 + i\beta)$, where β is the hysteretic damping costant). The damper masses are modelled with rigid body plane motion hypothesis. The Genetic Algorithm method is used to approximate the experimental and numeric data, i.e. to calibrate the cable complex flexural stiffness.
(Barbieri and Barbieri, 2012) generalize to the nonlinear case the model defined above,

introducing nonlinear stiffness and nonlinear damping elements.
(Luo et al., 2014) firstly propose a linear analytical model of the Stockbridge damper based on the Wagner model (Wagner et al., 1973). However, this model cannot explain the experimental evidence that, as driving velocity increases, the mode frequencies decrease. This is due to the fact that nonlinear factors is not considered, especially the contact conditions between each two part of the damper, which have a significant effect on the stiffness of the structure. Hence, to include the contact conditions a 3D full-scale finite element model of the Stockbridge damper is developed.
(Langlois and Legeron, 2014a) propose a time history nonlinear model for the Stockbrige damper to predict its dynamic response for all expected amplitudes and frequencies. The model is built from simple experimental characterization tests to identify stiffness and damping properties.

From the aforementioned studies, it can be assessed that the development and/or the comparison with the linear model is fundamental for the definition of the dynamic behaviour of the Stockbridge damper. In fact, by comparing the experimental data and the linear model results it is possible to identify the quantities not properly captured by a linear formulation. These considerations are the starting point to develop a more refined nonlinear model, taking into account the critical aspects mentioned in (Hagedorn, 1982) and (EPRI, 2006).

2.4.2 Damper location

The efficiency of the damper depends significantly on its positioning. A Stockbridge-type damper is usually placed near a suspension clamp, trying to avoid having the damper located at a node, for all expected frequencies of aeolian vibration (Vecchiarelli (1997), Hagedorn (1982), EPRI (2006), Nigol et al. (1985)). In fact the damper clamp must experience a finite amount of motion to allow the damper to dissipate energy. The location of the damper will not coincide with that of a node, for any expected vibration frequency, if the damper is mounted away from the suspension clamp by a distance which is less than the loop length corresponding to the highest expected frequency of vibration.
Because of the travelling wave effects, a single damper placed near one end of a span is able to reduce the amplitude of the entire span, providing that there are no reflection points, such as heavy items within the span. Sometimes two dampers, one at each end of the span are required and for relatively long span (greater than 500 m) two dampers per end may be necessary (Vecchiarelli (1997), EPRI (2006)). Figure 2.21 shows the three mentioned distribution of Stockbridge dampers along the spans.
As described in section 2.2, the range of wind vibrations which causes aeolian vibration is about 1-7 m/s. The upper limit is determined by two aspects: higher velocity winds tend to become more turbulent and conductor self-damping increases at the higher frequencies. Because vibration loop length is a function of wind velocity, the position of a damper is rarely the optimal one; it is only possible to select a placement that will not be located at a node. The following formula give the loop length when the line parameters

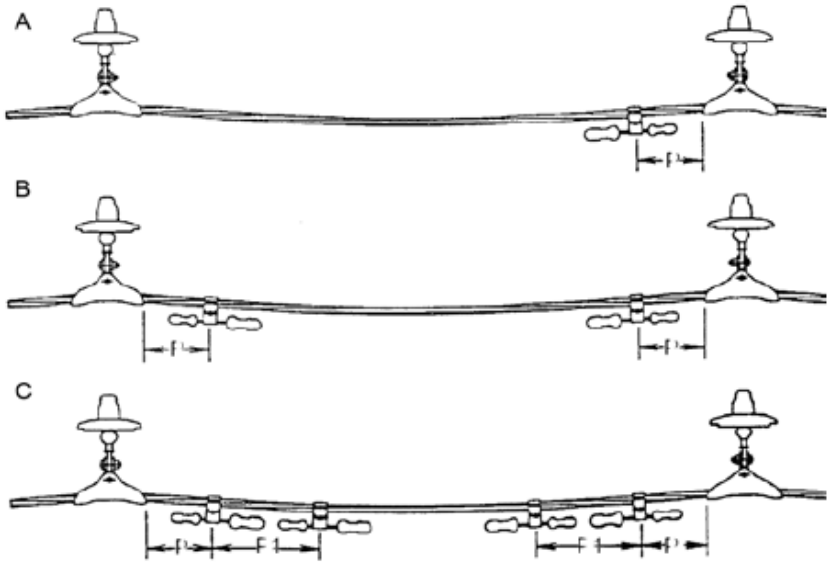

Figure 2.21: Distribution of Stockbridge dampers along the spans (EPRI, 2006).

and the wind velocity is known (EPRI, 2006):

$$l = \frac{2.703}{V_w} d \sqrt{\frac{H}{w}}, \tag{2.13}$$

where V_w is the wind velocity, l is the loop length, d is the conductor diameter, H is the conductor tension and w is the conductor mass per unit length.
A generic criterion for a damper positioning considers the installation of the damper at a distance P from the span end equal to 70-80 % of the loop length, corresponding to the maximum velocity considered. For example, considering the installation point of 80% of the shorter loop, the distance P can be calculated using the following equation (EPRI, 2006):

$$P = 0.31 d \sqrt{\frac{H}{w}}. \tag{2.14}$$

With very long span, a single damper at each end may not provide adequate protection; additional dampers can then be placed at each end spacing them along the conductor in patterns calculated to minimize the number of dampers that could simultaneously fall near a node. However this procedure is effective up to a certain limit, because the amount of damping doesn't increase in proportion to the number of dampers (EPRI, 2006).
(Nigol et al., 1985) enstablished optimum locations of dampers, with the recommendations to never place dampers at any point of symmetry along the conductor (i.e. 1/4, 1/3, 1/2, etc.). Otherwise the dampers fail to provide vibration protection at every 4^{th},

3^{rd} and 2^{nd} harmonic. One damper can be placed at a distance x_1 (1.2 to 1.8) for frequencies of 40-50 Hz and for normal design tensions. For longer span and higher tension, two dampers shall be used at distance x_1 (2.4 to 3.6 m) and x_2 (1.0 to 2.2) from the two terminals. When more than one damper is used, the ratio x_1/x_2 shall be 0.4 or 0.6.
The positioning of a damper is of paramount importance for its efficiency. In fact, if a damper or a system of dampers works satisfactorily, it reduces the conductor strain at all location in the span to a safe value, for all the frequencies in question. However, the distortion of the conductor waveform of an unsuitable damper or a damper collocated in an unsuitable position, can lead to an increase in strain in the conductor at the damper clamp and/or at the span end (Ervik et al., 1986).

2.5 Modelling of the system cable plus dampers

Several authors propose a model to describe the cable-plus-dampers system. The approach proposed by (Claren and Diana (1969), Nigol et al. (1985), Vecchiarelli (1997), Meynen et al. (2005)) is a combination of a numerical and an experimental method: the single conductor is modelled as an axially loaded Euler-Bernoulli beam and the Stockbridge damper is represented by a concentrated force on the conductor. The force is expressed in terms of the velocity of the conductor in correspondencence of the point of attachment of the damper and of the damper impedance, which are usually obtained experimentally.
The work of (Barry, 2010) is one of the starting study regarding the analysis of the transmission line aeolian vibration based on the Finite Element Method. The author attempt to depart from the aforementioned conventional method and model both conductor and damper as one unified system to take into account their two-way coupling. (Barry, 2010) demonstrates the efficacy of the Finite Element model, but the procedure proposed is quite cumbersome and computationally demanding. To avoid these shortcoming, (Barry et al., 2014) propose an analytical approach based on double-beam concept.
A recent study of (Barbieri et al., 2017) returns to the finite element modelling to take into account of the geometric nonlinearities of the cable, that are accentuated in the case of low cable load.
(Lu and Chan, 2007) develop a model for analyzing aeolian vibration of a span of a single conductor with multiple dampers. The authors combine an impedance transfer technique and a forced vibration method. The conductor is treated as a tensioned beam and dampers are caracterized by a (2x2) impedance matrix, to take into account damper's rotational effect. Modes are identified collocating a unit test load, with varying frequency, at midspan and evaluating the response of the system through a forced vibration analysis: natural frequencies corresponds to the peak responses.
The work of (Lu and Chan, 2007) is the reference point for the development of the cable plus dampers model of this thesis, as explained in detail in chapter 3.

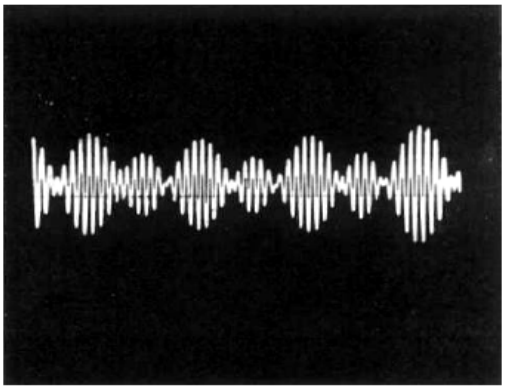

Figure 2.22: Record of aeolian conductor vibration (EPRI, 2006)

2.6 Energy Balance Method

As already described in section 2.2, the onset of aeolian vibration is defined by the matching of the Strouhal frequency with one of the natural frequencies of the conductor; once the aeolian vibration phenomenon is initiated it is self-sustained due to the lock-in effect.
The energy balance method is the most popular approach used to predict the steady-state aeolian vibration of the conductor-dampers system. This method states that the maximum amplitude of vibration for each of the excited vibration modes is the one for which the power imparted by the wind is equal to the power dissipated through the conductor self-damping plus the power dissipated by dampers. This power balance is expressed through the following equation:

$$P_w = P_d + P_c, \tag{2.15}$$

where P_w represents the wind power, P_d is the power dissipated by the dampers and P_c is the power dissipated through conductor self-damping.
The first drawback of the Energy Balance Method is that it is based on the assumption of mono-modal vibrations. Whereas, due to the wind variation in time and along the span, more than one vibration mode at a time can be excited and so the vibration amplitude along the span exhibits a beat pattern (Figure 2.22)(EPRI (2006), Vecchiarelli et al. (2000), Richardson (1996)). When more than one frequency is excited, the span vibration is no longer represented by a sinusoidal function and no vibration nodes are observed. Furthermore, as emphasized in (EPRI, 2006), it must be kept in mind that, in reality, the wind structure cannot be represented by a stationary random process with constant mean value. In fact, if the mean wind changes, a continuous transient condition is experienced by the cable and aeolian vibration maximum amplitude can never be reached. However, the reliability of results of the Energy Balance Principle is no better than the background data used in them, particularly data on the power supplied by the wind during aeolian vibration and data of self-damping in stranded

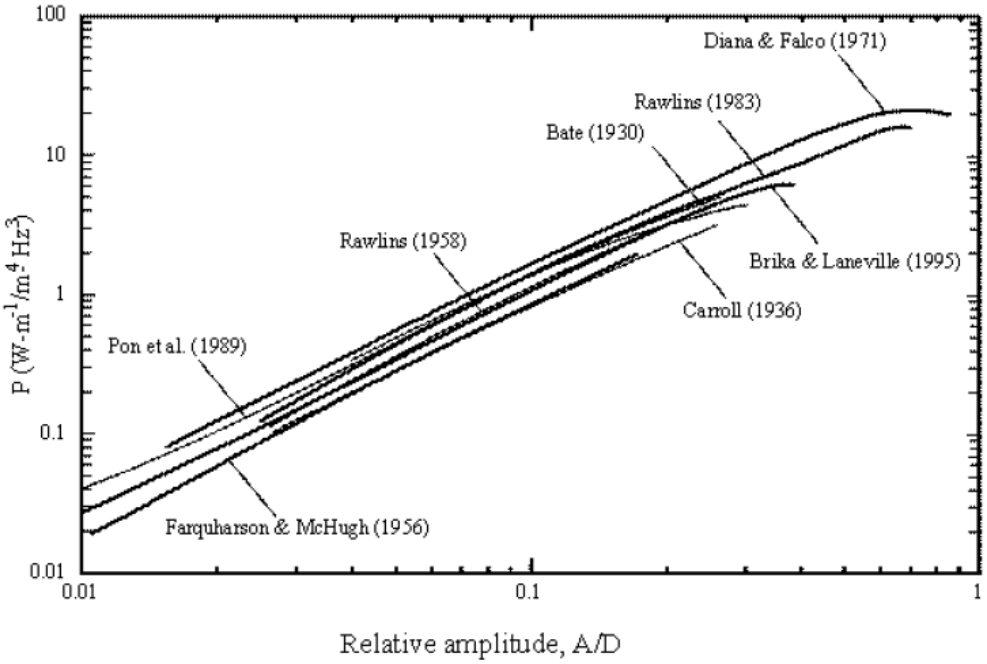

Figure 2.23: Maximum wind power input coefficient per unit length in the case of a solitary conductor (EPRI, 2006).

conductors.

2.6.1 The wind power input

The wind energy input can be evaluated through wind tunnel tests, but it must be taken into account that the wind tunnel tests to evaluate the maximum energy input are made on rigid or flexible cylinders, leading to different results. Figure 2.23 shows the experimental data of the maximum power coefficient measured by several researchers. The curves representing the flexible cylinder tests are in Rawlins (1983) and Brika and Laneville (1995), while all the others represent the rigid cylinder tests.

Attention must be paid to the fact that the maximum wind energy input based on a rigid cylinder represent a conservative choice, whereas, the maximum wind energy input based on flexible cylinder is less so in the real case, because, due to the beating phenomenon, no nodes are present (EPRI (2006), Vecchiarelli (1997)).
Most of the empirical functions, derived from wind tunnel tests, for a wind power imparted by a unit length of conductor P_w, can be expressed in the following form (see e.g. EPRI (2006), Langlois and Legeron (2014b), Vecchiarelli (1997)):

$$P_w = f^3 D^4 fnc(A/D), \tag{2.16}$$

where f is the vibration frequency, D is the conductor diameter, A/D is the nondimen-

sional antinode amplitude of vibration and the *fnc(A/D)* are reported in Figure 2.23. An analytical expression for the *fnc(A/D)* is given, as an example, in the IEC standard 61897 (IEC 61897 1998) (EPRI, 2006):

$$fnc(A/D) = 10^z \tag{2.17}$$

where

$$z = \sum_{n=0}^{8} a_n X_n$$

$$X = log(A/D)$$

$$a_0 = -0.491949$$

$$a_1 = 11.8029$$

$$a_2 = -43.5532$$

$$a_3 = -78.5876$$

$$a_4 = -86.1199$$

$$a_5 = -58.1808$$

$$a_6 = -23.6082$$

$$a_7 = -5.26705$$

$$a_8 = -0.495885.$$

The coefficients depicted in Figure 2.23 are obtained for ideal laminar air flow. In nature, air flow is always turbulent to some extent, which results in a lesser power entering the system, i.e. lower vibration amplitudes.

2.6.2 Power dissipated by the conductor

The conductor itself, as previously stated, has the capability to dissipate power through the inter-strand friction mechanism. In literature empirical formulas are available to predict the power dissipation by the conductor self-damping (P_c), having the following form (see e.g EPRI (2006), Vecchiarelli et al. (2000)):

$$\frac{P_c}{L} = k\frac{A^l f^m}{T^n}, \tag{2.18}$$

where T is the conductor tensile load, A is the antinode amplitude of vibration corresponding to natural frequency *f*. k is a factor of proportionality, which depends on the conductor characteristics, l, m, n are the amplitude exponent, frequency exponent and tension exponent, respectively. Table 2.1 summarizes the exponent values, determined by various authors, together with the method of measurement used (Inverse Standing Wave Ratio (ISWR) or Power Method (PT)) and the test span length.

Investigations	l	m	n	Method	Span length (m)
Tompkings et al. (1956)	2.3-2.6	5.0-6.0	1.9	ISWR	36
Claren & Diana (1969b)	2.0	4.0	2.5;3.0;1.5	PT	46
Rawlings (1983)	2.2	5.4	-	ISWR	36
Kraus & Hagedorn (1991)	2.47	5.38	2.80	PT	30
Noiseux (1991)	2.44	5.63	2.76	ISWR	63
Mech. Lab Politecnico di Milano	2.3-2.6	5.0-6.0	1.9	ISWR	36
Tompkings et al. (1956)	2.43	5.5	2	ISWR	46
Foti et al. (2017)	2	5	2	-	-

Table 2.1: Comparison of conductor self-damping empirical parameters, adapted from (EPRI, 2006).

The scattering in the values of the exponents can be related to the different experimental set-ups, measurement techniques and measurement errors.
The proportionality coefficient k should be evaluated for each particular case through experimental tests. When experimental data is missing, the following experimental rule can be used for ACSR conductor (Foti et al. (2017), Lilien (2013)):

$$k = \frac{D}{\sqrt{RTS \cdot m}}, \tag{2.19}$$

where D is the conductor diameter (mm), RTS is the Rated Tensile Strenght (kN) and m is the mass per unit of length of the cable (kg/m).
In the case that no experimental data are available, the approach proposed by (Noiseux, 1992) can be used. It is based on the so-called similarity laws for the internal damping of stranded cables in transverse vibrations, that are derived from the assumption of a hysteretic loss factor associated to the flexural rigidity of the conductor and the assumption that this loss factor is the same for all conductors of the same construction. Noiseaux proposes this expression for the power dissipated by the conductor per unit of length:

$$\frac{P_c}{L} = D^4 \sigma_{al}^{-2.76} A^{2.44} f^{5.63}, \tag{2.20}$$

where D is the overall conductor diameter (in mm) and σ_{al} is the stress in the aluminium wires (in N/m^2).
A recent study of (Foti et al., 2017) reports the following expression for the dissipated energy per unit of length of ACSR cables:

$$\frac{P_c}{L} = 4\pi^4 m^2 E I_{max} \frac{f^5 y_{max}^2}{T^2}. \tag{2.21}$$

The proposed relation express in closed form the upper-bound of the cable self-damping in the form of the power law of Equation 2.18 with exponents within the ranges defined in Table 2.1 and lead to a proportionality coefficient k which is related only to the mass and bending stiffness of the cable.

2.6.3 Power dissipated by dampers

A damper acts on a conductor in two principal ways (Ervik et al., 1986):

- it dissipates energy and thus reduces the free span amplitude,
- it determines a distortion of the deflection shape of the conductor, consequently the vibration modes of a cable plus damper differ from those of tha cable alone.

Due to point 2, it should be necessary to use a mathematical model of the system damper-plus-cable able to reproduce this distortion, to correctly evaluate the damper amplitude of vibration. Once the latter is known, the power dissipated by the damper system (P_d) can be computed through the following relation (EPRI (2006), Claren and Diana (1969)):

$$P_d = \pi F_i u_i^2 sin(\phi_i), \tag{2.22}$$

where F_i is the damper force per unit displacement of the damper clamp, as measured through a shaker test at different vibration velocities. u_i is the conductor vibration amplitude at the clamp of damper i, ϕ_i is the phase between force and displacement, as measured through a shaker test. Changing the damper force, the maximum damping that can be introduced in the system can be evaluated and from this, the formulation of the optimum damper is derived (EPRI (2006), Claren and Diana (1969)):

$$F_{opt} = \omega\sqrt{Tm} \tag{2.23}$$

$$\phi_{opt} = \pi/2. \tag{2.24}$$

F_{opt} represents the optimum force per unit displacement of the damper clamp and is a linear function of the vibration frequency *f*. ω is the circular frequency, T is the conductor tensile load, m is the conductor mass per unit length and ϕ_{opt} is the optimum phase between force and displacement.

For the evaluation of the power dissipated by the cable-plus-damper system three different possibilities are available, as already introduced in section 2.4:

- computation of the modes of vibration of the cable-plus-damper system through an analytical procedure which comprehends also a mechanical model of the damper.
- *Direct method*: the damper response to a harmonic excitation imparted to the damper clamp is directly measured by mounting the damper on a shaker in a laboratory. In this case it is not necessary the formulation of a mechanical model of the damper and the measured response can be introduced into the cable model as a force transmitted by the damper. The cable model must be able to represent the cable-damper interaction, i.e. the mode of vibration distortion due to the damper presence.
- The *Basic method* avoids the task of reproducing the cable-damper interaction: the power dissipated by the damper is directly measured on a laboratory span as a function of the cable antinode vibration amplitude at all the vibration modes of interest for the aeolian vibration phenomenon.

Chapter 3

Conductor model

In this work a somewhat new approach is developed for the modelling of the conductor-plus-dampers system, based on the concept of dynamic substructuring. In order to perform modal analysis (see chapter 5) the mechanical impedance of the overall system has to be computed. To this aim the dampers are treated as substructures connected to the conductor (principal system), in turn subdivided into a number of elements, depending on the loading conditions and on the number of dampers or other devices connected to it. The mechanical impedance is computed separately for each substructures and subsequently the assembled impedance is derived through coupling procedure.
This approach has several advantages:

- substructures can be modelled in the domain that is most appropriate, for instance experimentally obtained substructures can be combined with numerical models.
- The computational effort can be significantly reduced with respect to other numerical approaches, e.g. the Finite Element Method. Many authors model the cable-plus-dampers system using the Finite Element Method (see section 2.5), but this approach, whenever applied to the modelling of aeolian vibrations, can be very computationally demanding. Infact, as already mentioned, aeolian vibrations typically excite the higher modes of the cable, characterized by very small wavelengths; hence to properly capture these modal shapes a very refined mesh would be necessary. By contrast, with direct assembly of the impedances it is possible to directly assemble each physical element and for very simple cases this could also be done by hand.
- This procedure takes into account of the cable-dampers interaction, hence the modal shapes and the response of the system at an arbitrary excitation frequency include the distortional effect due to the presence of dampers.

The modelling of the conductor is adressed in this chapter, whereas the modelling of the Stockbridge-type damper is treated in chapter 4.
The mechanical model for the conductor-plus-dampers system is implemented in a custom design *Matlab* program, called *CBFD* (*Continuos Beams in Frequency Domain*), to

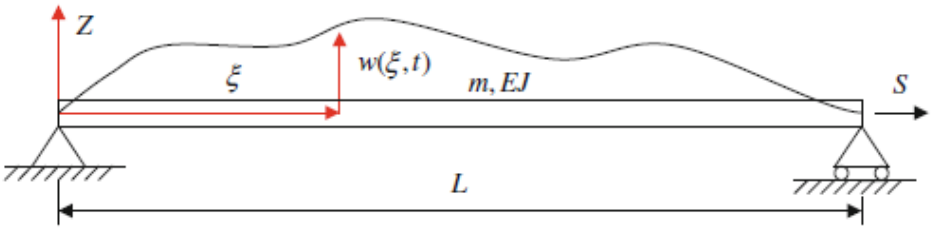

Figure 3.1: Tensioned beam (Cheli and Diana, 2015).

perform modal analysis (chapter 5) and to apply the Energy Balance Method (chapter 6) in order to predict the aeolian vibration level.

This chapter is organized as follows: section 3.1 reports the conductor equation of motion, section 3.2 derives the equation of motion for a slack cable, section 3.3 describes the element library that can be used within the Matlab code and section 3.4 shows some benchmarks to validate the conductor model.

For the derivation of section 3.1 and section 3.2 reference is made to (Geradin and Rixen, 1997) and (Cheli and Diana, 2015). Whereas the impedance computation described in section 3.3 is developed starting from the work of (Lu and Chan, 2007).

3.1 Conductor Equation of Motion

The conductor is modelled as an Euler-Bernoulli beam, with bending stiffness EI and subjected to an axial tension S (Figure 3.1).
To derive the equation of motion of the conductor the following assumptions are considered:

- the ratio of the conductor length to its diameter is very small (L/D greater than 20), hence Euler-Bernoulli beam theory can be applied.
- The conductor mass per unit of length m is uniform along the span, since the conductor diameter is constant.
- The tension S is assumed to be constant along the span. It is known that in practise the tension varies from a maximum at the clamp ends to a minimum in the middle of the conductor. However, this variation can be neglected for small and moderate span lengths (see subsection 2.3.3).
- The cable flexural stiffness EI is assumed to be constant. This assumption is reasonable since EI is small for most conductors, even if in reality the flexural rigidity varies along the span.

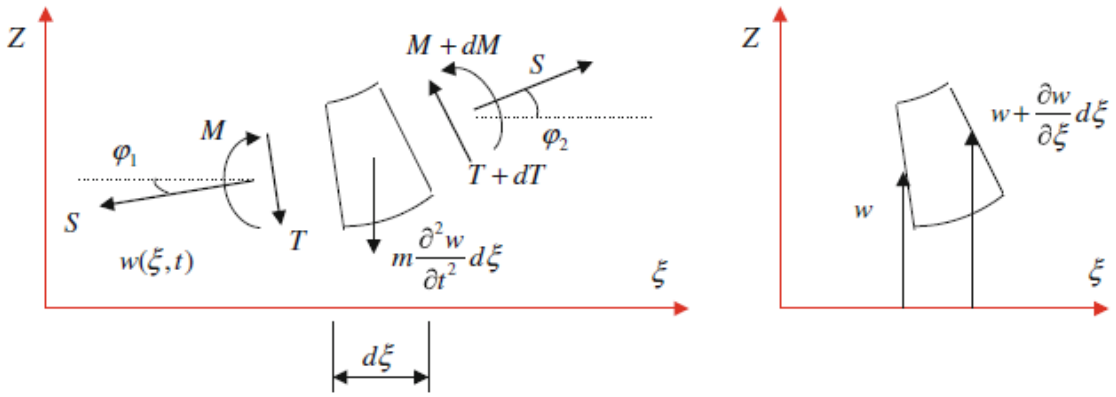

Figure 3.2: Tensioned beam: free-body diagram (Cheli and Diana, 2015).

Figure 3.2 shows the free-body diagram of a differential element of original length $d\xi$ of the conductor. $w(\xi,t)$ denotes the transverse deflection. T, M and S are respectively the shear force, bending moment and tension acting at the left-end side of the conductor element. $T+dT$, $M+dM$ and $S+dS$ are the shear force, bending moment and tension acting at the right-end side of the element. $m\dfrac{\partial^2 w}{\partial t^2}d\xi$ represents the only inertia force due to the motion of the element itself, since the rotatory inertia of the cross-sections can be neglected under the hypothesis of Euler-Bernoulli beam theory of no shear deformation. The internal actions T, M and S are functions of both space and time:

$$T = T(\xi,t) \qquad M = M(\xi,t) \qquad S = S(\xi,t). \tag{3.1}$$

The equilibrium equation with translation in a vertical direction z, disregarding the higher order infinitesimal terms, is given by:

$$-T - m\frac{\partial^2 w}{\partial t^2}d\xi + T + dT - S\sin\varphi_1 + S\sin\varphi_2 = 0 \rightarrow \frac{\partial T}{\partial \xi}d\xi - m\frac{\partial^2 w}{\partial t^2}d\xi + S\frac{\partial^2 w}{\partial \xi^2}d\xi = 0. \tag{3.2}$$

The dynamic equilibrium equation at rotation around the left side of the generic element becomes:

$$T(\xi,t) = -\left(\frac{\partial M(\xi,t)}{\partial \xi}\right). \tag{3.3}$$

By deriving Equation 3.3:

$$\frac{\partial T(\xi,t)}{\partial \xi} = -\left(\frac{\partial^2 M(\xi,t)}{\partial \xi^2}\right) \tag{3.4}$$

and substituting Equation 3.4 into Equation 3.2, it is obtained:

$$-\left(\frac{\partial^2 M(\xi,t)}{\partial \xi^2}\right) + S\left(\frac{\partial^2 w(\xi,t)}{\partial \xi^2}\right) = m\frac{\partial^2 w}{\partial t^2}. \tag{3.5}$$

The equation of motion is derived by substituting the moment-curvature relationship

$$M = EI\frac{\partial^2 w}{\partial \xi^2} \tag{3.6}$$

into Equation 3.5:

$$EI\frac{\partial^4 w}{\partial \xi^4} - S\frac{\partial^2 w}{\partial \xi^2} = -m\frac{\partial^2 w}{\partial t^2}. \tag{3.7}$$

The equation of free vibration of the beam is deduced from Equation 3.7 by assuming harmonic motion $w(\xi, t) = w(\xi)sin(\omega t)$:

$$EI\frac{d^4 w}{d\xi^4} - S\frac{d^2 w}{d\xi^2} - \omega^2 m w = 0, \tag{3.8}$$

with the associated boundary conditions at $\xi = 0$ and $\xi = l$:

- on the displacement

$$w = 0 \qquad \text{or} \qquad T = EI\frac{\partial^3 w}{\partial \xi^3} - S\frac{\partial w}{\partial \xi} = 0 \tag{3.9}$$

- on the rotation

$$\frac{dw}{d\xi} = 0 \qquad \text{or} \qquad M = EI\frac{\partial^2 w}{\partial \xi^2} = 0. \tag{3.10}$$

The equation of free vibration of the tensioned beam is the starting point for the definition of the Euler-Bernoulli beam element describing the conductor behaviour (see subsection 3.3.1).
The element library of section 3.3 includes also an Euler-bernoulli beam element without pre-stressing (subsection 3.3.2). This element is used to model the messenger cable of the Stockbridge damper, which usually is a slack cable. The derivation of the free vibration equation of the Euler-Bernoulli beam without pre-tension is reported in section 3.2.

3.2 Equation of motion for a slack cable

To take into account of the flexural stiffness, a cable without pre-tension (slack cable) can be modelled with an Euler-Bernoulli beam element. The equation of motion and the free vibration equation for this case can be obtained setting the pretension *S=0* respectively into Equation 3.7 and Equation 3.8.
Starting from the free vibration equation, the impedance of the Euler-Bernoulli beam element is derived in subsection 3.3.2.
The beam considered is homogenous, i.e. the transverse section A, bending stiffness EI and mass per unit length m is constant along the beam length. $w(\xi, t)$ represents the displacement along z of the generic section of abscissa ξ along the beam (see Figure 3.3). Figure 3.4 shows an infinitesimal beam element of length $d\xi$. M and T are respectively

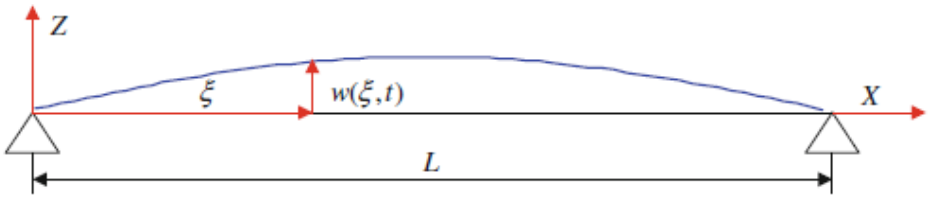

Figure 3.3: Transverse vibration in an Euler-Bernoulli beam (Cheli and Diana, 2015).

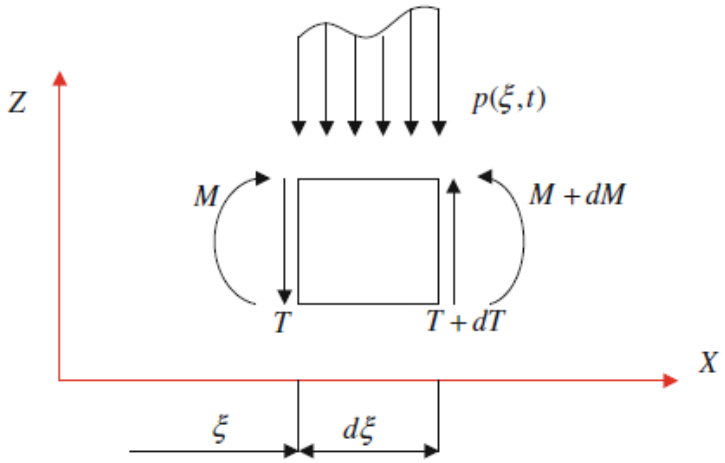

Figure 3.4: Euler-Bernoulli beam in the absence of axial load: free-body diagram (Cheli and Diana, 2015).

the bending moment and shear force that the rest of the beam exerts on the element considered and they are functions of both time and space:

$$M = M(\xi, t) \qquad\qquad T = T(\xi, t). \tag{3.11}$$

$p(\xi, t)$ represents the inertia force acting on the element:

$$p(\xi, t)d\xi = md\xi\left(\frac{\partial^2 w(\xi, t)}{\partial t^2}\right). \tag{3.12}$$

Two dynamic equilibrium equations can be written for the infinitesimal element. The equation relative to the translation in the vertical direction z, neglecting higher order terms, becomes:

$$\frac{\partial T}{\partial \xi}d\xi = md\xi\frac{\partial^2 w}{\partial t^2}. \tag{3.13}$$

The second equation is the dynamic equilibrium equation at rotation, that gives, neglecting higher order terms:

$$\frac{\partial M(\xi, t)}{\partial \xi} = -T(\xi, t). \tag{3.14}$$

Substituting Equation 3.14 into Equation 3.13, the following expression is obtained:

$$\frac{\partial^2 M}{\partial \xi^2} d\xi = -m \frac{\partial^2 w}{\partial t^2}. \tag{3.15}$$

Taking into account the moment-curvature relation of Equation 3.6, the equation of motion is derived from Equation 3.15:

$$EI \frac{\partial^4 w}{\partial \xi^4} = -m \frac{\partial^2 w}{\partial t^2}. \tag{3.16}$$

The equation of free vibration of the beam is deduced from Equation 3.16 by assuming harmonic motion $w(x,t) = w(x)sin(\omega t)$:

$$EI \frac{\partial^4 w}{\partial \xi^4} - \omega^2 m w = 0, \tag{3.17}$$

with the associated boundary conditions at $\xi = 0$ and $\xi = l$:

- on the displacement

$$w = 0 \qquad \text{or} \qquad T = EI \frac{\partial^3 w}{\partial \xi^3} = 0 \tag{3.18}$$

- on the rotation

$$\frac{dw}{d\xi} = 0 \qquad \text{or} \qquad M = EI \frac{\partial^2 w}{\partial \xi^2} = 0. \tag{3.19}$$

3.3 Element library

This section describes the types of elements used to model the conductor or the messenger cable of the Stockbridge damper in the Matlab code *CBFD*. Starting from the free vibration equation of the beam, a procedure is enstablished to compute directly the impedance matrix of each element (subsection 3.3.1 and subsection 3.3.2).
The impedance matrix of the Euler-Bernoulli beam is also computed through an alternative approach (subsection 3.3.3). It is derived through the definition of the mass matrix and stiffness matrix of each element. The latter are calculated through the software *Wolfram Mathematica* (usually termed *Mathematica*), which is equipped with an efficient system for symbolic integration.
The definition of the mass and stiffness matrix allows to introduce a viscous or hysteretic damping matrix, representing the cable self-damping. The latter is neglected in Equation 3.8 and Equation 3.17, infact no damping terms are present. This is allowed because the damping of the cable is rather small and is taken into account only in the power balance, through empirical formulas, as described in section 2.6. However, these formulas are affected by relevant uncertainties, as a small scatter in the experimental determination of their coefficients, leads to large differences in the value of the dissipated

power. Hence, the inclusion of the cable self-damping inside the conductor model can be useful to give a more realistic representation of the system behaviour, without having to rely on experimental tests.
(Noiseux, 1992) enstablishes a procedure to take into account the cable self-damping considering a complex flexural rigidity EI in Equation 3.8 and Equation 3.17. This leads to complex wavenumbers, not so easy to manage, hence, in this work, the equivalent approach described in subsection 3.3.3 is pursued.

3.3.1 Pre-stressed Euler-Bernoulli beam element: direct computation of the impedance matrix

Input and definitions

Input parameters:

- length of the element l;
- mass per unit length m;
- bending stiffness EI
- (constant) axial force S

Generalized nodal displacements and forces are shown in Figure 3.5 together with the local reference system defined on the element and the sign convention for bending moments and shear forces. Quantities with subscripts 1 and 2 are respectively referred to node 1 and 2 of the element.

Element impedance matrix

The impedance matrix of the element relates the (complex) nodal generalized forces $\mathbf{p}$ and displacements $\mathbf{q}$:

$$\mathbf{p} = \mathbf{Z} \cdot \mathbf{q}. \tag{3.20}$$

In order to evaluate the element impedance matrix $\mathbf{Z}$, the free vibration problem of the beam is first solved (see Equation 3.8).
Denoting as $w(x)$ and ω respectively: the vertical displacement of the beam centerline and the circular frequency, then free-vibrations satisfies the equation:

$$EI\frac{d^4w(x)}{dx^4} - S\frac{d^2w(x)}{dx^2} - \omega^2 m w(x) = 0. \tag{3.21}$$

The following non-dimensional parameters are introduced:

$$z = \sqrt{\sqrt{\left[\left(\frac{S}{2EI}\right)^2 + \frac{m\omega^2}{EI}\right]} + \frac{S}{2EI}} \quad and \quad a = \sqrt{\sqrt{\left[\left(\frac{S}{2EI}\right)^2 + \frac{m\omega^2}{EI}\right]} - \frac{S}{2EI}} \tag{3.22}$$

(a) *Generalized nodal displacements.*

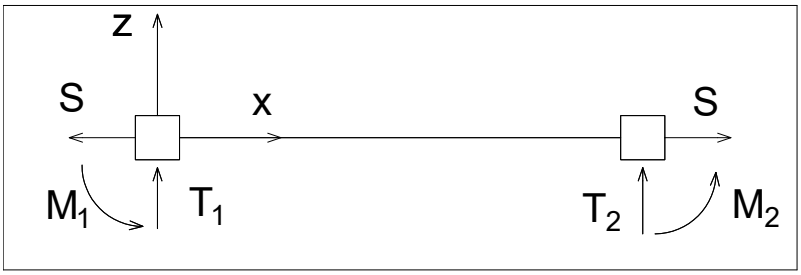

(b) *Generalized nodal forces.*

Figure 3.5: Sketch of the pre-stressed Euler-Bernoulli beam element.

The general solution of Equation 3.21 is then expressed as:

$$w(x; z, a) = \mathbf{s}(x; z, a)^T \cdot \mathbf{a}. \tag{3.23}$$

where $\mathbf{s}$ is a column vector collecting linear combinations of trigonometric and hyperbolic functions, having the following expression:

$$\mathbf{s}(x; z, a) = \begin{bmatrix} e^{-zx} \\ e^{[z(x-l)]} \\ sin(ax) \\ cos(ax) \end{bmatrix}. \tag{3.24}$$

$\mathbf{a}$ is a vector of integration constants which depends on the boundary conditions at the nodes of the element.
Starting from Equation 3.23 and denoting with an apex derivation with respect to x, the nodal generalized displacements can be expressed as a function of the unkwnown integration constants listed in $\mathbf{a}$:

$$\mathbf{q}(z, a) = \mathbf{A}(z, a) \cdot \mathbf{a}. \tag{3.25}$$

$\mathbf{A}(z, a)$ is a (4x4) matrix, containing the following quantities:

$$\mathbf{A}(z,a) = \begin{bmatrix} \mathbf{s}(x=0;z,a)^T \\ \mathbf{s'}(x=0;z,a)^T \\ \mathbf{s}(x=l,z,a)^T \\ \mathbf{s'}(x=l,z,a)^T \end{bmatrix}. \tag{3.26}$$

According to the definitions here adopted (see Figure 3.5), the bending moment and the shear force along the element can be expressed respectively as $M(x) = EI\dfrac{d^2w(x)}{dx^2}$ and $T(x) = -EI\dfrac{d^3w(x)}{dx^3} - S\dfrac{dw(x)}{dx}$. Also the generalized nodal forces can be expressed as a function of the unknown integration constants listed in $\mathbf{a}$. In fact, by exploiting the definitions above and by imposing the equilibrium of the element nodes, the following relation is obtained:

$$\mathbf{p}(z,a) = \mathbf{B}(z,a) \cdot \mathbf{a}. \tag{3.27}$$

$\mathbf{B}$ is a (4x4) matrix defined as:

$$\mathbf{B}(z,a) = \begin{bmatrix} EI\mathbf{s'''}(x=0,z,a)^T - S\mathbf{s'}(x=0,z,a)^T \\ -EI\mathbf{s''}(x=0,z,a)^T \\ -EI\mathbf{s'''}(x=l,z,a)^T + S\mathbf{s'}(x=l,z,a)^T \\ EI\mathbf{s''}(x=l,z,a)^T \end{bmatrix}. \tag{3.28}$$

By combining Equation 3.25 and Equation 3.27, the following expression is obtained:

$$\mathbf{p}(z,a) = \mathbf{B}(z,a) \cdot \mathbf{A}^{-1}(z,a) \cdot \mathbf{q}(z,a). \tag{3.29}$$

Finally, by comparing Equation 3.20 and Equation 3.29,the element impedance matrix $\mathbf{Z}$ is derived:

$$\mathbf{Z}(z,a) = \mathbf{B}(z,a)\mathbf{A}(z,a)^{-1}. \tag{3.30}$$

Displacement field at given frequency: solution post-processing at the element level

Once the nodal displacements are known from the solution of the structural problem, the unknown constant vector, $\mathbf{a}$, is obtained by solving Equation 3.25:

$$\mathbf{a} = \mathbf{A}^{-1}(z,a) \cdot \mathbf{q}(z,a). \tag{3.31}$$

According to the definitions introduced in section 3.3.1, the displacements of the beam centerline can be evaluated as follows:

$$w(x;z,a) = \mathbf{r}^T(x;z,a) \cdot \mathbf{q}(z,a), \tag{3.32}$$

where $\mathbf{r}^T(x;z,a)$ is a (1x4) real vector, containing the *shape functions* that allow to describe the displacement field w as a function of the nodal generalized displacements. It is defined as:

$$\mathbf{r}^T(x;\mu) = \mathbf{s}^T(x;\mu) \cdot \mathbf{A}^{-1}(\mu). \tag{3.33}$$

From Equation 3.32 and Equation 3.33 the real and imaginary parts of the displacement field are simply obtained as:

$$\Re[w(x;z,a)] = \mathbf{r}^T(x;z,a) \cdot \Re[\mathbf{q}(z,a)] \quad \text{and} \quad \Im[w(x;z,a)] = \mathbf{r}^T(x;z,a) \cdot \Im[\mathbf{q}(z,a)] \tag{3.34}$$

3.3.2 Euler-Bernoulli beam element: direct computation of the impedance matrix

Input and definitions

Input parameters:

- length of the element l;
- mass per unit length m;
- bending stiffness EI.

Generalized nodal displacements and forces are shown in Figure 3.6 together with the local reference system defined on the element and the sign convention for bending moments and shear forces. Quantities with subscripts 1 and 2 are respectively referred to node 1 and 2 of the element.

Element impedance matrix

The impedance matrix of the element relates the (complex) nodal generalized forces $\mathbf{p}$ and displacements $\mathbf{q}$:

$$\mathbf{p} = \mathbf{Z} \cdot \mathbf{q}, \tag{3.35}$$

with:

$$\mathbf{p} = \begin{bmatrix} T_1 \\ M_1 \\ T_2 \\ M_2 \end{bmatrix} \quad \text{and} \quad \mathbf{q} = \begin{bmatrix} w_1 \\ \varphi_1 \\ w_2 \\ \varphi_2 \end{bmatrix}. \tag{3.36}$$

In order to evaluate Z, the free vibration problem of the beam is first solved. Denoting as w(x) and ω respectively: the vertical displacements of the beam centerline and the circular frequency, then free-vibrations satisfies the following equation (see Equation 3.17):

$$\frac{d^4 w(x)}{dx^4} - \omega^2 \frac{m}{EI} w(x) = 0. \tag{3.37}$$

(a) *Generalized nodal displacements.*

(b) *Generalized nodal forces.*

Figure 3.6: Sketch of the Euler-Bernoulli beam element.

The problem can be restated in non-dimensional form by introducing the following non-dimensional variables: $\xi = \frac{x}{l}$ and $\eta = \frac{w}{l}$. Hence, Equation 3.37 becomes:

$$\frac{d^4\eta(\xi)}{d\xi^4} - \mu^4\eta(\xi) = 0, \tag{3.38}$$

with the following definition (non-dimensional eigenvalue):

$$\mu = l \cdot \sqrt[4]{\omega^2 \cdot \frac{m}{EI}}. \tag{3.39}$$

The general solution of Equation 3.38 can be expressed as:

$$\eta(\xi;\mu) = \mathbf{s}(\xi;\mu)^T \cdot \mathbf{a}, \tag{3.40}$$

where $\mathbf{s}$ is a column vector collecting linear combinations of trigonometric and hyperbolic functions (sometimes referred also as *Duncan functions*), having the following expression:

$$\mathbf{s}(\xi;\mu) = \begin{bmatrix} sin(\mu\xi) + sinh(\mu\xi) \\ cos(\mu\xi) + cosh(\mu\xi) \\ -sin(\mu\xi) + sinh(\mu\xi) \\ -cos(\mu\xi) + cosh(\mu\xi) \end{bmatrix}. \tag{3.41}$$

$\mathbf{a}$ is a vector of integration constants which depends on the boundary conditions at the nodes of the element.

Starting from Equation 3.40 and denoting with an apex derivation with respect to the non-dimensional coordinate ξ the nodal generalized displacements can be expressed as a function of the unkwnown integration constants listed in **a**:

$$\mathbf{q}(\mu) = \mathbf{A}(\mu) \cdot \mathbf{a}. \tag{3.42}$$

$\mathbf{A}(\mu)$ is a (4x4) matrix, containing the following quantities:

$$\mathbf{A}(\mu) = \begin{bmatrix} l \cdot \mathbf{s}(\xi = 0, \mu)^T \\ \mathbf{s'}(\xi = 0, \mu)^T \\ l \cdot \mathbf{s}(\xi = 1, \mu)^T \\ \mathbf{s'}(\xi = 1, \mu)^T \end{bmatrix}, \tag{3.43}$$

remembering that:

$$w = \eta \cdot l \quad \text{and} \quad \varphi = \frac{dw}{dx} = \frac{d(\eta \cdot l)}{d\xi} \cdot \frac{d\xi}{dx} = \frac{d\eta}{d\xi}. \tag{3.44}$$

According to the definitions here adopted (see Figure 3.6), the bending moment and the shear force along the element can be expressed respectively as $M(x) = EI\dfrac{d^2w(x)}{dx^2}$ and $T(x) = -EI\dfrac{d^3w(x)}{dx^3}$. Also the generalized nodal forces can be expressed as a function of the unknown integration constants listed in **a**. In fact, by exploiting the definitions above and by imposing the equilibrium of the element nodes, the following relation is obtained:

$$\mathbf{p}(\mu) = \mathbf{B}(\mu) \cdot \mathbf{a}. \tag{3.45}$$

B is a (4x4) matrix defined as:

$$\mathbf{B}(\mu) = \frac{EI}{l^2} \begin{bmatrix} \mathbf{s'''}(\xi = 0, \mu)^T \\ -l \cdot \mathbf{s''}(\xi = 0, \mu)^T \\ -\mathbf{s'''}(\xi = 1, \mu)^T \\ l \cdot \mathbf{s''}(\xi = 1, \mu)^T \end{bmatrix}. \tag{3.46}$$

When $\mu = 0$ (static problem), **A** is a full-rank matrix; on the other hand, **B** is singular.
By combining Eqs. 3.42 and 3.45:

$$\mathbf{p}(\mu) = \mathbf{B}(\mu) \cdot \mathbf{A}^{-1}(\mu) \cdot \mathbf{q}(\mu). \tag{3.47}$$

Finally, by comparing Equation 3.35 and Equation 3.47, the element impedance matrix **Z** is obtained:

$$\mathbf{Z}(\mu) = \mathbf{B}(\mu) \cdot \mathbf{A}^{-1}. \tag{3.48}$$

Displacement field at given frequency: solution post-processing at the element level

Once the nodal displacements are known from the solution of the structural problem, the unknown constant vector, $\mathbf{a}$, is obtained by solving Equation 3.42:

$$\mathbf{a} = \mathbf{A}^{-1}(\mu) \cdot \mathbf{q}(\mu). \tag{3.49}$$

According to the definitions introduced in section 3.3.2, the displacement of the beam centerline can be evaluated as follows:

$$w(x;\mu) = \mathbf{r}^T(x;\mu) \cdot \mathbf{q}(\mu), \tag{3.50}$$

where $\mathbf{r}^T(x;\mu)$ is a (1x4) real vector, containing the *shape functions* that allow to describe the displacement field w as a function of the nodal generalized displacements. It is defined as:

$$\mathbf{r}^T(x;\mu) = l \cdot \mathbf{s}^T(x;\mu) \cdot \mathbf{A}^{-1}(\mu). \tag{3.51}$$

From Equation 3.50 and Equation 3.51 the real and imaginary parts of the displacement field are simply obtained as:

$$\Re[w(x;\mu)] = \mathbf{r}^T(x;\mu) \cdot \Re[\mathbf{q}(\mu)] \quad \text{and} \quad \Im[w(x;\mu)] = \mathbf{r}^T(x;\mu) \cdot \Im[\mathbf{q}(\mu)] \tag{3.52}$$

3.3.3 Euler-Bernoulli beam element - computation of the stiffness, mass and damping matrices with *Mathematica*

The stiffness matrix $\mathbf{K}$ and the mass matrix $\mathbf{M}$ are derived from the expressions of the elastic and potential energy, associated to a harmonic motion with frequency ω:

$$\mathbf{q} = \bar{\mathbf{q}} \cdot e^{i\omega t}. \tag{3.53}$$

Then, the damping matrix $\mathbf{C}$ is computed multiplying $\mathbf{K}$ by the hysteretic damping coefficient μ. Substituting Equation 3.53 into Equation 3.50, the vertical displacement field can be expressed in the following way:

$$w(x;\mu;t) = \mathbf{r}^T(x;\mu) \cdot \bar{\mathbf{q}} e^{i\omega t}. \tag{3.54}$$

The derivatives of the displacement field with respect to x and time t have the following expressions:

$$\begin{aligned} w' &= \mathbf{r}'^T \cdot \bar{\mathbf{q}} e^{i\omega t}, \\ w'' &= \mathbf{r}''^T \cdot \bar{\mathbf{q}} e^{i\omega t}, \\ \dot{w} &= \mathbf{r}^T \cdot \bar{\mathbf{q}} e^{i\omega t} i\omega. \end{aligned} \tag{3.55}$$

The stiffness matrix $\mathbf{K}$ and the mass matrix $\mathbf{M}$ are derived from the expressions respectively of the potential and kinetic energy; taking into account Equation 3.55:

$$E = \frac{1}{2}\int_0^l EIw''^2 dx = \frac{1}{2}\mathbf{q}^T \int_0^l EI\mathbf{r}''\mathbf{r}''^T dx \mathbf{q} e^{i\omega t} \rightarrow \mathbf{K}(\mu) = \int_0^l EI\mathbf{r}''\mathbf{r}''^T dx \tag{3.56}$$

$$T = \frac{1}{2}\int_0^l m\ddot{w}^2 dx = -\frac{1}{2}\omega^2 \mathbf{q}^T \int_0^l m\mathbf{r}\mathbf{r}^T dx \mathbf{q} e^{i\omega t} \rightarrow \mathbf{M}(\mu) = \int_0^l m\mathbf{r}\mathbf{r}^T dx. \tag{3.57}$$

Then, the impedance of the element $\mathbf{Z}$ can be expressed as:

$$\mathbf{Z}(\mu) = \mathbf{K}(\mu) - \omega^2\mathbf{M}(\mu) + i\mathbf{C}(\mu), \tag{3.58}$$

where $\mathbf{C}$ represents the hysteretic damping matrix: $\mathbf{C} = \mu\mathbf{K}$. $\mathbf{K}$ and $\mathbf{M}$, as previously mentioned, are integrated with *Mathematica*; the result of the integration are reported in Appendix A.
The introduction of the hysteretic damping matrix allows to model the behavior of the messenger cable and therefore of the Stockbridge-type damper, as illustrated in chapter 4.

For a first validation of the element in exam, two checks are carried out:

- as the circular frequency $\omega \rightarrow 0$, which implies that also $\mu \rightarrow 0$ (see Equation 3.39), the stiffness matrix $\mathbf{K}(\mu)$ has to tend to the static stiffness matrix $\mathbf{K}_{static}$:

$$\mathbf{K}_{static} = \begin{bmatrix} \frac{12EI}{l^3} & \frac{6EI}{l^2} & -\frac{12EI}{l^3} & \frac{6EI}{l^2} \\ & \frac{4EI}{l} & -\frac{6EI}{l^2} & \frac{2EI}{l} \\ symm. & & \frac{12EI}{l^3} & \frac{4EI}{l} \\ & & & \frac{4EI}{l} \end{bmatrix}. \tag{3.59}$$

- Considering the case without damping, as ω^2 tend to the eigenvalues of the system in exam (e.g. for the case of the simply supported beam $\omega_n^2 = \frac{EI}{m}\left(\frac{n\pi}{l}\right)^4$) the determinant of the impedance matrix $\mathbf{Z}$ has to tend to zero: $det(\mathbf{Z}) = det(\mathbf{K} - \omega^2\mathbf{M}) \rightarrow 0$ ($\mathbf{Z}$ is a function of μ, hence in this calculation ω has to be replaced with this expression in terms of μ).

3.4 Mechanical behaviour of a single conductor

To validate the elements described in section 3.3, the natural frequencies and the vibration modes are evaluated for three different benchmarks. The first two are analized using both the Euler-Bernoulli element defined in subsection 3.3.2 and the one defined in *Mathematica* (subsection 3.3.3). In the third one an ACSR conductor is modelled with the pre-stressed Euler-Bernoulli element proposed in subsection 3.3.1.

3.4.1 Cantilever beam

A homogeneous cantilever beam with rectangular cross-section is considered. The data of the problem are listed here below:

- cross-section dimensions: width b=0.3 m and height h=0.5 m.
- Length of the beam $L = 10$ m;
- linear mass of the beam m= 375 kg/m;
- bending stiffness of the beam $EI = 109375000\ Nm^2$ (obtained considering: Young modulus E=$35 \cdot 10^9\ N/m^2$ and the moment of inertia I=$1/12bh^3$);

The expressions for the vibration eigenfrequencies ω_n^2 of a uniform cantilever beam are available in literature (see e.g. Geradin and Rixen, 1997), here the first three modes are considered:

$$\omega_n^2 = \mu_n^4 \frac{EI}{ml^4}, \tag{3.60}$$

where n=1,2,3 and $\mu_1 = 1.875$, $\mu_2 = 4.694$, $\mu_3 = 7.855$.
For the numerical model one Euler-Bernoulli beam element is used and a unit harmonic displacement is applied at the tip of the cantilever to find modes (detailed description of the procedure for mode computation is adressed in chapter 5). A frequency range bounded by 0.001 rad/s and 350 rad/s has been spanned with a step equal to 0.001 rad/s.
The analytical and numerical circular frequencies are compared in Table 3.1; the two sets of values compare very well.

Mode number	Analytical [Hz]	Numerical [Hz]	Error [%]
1	3.021791	3.022111	0.0106
2	18.93867	18.93940	0.0038
3	53.03418	53.03090	0.0062

Table 3.1: First three natural frequencies of the cantilever beam

The modal shapes corresponding to the natural frequecies computed are reported in Figure 3.7.They are adimensionalized with respect to the real component of the maximum value of the displacement along the beam. The imaginary part is null because no damping has been considered.

The same model is run using the type of element derived with *Mathematica*; the results coincide with the ones of the previous analysis.

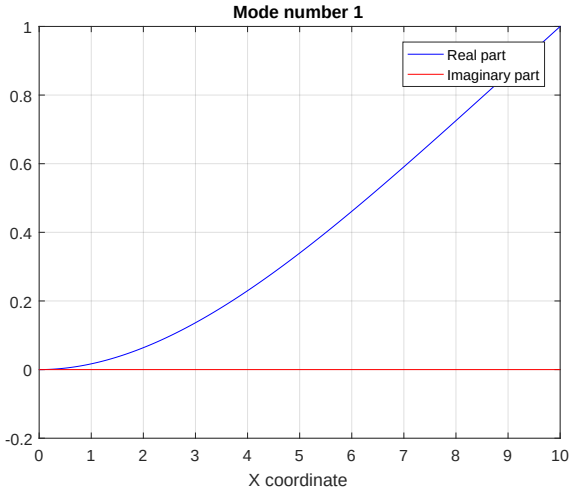

(a)

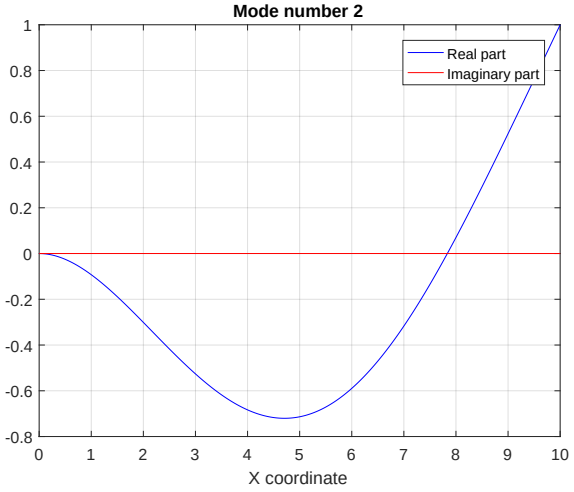

(b)

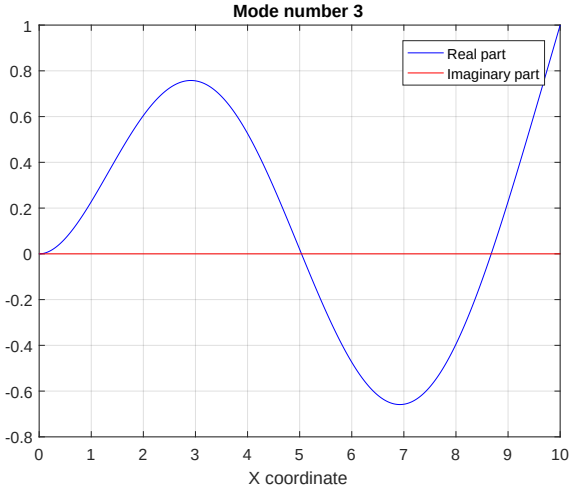

(c)

Figure 3.7: First three modes of the cantilever beam.

3.4.2 Simply supported beam

A homogeneous simply supported beam with rectangular cross-section is considered. The data of the problem are listed here below:

- cross-section dimensions: width b=0.4 m and height h=0.6 m.
- Length of the beam $L = 25$ m;
- linear mass of the beam m= 600 kg/m;
- bending stiffness of the beam $EI = 252000000\ Nm^2$ (obtained considering: Young modulus E=$35 \cdot 10^9\ N/m^2$ and the moment of inertia I=$1/12bh^3$);

Closed form analytical solution for the eigenfrequencies ω_n^2 of the simply supported beam are available in literature (see e.g. Geradin and Rixen, 1997):

$$\omega_n^2 = \frac{(n\pi)^4 EI}{ml^4}. \tag{3.61}$$

Also in this case the first three eigenfequencies are considered.
For the numerical model one Euler-Bernoulli beam element is used and a unit harmonic rotation is applied in correspondence of the first support (node 1) to find modes. A frequency range bounded by 0.001 rad/s and 100 rad/s has been spanned with a step equal to 0.001 rad/s.
The analytical and numerical circular frequencies are compared in Table 3.2; the two sets of values compare very well.

Mode number	Analytical [Hz]	Numerical [Hz]	Error [%]
1	1.62879	1.62871	0.0049
2	6.51517	6.51517	0.0000
3	14.6591	14.6590	0.0007

Table 3.2: First three natural frequencies of the simply supported beam

The modal shapes corresponding to the natural frequecies computed are reported in Figure 3.8. The results using the beam element derived in *Mathematica* coincide with the ones reported in Table 3.2.

3.4.3 Drake conductor

An example, concerning the evaluation of the natural frequencies and vibration modes of an undamped conductor, taken from (EPRI, 2006), is considered. The data of the problem are listed here below:

- Drake conductor;

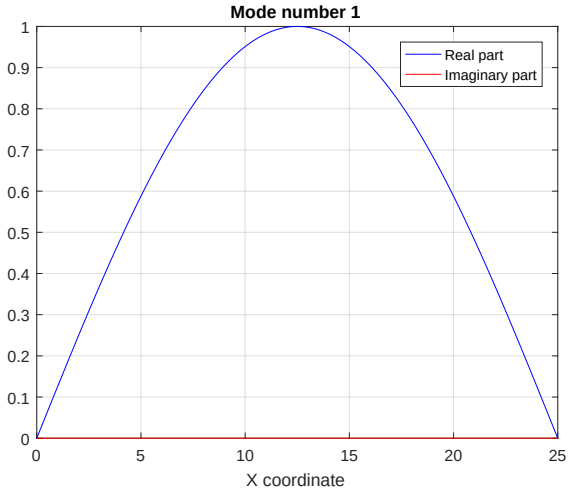

(a)

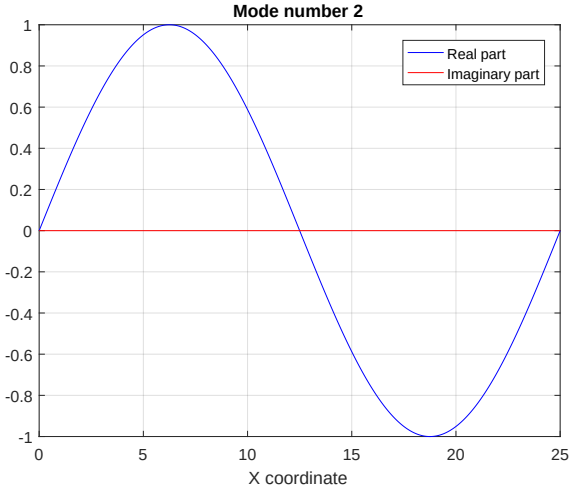

(b)

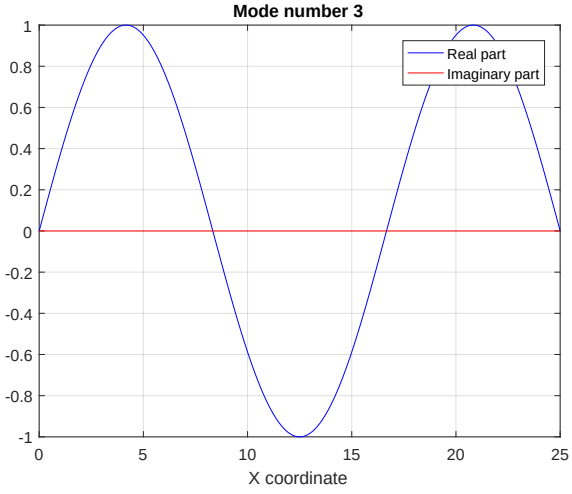

(c)

Figure 3.8: First three modes of the simply supported beam.

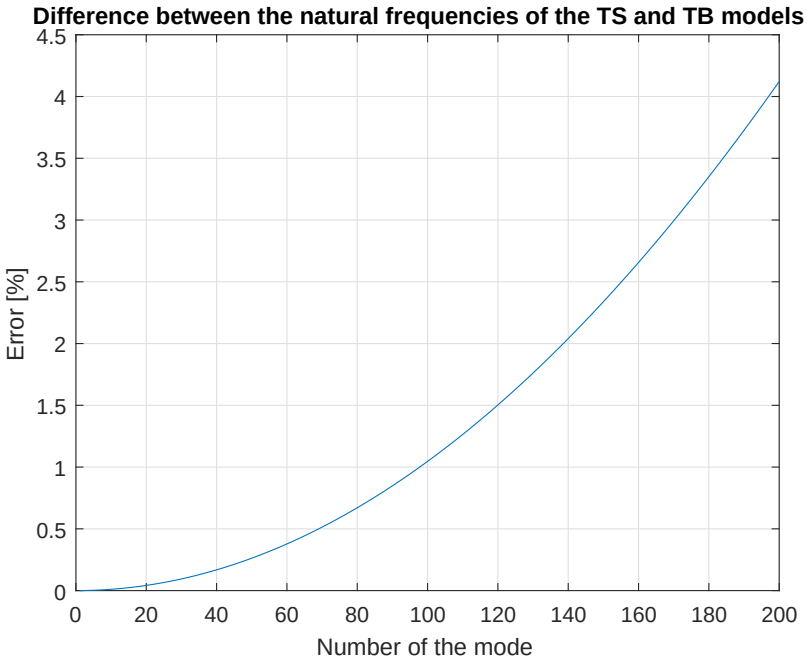

Figure 3.9: Difference between the natural frequencies evaluated with the Taut Beam (TB) model and with the Taut String (TS) one.

- length of the cable L = 366 m;
- linear mass of the cable m= 1.628 kg/m;
- axial force in the cable S = 28.024 kN (≈ 20% of the ultimate tensile strength (UTS));
- bending stiffness of the cable EI = 0.5 EImax = 800 Nm^2;
- pinned ends.

Closed form analytical solutions are available both for the *Taut String* (TS) model as well as for the *Taut Beam* (TB) one, as reported in subsection 2.3.3.

The natural frequencies of the cable have been evaluated according to both models. As shown in Figure 3.9, the results differ of less than the 4.5 % considering the first 200 modes of the structure.

A mesh of two equally spaced elements is considered for the numerical model. Symmetric modes are found by applying an unitary harmonic displacement at the midspan; skew-symmetric modes are found by applying an unitary rotation at midspan. A frequency range bounded by 0.001 rad/s and 250 rad/s has been spanned with a step equal to 0.001 rad/s.

The results of the model are compared with those of the TB analytical model and, as can be seen from Table 3.3 and Table 3.4, predictions of the two models match very well.

Mode number	TB analytical [Hz]	Numerical [Hz]	Error [%]
1	0.17922368	0.1792880	0.0359
2	0.53771499	0.53770500	0.0018
3	0.89620673	0.89628110	0.0083
4	1.2547211	1.2546980	0.0018
5	1.6132671	1.6132741	0.0004
50	17.96239	17.92634	0.2010
100	37.12382	37.12377	0.0001

Table 3.3: Symmetric modes

Mode number	TB analytical [Hz]	Numerical [Hz]	Error [%]
1	0.3584748	0.3584965	0.0060
2	0.71695860	0.71691344	0.0063
3	1.0754605	1.0754895	0.0027
4	1.4339896	1.4340656	0.0053
5	1.7925548	1.7924825	0.0040
50	18.11118	18.11112	0.000331
100	37.32482	37.32478	0.000107

Table 3.4: Skew-symmetric modes

The modal shapes of the first 5 symmetric and skew-symmetric modes along with mode 50 and mode 100, evaluated by the numerical model are shown in Figure 3.10 and Figure 3.11. For mode 50 and 100 also a zoom of the symmetric and skew-symmetric modal shapes near the left support are reported in Figure 3.12.
It can be noticed that, looking at the just mentioned figures, to reproduce the higher order modes, a Finite Element model would require a very refined mesh, whereas only two elements are here used.

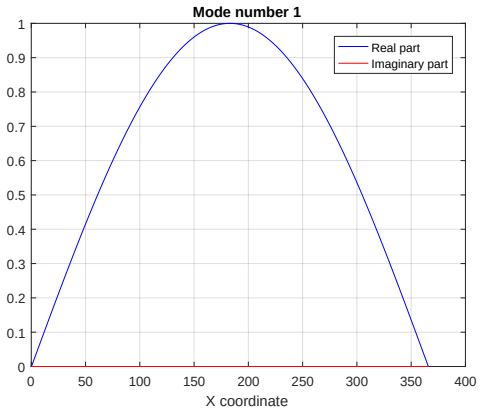

(a) *Symmetric mode number 1*

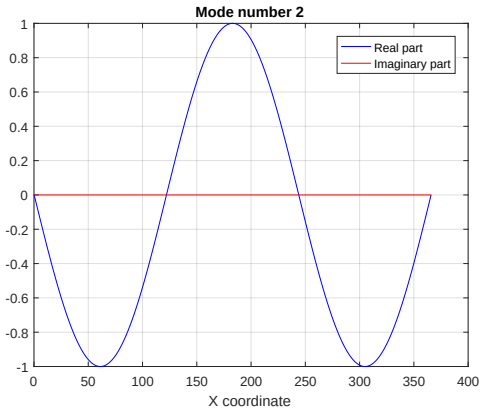

(b) *Symmetric mode number 2*

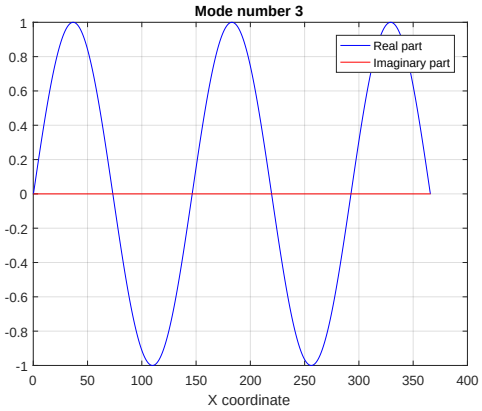

(c) *Symmetric mode number 3*

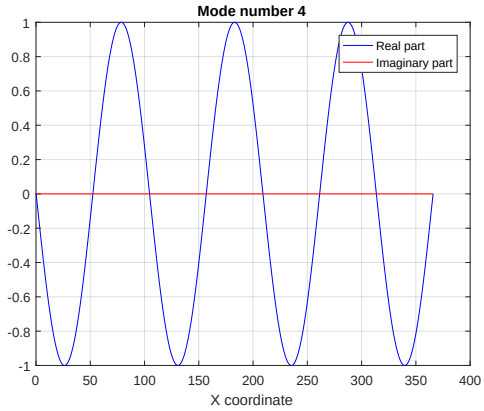

(d) *Symmetric mode number 4*

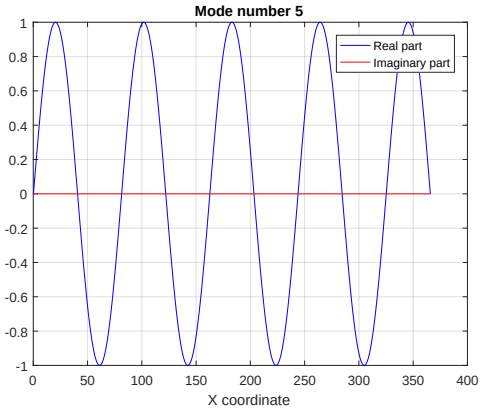

(e) *Symmetric mode number 5*

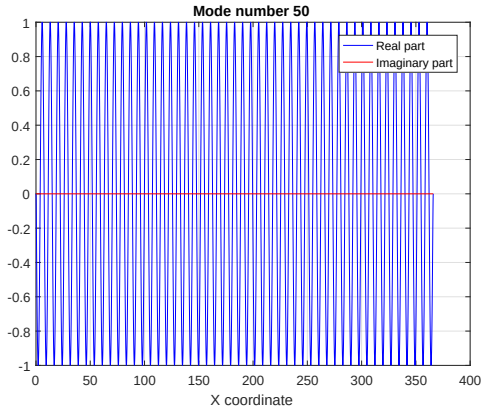

(f) *Symmetric mode number 50*

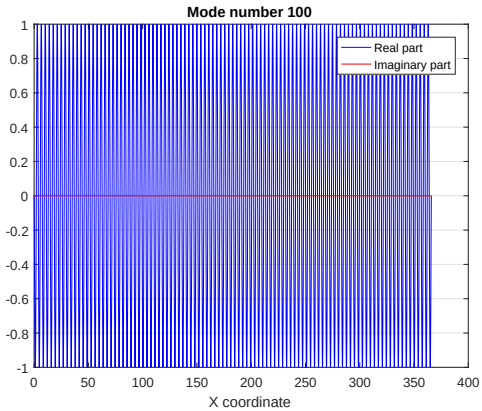

(g) *Symmetric mode number 100*

Figure 3.10: Symmetric modal shapes.

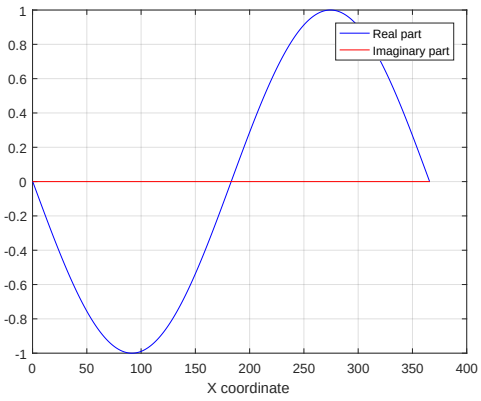

(a) *Skew-symmetric mode number 1*

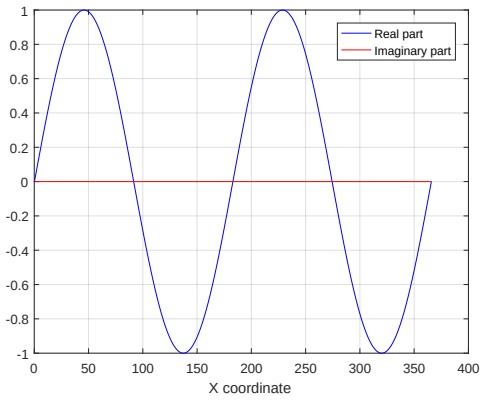

(b) *Skew-symmetric mode number 2*

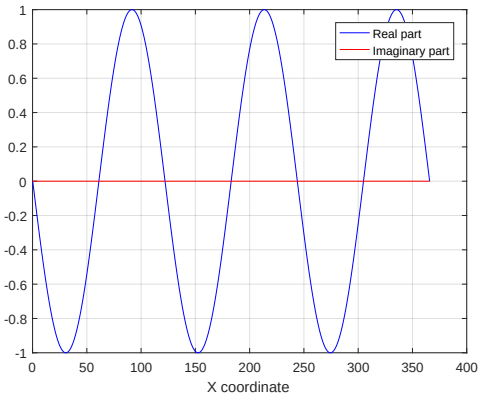

(c) *Skew-symmetric mode number 3*

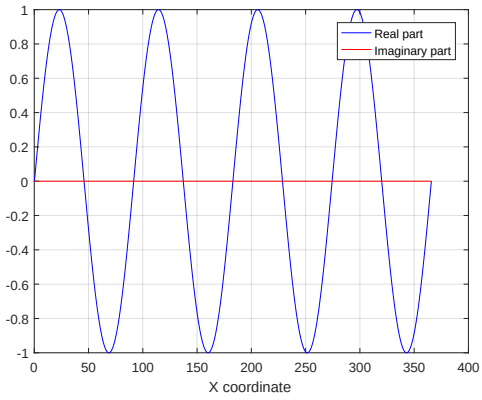

(d) *Skew-symmetric mode number 4*

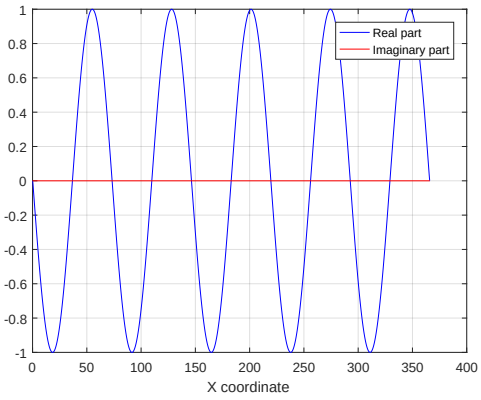

(e) *Skew-symmetric mode number 5*

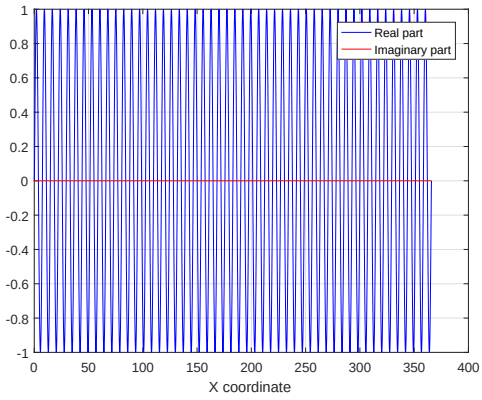

(f) *Skew-symmetric mode number 50*

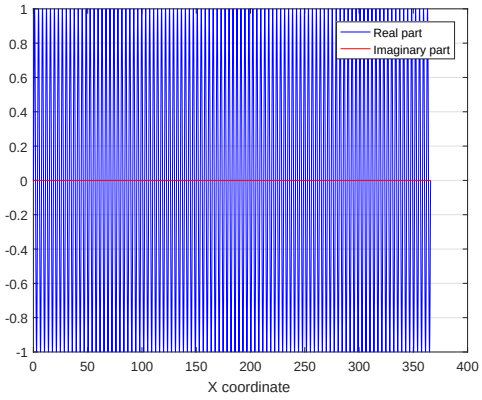

(g) *Skew-symmetric mode number 100*

Figure 3.11: Skew-symmetric modal shapes.

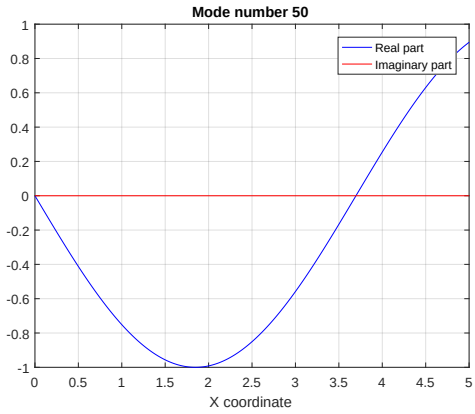

(a) *Symmetric mode number 50: zoom in correspondence of the left support.*

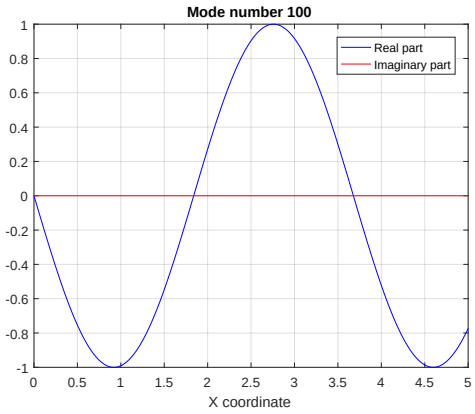

(b) *Symmetric mode number 100: zoom in correspondence of the left support.*

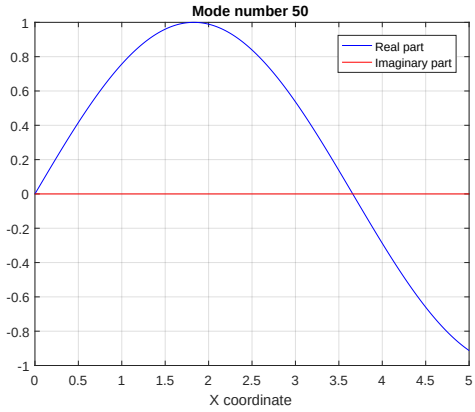

(c) *Skew-symmetric mode number 50: zoom in correspondence of the left support.*

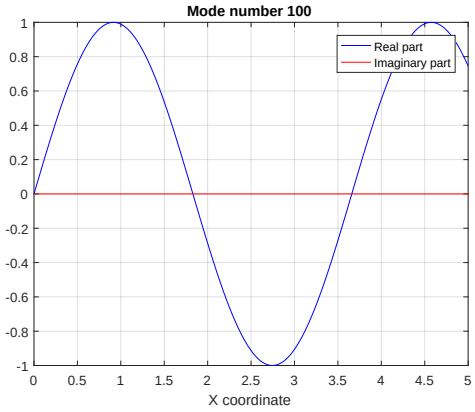

(d) *Skew-symmetric mode number 100: zoom in correspondence of the left support.*

Figure 3.12: Zoom of the symmetric and skew-symmetric modal shapes near the left support.

Chapter 4

Stockbridge damper model

The Stockbridge-type damper is the most common type of transmission line damper. Despite its apparently simple structure, its modelling is not so straightforward.
In this work two linear model are proposed: *linear model 1* and *linear model 2*. Both model describe each arm of the Stockbridge damper as a cantilever beam with a lumped tip mass and fix constraint. The base motion, i.e. the movement of the clamp due to the conductor vibration, is translated into inertia generalized forces acting in correspondence of the centroid of the concentrated mass. Then, through equilibrium consideration, the force at the clamp and thus the impedance of the damper are derived. Both models are based on a beam-like description of the messenger cable. *Linear model 1* treats the messenger cable as a massless Euler-Bernoulli beam, hence the mass matrix $\mathbf{M}$ of the system coincides with that of the damper and the stiffness matrix $\mathbf{K}$ is composed by the usual coefficients of the static stiffness matrix of an Euler-bernoulli beam.
Linear model 2 describes the messenger cable as the Euler-Bernoulli beam described in subsection 3.3.3, hence its mass contributes to the mass matrix of the system. Using, this type of element, both $\mathbf{M}$ and $\mathbf{K}$ are functions of the exciting frequency.
The hysteretic damping of the messenger cable is taken into account, in both models, with two distinct modal damping parameters; this is necessary to correctly reproduce the frequency and amplitude of the two peaks of the damper response.
The common starting point for the definition of the two models is the derivation of the equations of motion for the Stockbridge damper, adressed in section 4.1).
section 4.4 describes how the impedance of the Stockbridge damper is taken into account and assembled inside the Matlab code *CBFD*. Finally, in section 4.5, two benchmarks are proposed to validate the Stockbridge model 1 and 2.

4.1 Equations of motion of Stockbridge dampers

As already described in section 2.4, the Stockbridge damper is composed by a short metallic strand, known as the "messenger cable", and two rigid bodies attached at its extremities. The connection between the damper and the suspended cable is ensured by means of a rigid clamp. When the device is actuated through a clamp motion, the

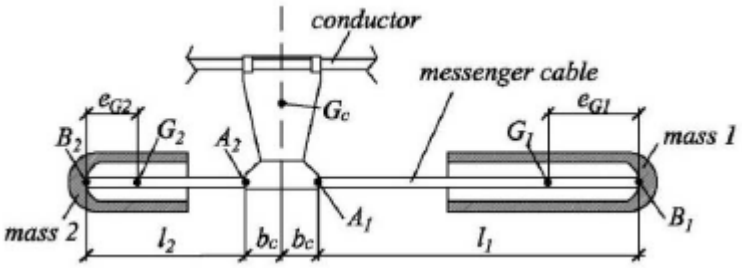

(a)

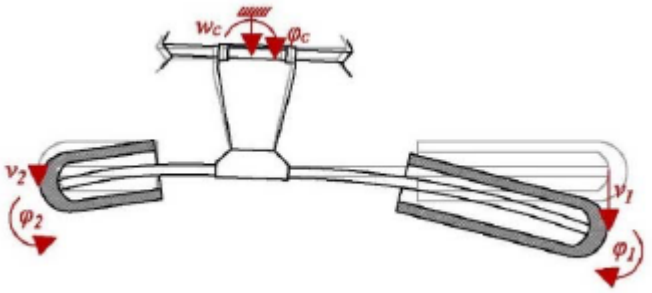

(b)

Figure 4.1: (a) Schematic representation of a Stockbridge dampers. (b) Kinematics of the damper (Foti and Martinelli, 2018)

.

two sides of the messenger cables behave basically as cantilevers with lumped masses at their ends.
A schematic representation of a Stockbridge damper is depicted in Figure 4.1.

The damping device is connected to the cable through a rigid clamp, which prevents relative displacements and rotations at the interface (points A_1 and A_2 in Figure 4.1). A rigid body is attached at the end of each branch of the messenger cable (points B_1 and B_2 in Figure 4.1). Several different design options have been proposed for these bodies (EPRI, 2006); here it is assumed that the connection between them and the messenger cables can be modeled as perfectly rigid.
When the suspended cable undergoes in-plane oscillations, as it is usually assumed to study aeolian vibrations, the clamp translates and rotates rigidly, following the motion of the cable. Then, the two sides of the messenger cable behave basically as uncoupled planar cantilevers, with lumped masses at their ends, subject to a prescribed support motion (Foti and Martinelli, 2018). The dynamic behaviour of each arm of the damper can be described in terms of two Lagrangian coordinates, representing the vertical translation and the rotation of the lumped mass. In the following it is denoted as v_i and φ_i, respectively: the relative downward vertical displacement with respect to the clamp and the clockwise rotation of the ith mass of the damper (see Figure 4.1).

Under the assumption of small displacements and rotations, the vertical translation of the centroid of the ith damper mass w_{Gi} can be expressed as:

$$w_{Gi} = v_i - e_{Gi}\varphi_i + w_c + \varepsilon_i b_c \varphi_c, \tag{4.1}$$

with $\varepsilon_i = (-1)^{i-1}$ and i=1,2. e_{Gi} represents the distance between the centroid of the ith mass and the tip section B_i of the messenger cable; b_c is the characteristic length of the clamp shown in Figure 4.1.
The equations of motion of each mass of the damper are derived in subsection 4.1.1, considering a generic input motion of the clamp. Then, starting from the knowledge of the motion of the damper masses, general closed-form expressions to evaluate the forces acting at the clamp of the damper are obtained in subsection 4.1.2.

4.1.1 Equations of motion of the damper masses

For a generic combination of translation (w_c) and rotation (φ_c) of the clamp, the dynamic configuration of the ith mass of the Stockbridge damper can be described by means of the two Lagrangian coordinates previously introduced: the relative displacement v_i of the end section of the messenger cable (B_i) with respect to the clamped section (A_i) and the rotation of the mass φ_i.
To derive the equations of motion of the damper masses, the clamp is considered as fixed, and the imposed displacement v_c and imposed rotation φ_c are accounted for through inertia forces applied in correspondence of the centroid of the damper masses.

The kinetic energy T_i of the system is expressed as a function of the Lagrangian coordinates v_i and φ_i:

$$T_i = \frac{1}{2} m_i \dot{w}_{Gi}^2 + \frac{1}{2} I_{Gi} \dot{\varphi}_i{}^2, \tag{4.2}$$

where $w_{Gi} = v_i - e_{Gi}\varphi_i$, I_{Gi} is the moment of inertia of the ith mass with respect to its centroid and the dot denotes derivative with respect to time. Substituting the expression of w_{Gi} in Equation 4.2, the kinetic energy can be rewritten as:

$$T_i = \frac{1}{2}[m_i \dot{v}_i{}^2 + (m_i e_{Gi}^2 + I_{Gi})\dot{\varphi}_i^2 - 2 m_i e_{Gi} \dot{v}_i \dot{\varphi}_i]. \tag{4.3}$$

The mass matrix of the ith damper masses $\mathbf{M_{di}}$ is obtained through inspection of Equation 4.3:

$$\mathbf{M_{di}} = \begin{bmatrix} m_i & -m_i e_{Gi} \\ -m_i e_{Gi} & I_{Gi} + m_i e_{Gi}^2, \end{bmatrix} \tag{4.4}$$

The term $I_{Gi} + m_i e_{Gi}^2$ represents the moment of inertia of the mass i with respect to the end section of the messenger cable B_i (Huygens-Steiner theorem).
Considering a generic translation w_c and rotation φ_c of the clamp, the generalized inertia forces can be expressed in the following way:

$$\begin{cases} F_i^{iner} = -m_i \ddot{w}_{Gi} = -m_i(\ddot{v}_i - e_{Gi}\ddot{\varphi}_i + \ddot{w}_c + \varepsilon_i b_c \ddot{\varphi}_c) & \text{(4.5a)} \\ M_i^{iner} = -I_{Gi}(\ddot{\varphi}_i + \ddot{\varphi}_c). & \text{(4.5b)} \end{cases}$$

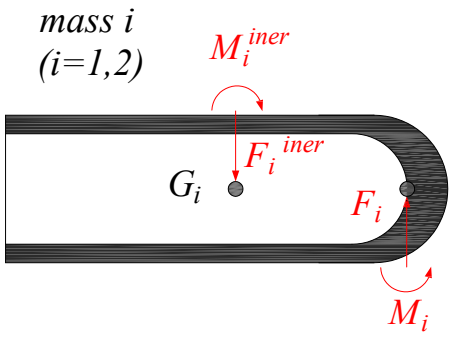

Figure 4.2: Dynamic equilibrium of the *ith* damper mass.

Imposing the dynamic equilibrium of the ith damper mass, the equations of motion are obtained. Figure 4.2 shows the forces acting on the damper mass; F_i and M_i respresent the generalized restoring forces exerted by the messenger cable.

Imposing vertical translational equilibrium and rotational equilibrium with respect to point B_i, the following system of equation is obtained:

$$\begin{cases} -F_i^{iner} + F_i = 0 & \text{(4.6a)} \\ -M_i^{iner} + M_i + F_i^{iner} e_{Gi} = 0. & \text{(4.6b)} \end{cases}$$

By substituting in Equation 4.6a and Equation 4.6b the expressions of the generalized inertia forces (Equation 4.5a and Equation 4.5b), the sought equations of motion are obtained:

$$\begin{cases} m_i \ddot{v}_i(t) - m_i e_{Gi} \ddot{\varphi}_i(t) + F_i(v_i, \varphi_i, t) = -m_i \ddot{w}_c(t) - m_i \varepsilon_i b_c \ddot{\varphi}_c(t) & \text{(4.7a)} \\ -m_i e_{Gi} \ddot{v}_i(t) + (I_{Gi} + e_{Gi}^2 m_i) \ddot{\varphi}_i(t) + M_i(v_i, \varphi_i, t) = m_i e_{Gi} \ddot{w}_c(t) + \\ m_i e_{Gi} \varepsilon_i b_c \ddot{\varphi}_c(t). & \text{(4.7b)} \end{cases}$$

4.1.2 Generalized forces acting at the damper clamp

The external force F_c and moment M_c acting at the clamp can be evaluated through simple equilibrium considerations.
At a generic instant of time t the forces acting on the clamp are the external force and moment F_c and M_c, the shear forces and bending moment exerted by each side of the messenger cable on the clamp and the generalized inertia forces due to both the translational and the rotational inertia of the clamp F_c^{iner} and M_c^{iner}. The latter can be expressed as: $F_c^{iner} = m_c \ddot{w}_c$ and $M_c^{iner} = I_{Gc} \ddot{\varphi}_c$, where m_c and I_{Gc} represent, respectively, the mass of the clamp and the moment of inertia with respect to its centroid. Figure 4.3 shows all the forces just mentioned.

The external force F_c and M_c are obtained imposing vertical translational and rotational equilibrium of the clamp:

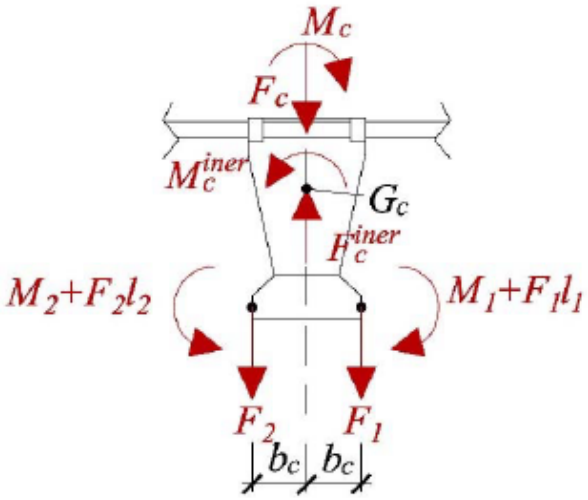

Figure 4.3: Dynamic equilibrium of the clamp (Foti and Martinelli, 2018)

$$\begin{cases} F_c = F_c^{iner} - (F_1 + F_2) & \text{(4.8a)} \\ M_c = M_c^{iner} + M_2 - M_1 + F_2(l_2 + b_c) - F_1(l_1 + b_c) & \text{(4.8b)} \end{cases}$$

By taking into account the equations of motion of the damper masses (Equation 4.7a and Equation 4.7b), Equation 4.8a and Equation 4.8b can be re-written in the following way:

$$\begin{cases} F_c = (m_1 + m_2 + m_c)\ddot{w}_c + (m_1 - m_2)b_c\ddot{\varphi}_c + m_1\ddot{v}_1 + m_2\ddot{v}_2 - m_1 e_{G1}\ddot{\varphi}_1 \\ \qquad -m_2 e_{G2}\ddot{\varphi}_2 & \text{(4.9a)} \\ M_c = (m_1 l_1^* - m_2 l_2^* +)\ddot{w}_c + (I_{Gc} + m_1 b_c l_1^* + m_2 b_c l_2^*)\ddot{\varphi}_c + m_1 l_1^*\ddot{v}_1 \\ \qquad -m_2 l_2\ddot{v}_2 + (I_{G1} - m_1 e_{G1} l_1^*)\ddot{\varphi}_1 - (I_{G2} - m_2 e_{G2} l_2^*)\ddot{\varphi}_2, & \text{(4.9b)} \end{cases}$$

where $l_i^* = l_i + b_c - e_{Gi}$ and i=1,2.

For the case of symmetric Stockbridge dampers, the general Equation 4.9a and Equation 4.9b can be re-written as:

$$\begin{cases} F_c = (2m_d + m_c)\ddot{w}_c + 2m_d\ddot{v}_d - 2m_d e_{Gd}\ddot{\varphi}_d & \text{(4.10a)} \\ M_c = (I_{Gc} + 2m_d b_c l_d^*)\ddot{\varphi}_c, & \text{(4.10b)} \end{cases}$$

where m_d, I_{Gd} and e_{Gd} are the relevant inertial and geometric properties of the damper masses. l_d* is defined as $l_d^* = l_1 + b_c - e_{G1} = l_2 + b_c - e_{G2}$, while $v_1 = v_2 = v_d$ and $\varphi_1 = \varphi_2 = \varphi_d$ are, respectively, the relative vertical displacement and the rotation of the damper masses.

4.1.3 Introduction of the damping model

The purpose of the procedure proposed here below is the definition of a different damping coefficient for each mode.
The following hypotheses are considered:

- symmetric damper,
- messenger cable with linear elastic sectional behaviour, such that $M(x) = EI\chi(x)$ where:

  x is the abscissa along the cable axis;

  M is the bending moment;

  χ is the curvature;

  EI is the flexural stiffness.
- Only the effect of a vertical displacement of the clamp $w_c = w_c(t)$ is considered.

The Lagrangian coordinates v (downward vertical displacement of the end section of the messenger cable) and ϕ (clockwise rotation of the end section of the messenger cable) are collecting in vector $\mathbf{q}$:

$$\mathbf{q} = \begin{bmatrix} v \\ \varphi \end{bmatrix} \tag{4.11}$$

Equations of motion for the undamped system

Considering the aforementioned hypotheses, the equation of motion 4.7a and 4.7b for the undamped system can be rewritten in the following form:

$$\begin{cases} m\ddot{v} - me_G\ddot{\varphi} + F = -m\ddot{w}_c & \text{(4.12a)} \\ -me_G\ddot{v} + (I_G + me_G^2)\ddot{\varphi} + M = me_G\ddot{w}_c. & \text{(4.12b)} \end{cases}$$

At this point, it is introduced the mass matrix $\mathbf{M}$ and the stiffness matrix $\mathbf{K}$ of the system, whose expressions are different based on the model considered, as specified in section 4.2 and section 4.3.
The equations of motion can be rewritten as:

$$\mathbf{M}\ddot{\mathbf{q}}(t) + \mathbf{K}\mathbf{q}(t) = \mathbf{F}\ddot{w}_c(t), \tag{4.13}$$

where the vector $\mathbf{F}$ has the following expression: $\mathbf{F} = \{-m; me_G\}^T$. The force F_c and the moment M_c transmitted by the clamp to the conductor can be computed in the following way:

$$\begin{cases} F_c = (2m + m_c)\ddot{w}_c(t) + \mathbf{a}^T\ddot{\mathbf{q}}(t) & \text{(4.14a)} \\ M_c = 0, & \text{(4.14b)} \end{cases}$$

where m_c is the mass of the clamp and $\mathbf{a} = \{2m; -2me_G\}^T$. Due to the fact that only a vertical displacement of the clamp is considered, the moment M_c turns out to be zero. The following notation is now introduced:

- φ_i and λ_i^2 are the eigenvectors and eigenvalues of the generalized eigenvalue problem associated to Equation 4.13;
- Φ is the spectral matrix obtained ordering by columns the eigenvectors φ_i;
- $\mathbf{p}$ are the principal coordinates of the system.

The following relation holds true:

$$\mathbf{q}(t) = \Phi\mathbf{p}(t) \tag{4.15}$$

and the equations of motion 4.13 can be re-written in terms of principal coordinates in this way:

$$\bar{\mathbf{m}}\ddot{\mathbf{p}}(t) + \bar{\mathbf{k}}\mathbf{p}(t) = \bar{\mathbf{f}}\ddot{w}_c(t), \tag{4.16}$$

where:

$$\bar{\mathbf{m}} = \Phi^T\mathbf{M}\Phi \tag{4.17a}$$

$$\bar{\mathbf{k}} = \Phi^T\mathbf{K}\Phi \tag{4.17b}$$

$$\bar{\mathbf{f}} = \Phi^T\mathbf{F}. \tag{4.17c}$$

Equations of motion for the damped system

The modal hysteretic damping matrix is defined as follows:

$$\bar{\mathbf{h}} = \begin{bmatrix} \mu_1 k_1 & 0 \\ 0 & \mu_2 k_2, \end{bmatrix}, \tag{4.18}$$

where $diag(\bar{\mathbf{k}}) = \{k_1, k_2\}^T$.
The modal viscous damping matrix is expressed as:

$$\bar{\mathbf{c}} = \begin{bmatrix} \omega_1\xi_1 & 0 \\ 0 & \omega_2\xi_2, \end{bmatrix}. \tag{4.19}$$

Hence, equations 4.16 can be generalized in the following way:

$$\bar{\mathbf{m}}\ddot{\mathbf{p}}(t) + 2\bar{\mathbf{c}}\dot{\mathbf{p}}(t) + (\bar{\mathbf{k}} + i\bar{\mathbf{h}})\mathbf{p}(t) = \bar{\mathbf{f}}\ddot{w}_c(t), \tag{4.20}$$

Frequency response of the system

Considering an harmonic motion of the support:

$$w_c(t) = \hat{w_c} exp(i\omega t), \tag{4.21}$$

the stationary response of the system can be expressed as:

$$\mathbf{p}(t) = \hat{\mathbf{p}} exp(i\omega t). \tag{4.22}$$

Substituting Equation 4.21 and Equation 4.22 into Equation 4.20, it is found that:

$$\hat{\mathbf{p}} = -\omega^2 \mathbf{z}(\omega) \hat{w_c}, \tag{4.23}$$

where $\mathbf{z}(\omega)$ is a vector of dimensions (2x1) defined as follows:

$$\mathbf{z}(\omega) = (-\omega^2 \bar{\mathbf{m}} + i2\omega\bar{\mathbf{c}} + (\bar{\mathbf{k}} + i\bar{\mathbf{h}}))^{-1}\bar{\mathbf{f}}. \tag{4.24}$$

The force F_c of Equation 4.14a can be expressed as:

$$F_c(t) = \hat{F_c} exp(i\omega t). \tag{4.25}$$

Taking into account Equation 4.14a, Equation 4.15 and Equations from 4.21 to 4.24, it is obtained:

$$\hat{F_c} = -\omega^2(2m + m_c)\hat{w_c} + \omega^4 \mathbf{a}^T \Phi \mathbf{z}(\omega)\hat{w_c}. \tag{4.26}$$

At this point it is possible to define the impedance function as follows:

$$Imp = \frac{\hat{F_c}}{\hat{w_c}}. \tag{4.27}$$

Substituting the expression for $\hat{F_c}$, Equation 4.27 can be rewritten as:

$$Imp = i\omega(2m + m_c) - i\omega^3 \mathbf{a}^T \Phi \mathbf{z}(\omega). \tag{4.28}$$

In the next two sections, the mass matrix $\mathbf{M}$ and stiffness matrix $\mathbf{K}$, introduced in Equation 4.13, are specified for the *linear model 1* and *linear model 2*.

4.2 Linear model 1

Linear model 1 treats the messenger cable as a massless Euler-Bernoulli beam, hence the mass matrix $\mathbf{M}$ of the system coincides with that of the damper mass and the stiffness matrix $\mathbf{K}$ is composed by the usual coefficients of the static stiffness matrix of an Euler-bernoulli beam:

$$\mathbf{M} = \begin{bmatrix} m; -me_G \\ -me_G; I_G + e_G^2 \end{bmatrix}; \qquad \mathbf{K} = \begin{bmatrix} 12EI/l^3; -6EI/l^2 \\ -6EI/l^2; 4EI/l \end{bmatrix}. \tag{4.29}$$

4.3 Linear model 2

Linear model 2 models the messenger cable as the Euler-Bernoulli beam described in subsection 3.3.3, hence its mass contributes to the mass matrix of the system. Using, this type of element, both **M** and **K** are functions of the exciting frequency and their full expressions are reported in Appendix B.

4.4 Stockbridge damper element

Within the Matlab code *CBFD*, the mechanical behavior of the Stockbridge damper is completely characterized through the (complex) impedance matrix **H**, which allow to take into account also the rocking effects, particularly important for the case of asymmetric dampers. If only the vertical motion of the clamp is considered, the impedance function $H_{F/d}(\omega)$, at a generic circular frequency ω, gives the ratio between the restoring force (the force at the damper clamp) and the displacement of the interface node (i.e. the node of the conductor the damper is attached at). The impedance function $H_{F/d}(\omega)$ is computed by dividing Equation 4.26 by the imposed displacement w_c.
This is valid for the linear model, for which the impedance is computed for a fixed value of imposed displacement (or in some case velocity) of the clamp; thus neglecting the dependence of the impedance on the vibration amplitude level. Whereas, if this nonlinear behavior wants to be taken into account, the impedance of the damper can be provided as a set of tables. Each table lists, at a discrete set of frequencies, the real and imaginary part of $H_{F/d}(\omega)$. Different tables correspond to different nodal displacement amplitudes and during the numerical procedure, the values of $H_{F/d}(\omega)$ at a generic frequency and amplitude, are then obtained via interpolation.

4.5 Validation

The response of the Stockbridge damper model is compared with the experimental results and with the numerical models published by (Sauter, 2003) and (Langlois and Legeron, 2014a).
(Sauter, 2003) proposes a model to represent the statical hysteresis of the messenger cable. The cable behavior is described through the *distributed* or *local Masing model*, which comprises distributed Jenkin elements, to represent the dependence of the damper characteristics on the vibration amplitude and on the particular considered section of the messenger cable. The local mechanical properties of the wire cable are identified experimentally in the time domain. In particular, the moment-curvature relation is determined experimentally at every location of the wire cable subjected to dynamic flexural deformations. The goal of Sauter, using this type of approach, is to simulate the damper impedances based on data obtained from a simple experiment carried out with a piece of damper cable.
(Langlois and Legeron, 2014a) develop a Finite Element non linear model based on a direct time integration scheme, to predict the dynamic response of the Stockbridge

damper for all expected amplitudes and frequencies. The model is built from simple experimental characterization tests to identify stiffness and damping properties.

Sauter model

The response of the Stockbridge damper model is first compared with the experimental results published by (Sauter, 2003).
The available experimental data represent the curve $|\Re(Imp)|$ for different values of the vibration velocity of the clamp (sweep at constant velocity), where *Imp* is defined in Equation 4.28. The model here used is the *linear model 2*; in section 4.5 a comparison between *linear model 1* and *linear model 2* is proposed.
For both values of the clamp velocities reported by Sauter is relatively easy to identify the sets of parameters (EI, μ_1, μ_2) or (EI, ξ_1, ξ_2), corresponding respectively to a hysteretic or viscous damping model, which well approximate the two peaks of the experimental frequency response function. The geometric characteristics of the damper in exam are:

- symmetric damper
- mass of the messenger cable $m_c = 0.1$ kg/m,
- mass of the weights $m = 0.856\ kg$,
- mass of the clamp $m_{clamp} = 0\ kg$,
- moment of inertia of the weights with respect to their centroid $I_g = 0.001814$,
- length of the messenger cable $l = 0.1875\ m$,
- distance between the centroid of the weights and their point of attachment with the messenger cable $e_G = 0.0325\ m$.

In the figures reported here below, experimental data are marked with empty squares and the model predictions by continuous curves. Figures from 4.4 to 4.8 refer to the case of an imposed clamp velocity of 50 mm/s. The parameters of the hysteretic model (EI, μ_1, μ_2) are calibrated in order to capture the experimental peaks. Figure 4.4 and Figure 4.5 shows different curves, corresponding, respectively, to different values of μ_1 and μ_2. Figure 4.6 reports the impedance curves for different values of the flexural stiffness *EI*. The parameters of the hysteretic model that allow to well fit the experimental response are:

- $\mu_1 = 0.32$,
- $\mu_2 = 0.18$,
- $EI = 12\ Nm^2$.

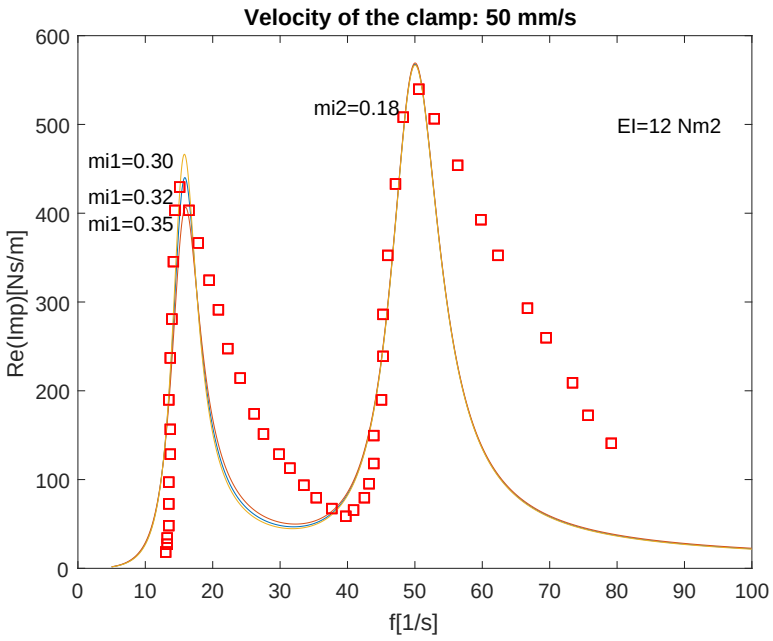

Figure 4.4: $|\Re(Imp)|$ curves for an imposed velocity of the clamp of 50 mm/s and for different values of μ_1

Figure 4.7 proposes a comparison between the hysteretic model, considering the parameters just defined, and the viscous model, obtained setting $\mu_1 = \mu_2 = 0$, $\xi_1 = 0.15$, $\xi_2 = 0.10$ and $EI = 12\ Nm^2$. Since the difference between the two models is small and since the damping behaviour of the messenger cable is mainly of hysteretic type, in the following reference is made to the impedance provided by the hysteretic model.
Figure 4.8 reports the curve related to the Sauter model, the experimental data and the curve of the hysteretic model developed in this work. The latter, despite being a linear model, manages to capture the two peaks of the experimental response better than the Sauter model, which overestimates the frequencies of the two peaks and the amplitude of the first one..

The same results reported for the case of an imposed velocity of the clamp of 50 mm/s are proposed also for an imposed velocity of 200 mm/s. Figure 4.9 shows different curves obtained varying the value of μ_2 and for a flexural rigidity EI equal to 7 Nm^2. The parameters of the hysteretic model that allow to well fit the experimental response are:

- $\mu_1 = 0.44$,
- $\mu_2 = 0.28$,
- $EI = 7\ Nm^2$.

Figure 4.10 proposes a comparison between the hysteretic model, considering the pa-

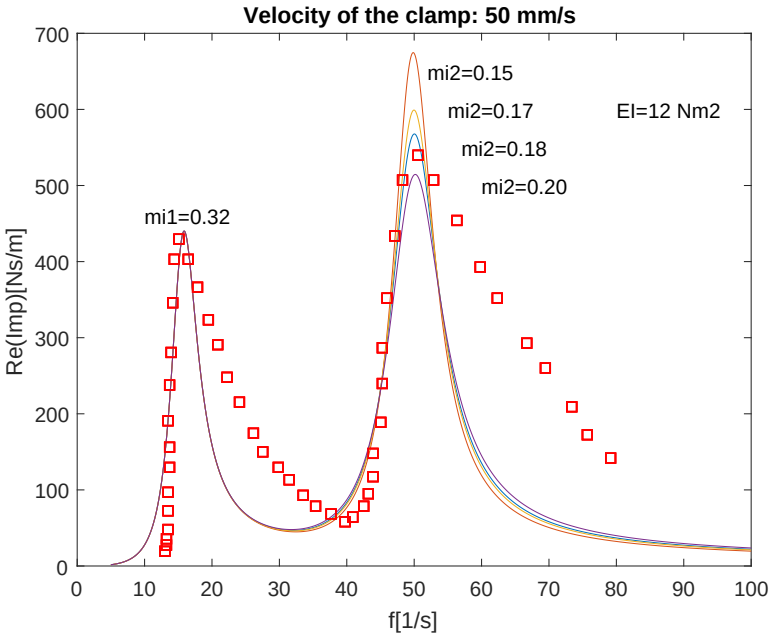

Figure 4.5: $|\Re(Imp)|$ curves for an imposed velocity of the clamp of 50 mm/s and for different values of μ_2

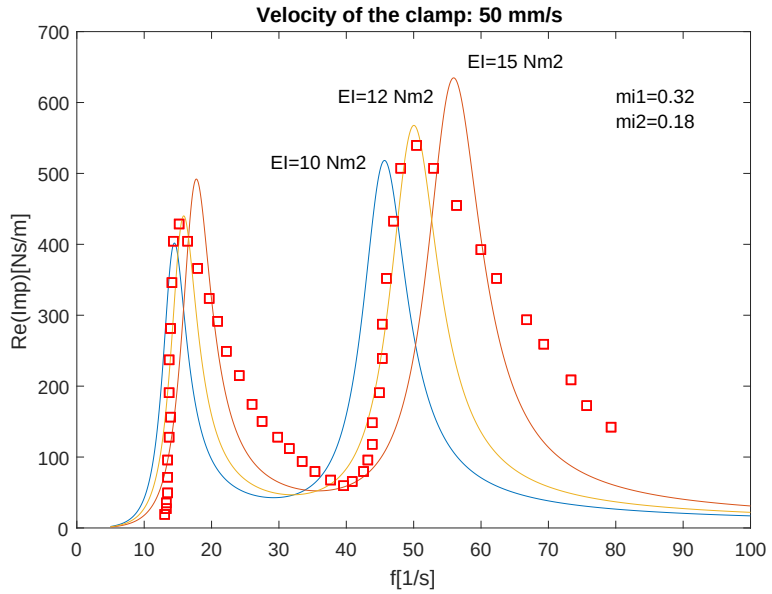

Figure 4.6: $|\Re(Imp)|$ curves for an imposed velocity of the clamp of 50 mm/s and for different values of EI

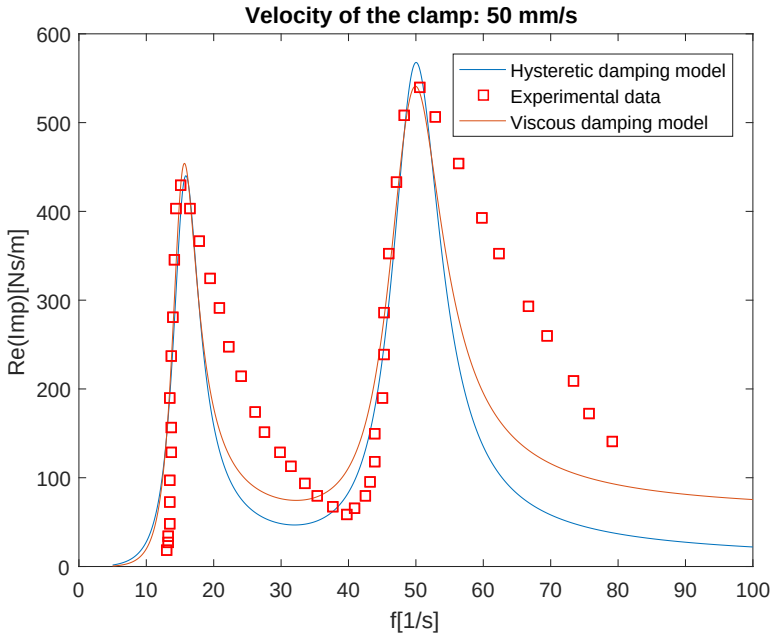

Figure 4.7: $|\Re(Imp)|$ curves for an imposed velocity of the clamp of 50 mm/s: comparison in between viscous and hysteretic model

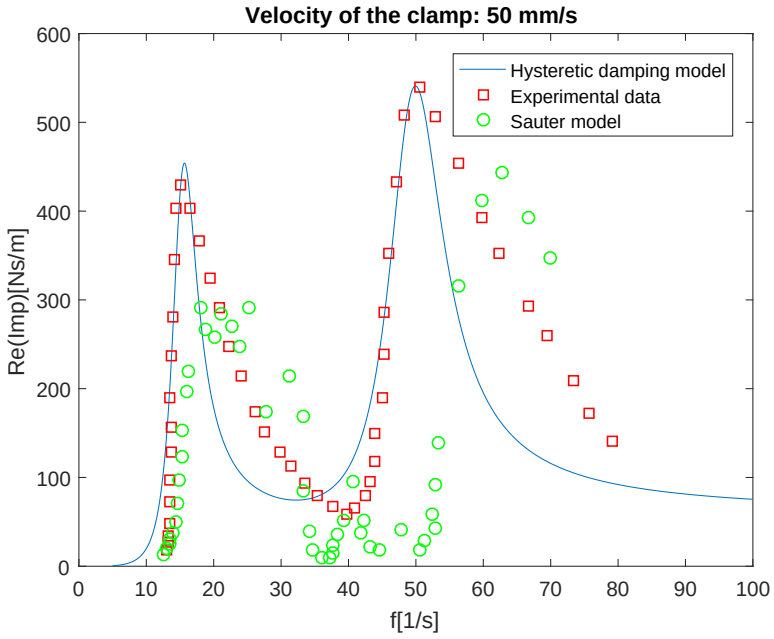

Figure 4.8: $|\Re(Imp)|$ curves for an imposed velocity of the clamp of 50 mm/s: comparison among Sauter model, experimental data and hysteretic model, developed in this work.

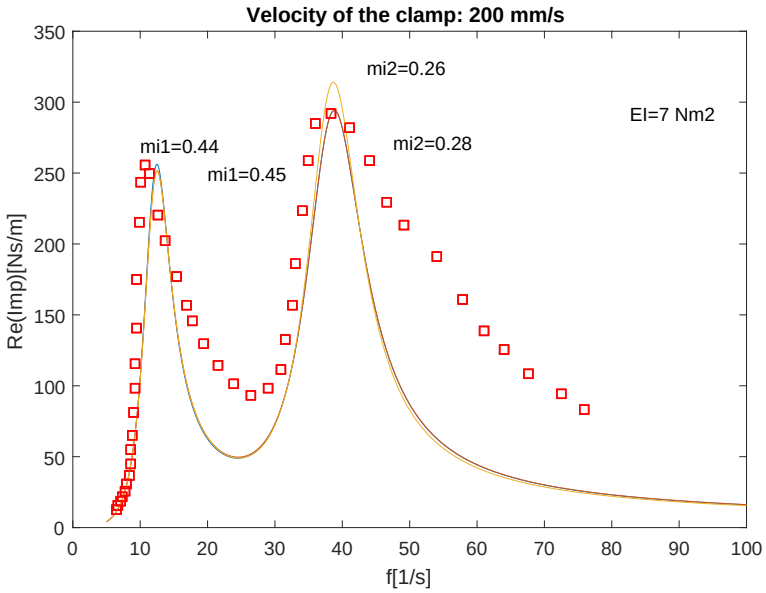

Figure 4.9: $|\Re(Imp)|$ curves for an imposed velocity of the clamp of 200 mm/s and for different values of μ_2

rameters just defined, and the viscous model, obtained setting $\mu_1 = \mu_2 = 0$, $\xi_1 = 0.22$, $\xi_2 = 0.16$ and $EI = 7\ Nm^2$. Figure 4.11 reports the comparison with the Sauter model; the previous considerations hold true also for this case.

Table 4.1 summarizes the parameters of the hysteretic and viscous models that allow to well capture the experimental response.

Clamp velocity [mm/s]	μ_1	μ_2	ξ_1	ξ_2	EI $[Nm^2]$
50	0.32	0.18	0.15	0.10	12
200	0.44	0.28	0.22	0.16	7

Table 4.1: Parameters of the model for the two imposed velocity of the clamp considered.

It can be noticed that, as the velocity of the clamp increases, the damping parameters $(\mu_1, \mu_2, \xi_1, \xi_2)$ increases, whereas the flexural stiffness EI decreases.

Langlois model

The data reported by (Langlois and Legeron, 2014a) are related to a Stockbridge damper with the following geometric characteristics:

- symmetric damper

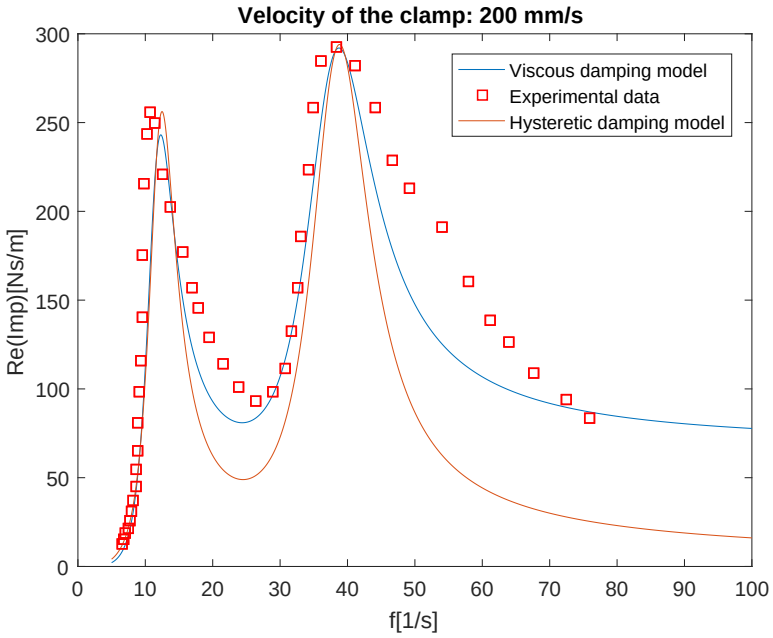

Figure 4.10: $|\Re(Imp)|$ curves for an imposed velocity of the clamp of 200 mm/s: comparison in between viscous and hysteretic model

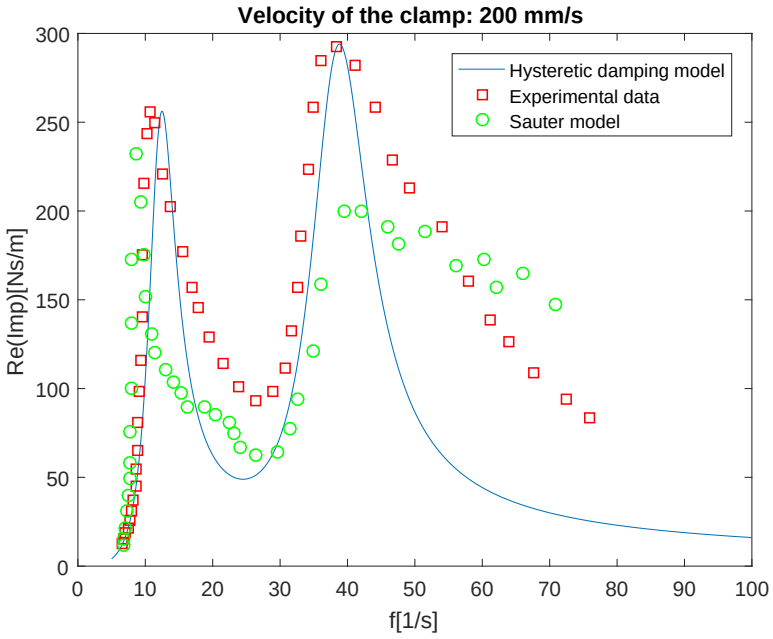

Figure 4.11: $|\Re(Imp)|$ curves for an imposed velocity of the clamp of 200 mm/s: comparison among Sauter model, experimental data and hysteretic model, developed in this work.

- mass of the weights $m = 3.021\ kg$,
- mass of the clamp $m_{clamp} = 0.5340\ kg$
- moment of inertia of the weights with respect to their centroid $I_g = 0.0017$,
- length of the messenger cable $l = 0.129\ m$,
- distance between the the centroid of the weights and their points of attachment with the messenger cable $e_G = 0.0306\ m$.

Also in this case the Stockbridge damper is modelled through the *linear model 2*, assuming a linear mass of the cable $m = 0.1\ kg/m$.
The available experimental data represent the modulus of the force transmitted at the clamp, for three different values of the clamp displacement (sweep at constant displacement): 0.2 mm, 1 mm and 3 mm. In the figures reported here below, experimental data are marked with empty squares and the model predictions by continuous curves. Figures from 4.12 to 4.15 refer to the case of an imposed clamp displacement of 0.2 mm. Figure 4.12 and Figure 4.13 show different curves, corresponding, respectively, to different values of μ_2 and of the flexural stiffness EI. The parameters of the hysteretic model that allow to well fit the experimental response are:

- $\mu_1 = 0.33$,
- $\mu_2 = 0.22$,
- $EI = 3.8\ Nm^2$.

It can be noticed that, with this parameters, the first experimental peak is well captured, whereas, the frequency of the second peak is overestimated. As can be seen from the Figure 4.13, a flexural stiffness equal to $2.5Nm^2$ allow to correctly represent the second experimental frequency, but, on the other hand, overestimates the first one. The criterion adopted to define the set of parameters itemized below, is that the first experimental peak is correctly identified.
Figure 4.14 proposes a comparison between the hysteretic model and the viscous model, obtained setting $\mu_1 = \mu_2 = 0$, $\xi_1 = 0.17$, $\xi_2 = 0.13$ and $EI = 3.8\ Nm^2$. Figure 4.15 reports the curve corresponing to the Langlois model.

The same graphs are reported also for the case of an imposed clamp displacement of 1 mm (figures from 4.16 to 4.19) and 3 mm (figures from 4.19 to 4.22). The set of parameters defined to identify the experimental curve of 1 mm are:

- $\mu_1 = 0.39$,
- $\mu_2 = 0.17$,
- $EI = 1.8\ Nm^2$,
- $\xi_1 = 0.17$,

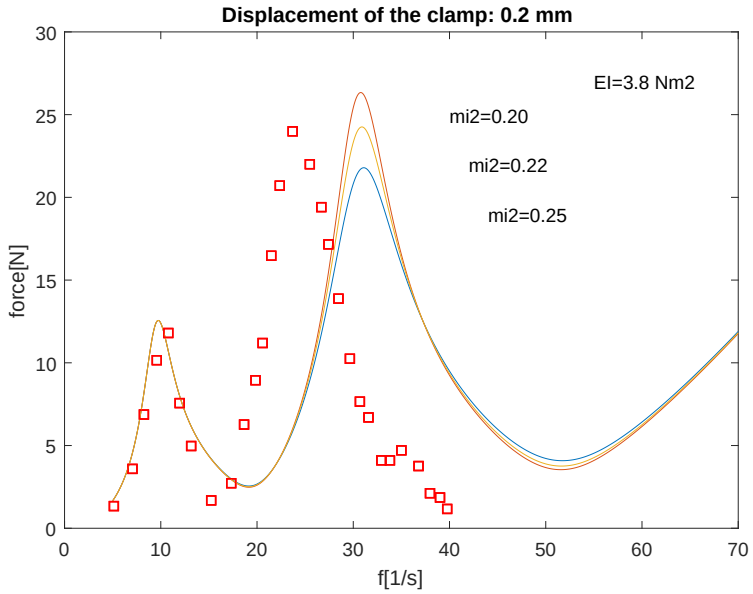

Figure 4.12: Curves of the force modulus for an imposed displacement of the clamp of 0.2 mm and for different values of μ_2

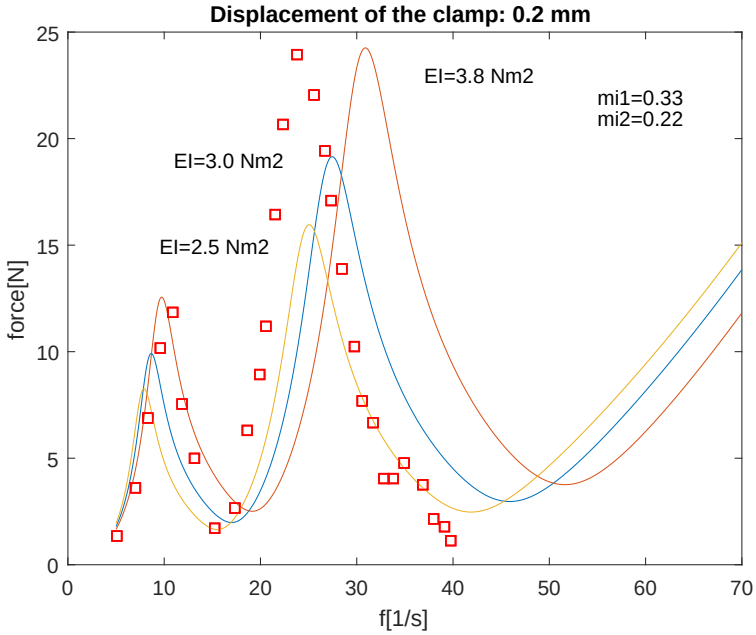

Figure 4.13: Curves of the force modulus for an imposed displacement of the clamp of 0.2 mm and for different values of EI

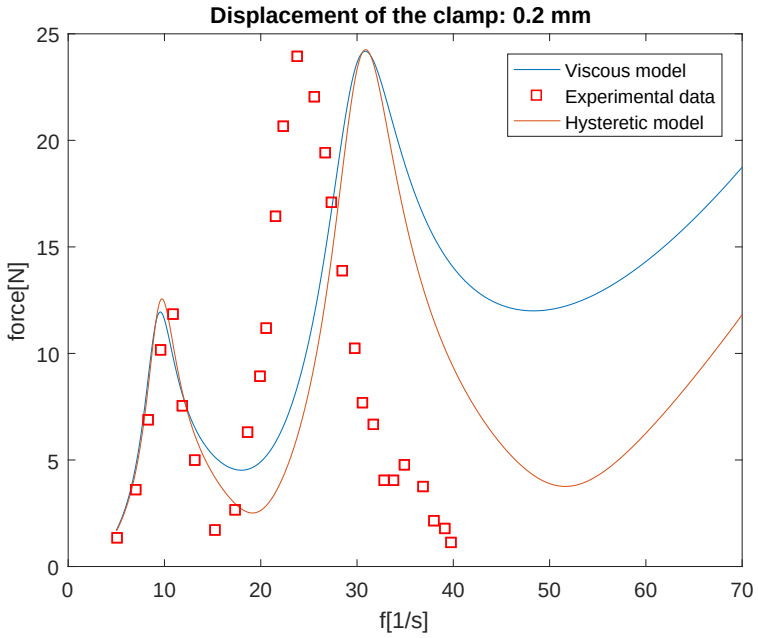

Figure 4.14: Curves of the force modulus for an imposed displacement of the clamp of 0.2 mm: comparison in between viscous and hysteretic model

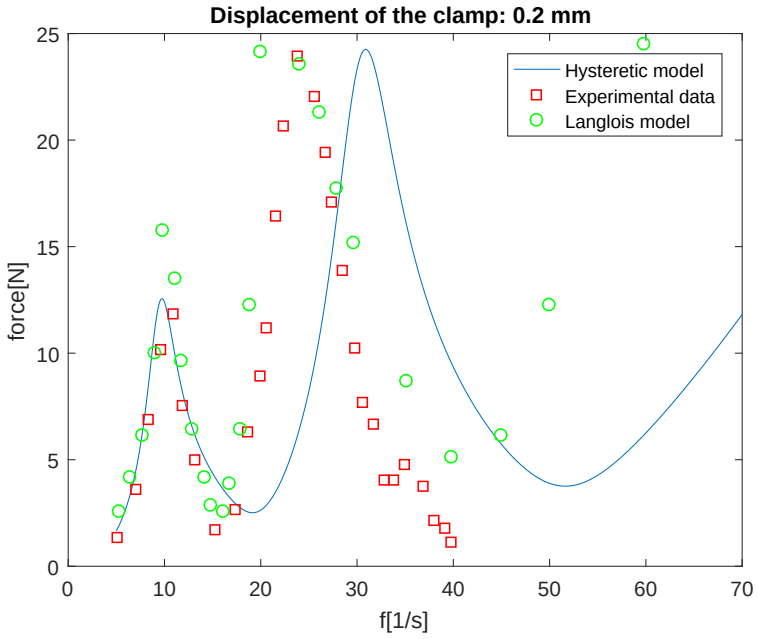

Figure 4.15: Curves of the force modulus for an imposed displacement of the clamp of 0.2 mm: comparison with the model of Langlois.

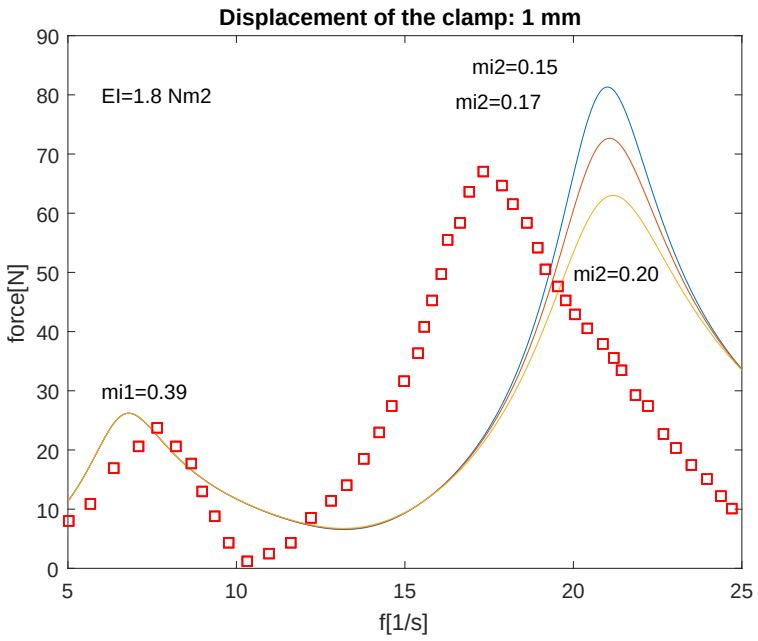

Figure 4.16: Curves of the force modulus for an imposed displacement of the clamp of 1 mm and for different values of μ_2

- $\xi_2 = 0.09$.

For the case of 3 mm, only the first peak is reported and the selected parameters are:

- $\mu_1 = 0.24$,
- $EI = 1.3\ Nm^2$,
- $\xi_1 = 0.12$.

Table 4.2 summarizes the parameters of the hysteretic and viscous models assumed to identify the experimental response, for the three different imposed displacement of the clamp.

Clamp displacement [mm]	μ_1	μ_2	ξ_1	ξ_2	$EI\ [Nm^2]$
0.2	0.33	0.22	0.17	0.13	3.8
1	0.39	0.17	0.17	0.09	1.8
3	0.24	-	0.12	-	1.3

Table 4.2: Parameters of the model for the three imposed displacement of the clamp considered.

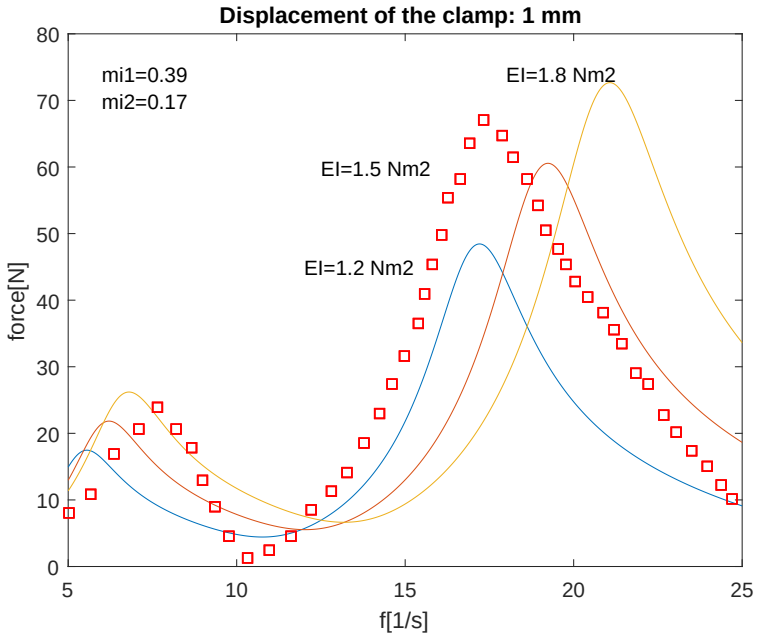

Figure 4.17: Curves of the force modulus for an imposed displacement of the clamp of 1 mm and for different values of EI

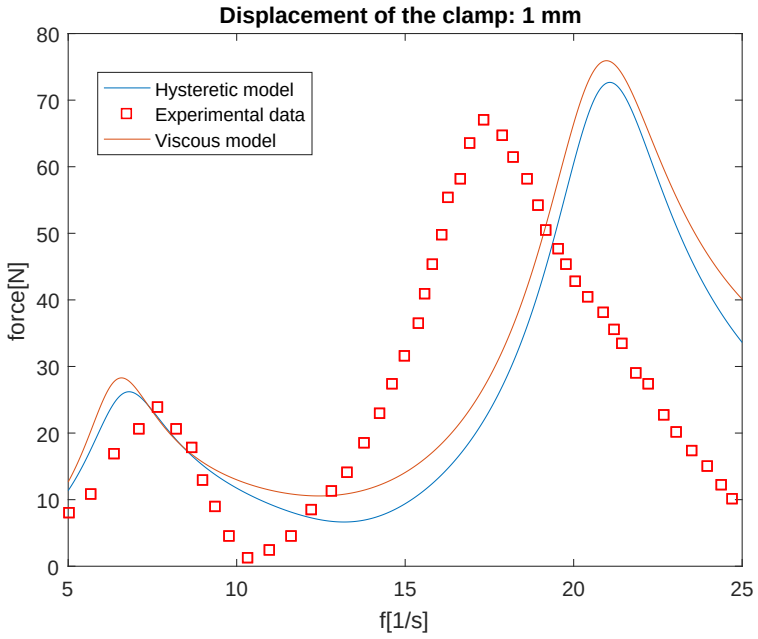

Figure 4.18: Curves of the force modulus for an imposed displacement of the clamp of 1 mm: comparison in between viscous and hysteretic model

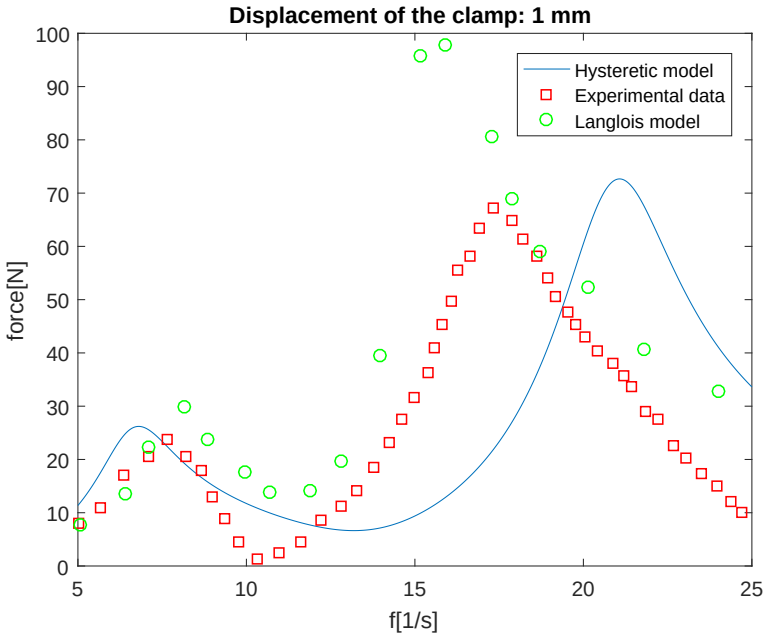

Figure 4.19: Curves of the force modulus for an imposed displacement of the clamp of 1 mm: comparison with the model of Langlois.

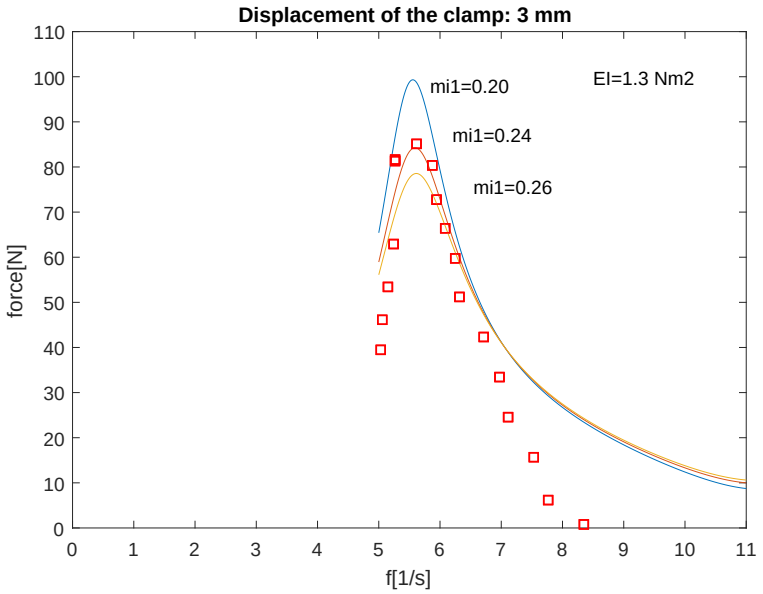

Figure 4.20: Curves of the force modulus for an imposed displacement of the clamp of 3 mm and for different values of μ_1

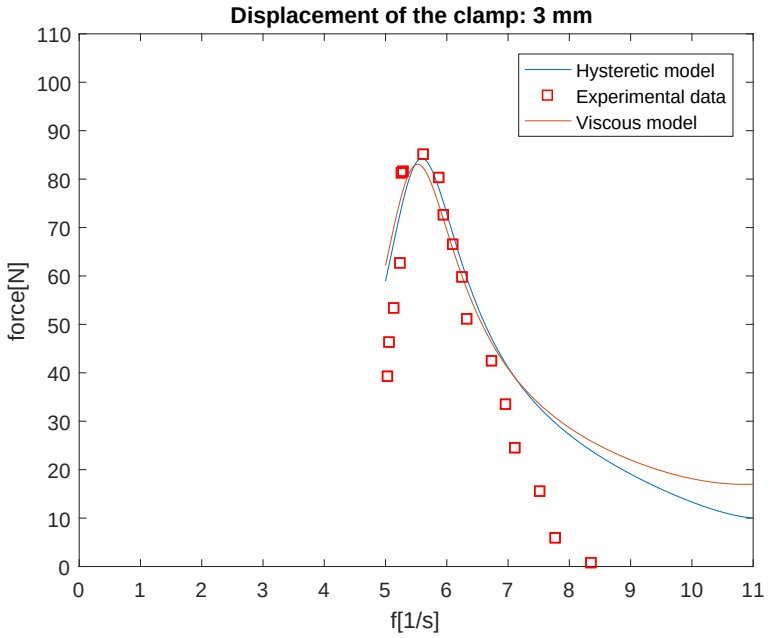

Figure 4.21: Curves of the force modulus for an imposed displacement of the clamp of 3 mm: comparison in between viscous and hysteretic model

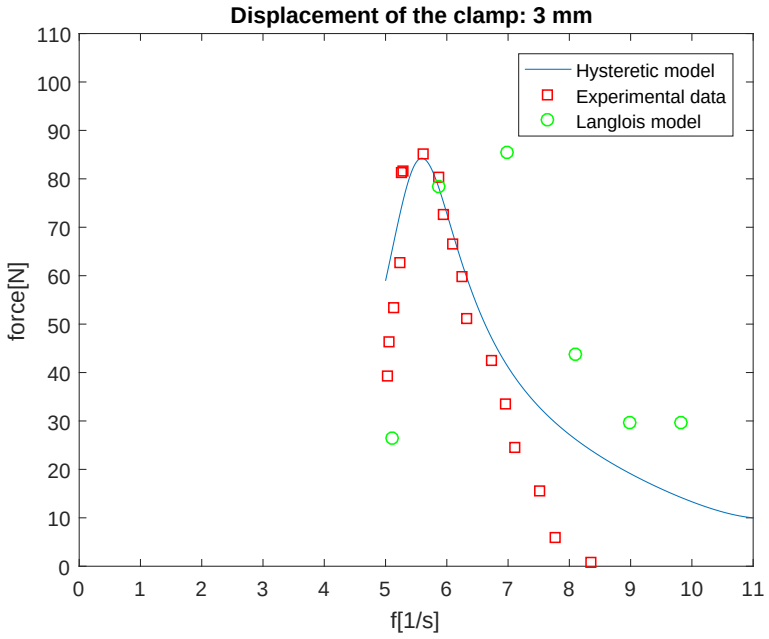

Figure 4.22: Curves of the force modulus for an imposed displacement of the clamp of 3 mm: comparison with the model of Langlois.

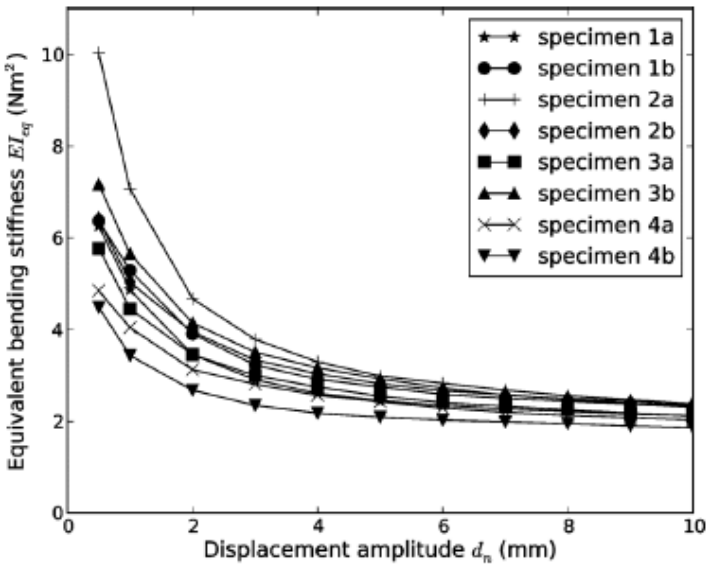

Figure 4.23: Equivalent bending stiffness as a function of the displacement amplitude (Langlois and Legeron, 2014a).

(Langlois and Legeron, 2014a) treat each arm of the Stockbridge as a cantilever to define an equivalent bending stiffness, an average stiffness on all the sections of the arm, whose trend as a function of the imposed displacement is reported in Figure 4.23. It can be noticed that the values of the flexural stiffness reported in Table 4.2 are close to the minimum value of the flexural stiffness of Figure 4.23 (EI_{min}), around 2 Nm^2. This means that the values of the clamp displacements considered (0.2 mm, 1mm and 3 mm), make the messenger cable work under large amplitude displacements. The curvature level is high enough to make the cable work in the slipping state (*full slip* condition): the strands basically reacts as a bundle of individually bent wires, hence EI coincides to the minimum attainable value EI_{min}.
The values of EI defined for the experimental curve of Sauter are larger with repect to this minimum value. This can be explained considering that the curves of Sauter are obtained with a sweep at constant velocity, hence for large frequencies the messenger cable works with small amplitudes displacements (so EI is closer to EI_{max} than to EI_{min}) and for small frequencies with large amplitude displacements (EI is closer to EI_{min} than to EI_{max}).

Considerations on the results

From the comparison with the results of Sauter e Langlois, the following conclusions can be drawn:

- using a linear model, it is necessary to introduce two different modal damping parameters, in order to correctly reproduce the frequency and the amplitude of

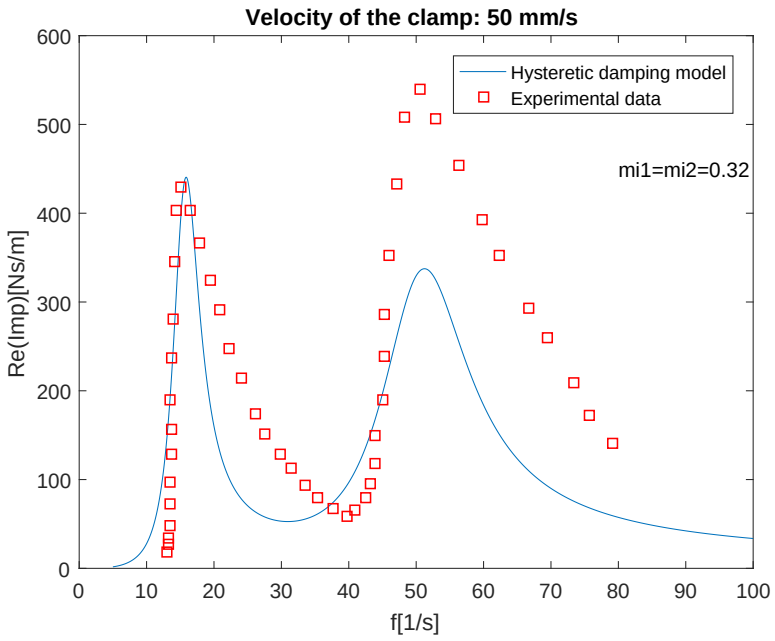

Figure 4.24: $|\Re(Imp)|$ curves for an imposed velocity of the clamp of 50 mm/s, assuming $\mu_1 = \mu_2 = 0.32$

the two peaks of the response. In fact, by selecting a modal damping parameter equal for both modes, only one peak of the response can be correctly captured. Figure 4.24 and Figure 4.25 show the impedance curve obtained if a unique modal damping parameter is selected, as the one that best describes the first or second mode, for the case of Sauter of an imposed velocity of the clamp of 50 mm/s.
This is linked to the physics of the Stockbridge damper dissipation mechanism, as pointed out in (Foti and Martinelli, 2018). The authors describe the cyclic bending behaviour of the cross-sections of the messenger cable through the Bouc-Wen hysteretic model, identifying the constitutive parameters of the model from the results of quasi-static bending tests, due to the rate-independent dissipative behaviour of the cable. In particular the trend along the cable, modelled as a cantilever beam, of the identified values of the parameters EI_{max} and EI_{min}, shows the presence of two *boundary layer regions*: one near the clamp and the other near the tip. Figure 4.26 reports a comparison between the values of EI_{max} and EI_{min} identified from the static cyclic test and the theoretical values, computed through the expressions reported in (Foti and Martinelli, 2016a). It can be noticed that, over a wide central region of the cable, the identified values of EI_{max} and EI_{min} tend to be constant, whereas in correspondence of the boundary layer regions, they drastically depart from the *far-field* constant value.
The authors show that an increase of the boundary layer length of the clamp lead to an increase of both resonance peaks and to a reduction of their separation with a

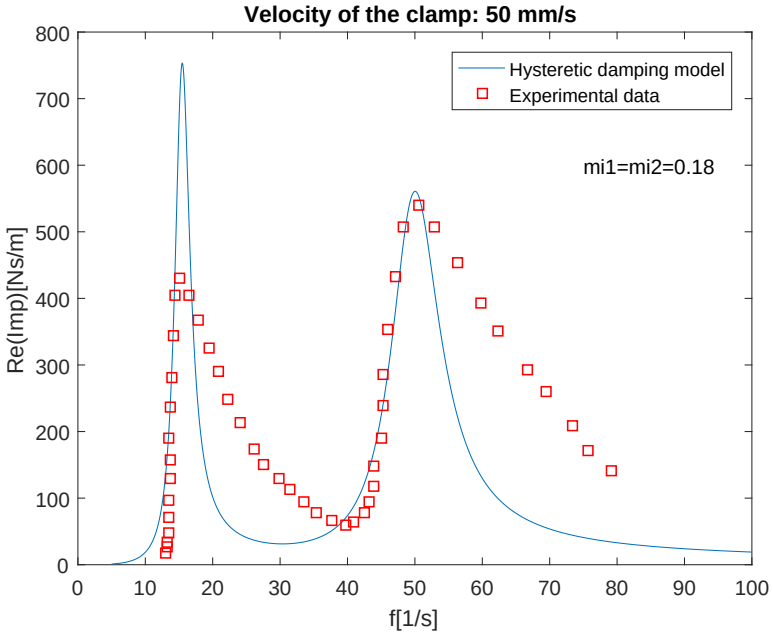

Figure 4.25: $|\Re(Imp)|$ curves for an imposed velocity of the clamp of 50 mm/s, assuming $\mu_1 = \mu_2 = 0.18$

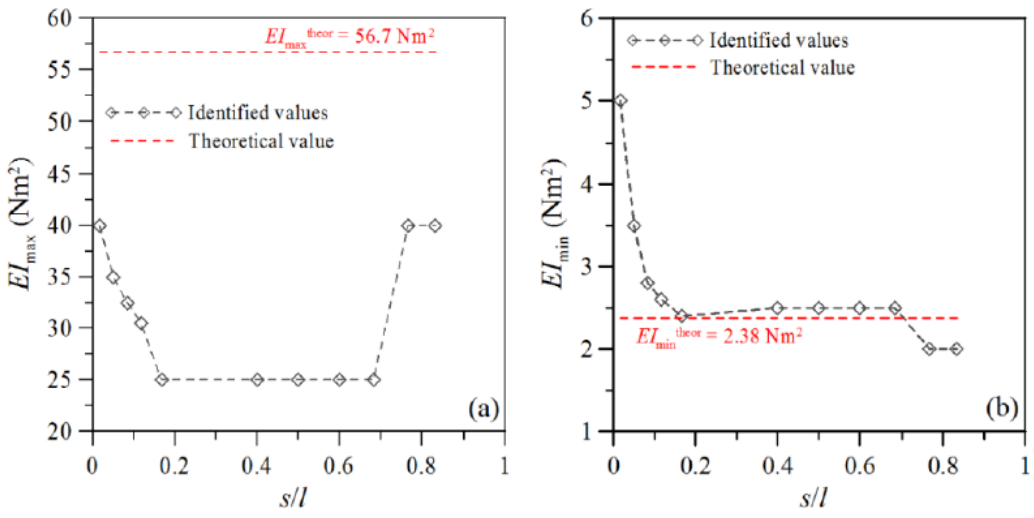

Figure 4.26: Maximum and minimum values of the cross-sectional bending stiffness of the messenger cable as a function of the non dimensional arc-length coordinate s/l (Foti and Martinelli, 2016a).

shift of both towards the central frequency. Whereas, the boundary layer length at the tip mainly affects the resonance related to second mode, shifting the resonance peak to higher frequencies and higher values as it increases.
Hence, to properly capture the dynamic response of the Stockbridge damper, the effects of the end zones of the messenger cable must be taken into account. Since the model here proposed does not define these boundary effects, it is necessary to introduce two distinct modal damping parameters, in order to correctly capture the two peaks of the experimental response.
Even if not developed, the effects of boundary layers are easily implemented with the approach proposed in this chapter. To this aim, the messenger cable can be modelled through an Euler-Bernoulli beam element with variable bending stiffness or introducing more elements, each of them characterized by different value of the bending stiffness. In this second case, neglecting the mass of the messenger cable, the coordinates of the additional degrees of freedom would be static degrees of freedom and therefore can be condensed.

- Linear models allow to reproduce, with an acceptable precision, the ascending branches of the two peaks of the F.R.F. The descending branches, on the other hand, are not captured correctly, as the linear model is not able to reproduce the dissymmetry of the peaks.

- as a consequence of the previous item, also the FRF region between the two peaks is not represented correctly.

- The model parameters must be identified for different amplitude values of the clamp motion to take into account the nonlinearity of the problem. It is reasonable to assume that the parameters vary continuously with an amplitude parameter A of the motion of the support. In particular, it is reasonable to expect that: EI decreases as A increases; (μ_1, μ_2) and (ξ_1, ξ_2) increases as A increases. In general $EI = EI(A)$, $\mu_1 = \mu_1(A)$, $\mu_2 = \mu_2(A)$, $\xi_1 = \xi_1(A)$, $\xi_2 = \xi_2(A)$ can be nonlinear function of A.

Comparison between linear model 1 and linear model 2

The results reported up to now make reference to *linear model 2*, which considers the contribution of the distributed mass of the messenger cable. *Linear model 1*, instead, considers the messenger cable as massless beam. Since the mass of the cable is very small compared to the mass of the damper weights, the difference in the results is small as well, as can be seen from Figure 4.27, which reports the results using *linear model 1*, for the case of Sauter with an imposed velocity of the clamp of 50 mm/s. The curves are derived considering the hysteretic parameters specified in section 4.5, i.e.:

- $\mu_1 = 0.32$,

- $\mu_2 = 0.18$,

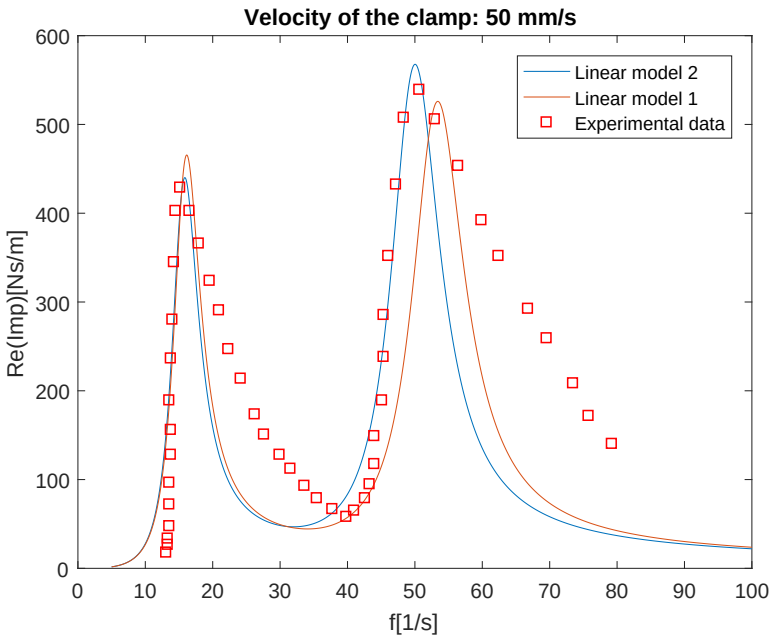

Figure 4.27: $|\Re(Imp)|$ curves for an imposed velocity of the clamp of 50 mm/s: comparison between *linear model 1* and *linear model 2*

.

- $EI = 12\ Nm^2$.

From Figure 4.27 it can be noticed, however, as, with these parameters, *linear model 1*, doesn't capture well the two experimental peaks. The set of parameters which allow *linear model 1* to best fit the experimental data are the following (Figure 4.28):

- $\mu_1 = 0.32$,
- $\mu_2 = 0.17$,
- $EI = 11\ Nm^2$.

As the mass of the system considered with model 1 is a little bit smaller than the one of model 2 (since the first disregard the mass of the messenger cable), is reasonable that a smaller EI is needed to represent the same experimental natural frequencies.

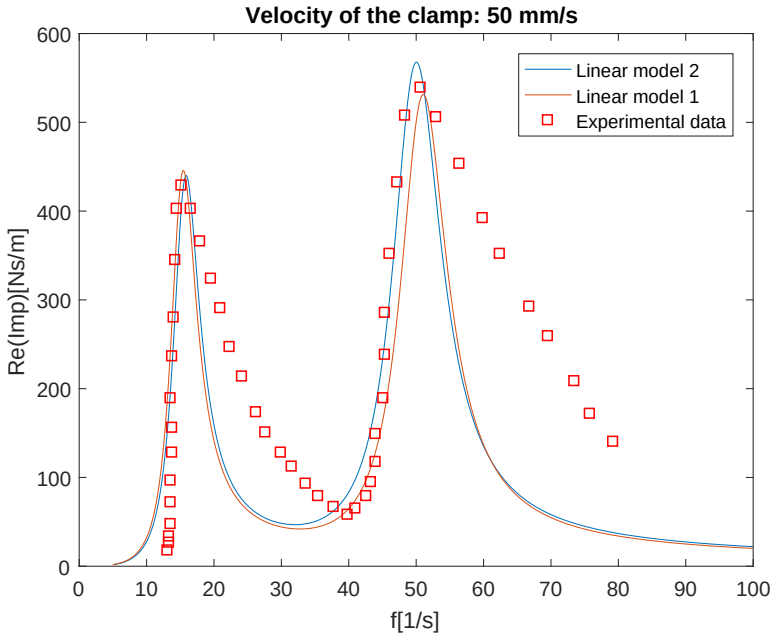

Figure 4.28: $|\Re(Imp)|$ curves for an imposed velocity of the clamp of 50 mm/s: comparison between *linear model 1* and *linear model 2*

.

Chapter 5

Modal analysis

The determination of the mode shapes, which define the relative magnitude of vibration at every points of the system for a given natural frequency, is the essential part of the aeolian vibration modeling (Lu and Chan, 2007). Modal analysis is used in this work to validate the analytical model of the conductor (chapter 3), and of the conductor-plus-dampers system (section 5.2).
For the computation of the natural frequencies and modal shapes, an *ad hoc* program in Matlab environment is developed, based on the element formulation described in section 3.3.
Modes are calculated through a frequency sweep analysis: a harmonic generalized dispacement (displacement or rotation) is imposed, in correspondence of a node of the structure. Varying the circular frequency within a input-defined range, it is computed a suitable frequency response function, whose zeros correspond to the natural circular frequencies. This forced vibration method to find modes can easily handle non-proportional damping, which is typical for the problem in concern, without having to solve a complex eigenvalue problem.
In section 5.1 the program workflow is pointed out, with the specification of the pertinent variables of the problem and a detailed description of the core function of the code (subsection 5.1.1). In section 5.2 an example is proposed to validate the model of the conductor-plus-damper system.

5.1 Program overview

The conceptual design of the program is depicted in Figure 5.1. The main program *CBFD* (which stands for *Continuous Beams in Frequency Domain*) calls various sub-routines in an orderly fashion, as depicted in Figure 5.2.

Looking at the flowchart of Figure 5.2, the program workflow can be broken down into several steps:

- reading of the input file (`fname`) and initialization of the variables of interest, saved inside the data structure `structure`, within the sub-routine *Read Input*.

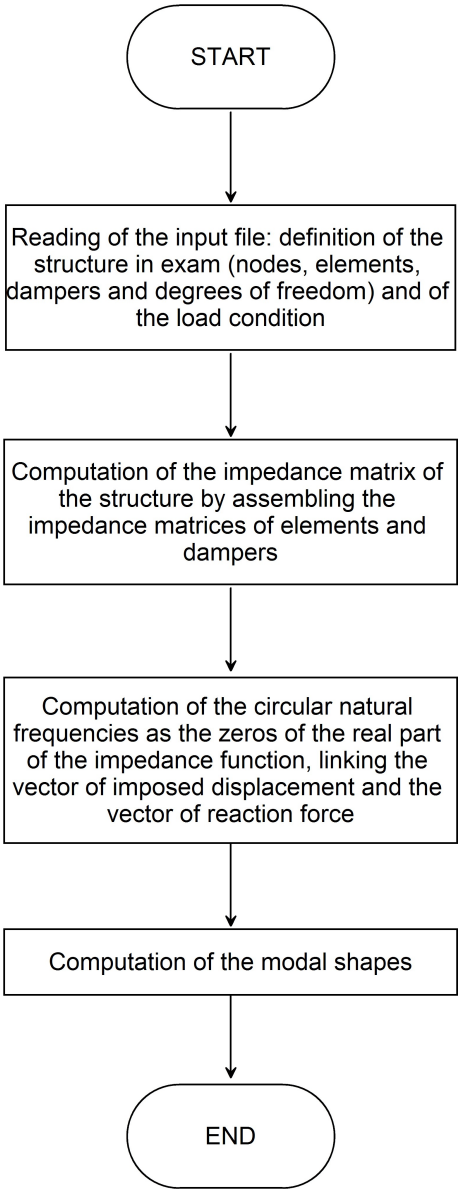

Figure 5.1: Conceptual design of the *CBFD* program

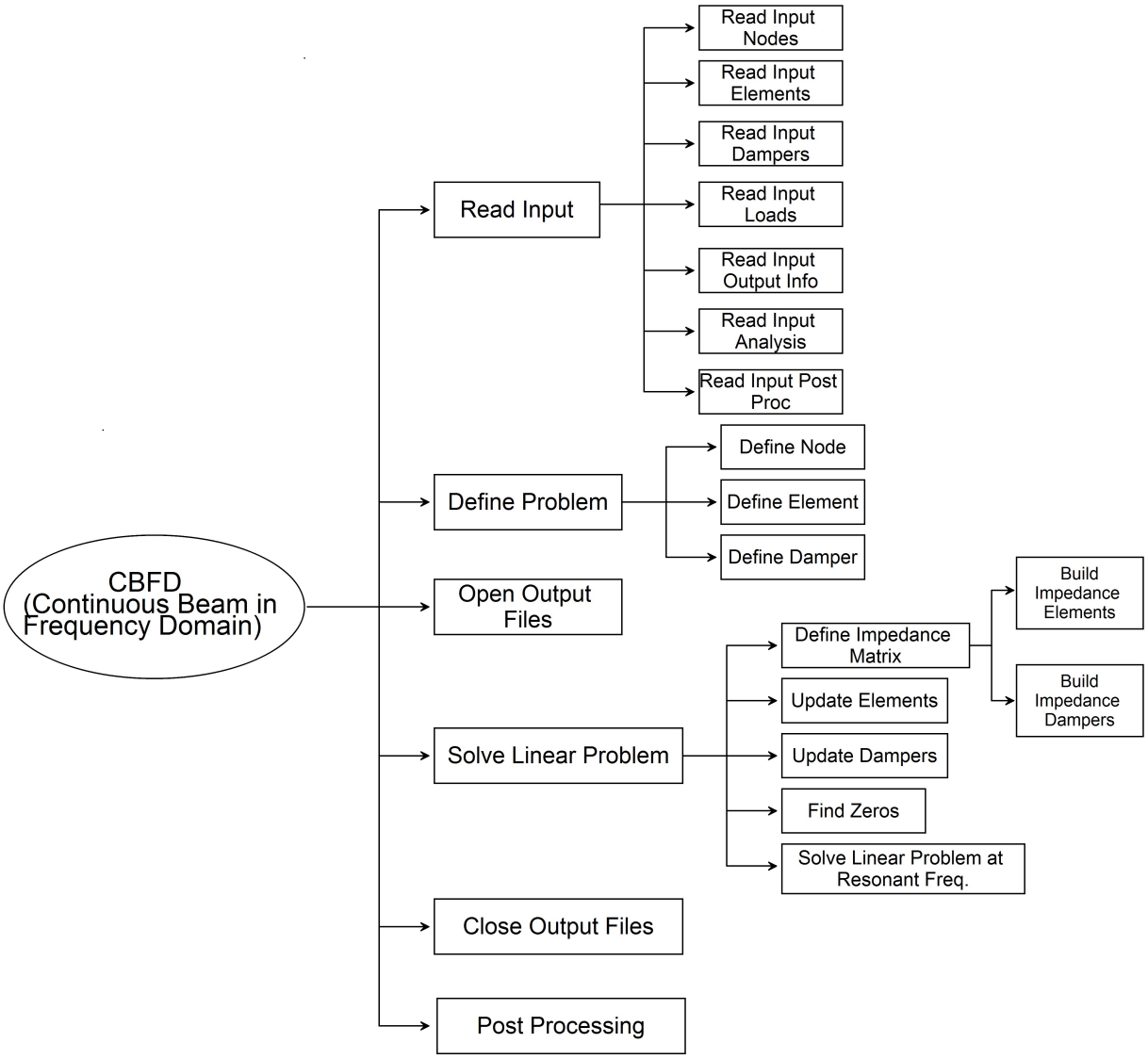

Figure 5.2: Flowchart of the sub-routines called by the main program *CBFD*

In the first part of the input file are specified the following quantities: number of elements (`structure.nele`), number of dampers (`structure.ndamp`), number of nodes (`structure.nnodi`), number of degrees of freedom (`structure.Ntot`). The functions called by *Read Input* (see Figure 5.2) read and save the following quantities:

- coordinates of the nodes (`structure.xx`) and nodal global degrees of freedom (`structure.ix`) (*Read Input Nodes*);
- element connectivity (`structure.incid`), number of element types (`structure.nELTY`), the element type data sources (`structure.ELTY` and `structure.ELass`): text files containing for every different element types the element methods, i.e. the names of the specific functions needed for the initialization, computation of the impedance matrix and post-processing phase of the element, the mass per unit length, the flexural stiffness and the axial force (*Read Input Elements*). In the case of variable axial force along the span of the conductor, it is possible to define the pre-tension not as a constitutive feature of the element (in this case it would be necessary to define as many type of elements as the number of conductor portion with constant pre-tension) but assigning the value of the axial force for each element in the main input file (`structure.ELprestr`).
- If the number of dampers are different from zero, the sub-routine *Read Input Dampers* reads and stores the damper connectivity (`structure.Dincid`), the number of damper types (`structure.nDTy`) and the damper type data sources text files (`structure.Dass`), containing for every different damper types the damper methods (names of the specific functions needed for the initialization, computation of the impedance matrix and post-processing phase of the damper), and some quantities needed for the computation of the impedance matrix (e.g. for each arm of the Stockbridge damper: value of the concentrated mass, cable mass per unit length, flexural stiffness, hysteretic coefficient, cable length, distance between the attachment point and the centroid of the mass and moment of inertia of the mass with respect to its centroid).
- The sub-routine *Read Input Loads* reads and saves in the data structure the quantities related to the generalized imposed displacement, in particular: node and direction, real and imaginary component (`structure.Gloads`) and the circular frequency range (`structure.loads-freq-range`): initial circular frequency, final circular frequency and step. It is assumed for simplicity and not affecting the generality of the problem, that the imaginary component of the imposed displacement is zero; this choice will be clearer after reading the description of the function *Solve Linear Problem*).
- In the input file are also specified the output information requested for nodes, elements and dampers; they are stored in the following field: `structure.OUTNODE`, `structure.OUTELE`, `structure.DAMP` (*Read Input Output Info*).
- The sub-routine *Read Input Analysis* read the specification about the analysis type (`structure.solver`): linear (1) or nonlinear (2). The nonlinear analysis

function is already developed inside the code, but still to be fully developed as regards the imposition of the Energy Balance Method.

– The last informations contained in the input file concern the post-processing phase and the calculation of the modes. In particular it is specified for what nodes and directions plotting the results, the number of modes to plot and the reference node and direction for the computation of the natural frequencies.

- Once the reading phase has been completed, preliminary calculations are performed within the sub-routine *Define Problem*. The data structure `structure` is extended to the fields `structure.nodes`, `structure.elements` and `structure.dampers`.
  The first field is defined by the function *Define Node*, which assign to each node the corresponding global degrees of freedom (`vgdl`) and the nodal position vector in several different configuration (`x`).
  Define Element reads the element types data source files, saving in `structure.elements` the element methods (`methods.init`, `methods.read`, `methods.impedance`, `methods.print` and `methods.post-proc`), the conductor pre-tension (`T`), the flexural stiffness (`EI`) and the conductor mass per unit of length (`m`). For each element are also stored the incidences (`incid`), the number of dofs for each element (`ngdl`), equal to 4 (2 per node) for the beam element adopted (see section 3.3), the nodal global dofs `vgdl`, the nodal coordinates (`x1` and `x2`) and the element length (`L`).
  Define Element initializes and defines the dimensions of the variables calculated later on by *Solve Linear Problem*: the real and imaginary part of nodal displacements of each element, the impedance matrix (`Red`, `ImD`, `ReZ` and `ImZ`) and the vector containing the modal shapes (`Redshape` and `Imdshape`).
  Similarly, *Define Damper* initializes and stores the same quantities already defined for elements, for dampers (`structure.dampers`).

- *Open Output Files* opens and writes the headers of all the output files related to nodes, elements, dampers and modes.

- *Solve Linear Problem* is the core of the program: here the structure impedance matrix and hence the modal shapes are computed. This function is described in detail in subsection 5.1.1.

- All the output files previously opened by *Open Output Files* are closed whithin *Close Output Files*.

- In the post-processing phase, the modal shapes are plotted along with the frequency response function in terms of displacements of the entities of interest (defined in *Read Input Post Proc*).

5.1.1 *Solve Linear Problem*

The flowchart of the function *Solve Linear Problem* is illustrated in Figure 5.3.

As can be seen by Figure 5.3, all the steps reported in the diagram are repeated until the circular frequency value `cfreq`, increased by the step `Dcfreq` at each iteration,

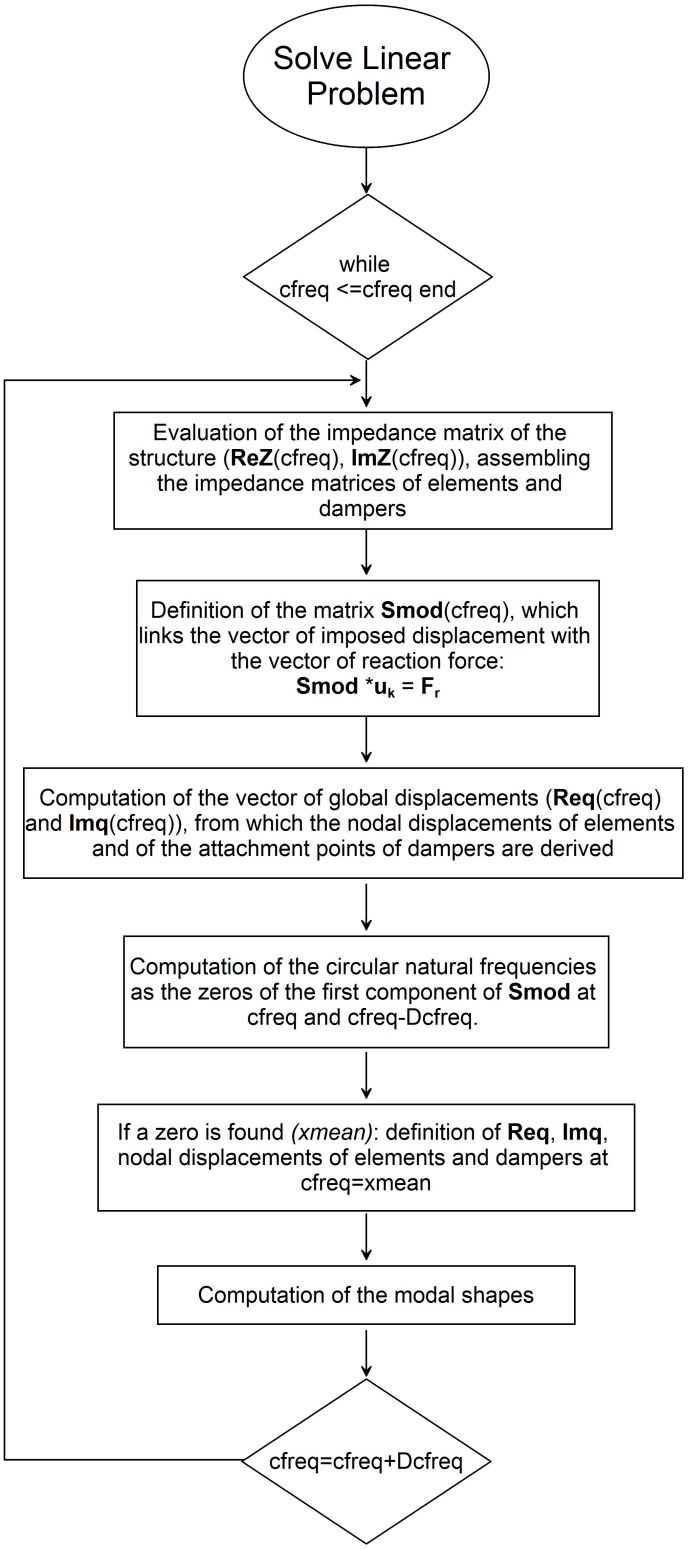

Figure 5.3: Flowchart of the function *Solve Linear Problem*

reaches the limit `cfreq end` defined by input.
The first calculated entity is the real and imaginary part of the impedance matrix of the structure (`ReZ` and `ImZ`), which are both square matrices of dimension equal to the number of global degrees of freedom (`Ntot`). The structure impedance matrix is defined assembling the impedance matrices of elements and dampers (the formation of the latter is explained in chapter 3 and chapter 4) .
The matrix $\mathbf{S}$, which links the displacement vector $\mathbf{q} = \begin{bmatrix}\mathbf{Req}\\ \mathbf{Imq}\end{bmatrix}$ and the vector of reaction forces $\mathbf{F} = \begin{bmatrix}\mathbf{ReF}\\ \mathbf{ImF}\end{bmatrix}$, has the following form:

$$\mathbf{S} = \begin{bmatrix}\mathbf{ReZ} & \mathbf{ImZ}\\ \mathbf{-ImZ} & \mathbf{ReZ}\end{bmatrix}. \tag{5.1}$$

The above expression can be easily derived taking into account that:

$$\mathbf{Z} = \mathbf{ReZ} + i \cdot \mathbf{ImZ} \tag{5.2}$$
$$\mathbf{q} = \mathbf{Req} + i \cdot \mathbf{Imq} \tag{5.3}$$
$$\mathbf{F} = \mathbf{ReF} + i \cdot \mathbf{ImF} \tag{5.4}$$
$$\mathbf{Z} \cdot \mathbf{q} = \mathbf{F} \rightarrow \Re(\mathbf{Z} \cdot \mathbf{q}) + i \cdot \Im(\mathbf{Z} \cdot \mathbf{q}) = \mathbf{ReF} + i \cdot \mathbf{ImF}; \tag{5.5}$$

the expression of $\mathbf{S}$ is obtained substituting Equation 5.2, Equation 5.3 and Equation 5.4 inside Equation 5.5 and rearranging terms in matrix format.
At this point a condensation procedure is introduced, leading to a reorganization of the matrix $\mathbf{S}$ and vectors $\mathbf{q}$ and $\mathbf{F}$. The purpose of this procedure is the definition of the matrix **Smod**, which links the vector of the imposed displacement $\mathbf{q_k}$ with the vector of the reaction forces $\mathbf{F}$.
The matrix $\mathbf{S}$ is partitioned in order to obtain:

$$\begin{bmatrix}\mathbf{S_{kk}} & \mathbf{S_{ku}}\\ \mathbf{S_{uk}} & \mathbf{S_{uu}}\end{bmatrix} \cdot \begin{bmatrix}\mathbf{q_k}\\ \mathbf{q_u}\end{bmatrix} = \begin{bmatrix}\mathbf{F}\\ \mathbf{0}\end{bmatrix}, \tag{5.6}$$

where $\mathbf{q_u}$ represents the vector of free displacements; reaction forces are different from zero only in correspondence of the imposed displacement $\mathbf{q_k}$.
By running the product between matrices, it is obtained:

$$\begin{cases} \mathbf{S_{kk}} \cdot \mathbf{q_k} + \mathbf{S_{ku}} \cdot \mathbf{q_u} = \mathbf{F} & \text{(5.7a)}\\ \mathbf{S_{uk}} \cdot \mathbf{q_k} + \mathbf{S_{uu}} \cdot \mathbf{q_u} = \mathbf{0}. & \text{(5.7b)} \end{cases}$$

From Equation 5.7b the vector of free displacements $\mathbf{q_u}$ as a function of $\mathbf{q_k}$ is derived:

$$\mathbf{q_u} = -\mathbf{S_{uu}^{-1}} \cdot \mathbf{S_{uk}} \cdot \mathbf{q_k}. \tag{5.8}$$

The substitution of Equation 5.8 into the first equation of the system delivers the searched expression for **Smod**:

$$(\mathbf{S_{kk}} - \mathbf{S_{ku}} \cdot \mathbf{S_{uu}^{-1}} \cdot \mathbf{S_{uk}}) \cdot \mathbf{q_k} = \mathbf{F} \quad \rightarrow \quad \mathbf{S_{mod}} = \mathbf{S_{kk}} - \mathbf{S_{ku}} \cdot \mathbf{S_{uu}^{-1}} \cdot \mathbf{S_{uk}}. \tag{5.9}$$

As previously specified, it is assumed that the imaginary component of the imposed displacement is zero: $\mathbf{q_k} = \begin{bmatrix} Req_k \\ 0 \end{bmatrix}$. Whereas, generally, the vector of reaction forces has both real and imaginary component different from zero: $\mathbf{F} = \begin{bmatrix} ReF \\ ImF \end{bmatrix}$.
The circular natural frequencies of the system coincide with the zeros of the real part of the reaction force **F**, equal to the first component of the matrix $\mathbf{S_{mod}}$ times the real value of the imposed displacement $\mathbf{q_k}$ (since, as already specified, the imaginary part of $\mathbf{q_k}$ is assumend to be null). The system under consideration is linear, thus the zeros of **F** coincide with the ones of $\mathbf{S_{mod}}(1,1)$. Hence it is possible to disregard the values of $\mathbf{q_k}$ and **F** for the computation of the circular natural frequencies: the latter are calculated directly as the zeros of $\mathbf{S_{mod}}(1,1)$. The details about this procedure are provided in subsection 5.1.2.
The subsequent step after the calculation of $\mathbf{S_{mod}}$, is the definition of the full vector of global displacements **Req** and **Imq** (see Figure 5.3) obtained by placing the components of $\mathbf{q_k}$ and $\mathbf{q_u}$ in the correct order, i.e. making reference to the numbering of global dofs (`vgdl`).
At this point the functions *Update Elements* and *Update Dampers* update the structure `elements` and `dampers`: starting from **Req** and **Imq** it is defined the displacements of the nodes of each element (`structure.elements.ReD` and `structure.elements.ImD`) and of the damper attachment points (`structure.dampers.ReD` and `structure.dampers.ImD`). For both elements and dampers, the force F (whose real and imaginary component is stored inside `structure.elements.ReF`, `structure.elements.ImF`, `structure.dampers.ReF` and `structure.dampers.ImF`) is defined:

$$F = Z \cdot q, \tag{5.10}$$

where $Z = ReZ + i \cdot ImZ$ and $q = ReD + i \cdot ImD$.
The code proceeds with the computation of the circular natural frequencies: in correspondence of a zero of $\mathbf{S_{mod}}(1,1)$ (`xmean`) the function *Solve Linear Problem at Resonant Frequency* is called. This function repeats exactly the same steps of *Solve Linear Problem* but for `cfreq=xmean`: definition of the global displacements, nodal displacements of each element and of the damper attachment points. These quantities are saved in the structure data `strucure.modes.solution`. Starting from the latter, modal shapes are identified. To this purpose, the nodal displacements at the resonant frequency are interpolated through the shape functions specific for the types of elements used in the analysis. At last, the modal shapes are adimensionalized with respect to the maximum real displacements and they are plotted in the post-processing phase.

5.1.2 Description of the function *Find Zeros*

To understand the functioning of *Find Zeros*, a digression on the concept of antiresonances is necessary. This is adressed in the next subsections, taking as reference (Geradin and Rixen, 1997).

Concept of dynamic influence coefficient matrix

Forced vibration of an n-degree-of-freedom oscillator is defined as the motion resulting from the application of a harmonic force with constant amplitude:

$$\mathbf{M} \cdot \ddot{\mathbf{q}} + \mathbf{K} \cdot \mathbf{q} = \mathbf{s} \cdot cos(\omega \cdot t), \tag{5.11}$$

where ω is the excitation frequency. The forced response is then the part of the response synchronous to the excitation:

$$\mathbf{q} = \mathbf{x} \cdot cos(\omega \cdot t). \tag{5.12}$$

Substituting the solution form 5.12 into the equations of motion yields the albebraic system governing the amplitude of the response:

$$(\mathbf{K} - \omega^2 \cdot \mathbf{M}) \cdot \mathbf{x} = \mathbf{s} \tag{5.13}$$

and, by assuming that $(\mathbf{K} - \omega^2 \cdot \mathbf{M})$ is non-singular,

$$\mathbf{x} = (\mathbf{K} - \omega^2 \cdot \mathbf{M})^{-1} \cdot \mathbf{s}. \tag{5.14}$$

The matrix $(\mathbf{K} - \omega^2 \cdot \mathbf{M})^{-1}$ is the *admittance matrix* or *dynamic influence coefficient matrix* of the system.
The matrix element $a_{kl}(\omega^2)$ represents the forced vibration amplitude of the degree of freedom q_k for a harmonic loading of unit amplitude applied on degree of freedom q_l.
From its very definition, the dynamic influence coefficient matrix extends to harmonic motion the concept of the static influence coefficient as classically used for the description of a structural system.

Spectral expansion of the dynamic influence coefficient matrix

It is now solved the algebraic relationship 5.13 by an eigenmode series expansion excluding the presence of rigid-body modes:

$$\mathbf{x} = \sum_{s=1}^{n} \alpha_s \cdot \mathbf{x}_{(s)}. \tag{5.15}$$

Substituting in Eq. 5.13 the amplitude development above and taking account of eigenmode orthogonality provides the n spectral coordinates of the amplitude vector $\mathbf{x}$:

$$\alpha_s = \frac{\mathbf{x}_{(s)}^T \cdot \mathbf{s}}{(\omega_s^2 - \omega^2) \cdot \mu_s}, \tag{5.16}$$

where $\mu_s = \mathbf{x}_{(s)}^T \cdot \mathbf{M} \cdot \mathbf{x}_{(s)}$ represents the *generalized mass* of mode s and ω_s^2 are the eigenfrequencies of the system in exam. By substituting Equation 5.16 into Equation 5.15, the forced response amplitude expression is obtained:

$$\mathbf{x} = \left(\sum_{s=1}^{n} \frac{\mathbf{x}_{(s)} \cdot \mathbf{x}_{(s)}^T}{(\omega_s^2 - \omega^2) \cdot \mu_s} \right) \cdot \mathbf{s}. \tag{5.17}$$

The spectral expansion of the dynamic influence coefficient matrix is deduced by comparing Equation 5.14 and Equation 5.17:

$$(\mathbf{K} - \omega^2 \cdot \mathbf{M})^{-1} = \sum_{s=1}^{n} \frac{\mathbf{x}_{(s)} \cdot \mathbf{x}_{(s)}^T}{(\omega_s^2 - \omega^2) \cdot \mu_s}. \tag{5.18}$$

In order to enstablish the properties of the dynamic influence coefficients, it is extracted from 5.18 a given coefficient $a_{kl}(\omega^2)$ by keeping in each outer product the term corresponding to components k and l:

$$a_{kl}(\omega^2) = \sum_{s=1}^{n} \frac{x_{k(s)} \cdot x_{l(s)}}{(\omega_s^2 - \omega^2) \cdot \mu_s}. \tag{5.19}$$

When the excitation frequency tends to zero ($\omega^2 \to 0$), the matrix $(\mathbf{K} - \omega^2 \cdot \mathbf{M})^{-1}$ converges to the static influence coefficient matrix $\mathbf{K}^{-1}$ of spectral expansion, whose terms can be expressed in the following way:

$$g_{kl} = \sum_{s=1}^{n} \frac{x_{k(s)} \cdot x_{l(s)}}{\omega_s^2 \cdot \mu_s}. \tag{5.20}$$

It can thus be deduced that the dynamic coefficient may be obtained from the static one g_{kl} by applying to each term of the spectral expansion of g_{kl} the *dynamic amplification factor* (see Equation 5.19):

$$\left(1 - \frac{\omega^2}{\omega_s^2} \right)^{-1}. \tag{5.21}$$

A principal coefficient $a_{kk}(\omega^2)$ possesses the following fundamental property:

$$\frac{da_{kk}}{d\omega^2} = \sum_{s=1}^{n} \frac{x_{k(s)}^2}{(\omega_s^2 - \omega^2)^2 \cdot \mu_s} > 0, \tag{5.22}$$

i.e. the principal coefficients of the dynamic influence matrix are always increasing with excitation frequency. This implies that two resonance eigenfrequencies ω_r and ω_{r+1} are separated by an *antiresonance frequency* noted ω_r^k:

$$\omega_r < \omega_r^k < \omega_{r+1}, \tag{5.23}$$

as illustrated in Figure 5.4.

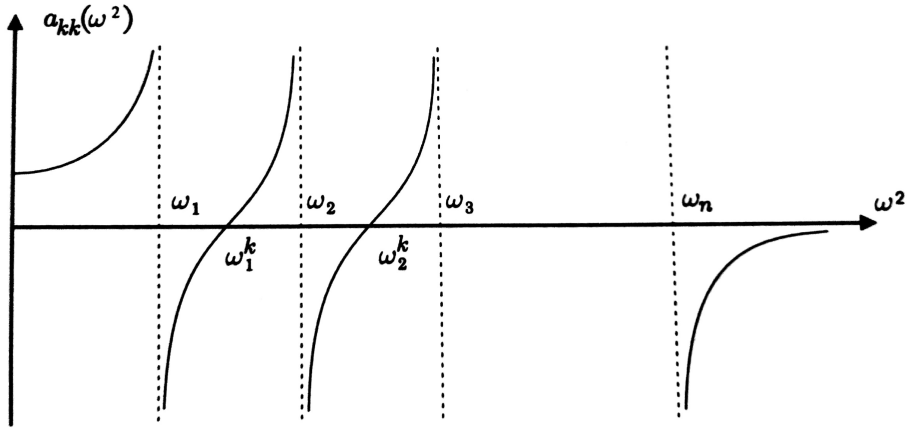

Figure 5.4: Principal dynamic influence coefficient (Geradin and Rixen, 1997).

By contrast with the resonance eigenfrequencies, the antiresonance frequencies are specific to the degree of freedom k associated with a_{kk}. From a physical point of view, they may be regarded as the resonance eigenfrequencies of the modified system obtained by fixing degree of freedom q_k.
The diagonal element $a_{kk}(\omega^2)$ also takes the form of the ratio of two polynomials in ω^2. The roots of the denominator are the eigenfrequencies of the system, whereas the numerator is of degree *n-1* and its roots are the *n-1* antiresonance frequencies associated with degree of freeedom k:

$$a_{kk}(\omega^2) = g_{kk} \cdot \frac{\prod_{s=1}^{n-1}\left(1-\left(\frac{\omega}{\omega_s^k}\right)^2\right)}{\prod_{s=1}^{n-1}\left(1-\left(\frac{\omega}{\omega_s}\right)^2\right)}. \tag{5.24}$$

Computation of the circular natural frequencies

As previously mentioned, the code computes the circular natural frequencies as the zeros of the component Smod(1,1)(ω); the latter is an impedance term, because links the reaction force vector with the imposed displacement vector.
Theoretically, in the absence of any damping contribution, in correspondance of the resonance frequencies there are vertical asymptotes. Numerically, the asymptotes are replaced with peaks, as the function Smod(1,1) is computed for a discrete number of ω-values.

The function *Find Zeros*, whose operating scheme is reported in Figure 5.5, is able to identify the resonance circular frequencies, disregarding the antiresonance circular frequencies.

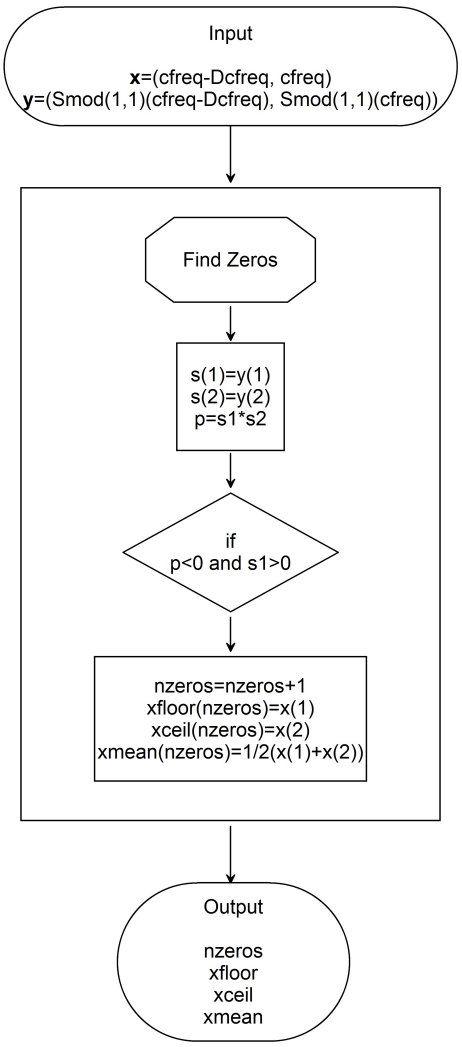

Figure 5.5: Flowchart of the function *Find Zeros*

The function *Find Zeros* is called by the sub-routine *Solve Linear Problem*, whithin the loop which spans all the circular frequencies inside the range and with the step defined in input. Attention is fixed on the *i-th* iteration. The input variables of *Find Zeros* are the vector `x` and the vector `y`, which contain respectively the circular frequency and Smod(1,1), corresponding to iteration *i-1* (`cfreq-Dcfreq`, `Smod(1,1)(cfreq-Dcfreq)`) and *i* (`cfreq`, `Smod(1,1)(cfreq)`). If the product `p` between `y` at iteration *i-1* and *i*, is less than zero, this means that the function Smod(1,1) crosses the circular frequency axis in the range between `cfreq-Dcfreq` and `cfreq`. The condition `s1`>0 ensures that a descending branch of the function Smod(1,1) is considered and then the zero represents a resonance circular frequency (see Figure 5.4). The latter is assumed equal to the mean value (`xmean`) in between `cfreq-Dcfreq` and `cfreq`. Finally, the number of zeros is updated and the procedure continues for the subsequent interval of circular frequencies.

5.2 Validation of the condutor-plus-damper system

A simple benchmark is considered in order to validate the assembly procedure of the conductor-plus-damper model. The natural frequencies and the corresponding modal shapes evaluated through the numerical model are compared to the analytical solution given by the *Rayleigh-Ritz method*.
The system in exam is composed by a simply supported conductor, equipped with a concentrated mass positioned at one quarter of its length.
For the numerical model the conductor is treated as an Euler-Bernoulli beam and the concentrated mass as a damper, whose impedance is only determined by the mass contribution.
In order to perform modal analysis, a unitary harmonic rotation is applied at midspan. The data of the problem are listed here below:

- Drake conductor;
- length of the cable L = 10 m;
- linear mass of the cable m= 1.628 kg/m;
- axial force in the cable T = 0 kN;
- bending stiffness of the cable EI = 0.5 EImax = 800 Nm^2;
- pinned ends.
- The concentrated mass is assumed to be equal to the beam linear mass times the span length: $m_s = m \cdot L = 16,28\ kg$.

The seldom exact analytical solution of this problem is provided by the *Rayleigh-Ritz* method (see e.g. Geradin and Rixen, 1997) and is illustrated here below.
The transverse displacement *w(x,t)* of the beam is described by a serie whose characteristic term is a function $\Psi_n(x)$ multiplied by a time dependent amplitude, denoted as

$q_n(t)$. The degrees of freedom of the Rayleigh-Ritz approximation are the n amplitudes $q_n(t)$; here n=10 is assumed. The displacement field w can therefore be described as:

$$w(x,t) = \sum_{n=1}^{10} \Psi_n(t) q_n(t), \tag{5.25}$$

or in matrix form as:

$$w(x,t) = \Psi^{\mathbf{T}}(x)\mathbf{q}(t). \tag{5.26}$$

The set of functions $\Psi_n(x)$ must satisfy separately the internal compatibility conditions (C^0 continuity) and the essential boundary conditions, i.e.:

$$w(0,t) = 0 \rightarrow \Psi_n(0) = 0 \tag{5.27}$$

$$w(l,t) = 0 \rightarrow \Psi_n(l) = 0. \tag{5.28}$$

The first ten eigenfunctions of the problem without the concentrated mass are chosen to approximate w, hence the vector Ψ and $\mathbf{q}$ have the following expressions:

$$\Psi(x) = \begin{bmatrix} sen\dfrac{\pi x}{L} \\ sen\dfrac{2\pi x}{L} \\ sen\dfrac{3\pi x}{L} \\ sen\dfrac{4\pi x}{L} \\ sen\dfrac{5\pi x}{L} \\ sen\dfrac{6\pi x}{L} \\ sen\dfrac{7\pi x}{L} \\ sen\dfrac{8\pi x}{L} \\ sen\dfrac{9\pi x}{L} \\ sen\dfrac{10\pi x}{L} \end{bmatrix} \quad \text{and} \quad \mathbf{q}(t) = \begin{bmatrix} q_1 \\ q_2 \\ q_3 \\ q_4 \\ q_5 \\ q_6 \\ q_7 \\ q_8 \\ q_9 \\ q_{10} \end{bmatrix}. \tag{5.29}$$

The mass matrix $\mathbf{M}$ can be identified from the expression of the kinetic enery:

$$T = \frac{1}{2}\int_0^L (\dot{w}(x,t))^2 m dx + \frac{1}{2}((\dot{w}(L/4,t))^2) m_s, \tag{5.30}$$

where the the first addend represents the contribution of the beam and the second one the contribution of the lumped mass.
By substituting Equation 5.26 into Equation 5.30, the kinetic energy can be rewritten in the following form:

$$T = \frac{1}{2}\dot{\mathbf{q}}^T \int_0^L m\Psi^T\Psi dx \dot{\mathbf{q}} + \frac{1}{2}\dot{\mathbf{q}}^T\Psi^T(L/4)\Psi(L/4)\dot{\mathbf{q}} m_s. \tag{5.31}$$

The expression of the mass matrix can be identified by inspection:

$$\mathbf{M} = \int_0^L m\Psi^T\Psi dx + m_s\Psi^T(x = L/4)\Psi(x = L/4). \tag{5.32}$$

The integration of Equation 5.32 and the subsequent calculations have been carry out with *Mathematica*. Introducing the hypothesis $m_s = mL$, the mass matrix $\mathbf{M}$ assume the following form:

$$\mathbf{M} = \begin{bmatrix} lm & \frac{lm}{\sqrt{2}} & \frac{lm}{2} & 0 & -\frac{lm}{2} & -\frac{lm}{\sqrt{2}} & -\frac{lm}{2} & 0 & \frac{lm}{2} & \frac{lm}{\sqrt{2}} \\ & \frac{3lm}{2} & \frac{lm}{\sqrt{2}} & 0 & -\frac{lm}{\sqrt{2}} & -lm & -\frac{lm}{\sqrt{2}} & 0 & \frac{lm}{\sqrt{2}} & lm \\ & & lm & 0 & -\frac{lm}{2} & -\frac{lm}{\sqrt{2}} & -\frac{lm}{2} & 0 & \frac{lm}{2} & \frac{lm}{\sqrt{2}} \\ & & & \frac{lm}{2} & 0 & 0 & 0 & 0 & 0 & 0 \\ & & & & lm & \frac{lm}{\sqrt{2}} & \frac{lm}{2} & 0 & -\frac{lm}{2} & -\frac{lm}{\sqrt{2}} \\ & & symm & & & \frac{3lm}{2} & \frac{lm}{\sqrt{2}} & 0 & -\frac{lm}{\sqrt{2}} & -lm \\ & & & & & & lm & 0 & -\frac{lm}{2} & -\frac{lm}{\sqrt{2}} \\ & & & & & & & \frac{lm}{2} & 0 & 0 \\ & & & & & & & & lm & \frac{lm}{\sqrt{2}} \\ & & & & & & & & & \frac{3lm}{2} \end{bmatrix} \tag{5.33}$$

and substituting the numerical data $\mathbf{M}$ becomes:

$$\mathbf{M} = \begin{bmatrix} 16.28 & 11.5117 & 8.14 & 0 & -8.14 & -11.5117 & -8.14 & 0 & 8.14 & 11.5117 \\ & 24.42 & 11.5117 & 0 & -11.5117 & -16.28 & -11.5117 & 0 & 11.5117 & 16.28 \\ & & 16.28 & 0 & -8.14 & -11.5117 & -8.14 & 0 & 8.14 & 11.5117 \\ & & & 8.14 & 0 & 0 & 0 & 0 & 0 & 0 \\ & & & & 16.28 & 11.5117 & 8.14 & 0 & -8.14 & -11.5117 \\ & & symm & & & 24.42 & 11.5117 & 0 & -11.5117 & -16.28 \\ & & & & & & 16.28 & 0 & -8.14 & -11.5117 \\ & & & & & & & 8.14 & 0 & 0 \\ & & & & & & & & 16.28 & 11.5117 \\ & & & & & & & & & 24.42 \end{bmatrix}. \tag{5.34}$$

The expression for the stiffness matrix $\mathbf{K}$ is derived by inspection of the elastic potential energy V_E, which can be written as:

$$V_E = \frac{1}{2}\int_0^L EI\chi^2(x,t)dx, \tag{5.35}$$

where χ can be approximated with the second derivative of the transverse displacement field w: $\chi \cong w''(x,t) = \Psi(x)''\mathbf{q}(t)$. The substitution of the expression of χ inside V_E gives:

$$V_E = \frac{1}{2}\mathbf{q}^T\int_0^L EI\Psi''^T\Psi''dx\ \mathbf{q} \rightarrow \mathbf{K} = \int_0^L EI\Psi''^T\Psi''dx. \tag{5.36}$$

The stiffness matrix $\mathbf{K}$ is obtained from the integration of Equation 5.36:

$$\mathbf{K} = diag\left(\frac{\mathrm{EI}\pi^4}{2l^3}, \frac{8\mathrm{EI}\pi^4}{l^3}, \frac{81\mathrm{EI}\pi^4}{2l^3}, \frac{128\mathrm{EI}\pi^4}{l^3}, \frac{625\mathrm{EI}\pi^4}{2l^3}, \frac{648\mathrm{EI}\pi^4}{l^3}, \frac{2401\mathrm{EI}\pi^4}{2l^3}, \frac{2048\mathrm{EI}\pi^4}{l^3}, \frac{6561\mathrm{EI}\pi^4}{2l^3}, \frac{5000\mathrm{EI}\pi^4}{l^3}\right), \tag{5.37}$$

substituting the numerical data:

$$\mathbf{K} = diag\left(\frac{2\pi^4}{5}, \frac{32\pi^4}{5}, \frac{162\pi^4}{5}, \frac{512\pi^4}{5}, 250\pi^4, \frac{2592\pi^4}{5}, \frac{4802\pi^4}{5}, \frac{8192\pi^4}{5}, \frac{13122\pi^4}{5}, 4000\pi^4\right). \tag{5.38}$$

The free vibration and harmonic motion assumptions yield the expression of the discretized eigenvalue problem:

$$\mathbf{Kq} = \omega^2\mathbf{Mq}. \tag{5.39}$$

By solving the characteristic equation derived from $det(\mathbf{K} - \omega^2\mathbf{M})$, the natural circular frequencies of the first ten modes reported in Table 5.1 are derived. The *i-th* modal shape is computed multiplying the vector of the shape fuctions Ψ times the *i-th* eigenvector. Figure 5.6 shows the modal shapes derived by the Rayleigh- Ritz method, computed with *Mathematica*. The red circle indicates the position of the lumped mass.

Mode number	Rayleigh-Ritz method [rad/s]	Numerical [rad/s]	Error [%]
1	1.51874	1.51850	0.01580
2	6.18940	6.18800	0.02262
3	17.7664	17.7605	0.03321
4	35.0056	35.0060	0.00114
5	48.4077	48.2475	0.33094
6	69.104	68.8440	0.37624
7	102.350	102.094	0.25012
8	140.022	140.022	0.00000
9	166.665	164.251	1.44841
10	204.500	201.289	1.57017

Table 5.1: First ten natural circular frequencies.

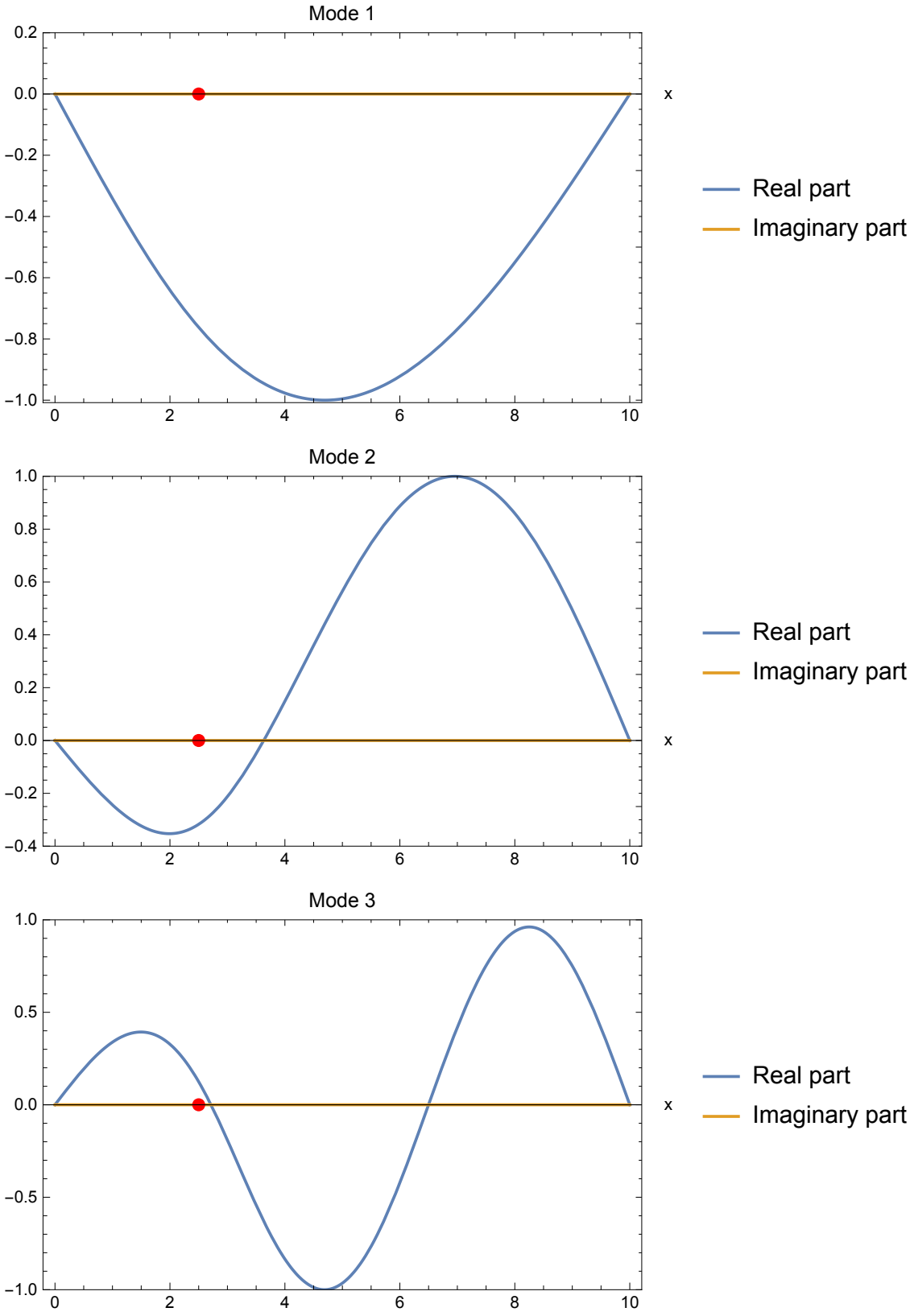
Mode 1
0.2
0.0
−0.2
−0.4
−0.6
−0.8
−1.0
0
2
4
6
8
10
x
Real part
Imaginary part
Mode 2
1.0
0.8
0.6
0.4
0.2
0.0
−0.2
−0.4
0
2
4
6
8
10
x
Real part
Imaginary part
Mode 3
1.0
0.5
0.0
−0.5
−1.0
0
2
4
6
8
10
x
Real part
Imaginary part

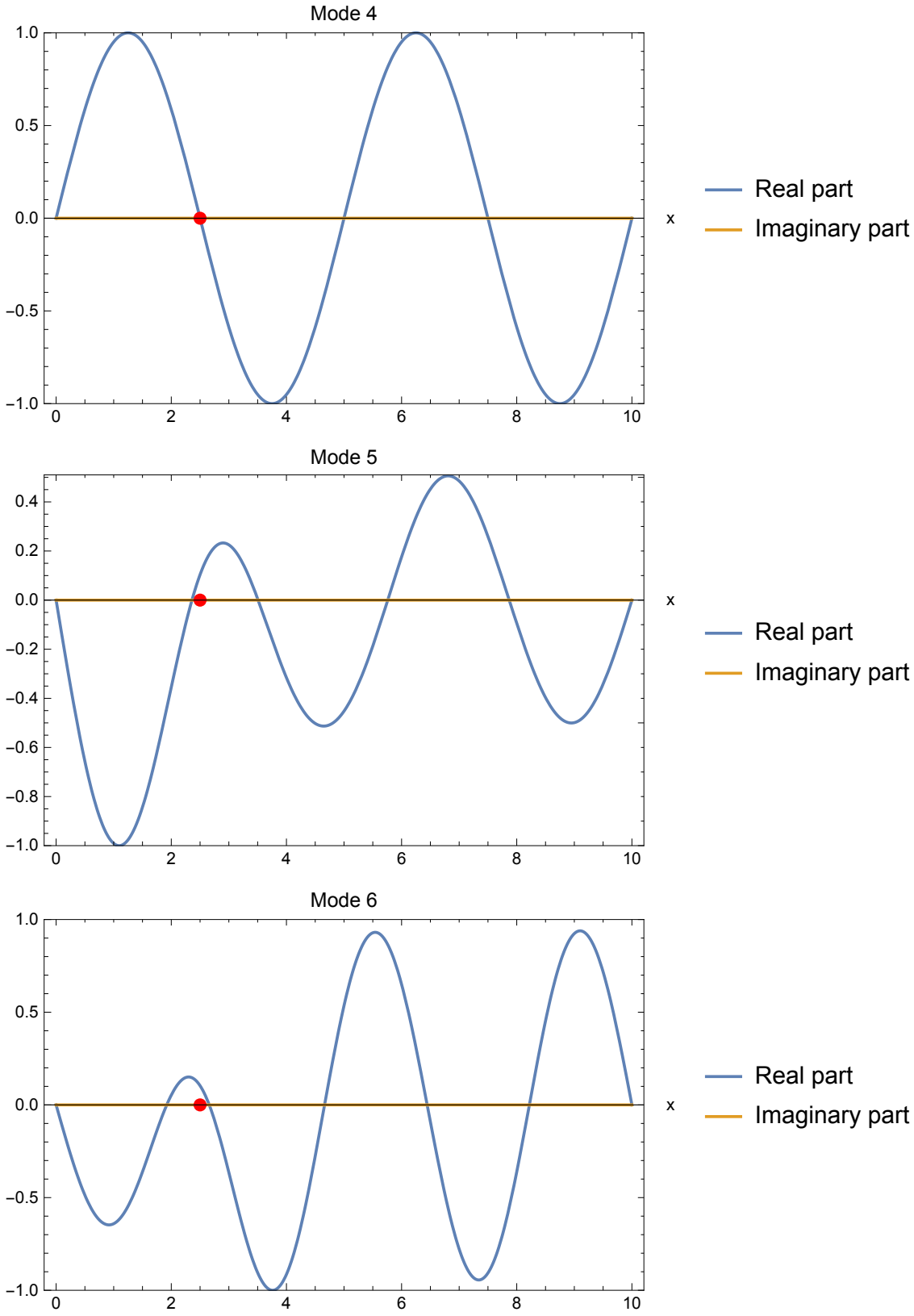
Mode 4
1.0
0.5
0.0
−0.5
−1.0
0
2
4
6
8
10
x
Real part
Imaginary part
Mode 5
0.4
0.2
0.0
−0.2
−0.4
−0.6
−0.8
−1.0
0
2
4
6
8
10
x
Real part
Imaginary part
Mode 6
1.0
0.5
0.0
−0.5
−1.0
0
2
4
6
8
10
x
Real part
Imaginary part

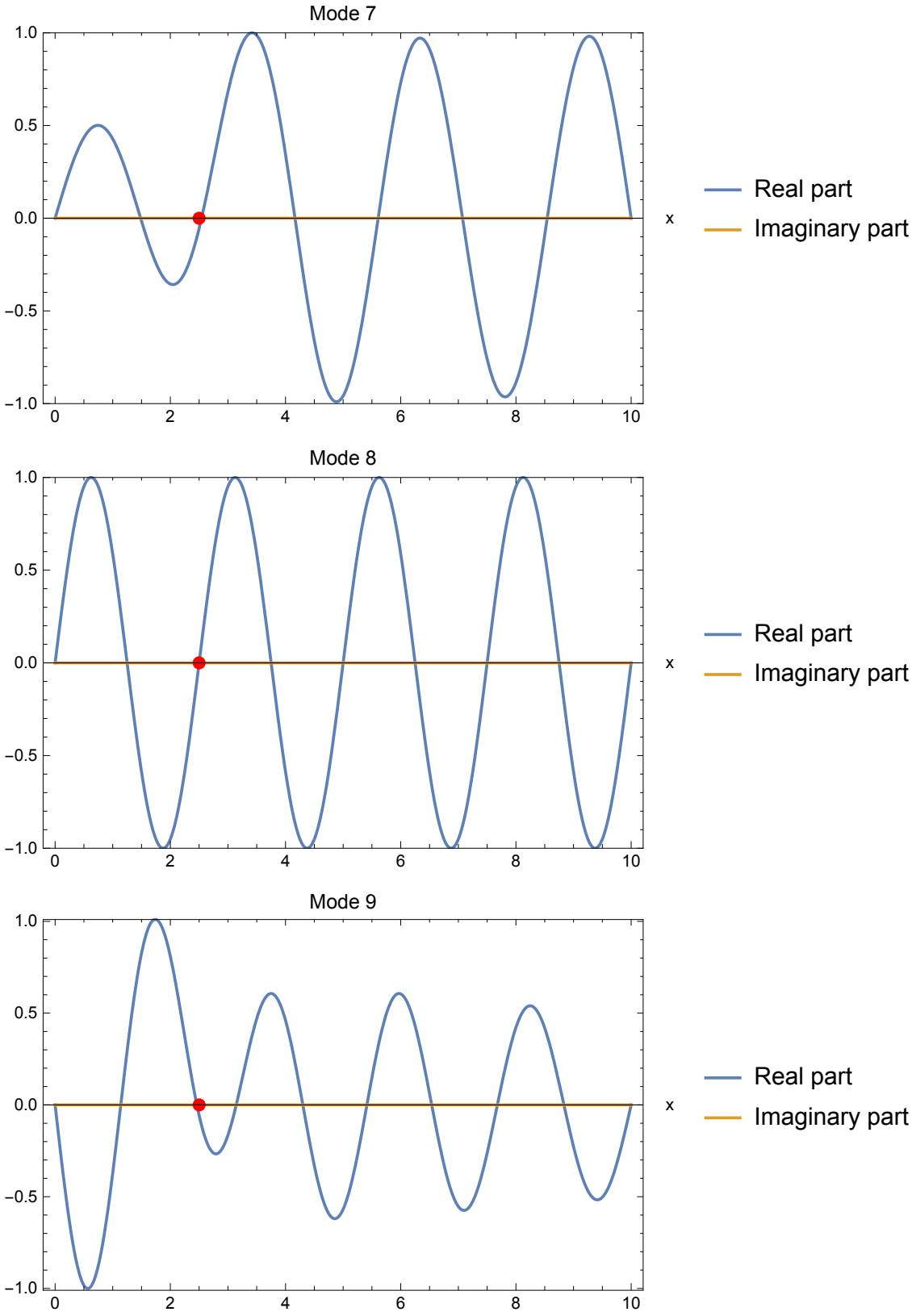
Mode 7
1.0
0.5
0.0
−0.5
−1.0
0
2
4
6
8
10
x
Real part
Imaginary part
Mode 8
1.0
0.5
0.0
−0.5
−1.0
0
2
4
6
8
10
x
Real part
Imaginary part
Mode 9
1.0
0.5
0.0
−0.5
−1.0
0
2
4
6
8
10
x
Real part
Imaginary part

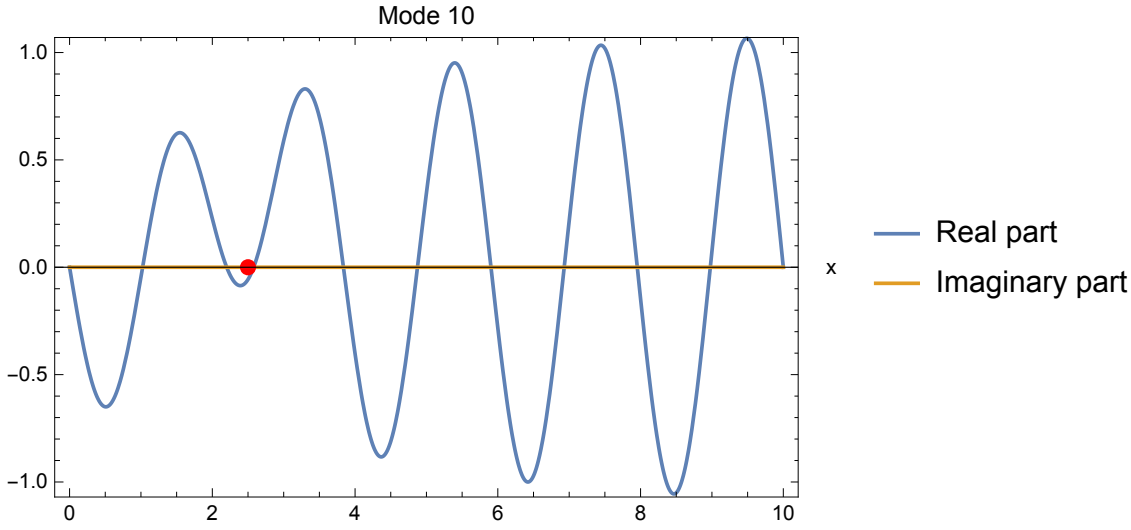

Figure 5.6

The results of the Rayleigh-Ritz method are compared with the ones given by the Matlab code. The numerical model consists of four nodes, placed in correspondence of the two supports, at L/4 (position of the lumped mass) and at midspan (where the rotation is applied), three Euler-Bernoulli elements and one damper to represent the lumped mass. The impedance of the latter is computed starting from the impedance of a translational linear damper:

$$Z = \frac{(k + i\omega c)(-m\omega^2)}{(-m\omega^2 + i\omega c + k)}, \tag{5.40}$$

where k is the stiffness of the damper, m the mass and c represents the damping coefficient. For the case in exam c is null, because no damping is considered, and the stiffness $k \to \infty$ as the mass is rigidly attached to the beam. The impedance for the lumped mass is obtained from Equation 5.40, taking the limit for $k \to \infty$:

$$\lim_{k\to\infty} \left(\frac{(k + i\omega c)(-m\omega^2)}{-m\omega^2 + i\omega c + k} \right) = -m\omega^2. \tag{5.41}$$

The first ten circular natural frequencies computed with the numerical model are reported in Table 5.1, which shows that numerical and analytical results match quite well. The modal shapes are reported in Figure 5.7; they correspond to those calculated with the Rayleigh-Ritz method (see Figure 5.6). The magenta square represents the position of the lumped mass.

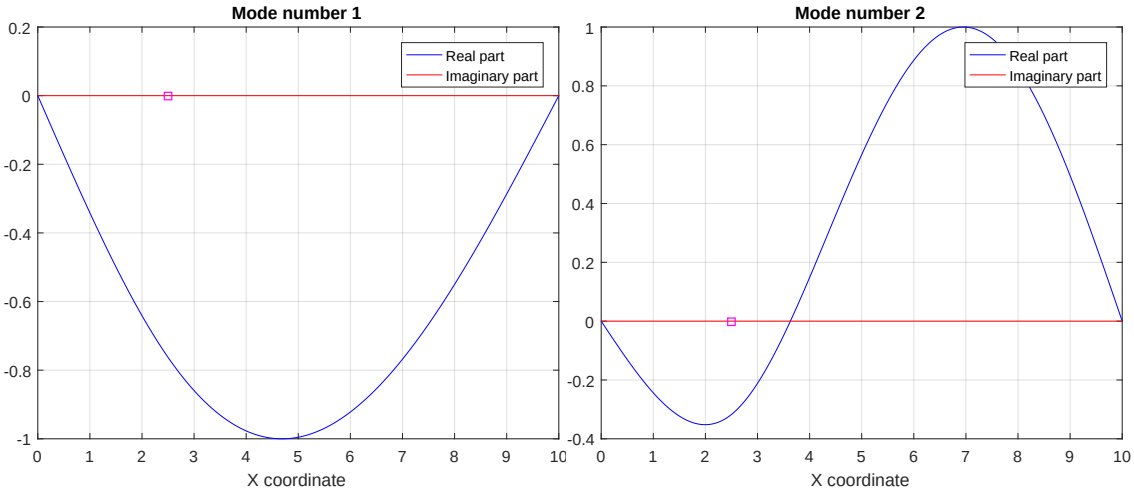
Mode number 1
Real part
Imaginary part
X coordinate
Mode number 2
Real part
Imaginary part
X coordinate

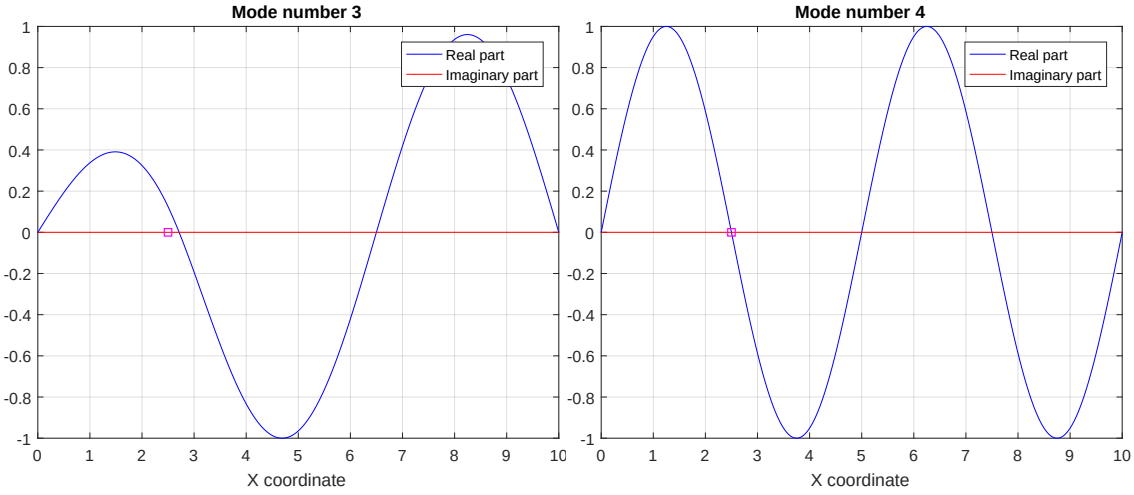
Mode number 3
Real part
Imaginary part
X coordinate
Mode number 4
Real part
Imaginary part
X coordinate

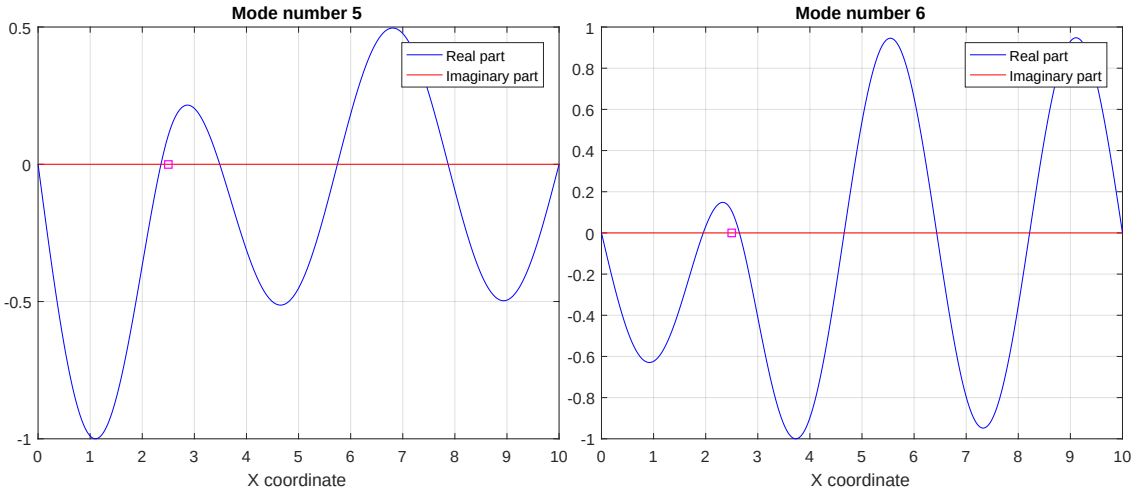
Mode number 5
Real part
Imaginary part
X coordinate
Mode number 6
Real part
Imaginary part
X coordinate

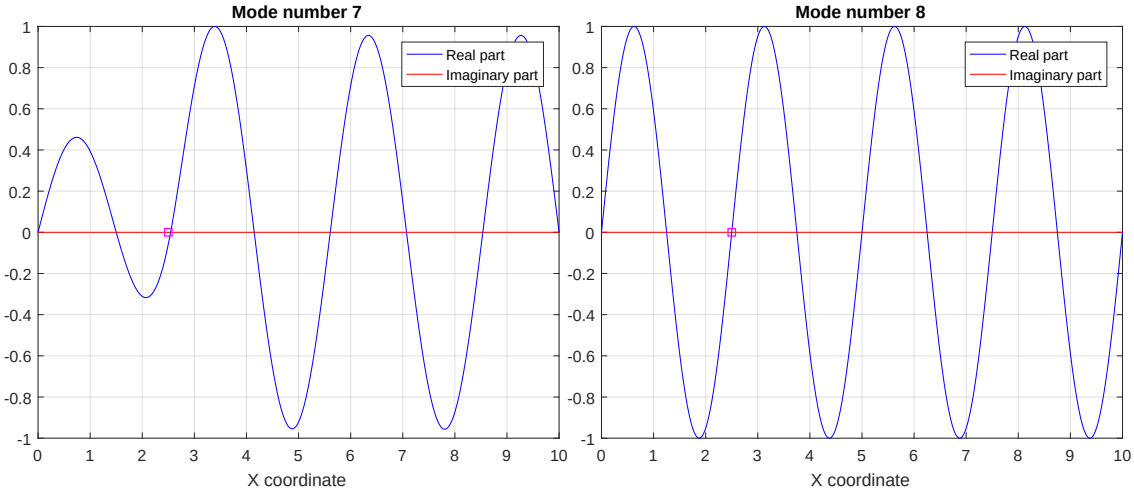
Mode number 7
Real part
Imaginary part
X coordinate
Mode number 8
Real part
Imaginary part
X coordinate

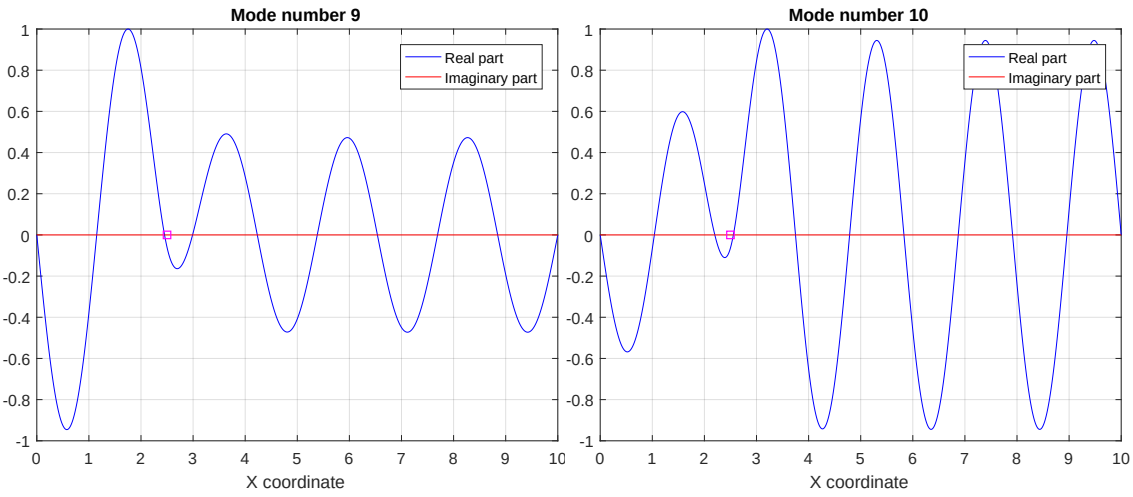

Figure 5.7: First ten modes computed with the numerical model.

It is possible to observe that, since the span is very small (L=10m), the lumped mass has an immediate effect on the modes of the conductor, noticeaby on further progressing vibration frequencies. It can be also noticed that, for example, for mode 10 and mode 17 (reported in Figure 5.8), the presence of the mass effectively reduces the displacement of the conductor.
Table 5.2 reports a comparison between the first ten natural frequencies, computed with the numerical model, with and without the lumped mass. The comparison between the two sets of values shows how the presence of the lumped mass causes a consistent reduction of the natural frequencies, compared to the case of the bare conductor. This is not surprising as it is known that natural frequency is inversely proportional to the mass.

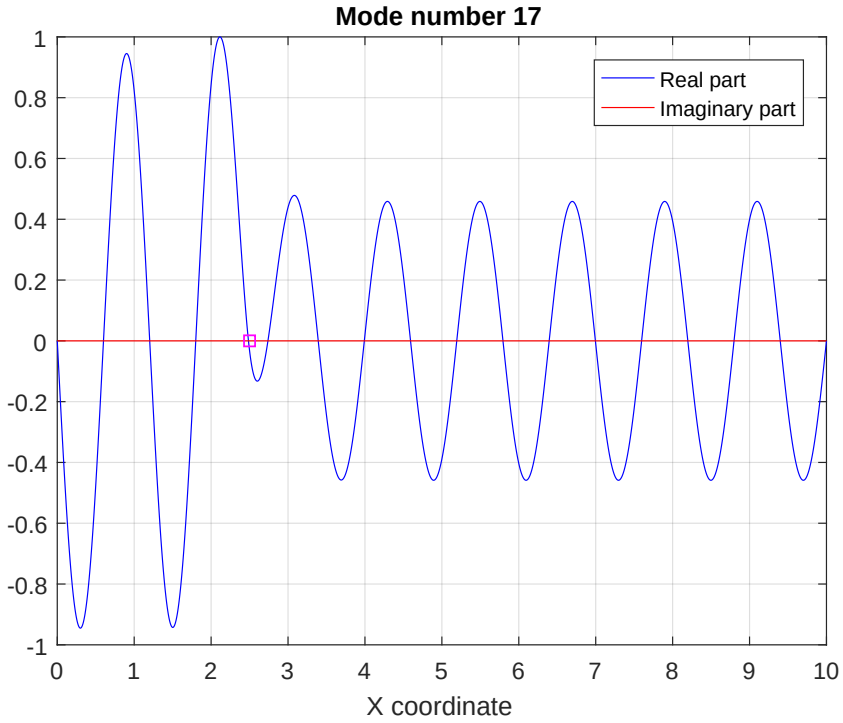

Figure 5.8: Mode number 17

Mode number	Circ. freq. with the lumped mass	Circ. freq. without the lumped mass
1	1.51850	2.18750
2	6.18800	8.75100
3	17.7605	19.6905
4	35.0060	35.0060
5	48.2475	54.6965
6	68.8440	78.7630
7	102.094	107.204
8	140.022	140.002
9	164.251	177.215
10	201.289	218.784

Table 5.2: First ten natural circular frequencies: comparison between the model with and without the lumped mass.

Chapter 6

Energy balance principle

The Energy Balance Method is used in this work to predict the steady-state aeolian vibration of the conductor and conductor-plus-dampers system; it is implemented through the function *Energy Balance Principle* inside the *CBFD* Matlab code. This method states that the maximum amplitude of vibration for each of the excited vibration modes is the one for which the power imparted by the wind is equal to the power dissipated through the conductor self-damping plus the power dissipated by dampers, as already stated in section 2.6.
For each natural frequency, identified according to the procedure discussed in chapter 5, the conductor vibration amplitudes is defined along the span as a function of a reference amplitude (the maximum antinodal displacement amplitude), which then enables the wind energy input and the energy dissipated by the conductor to be calculated. With the mode of vibration known, the motion of the dampers is determined as a function of the reference amplitude and the energy dissipated can then be computed.
The power dissipated through the conductor self-damping and the wind power are expressed through empirical relations with the form of the ones defined in subsection 2.6.1 and subsection 6.1.2. Whereas, the total power dissipated by dampers is determined starting from the definition of the generalized displacements at the damper clamp, for each modal shapes of the conductor-plus-dampers system. The latter, as already pointed out in chapter 5, are defined taking into account of the distortional effect of dampers.

This chapter is organized as follows: section 6.1 describes the function *Energy Balance Principle*, through which the energy balance is implemented inside the code *CBFD*; section 6.2 analyzed the aeolian vibration response of a single conductor, discussing the effect of the conductor tension and of the turbulence index on the level of vibration. Finally, section 6.3 deals with the response of a cable equipped with one Stockbridge-type damper.

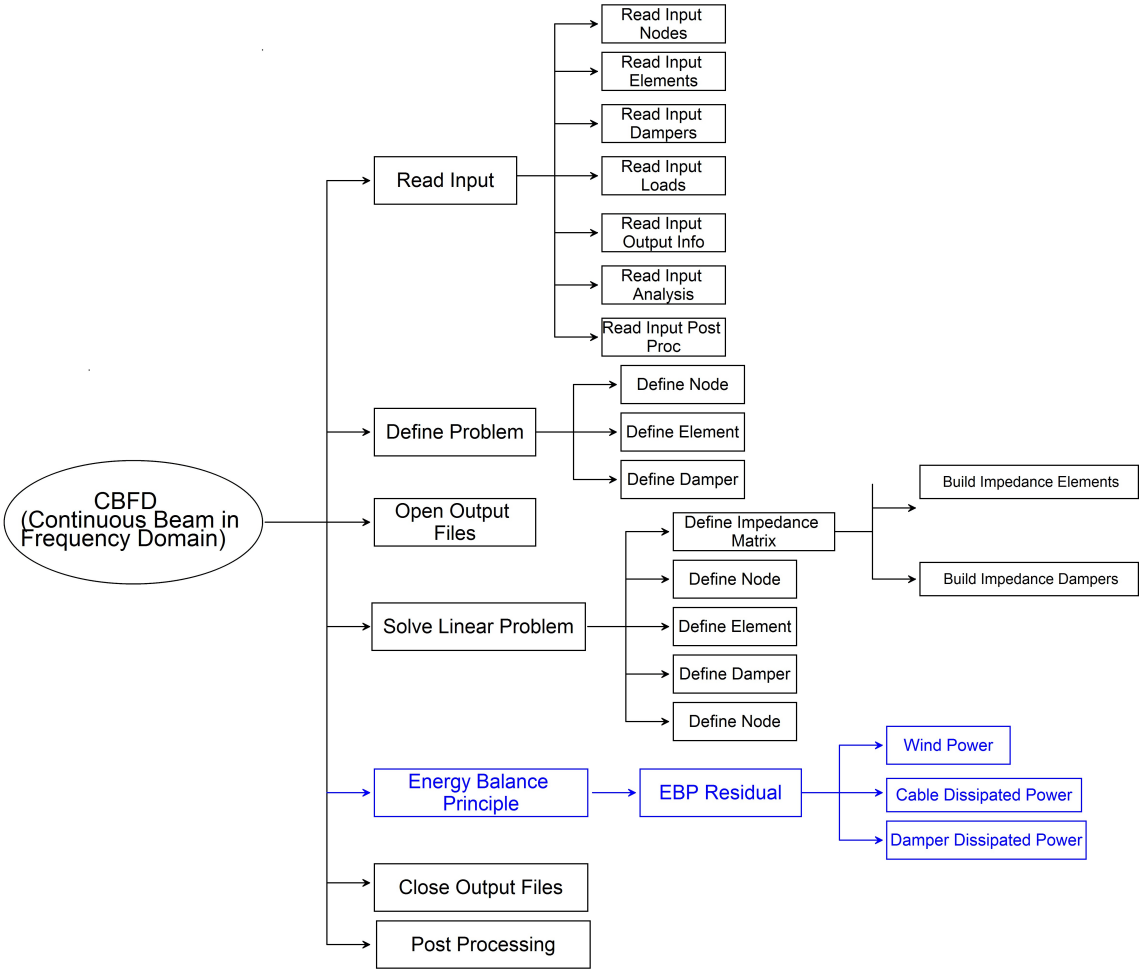

Figure 6.1: Flowchart of the sub-routines related to the *Energy Balance Principle* function.

6.1 Description of the function *Energy Balance Principle*

The positioning of *Energy Balance Principle* within the *CBFD* code is illustrated in Figure 6.1. The operating scheme of the *CBFD* code before the call to the *Energy Balance Principle* function is the one described in section section 5.1. The only difference is that the calculation of the power dissipated by dampers is introduced within *Solve Linear Problem* (see subsection 6.1.1).
The energy balance, for each natural frequency, is performed through the Matlab function *fsolve*, a solver of nonlinear equations and systems. The nonlinear equation to solve is given by *EBP Residual* and has the following form:

$$f(y_{max}) = P_w(y_{max}) - P_c(y_{max}) - P_d(y_{max}) = 0, \tag{6.1}$$

where P_w is the power imparted by the wind, P_c is the power dissipated by the conductor self-damping and P_d is the total power dissipated by dampers. The solver finds, for each natural frequency, the level of vibration y_{max} for which the function f is equal to zero. y_{max} represents the maximum antinodal displacement amplitude; it is computed as the maximum of the real component of each modal shapes of the conductor-plus-dampers system by the function *Solve Linear Problem*.
The vibration level given by the energy balance can be seen graphically as the point of intersection of the curves describing the wind input power, the power dissipated by the conductor and the power dissipated by dampers, as a function of the reference amplitude. To exclude the trivial solution, which represents always a point of intersection of the curves (see e.g. Figure 6.5), it is necessary to give in input to the function *fsolve* a proper initial guess, which in this case is represented by the value of the cable diameter, as it is generally accepted that the amplitude of aeolian vibrations is limited to this value.

Subsection 6.1.1, subsection 6.1.2 and subsection 6.1.3, describe, respectively, how the power dissipated by dampers, the power dissipated by the cable and the wind power are calculated.

6.1.1 Power dissipated by dampers

The wind power and the power dissipated by the conductor are expressed as functions of the reference amplitude, which coincide with the maximum of the real component of each modal shapes of the conductor-plus-dampers system (here indicated as y_{max}). Therefore, to determine the level of vibration through the EBP also the power dissipated by dampers have to be expressed in terms of this variable.
Figure 6.2 schematically represents the steps for the computation of the power dissipated by dampers and for the application of the energy balance.

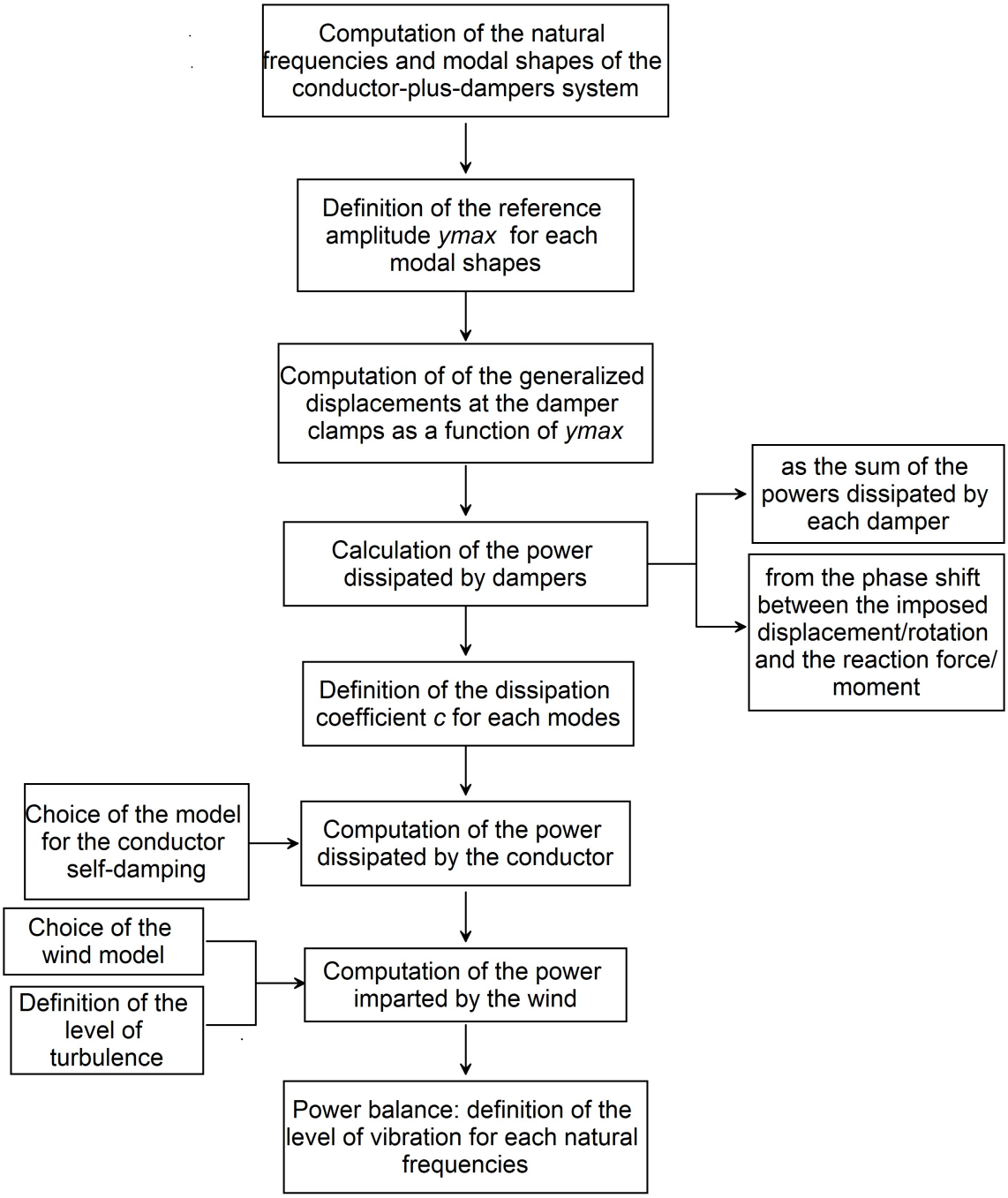

Figure 6.2: Steps for the computation of the power dissipated by dampers and for the application of the energy balance .

Due to the system linearity (the conductor and the dampers are treated as linear elements), the total power dissipated by dampers is expressed as a quadratic function of y_{max}. In particular, for each mode considered, in the $y_{max} - P_d$ plane, the curve $P_d(y_{max})$ is a parabola passing through the origin of the axes (Figure 6.3), since, if y_{max} takes zero value, the displacements of the damper clamps and thus the power dissipated by them are null.

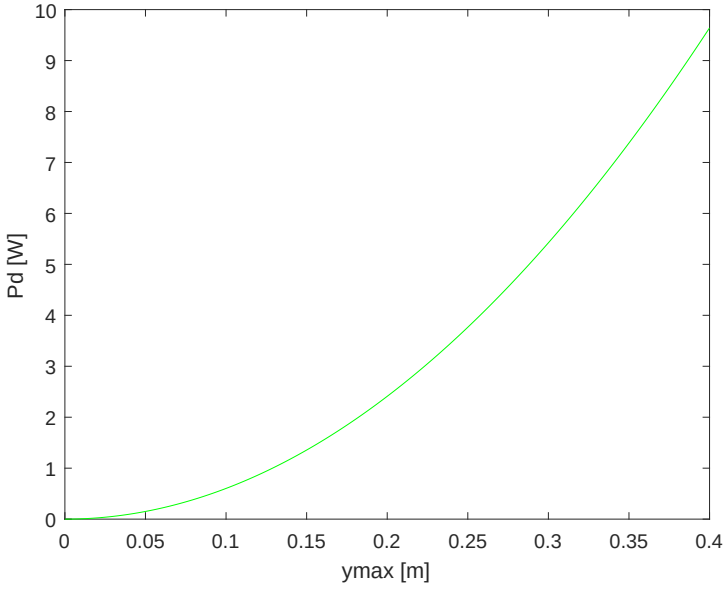

Figure 6.3: Typical trend of the total power dissipated by dampers as a function of y_{max}.

The set of coefficients $c_n = c(f_n)$ of the parabolas representing the total power dissipated by dampers at each natural frequency f_n can then be computed as the ratio in between the total power dissipated by dampers P_d and the square of y_{max}:

$$c_n = c(f_n) = \frac{P_d}{{y_{max}}^2}. \tag{6.2}$$

P_d can be equivalently computed following one of these two procedures:

- determination of P_d as the sum of the power dissipated by each dampers P_{di}: $P_d = \sum_{i=1}^{n} P_{di}$, where n represents the number of dampers attached at the conductor;
- calculation of P_d by means of the matrix S_{mod}, introduced in chapter 5.

The first option is now considered. P_{di} is computed within the function *Solve Linear Problem*, for each modes of the system. For a traslational damper, at a generic circular frequency ω, the displacement $d(t)$ and its work-conjugated force $F(t)$, can be

respectively espressed as:

$$d(t) = |d| \cdot sin(\omega t + \phi_d), \tag{6.3}$$
$$F(t) = |F| \cdot sin(\omega t + \phi_F). \tag{6.4}$$

The velocity $v(t)$ is obtained by deriving Equation 6.3 with respect to time:

$$v(t) = |v| \cdot sin(\omega t + \phi_v), \tag{6.5}$$

with the following definitions:

$$|v| = \omega \cdot |d|, \tag{6.6}$$
$$\phi_v = \frac{\pi}{2} - \phi_d. \tag{6.7}$$

The dissipated energy per cycle, can then be evaluated as follows:

$$E_{di} = \int_t^{t+T} F(t) \cdot v(t) dt = \int_t^{t+T} |F| \cdot |v| \cdot sin(\omega t + \phi_F) \cdot sin(\omega t + \phi_v) dt. \tag{6.8}$$

By substituting Equation 6.7 in Equation 6.8 and recalling the following trigonometric identity:

$$sin(\omega t + \phi) = sin(\omega t) \cdot cos(\phi) + cos(\omega t) \cdot sin(\phi), \tag{6.9}$$

from Equation 6.8 it is obtained:

$$E_{di} = \frac{\pi}{\omega} \cdot |F| \cdot |v| \cdot |sin(\phi_F - \phi_d)|. \tag{6.10}$$

Recalling Equation 6.6, the above expression is rewritten as follows:

$$E_{di} = \pi \cdot |F| \cdot |d| \cdot |sin(\phi_F - \phi_d)|. \tag{6.11}$$

Finally, the dissipated power is obtained by multiplying the expression for the energy 6.10 by the frequency of the mode under consideration:

$$P_{di} = \frac{\omega}{2} \cdot |F| \cdot |d| \cdot |sin(\phi_F - \phi_d)|. \tag{6.12}$$

Up to now the case of translational damper has been considered, whose impedance matrix H has the following form:

$$\begin{bmatrix} H_{11} & 0 \\ 0 & 0 \end{bmatrix}. \tag{6.13}$$

The moment M_c transmitted at the clamp is null and the force F_c can be expressed as:

$$\begin{bmatrix} H_{11} & 0 \\ 0 & 0 \end{bmatrix} \cdot \begin{bmatrix} v_c \\ \varphi_c \end{bmatrix} = \begin{bmatrix} F_c \\ M_c \end{bmatrix}, \tag{6.14}$$

where v_c and φ_c are, respectively, the displacement and the rotation at the damper clamp.
If also the effect of rocking is taken into account, an asymmetric damper is characterized by a full (2x2) impedance matrix:

$$\begin{bmatrix} H_{11} & H_{12} \\ H_{21} & H_{22} \end{bmatrix} \rightarrow \begin{bmatrix} H_{11} & H_{12} \\ H_{21} & H_{22} \end{bmatrix} \cdot \begin{bmatrix} v_c \\ \varphi_c \end{bmatrix} = \begin{bmatrix} F_c \\ M_c \end{bmatrix}. \tag{6.15}$$

In the case of a perfectly symmetric damper, the extra-diagonal terms H_{12} and H_{21} vanish.
M_c contributes to the energy dissipated by the damper, hence the damper dissipated power P_{di} is equal to the translational contribution of 6.16, plus the rotational term:

$$P_{di} = \frac{\omega}{2} \cdot (|F| \cdot |d| \cdot |sin(\phi_F - \phi_d)| + |M| \cdot |\varphi| \cdot |sin(\phi_M - \phi_\varphi)|), \tag{6.16}$$

where φ is the rotation at the damper clamp, for the mode considered, and M is the work-conjugated moment.

The second approach evaluates the total dissipated power by dampers starting from the definition of S_{mod} (see Equation 5.9):

$$\begin{bmatrix} S_{mod}(1,1) & S_{mod}(1,2) \\ S_{mod}(2,1) & S_{mod}(2,2) \end{bmatrix} \cdot \mathbf{q_k} = \mathbf{F_R}, \tag{6.17}$$

where $\mathbf{q_k} = \begin{bmatrix} Req_k \\ 0 \end{bmatrix}$ and $\mathbf{F_R} = \begin{bmatrix} ReF \\ ImF \end{bmatrix}$. If a displacement has been imposed to find modes (see chapter 5), the total power dissipated by dampers can be computed by Equation 6.16, by substituting the module of F with the modulus of $\mathbf{F_R}$ and the modulus of d with the modulus of $\mathbf{q_k}$:

$$P_d = \frac{\omega}{2} \cdot |\mathbf{F_R}| \cdot |\mathbf{q_k}| \cdot |sin(\phi_{F_R} - \phi_{q_k})|, \tag{6.18}$$

where

$$|\mathbf{q_k}| = Req_k \tag{6.19}$$

$$|\mathbf{F_R}| = \sqrt{ReF_R^2 + ImF_R^2} = \sqrt{(S_{mod}(1,1) \cdot Req_k)^2 + (S_{mod}(2,1) \cdot Req_k)^2} \tag{6.20}$$

If a rotation has been set for the mode calculation, the procedure is analogous; the total power dissipated by dampers is expressed by:

$$P_d = \frac{\omega}{2} \cdot |\mathbf{M_R}| \cdot |\varphi_\mathbf{k}| \cdot |sin(\phi_{M_R} - \phi_{\varphi_k})|, \tag{6.21}$$

where

$$|\varphi_\mathbf{k}| = Re\varphi_k \tag{6.22}$$

$$|\mathbf{M_R}| = \sqrt{ReM_R^2 + ImM_R^2} = \sqrt{(S_{mod}(1,1) \cdot Re\varphi_k)^2 + (S_{mod}(2,1) \cdot Re\varphi_k)^2}. \tag{6.23}$$

6.1.2 Power dissipated by the conductor

The function *Energy Balance Principle* allows to select the model for the cable self-damping and the model of the wind to be used in the analysis, then, according to the choice of the user, respectively, the function *Cable Dissipated Power* and *Wind Power* compute the power dissipated by the conductor and the power imparted by the wind.
The model for the cable self-damping adopted for the benchmarks proposed in the following sections estimates the power dissipated by the conductor through the following semi-empirical expression (Lu and Chan, 2015):

$$P_c = C_c \cdot \bar{A}, \tag{6.24}$$

where $\bar{A}$ denotes the non-dimensional antinode vibration amplitude (here defined as y_{max}) of the cable, defined as the ratio between the antinode vibration amplitude and the conductor diameter. The coefficient C_c depends upon the vibration frequency, according to the following expression:

$$C_c = 1.07 \cdot 10^6 \cdot E \cdot \sqrt{k_d} \cdot k_{max} \cdot k_0 \cdot L_0 \cdot D^7 \cdot f^{6+\alpha} \cdot V_c^{-5}. \tag{6.25}$$

The symbols adopted in Equation 6.25 along with the relative unit of measures are itemized here below:

- E (Pa) is the equivalent (i.e. defined accounting for the internal structure of the conductor) Young modulus of the conductor;
- k_d is an empirical factor which can be assumed equal to 0.54 for an ACSR conductor and to 0.65 for a stranded steel conductor;
- k_{max} is the reduction factor on the maximum conductor bending stiffness, which can be assumed equal to 0.5;
- L_0 (m) is the free span length;
- D (m) is the conductor diameter;
- f (Hz) is the vibration frequency;
- V_c is the conductor wave velocity, which can be evaluated as $V_c = \sqrt{H/m}$, denoting as H (N) the horizontal reaction at the end of the cable (as a first approximation in the numerical calculations the following approximation has been considered: $H = T$, where T is the axial force in the cable) and as m (kg) the mass per unit length of the conductor;
- k_0 and α are experimentally determined constants, which can be assumed respectively equal to: 0.0035 and -0.4332, for AAC conductors and to 0.0042 and -0.4256, for ACSR conductors.

In the applications proposed in the subsequent sections the following values are considered:

- $E = 5 \cdot 10^{10}\ Pa$,
- $k_d = 0.54$,
- $k_{max} = 0.5$,
- $k_0 = 0.0042$,
- $\alpha = -0.4256$.

6.1.3 Power impated by the wind

The wind model taken as reference for the following examples defines the wind power through the following expression:

$$P_w = B_w \cdot (-99.73 \cdot \bar{A}^3 + 101.62 \cdot \bar{A}^2 + 0.1627 \cdot \bar{A} + 0.2256) \cdot D^4 \cdot f^3 \cdot L_0, \qquad (6.26)$$

where B_w is a reduction factor which accounts for the turbulence level. B_w is defined as a function of: the wind turbulence intensity I_V (defined as in (Lu, 2003)) and the lock in index I_L which can be assumed equal to 0.09. The following expression holds:

$$B_w = \left[1 + \left(\frac{I_V}{I_L}\right)^2\right]^{-0.5}. \qquad (6.27)$$

6.2 Single conductor

In this section the aeolian vibration response of a single conductor is analyzed. The data of the simulation are taken from (EPRI, 2006) and are reported in Table 6.1 and Table 6.2

Data fo the simulation	
Span length	366 [m]
Constraints	fixed clamp
Type of Conductor	Drake
Type of wind	model of Diana, no turbulence

Table 6.1: Aeolian vibration response of a single conductor: data of the simulation.

Drake conductor		
Diameter	28	$[mm]$
Mass	1.628	$[kg]$
Flexural stiffness	800	$[Nm^2]$
Tension	28024 (20 % RTS)	[N]

Table 6.2: Drake conductor characteristics.

For the numerical model two pre-stressed Euler-Bernoulli beam elements are used; a unit harmonic displacement is applied at a distance of 100 m from the left clamp, in order to capture both symmetric and skew-symmetric modes. A frequency range bounded by 30 rad/s and 315 rad/s (corresponding to a frequency range of 5-50 Hz) has been spanned with a step equal to 0.01 rad/s.
Figure 6.4 shows the Drake conductor response to aeolian vibrations in terms of the maximum antinode amplitude of vibration (0-peak values), as a function of the frequency, related to the model here adopted and to (EPRI, 2006). The two curves match very well.
At each frequency, the level of vibration graphically corresponds to the intersection of the power imparted by the wind P_w and the power dissipated by the cable P_c. Figure 6.5 shows these curves for a fixed frequency of 10 Hz.
The level of vibration decreases with increasing frequency due to the fact that the power dissipated by the conductor self-damping increases faster than the wind power, as the frequency increases (see Equation 6.24 and Equation 6.26). Figure 6.6 shows the trend of the wind power curve and the dissipated power of the conductor for three values of frequency: 10 Hz, 20 Hz and 30 Hz. The points of intersection of P_w and P_c at each frequency are marked with red circles; the intersections in the negative plane are always neglected, as they don't have physical meaning.

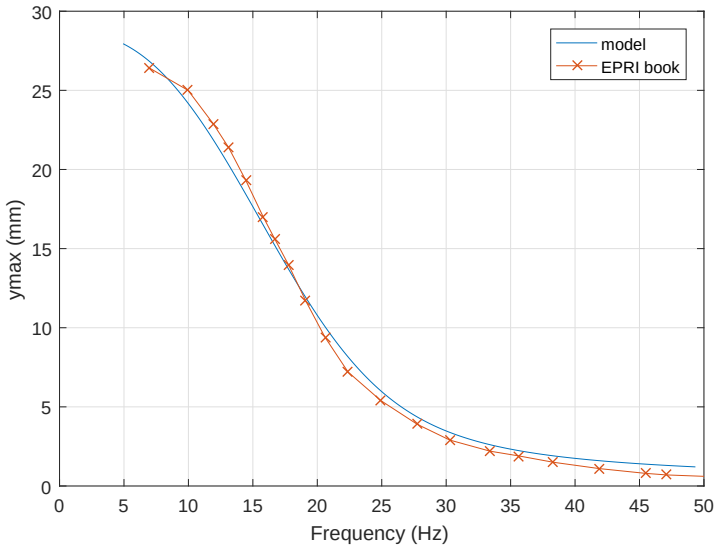

Figure 6.4: Drake conductor response to aeolian vibrations: maximum antinode amplitude of vibration.

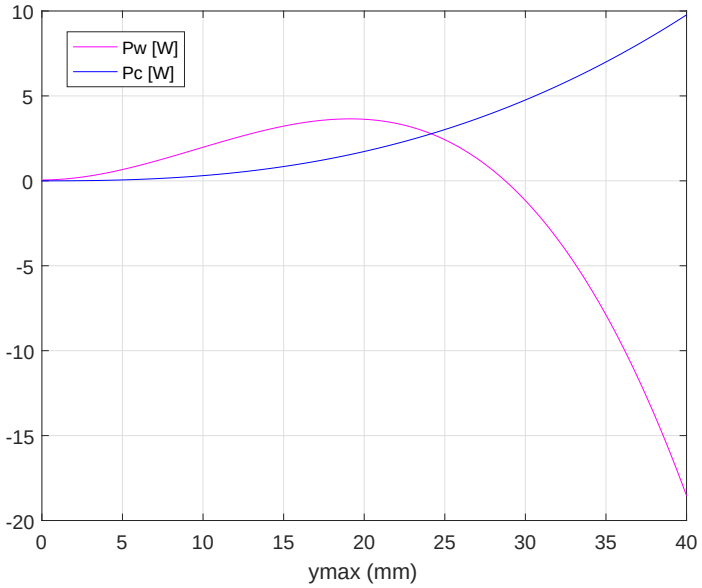

Figure 6.5: Power imparted by the wind and power dissipated by the cable as a function of y_{max}, for a fixed frequency of 10 Hz.

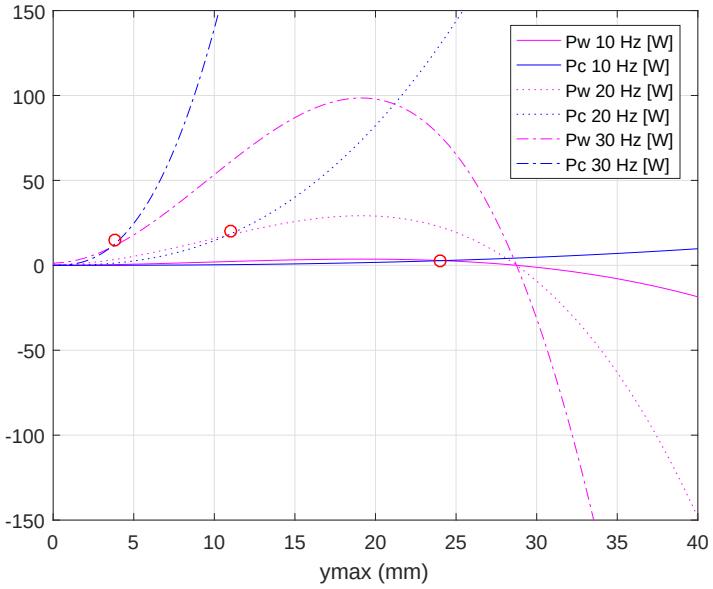

Figure 6.6: Power imparted by the wind and power dissipated by the cable as a function of y_{max}, for fixed frequencies of 10 Hz, 20 Hz and 30 Hz.

6.2.1 Effect of tension

The effect of the conductor tension T, for the simulation proposed in the previous section, is here analyzed. The data of the analysis remain unchanged with respect to the previous case; the Drake conductor response to aeolian vibrations is proposed for three different values of the conductor tension:

- T=20 % RTS=28024 N,
- T=25 % RTS=35030 N and
- T=30 % RTS=42036 N.

6.7a represents the maximum antinode amplitude of vibration as a function of frequency and 6.7b reports the power imparted by the wind (which obviously doesn't change changing the conductor tension) and the dissipated power due to the conductor self-damping, for the three values of the cable tension considered.
It can be noticed that, as the tension increases, the curve of the conductor dissipated power tend to flatten and the intersection with the wind power occurs in correspondence of a larger value of y_{max}, it follows that the amplitude of vibration for each frequency increases.
This fact can be seen from Equation 6.24, used to reproduce the conductor dissipated energy: an increase of tension reflects in a decrease of the dissipated power and then in an increase of the vibration level. Physically, it happens that, when the tension is

increased, the strands of the cable tend to lock and the frictional micro-slip, which is the main source of conductor self-damping, is reduced. Also the conductor self-damping is therefore reduced.

6.2.2 Effect of turbulence

As observed in section 2.2, the turbulence has the effect of reducing the power imparted to the conductor by the wind, leading to a decrease of the vibration level. What happens physically is that important wind velocity fluctuations cause the loss of syncronization between conductor vibration and vortex shedding, hence the phenomenon is always in transient conditions and the vibration amplitude doesn't manage to increase up to the maximum values.
This effect can be clearly seen from 6.8a and 6.8b, which shows the variation of the vibration level and of the power imparted by the wind for three different level of the turbulence index (indicated as I_V in Equation 6.27) :

- no turbulence: $I_V = 0$,
- $I_V = 0.15$ and
- $I_V = 0.25$.

6.3 Single conductor plus dampers

In this section the conductor equipped with a Stockbridge-type damper reported in (CIGRE, 2005) is analyzed. The data of the simulation are illustrated here below:

Conductor	
Type	ACSR Bersfort
Diameter	35.6 mm
Mass per unit length	2.37 kg/m
Tension	36 kN
Span length	
450 m	
Position of the damper	
one damper/span located 1.7 m from centre of the suspension clamp	

Table 6.3: Data of the simulation.

For the numerical model three pre-stressed Euler-Bernoulli beam elements are used, whose nodes are positioned in correspondence of the two clamps, at midspan and at the

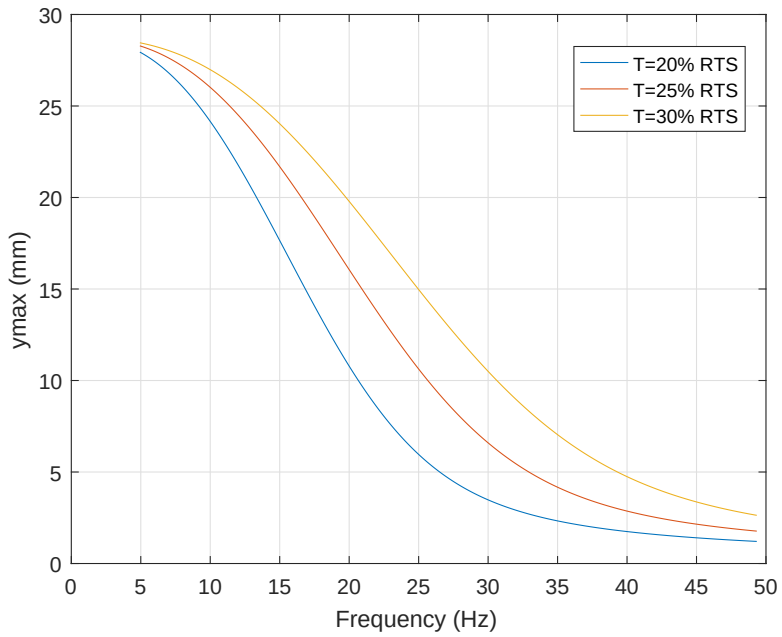

(a) *Effect of the conductor tension on the maximum antinode amplitude of vibration.*

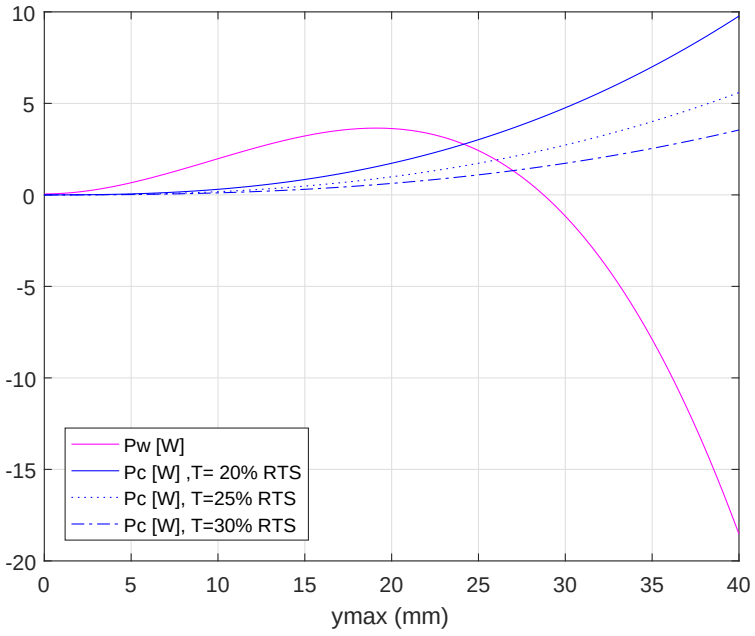

(b) *Effect of the conductor tension on the power dissipated by the conductor, for a fixed frequency of 10 Hz.*

Figure 6.7: Effect of tension.

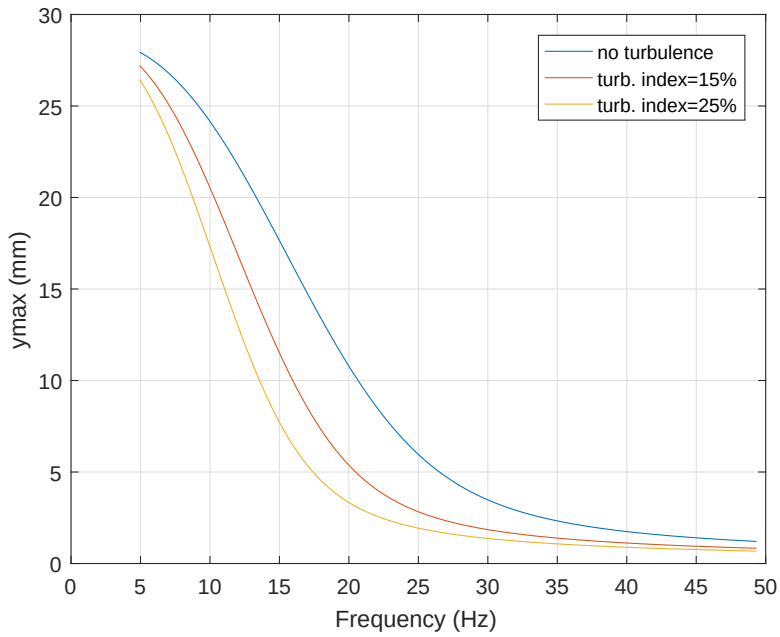

(a) *Effect of the turbulence on the maximum antinode amplitude of vibration.*

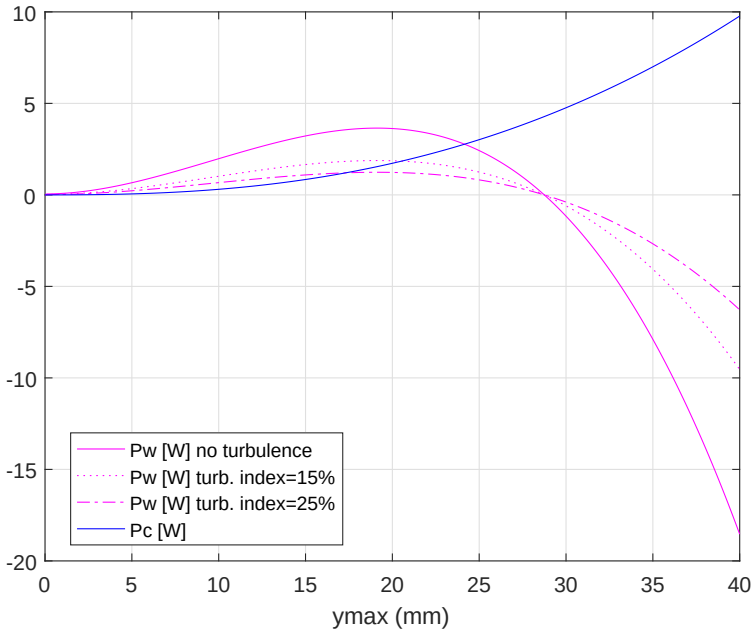

(b) *Effect of the turbulence on the power imparted by the wind, for a fixed frequency of 10 Hz.*

Figure 6.8: Effect of turbulence.

damper clamp. A unitary harmonic displacement is applied at midspan with a frequency sweep bounded by 25 rad/s and 315 rad/s (corresponding to a frequency range of 4-50 Hz) and a step equal to 0.01 rad/s. A sketch of the system in exam and of the mesh adopted are illustrated in Figure 6.9 and Figure 6.10.

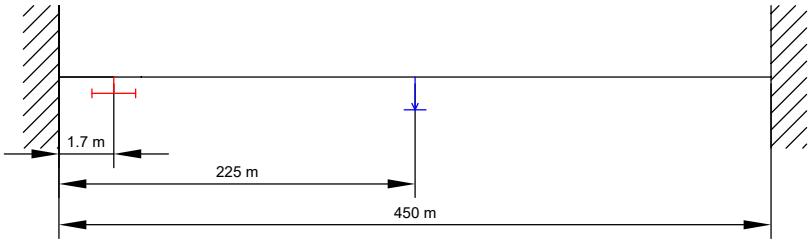

Figure 6.9: Sketch of the system in exam.

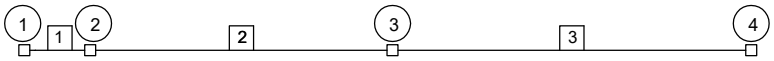

Figure 6.10: Sketch of the mesh adopted for the numerical simulation.

Figure 6.11 shows the impedance curves for different vibration velocity of the damper clamp, proposed in (CIGRE, 2005).
In this work, the Stockbridge damper is modelled as a linear element (see chapter 4), thus, the damper impedance is not supposed to depend on the vibration amplitude. To capture the damper behaviour over the whole frequency range of interest, three linear symmetric dampers (*damper 1*, *2* and *3*) with different impedance curves are modelled (Figure 6.12). The peaks and the natural frequencies of *damper 1* and *damper 3* are close, respectively, to the curve corresponding to 10 mm/s and 40 mm/s of Figure 6.11. *damper 2* ideally corresponds to an imposed velocity smaller than 4 mm/s, since the two peaks are higher with respect to the ones of the 4 mm-curve of Figure 6.11

6.3.1 Simulation with *damper 1*

The level of vibration, given by the application of the EBP, for the conductor equipped with *damper 1* along with the curve of the undamped conductor is reported in Figure 6.13; the red rectangle indicates the range of frequency over which the damper is

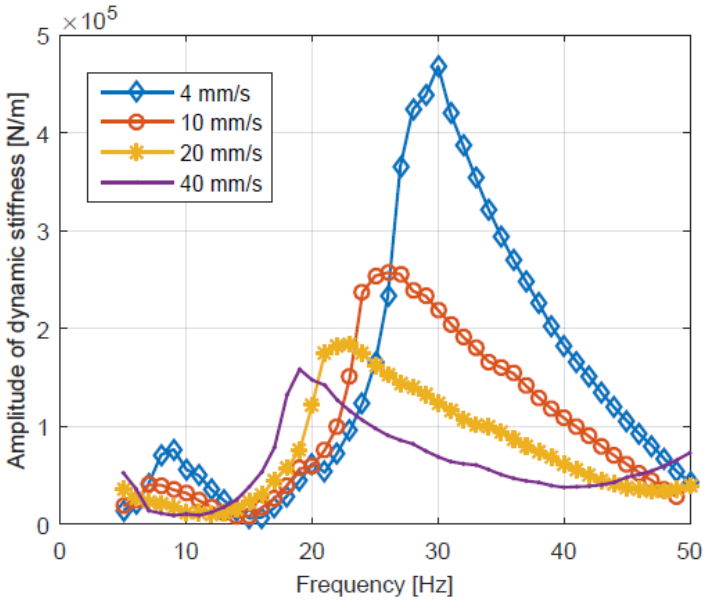

Figure 6.11: Impedance curves of the damper adopted in (CIGRE, 2005), corresponding to different values of the imposed clamp velocity.

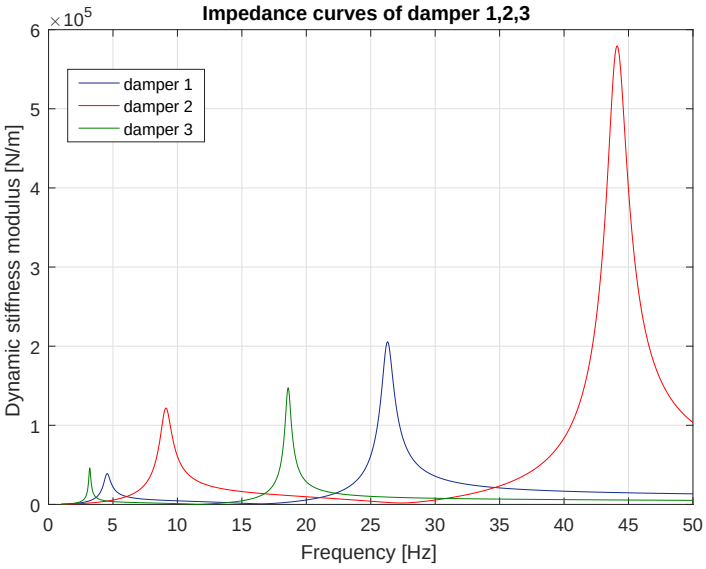

Figure 6.12: Impedance curves of *damper 1*,*2* and *3*.

effective. Figure 6.26 and Figure 6.27 shows, respectively, the total power dissipated by *damper 1* as a function of the maximum antinodal displacement for each mode and as a function of the level of vibration determined by the power balance. Figure 6.16, Figure 6.30 and Figure 6.24 report a comparison between the level of vibration and the power dissipated by *damper 1* obtained considering or not the rocking effect.
The same results are reported for *damper 2* (subsection 6.3.2) and *damper 3* (subsection 6.3.3).

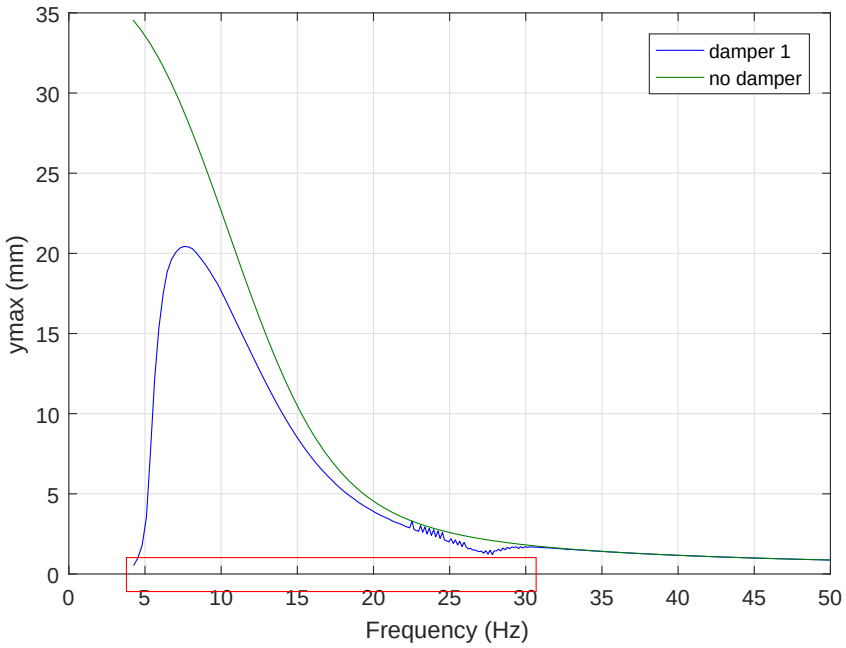

Figure 6.13: Level of vibration as a function of the frequency.

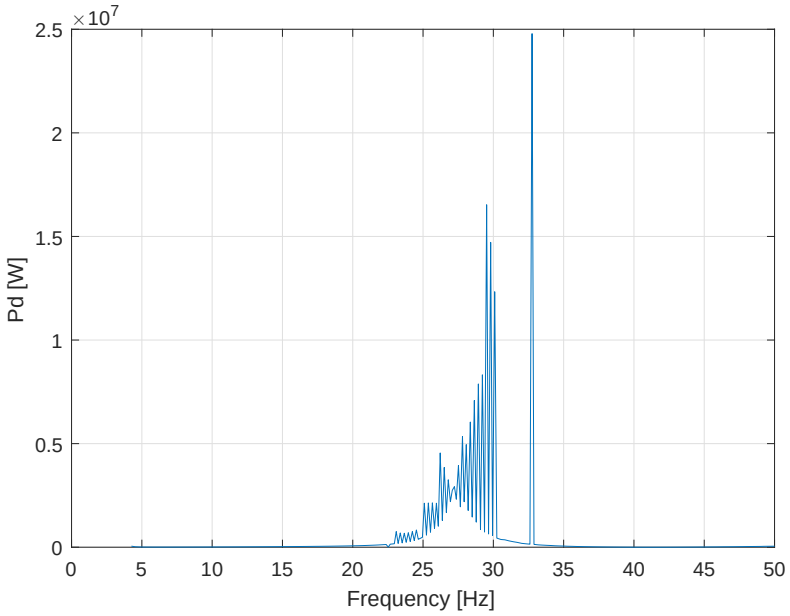

Figure 6.14: Power dissipated by *damper 1* for each modes.

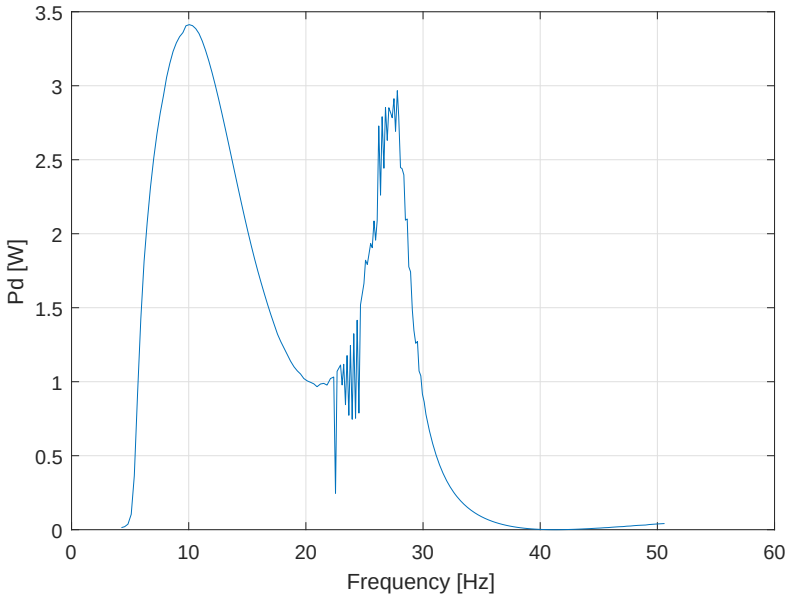

Figure 6.15: Power dissipated by *damper 1* for the level of vibration determined by the power balance.

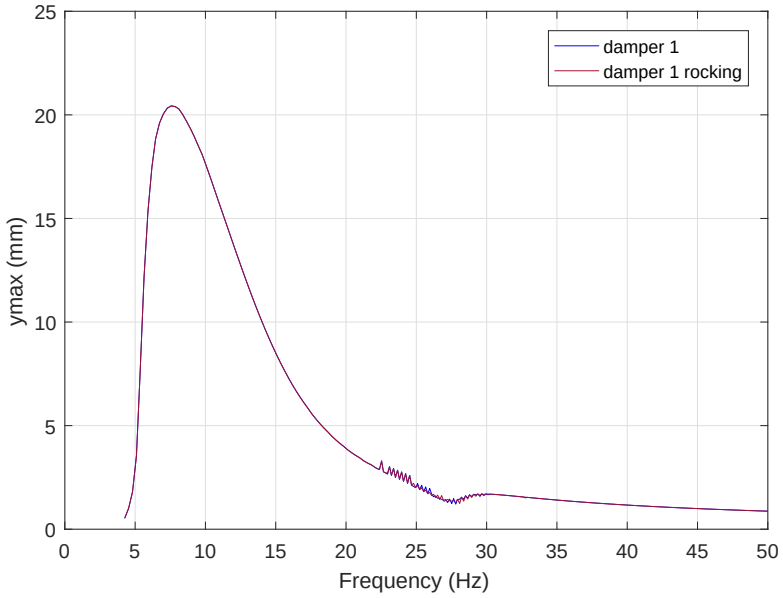

Figure 6.16: Effect of rocking on the level of vibration.

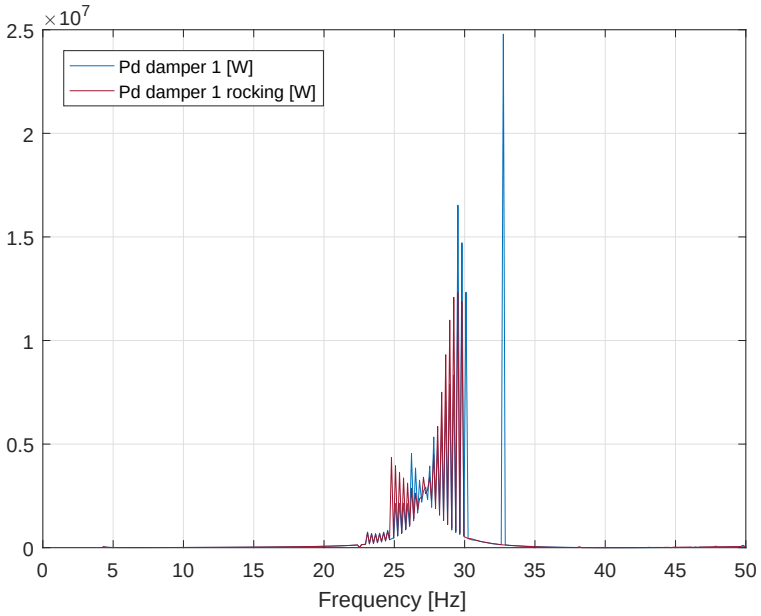

Figure 6.17: Power dissipated by *damper 1* for each modes, considering the rocking contribution.

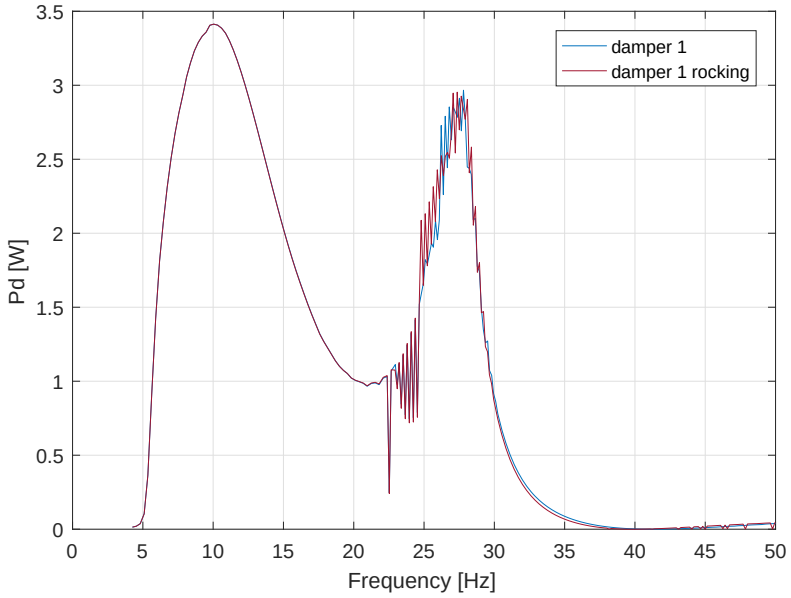

Figure 6.18: Power dissipated by *damper 1* for the level of vibration determined through the power balance, considering the rocking contribution.

6.3.2 Simulation with *damper 2*

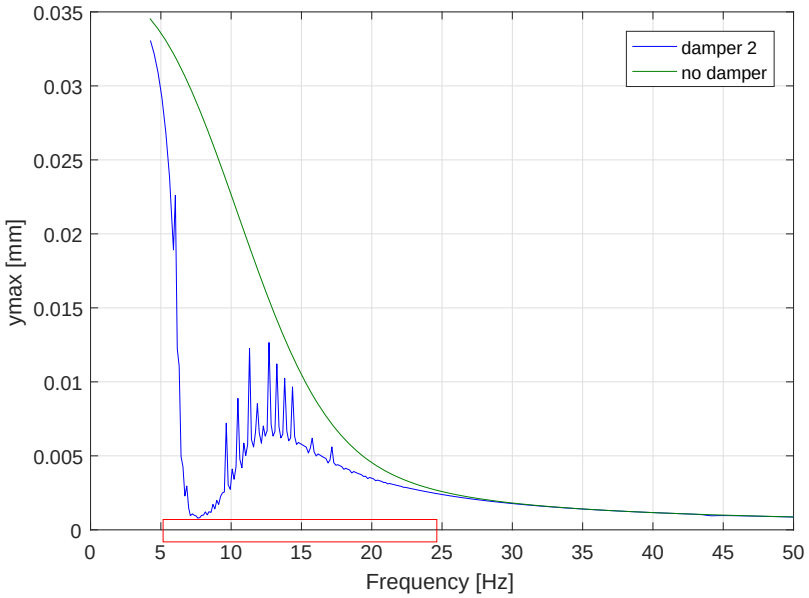

Figure 6.19: Level of vibration as a function of the frequency.

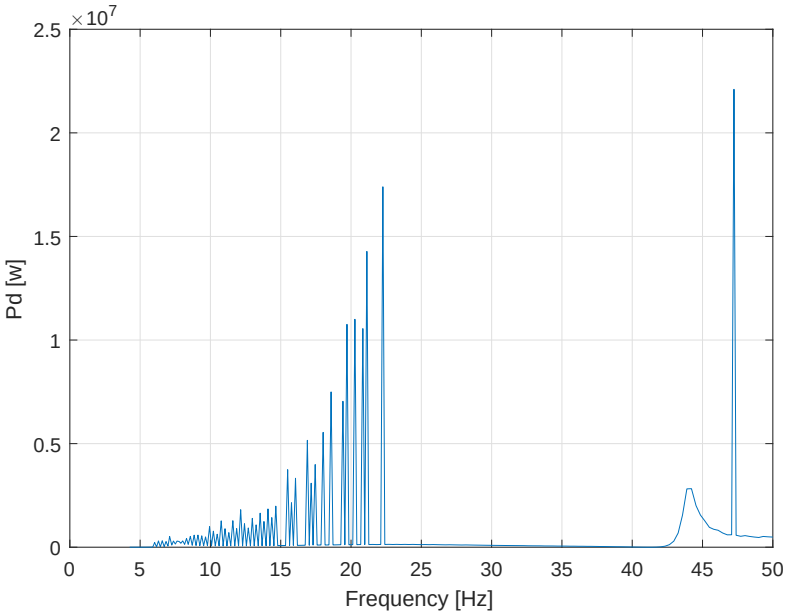

Figure 6.20: Power dissipated by *damper 2* for each modes.

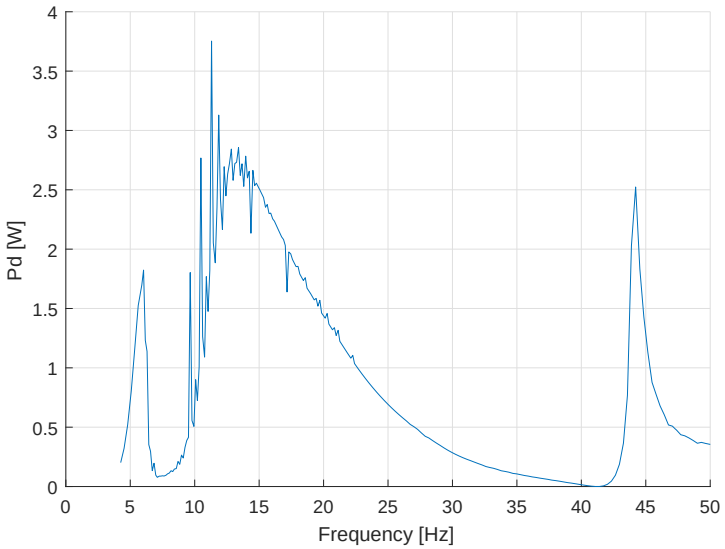

Figure 6.21: Power dissipated by *damper 2* for the level of vibration determined by the power balance.

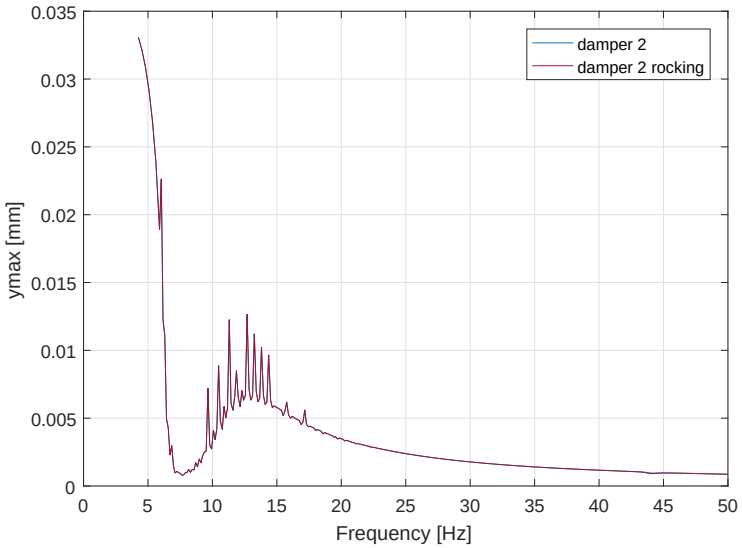

Figure 6.22: Effect of rocking on the level of vibration.

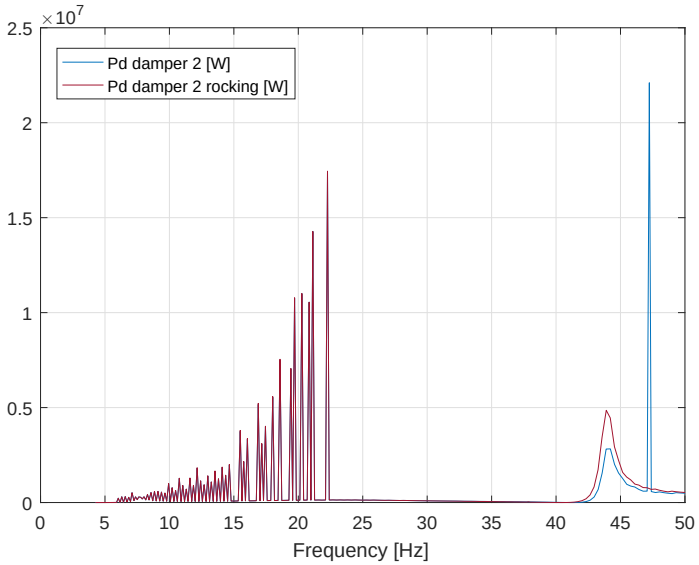

Figure 6.23: Power dissipated by *damper 2* for each modes, considering the rocking contribution.

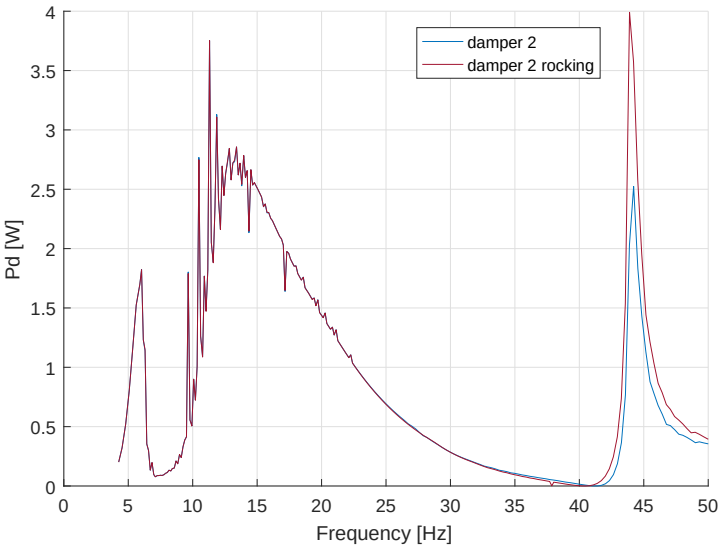

Figure 6.24: Power dissipated by *damper 2* for the level of vibration determined through the power balance, considering the rocking contribution.

6.3.3 Simulation with *damper 3*

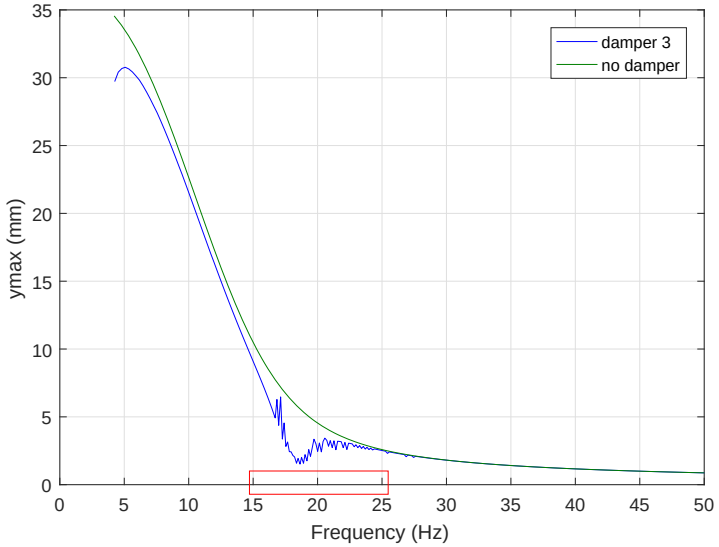

Figure 6.25: Level of vibration as a function of the frequency.

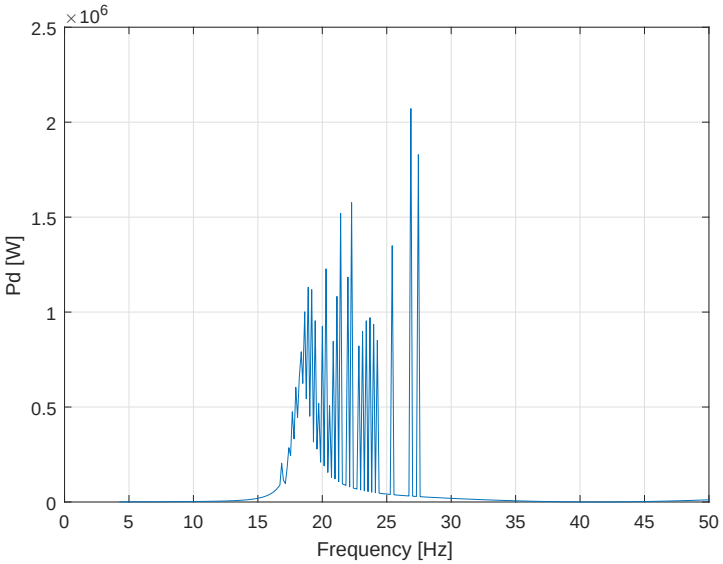

Figure 6.26: Power dissipated by *damper 3* for each modes.

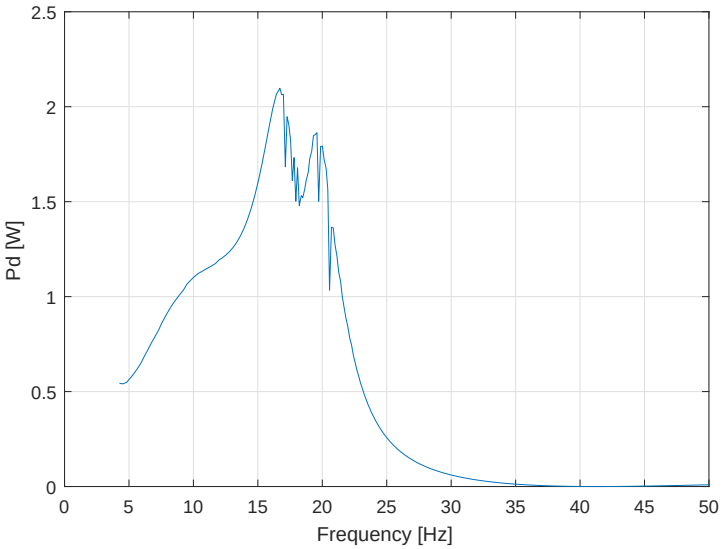

Figure 6.27: Power dissipated by *damper 3* for the level of vibration determined by the power balance.

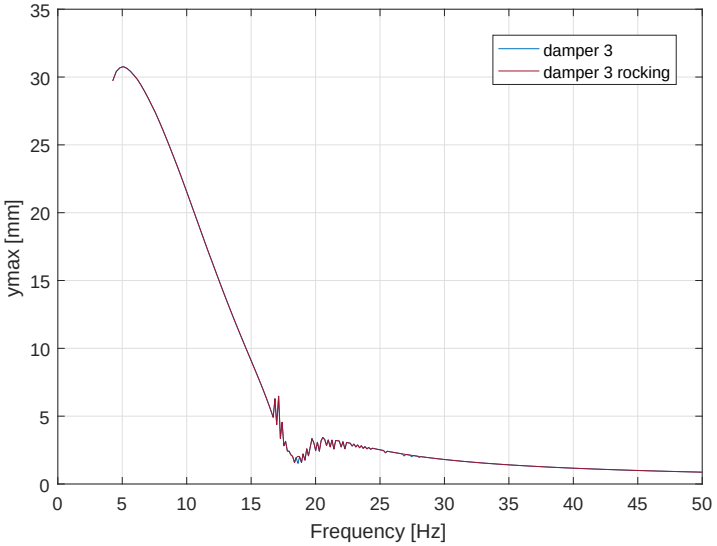

Figure 6.28: Effect of rocking on the level of vibration.

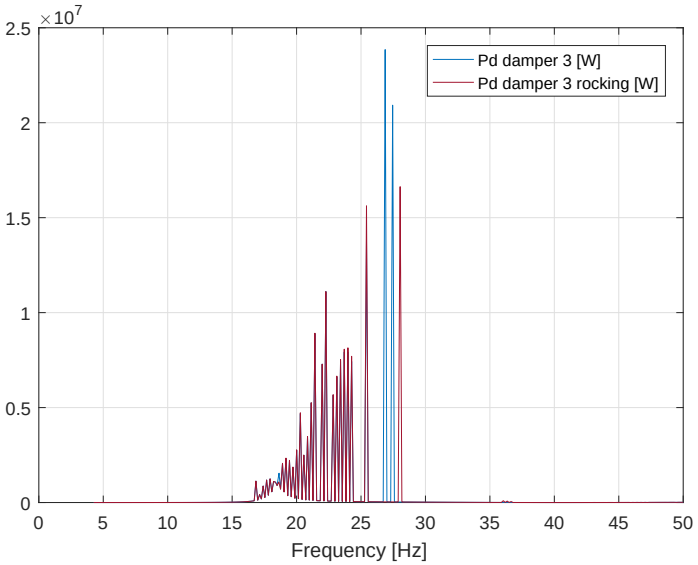

Figure 6.29: Power dissipated by *damper 3* for each modes, considering the rocking contribution.

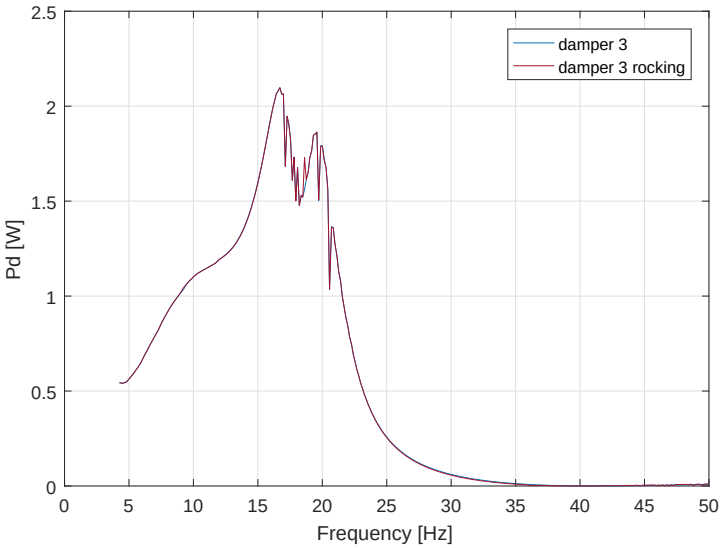

Figure 6.30: Power dissipated by *damper 3* for for the level of vibration determined by the power balance, considering the rocking contribution.

6.3.4 Concluding remarks

Looking at the results of the previous sections, the following conclusions can be drawn:

- *damper 1*, *2* and *3* are efficient over a different range of frequency. This is an expected result considering that the three dampers have different impedance curves, representing the damper linearized dynamic behaviour for the three clamp translation velocity considered. *Damper 1*, whose impedance curve corresponds to an imposed clamp velocity of 10 mm/s, is expected to be effective for an intermediate range of frequency and the results of Figure 6.13 shows that it limits the level of vibration in the range 5-30 Hz. *Damper 2*, whose impedance curve corresponds to a small imposed clamp velocity (less than 4 mm/s), is effective in the range 7-25 Hz and *damper 3*, representing the response of the damper to an imposed clamp velocity of 40 mm/s, reduces the level of vibration in the interval 15-25 Hz.

- The response of the system cable-plus-damper is quite different from the one reported in (CIGRE, 2005)(see Figure 6.31). This can be ascribed to the fact that with a linear model the self-tuning effect of the Stockbridge damper is lost.

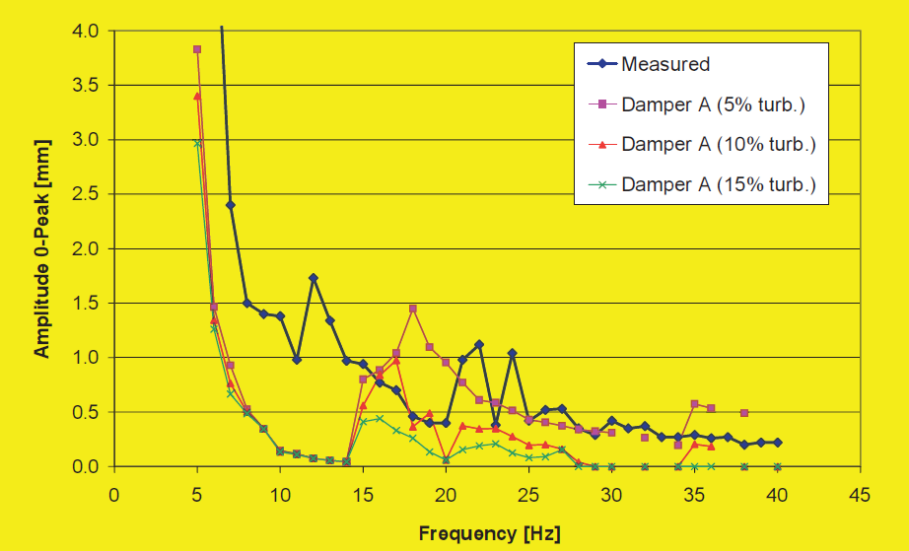

Figure 6.31: Results of (CIGRE, 2005); the impedance of damper A is the one reported in Figure 6.11.

- For the three case considered, the effect of rocking has a negligible contribution on the level of vibration. This can be explained observing that the greatest deviation between the damper dissipated power, considering or not the effect of rocking, occurs at high frequencies, when the amplitude of vibration is small due to the fact that the power dissipated by the conductor self-damping increases with increasing frequency. Furthermore, it has to be taken into account that the effect of rocking is generally more important in the case of asymmetric dampers (see e.g. (Diana et al., 2003a) and (Diana et al., 2003b)), whereas the damper here considered is symmetric.
  The formulation presented in this thesis is also able to deal with asymmetric dampers, whose impedance matrix is expressed by Equation 6.15 and its contribution to the power dissipation can be evaluated through Equation 6.16.

Chapter 7

Conclusion

This chapter summarizes the results obtained in this dissertation thesis, regarding the response of the conductor and conductor-plus-dampers system under aeolian vibration. Based on the achieved results, some future developments are proposed.

7.1 Conclusions

In the present work a somewhat new approach for the modelling of the conductor-plus-dampers system based on the concept of dynamic substructuring is developed. The natural frequencies are computed starting from the impedance matrix of the overall system, obtained assembling the contribution of each substructures. Dampers are treated as substructures connected to the principal system, represented by the conductor, in turn subdivided into a number of elements, depending on the loading conditions and on the number of devices connected to it.
This approach allows to:

- represent the higher modes of the structure with a very limited number of elements (as proven for example in section 3.4). Therefore, the computational effort is significantly reduced with respect to other numerical approaches, such as the Finite Element Method. The latter, despite having a great versatility, can be very computationally demanding, whenever applied to the modelling of aeolian vibrations, as to capture the cable higher modes, the ones excited by aeolian vibration, a very refined mesh is necessary.
  By contrast, with direct assembly of the impedances it is possible to directly assemble each physical element and for very simple cases this could also be done by hand.

- This procedure takes into account of the cable-dampers interaction, hence the modal shapes and the response of the system at an arbitrary excitation frequency include the distortional effect due to the presence of dampers.

- The impedance of substructures, like dampers, can be derived in the domain that is most appropriate and then introduced in the numerical model.

The conductor is modelled as a pre-tensioned Euler-Bernoulli beam, to take into account the cable bending stiffness. The latter has negligible influence on the eigenfrequencies and eigenmodes of the free cable vibrations (as demonstrated for the example of section 3.4), which are almost exactly those of a string without bending stiffness, but allows to consider, not only the force, but also the moment that the damper exerts on the conductor. Starting from the free-vibration equation of the tensioned beam, a procedure is established and validated to determine the impedance matrix of the beam elements, expressed as a linear combination of known shape functions and integration constants, which depend on the boundary conditions at the nodes of the element. For the cable without pre-tension (slack cable), modelled as an Euler-Bernoulli beam, the impedance matrix is computed also through an alternative approach which allows to introduce a viscous or hysteretic damping matrix, representing the cable self-damping.
To describe the Stockbridge damper two linear models are proposed. Both models are based on a beam-like description of the messenger cable and treat each arm of the damper as a cantilever beam with a lumped tip mass. The difference between *linear model 1* and *linear model 2* is that the former disregards the cable mass whereas the latter takes it into account. Since the mass of the cable is small compared to the mass of the damper weights, the difference in the results obtained with the two models is small too, but still perceptible. Due to the model linearity:

- the hysteretic damping of the messenger cable has to be taken into account with two distinct modal parameters to correctly reproduce the frequency and amplitude of the two peaks of the damper response. This is linked to the physics of the Stockbridge damper dissipation mechanism, in particular to the presence of two *boundary layer regions*, near the clamp and near the tip. The lengths of these end zones affect in different ways the amplitude of the peaks and the natural frequencies of the damper response. Since the model proposed does not define these boundary effects, it is necessary to introduce two distinct modal damping parameters, in order to correctly capture the damper behaviour.

- Linear models allow to reproduce, with an acceptable precision, the ascending branches of the two peaks of the damper impedance curve. Instead, the descending branches, and as a consequence the region between the two peaks, are not captured correctly, as the dissymmetry of the peaks is not correctly reproduced.

- Adopting a linear model the self-tuning effect of the Stockbridge damper is lost. The model parameters must be identified for different amplitude values of the clamp motion to take into account the nonlinearity of the problem.

The cable elements and the Stockbridge element are implemented in a custom design *Matlab* program, to perform modal analysis and to apply the Energy Balance Method

in order to predict the aeolian vibration level. The benchmark of section 6.2 shows how with only two elements the aeolian vibration response of a single conductor is correctly captured.
The conductor equipped with a Stockbridge damper, proposed in section 6.3, shows that the conductor is subjected to a smaller level of vibration with respect to the undamped case only over the frequency range for which the damper is effective. This frequency range is smaller with respect to the real case, since, adopting a linear model, the self-tuning effect is lost.

7.2 Future developments

Based on the achieved results, several future developments are possible:

- definition of a nonlinear model for the Stockbridge damper, able to take into account of the variation of the impedance terms in dependence of the amplitude of vibration of the damper clamp (self-tuning effect). This type of model is already implemented in the *CBFD* code, but not fully developed for what concerns the Energy Balance Method. The impedance of the damper is provided as a set of tables, listing at a discrete set of frequencies, the real and imaginary part of the impedance function. Different tables correspond to different nodal displacement amplitudes and during the numerical procedure, the values of impedance terms at a generic frequency and amplitude, can be obtained via interpolation.

- Sensitivity analysis to understand the influence of each damper parameters (such as the conterweight masses, the hysteretic damping coefficients and the cable length) on the damper impedance.

- Choice of a design criterion, for instance the one proposed in (Richardson, 1996), for the definition of the optimal number and position of damping devices, to guarantee a safe level of vibration for the entire conductor span.

- From the definition of the level of vibration through the Energy Balance Method, computation of the stresses in the most critical sections.

- Introduction in the conductor model of the self-damping contribution, extending the approach proposed for the cable without pre-tension. The cable self-damping is rather small and is usually taken into account only in the power balance, through empirical formulas. However, these formulas are affected by relevant uncertainties, as a small scatter in the experimental determination of their coefficients, leads to large differences in the value of the dissipated power. Hence, the inclusion of the cable self-damping inside the conductor model can be useful to give a more realistic representation of the system behaviour, taking into account for instance the boundary effects, without having to rely on experimental formulas.

Appendix A

Impedance matrix of the E-B element with *Mathematica*

A.1 Stiffness matrix K

$$
\begin{aligned}
K(1,1) = &-(\mathrm{EI}\mu^3(-4\mu-(2-2i)\sin((1+i)\mu)+\sin(2\mu)+(\frac{1}{2}-\frac{i}{2})\sin((2+2i)\mu)+\\
&4\mu\cos((1+i)\mu)-2\mu\cos(2\mu)-(2-2i)\sinh((1+i)\mu)+\\
&\sinh(2\mu)+(\frac{1}{2}-\frac{i}{2})\sinh((2+2i)\mu)+4\mu\cosh((1+i)\mu)-2\mu\cosh(2\mu)))/\\
&(16l^3(\cos(\mu)\cosh(\mu)-1)^2)\\
K(1,2) = &\ \mathrm{EI}\mu^2(\mu\sin(\mu)\cos(\mu)+\sinh(\mu)(2\sin(\mu)-\mu\cos(\mu))+\\
&\cosh(\mu)(\sinh(\mu)(\mu-2\sin(\mu)\cos(\mu))-\mu\sin(\mu))))/(4l^2(\cos(\mu)\cosh(\mu)-1)^2)\\
K(1,3) = &\ (\mathrm{EI}\mu^3(-\sin(\mu)+\sinh(\mu)(\mu\sin(\mu)\cos(\mu)-1)+\cosh(\mu)(\sin(\mu)\cos(\mu)+\\
&\sinh(\mu)(\cos(\mu)-\mu\sin(\mu)))))/(4l^3(\cos(\mu)\cosh(\mu)-1)^2)\\
K(1,4) = &-(\mathrm{EI}\mu^2(\mu\sin(\mu)+6\cos(\mu)+2\mu\sin^2(\mu)\sinh(\mu)-2(\cos(2\mu)+3)\cosh(\mu)+\\
&\sinh^2(\mu)(2\cos(\mu)-\mu\sin(\mu))+\cosh^2(\mu)(2\cos(\mu)-\mu\sin(\mu))))/\\
&(8l^2(\cos(\mu)\cosh(\mu)-1)^2)i/32)\mathrm{EI}\mu(12\sin((1+i)\mu)-\\
&(3-3i)\sin(2\mu)-3\sin((2+2i)\mu)+(-4-4i)\mu\cos((1+i)\mu)-\\
&(2-2i)\mu\cos(2\mu)-12\sinh((1+i)\mu)+(3-3i)\sinh(2\mu)+3\sinh((2+2i)\mu)+\\
&(4+4i)\mu\cosh((1+i)\mu)+(2-2i)\mu\cosh(2\mu)))/(l(\cos(\mu)\cosh(\mu)-1)^2)\\
K(2,2) = &\ (\mathrm{EI}\mu((6+6i)\sin((1+i)\mu)-3\sin(2\mu)-(3/2+3i/2)\sin((2+2i)\mu)-\\
&4i\mu\cos((1+i)\mu)-2\mu\cos(2\mu)-(6+6i)\sinh((1+i)\mu)+3\sinh(2\mu)+\\
&(3/3+3i/2)\sinh((2+2i)\mu)+\\
&4i\mu\cosh((1+i)\mu)+2\mu\cosh(2\mu)))/(16l(\cos(\mu)\cosh(\mu)-1)^2)\\
K(2,3) = &\ (\mathrm{EI}\mu^2(\mu\sin(\mu)+6\cos(\mu)+2\mu\sin^2(\mu)\sinh(\mu)-\\
&2(\cos(2\mu)+3)\cosh(\mu)+\sinh^2(\mu)(2\cos(\mu)-\mu\sin(\mu))\\
&+\cosh^2(\mu)(2\cos(\mu)-\mu\sin(\mu))))/(8l^2(\cos(\mu)\cosh(\mu)-1)^2)
\end{aligned}
$$

$$K(2,4) = (\mathrm{EI}\mu(-3\sin(\mu) + 2\mu\cos(\mu) + \sinh(\mu)(\mu\sin(\mu)\cos(\mu) + 3) + \cosh(\mu)(-2\mu + 3\sin(\mu)\cos(\mu) + \sinh(\mu)(\mu\sin(\mu) - 3\cos(\mu)))))/(4l(\cos(\mu)\cosh(\mu) - 1)^2)$$

$$K(3,3) = -(\mathrm{EI}\mu^3(-4\mu - (2-2i)\sin((1+i)\mu) + \sin(2\mu) + (1/2 + i/2)\sin((2+2i)\mu) + 4\mu\cos((1+i)\mu) - 2\mu\cos(2\mu) - (2-2i)\sinh((1+i)\mu) + \sinh(2\mu) + (\frac{1}{2} - \frac{i}{2})\sinh((2+2i)\mu) + 4\mu\cosh((1+i)\mu) - 2\mu\cosh(2\mu)))/(16l^3(\cos(\mu)\cosh(\mu) - 1)^2)$$

$$K(3,4) = (\mathrm{EI}\mu^2(-\mu\sin(\mu)\cos(\mu) + \sinh(\mu)(\mu\cos(\mu) - 2\sin(\mu)) + \cosh(\mu)(\mu\sin(\mu) + (\sin(2\mu) - \mu)\sinh(\mu))))/(4l^2(\cos(\mu)\cosh(\mu) - 1)^2)$$

$$K(4,4) = (\mathrm{EI}\mu((6+6i)\sin((1+i)\mu) - 3\sin(2\mu) - (3/2 + 3i/2)\sin((2+2i)\mu) - 4i\mu\cos((1+i)\mu) - 2\mu\cos(2\mu) - (6+6i)\sinh((1+i)\mu) + 3\sinh(2\mu) + (3/3 + 3i/2)\sinh((2+2i)\mu) + 4i\mu\cosh((1+i)\mu) + 2\mu\cosh(2\mu)))/(16l(\cos(\mu)\cosh(\mu) - 1)^2)$$

The damping matrix $\mathbf{C}$ is obtained multiplying the stiffness matrix K by the hysteretic coefficient μ.

A.2 Mass matrix M

$$
\begin{aligned}
M(1,1) &= (lm(4\mu-(6-6i)\sin((1+i)\mu)+3\sin(2\mu)+(3/2-3i/2)\sin((2+2i)\mu)-\\
&\quad 4\mu\cos((1+i)\mu)+2\mu\cos(2\mu)-(6-6i)\sinh((1+i)\mu)+3\sinh(2\mu)+\\
&\quad (3/2-3i/2)\sinh((2+2i)\mu)-4\mu\cosh((1+i)\mu)+2\mu\cosh(2\mu)))/\\
&\quad (4\mu(2-2\cos(\mu)\cosh(\mu))^2)\\
M(1,2) &= (l^2m(\mu\sin(\mu)\cos(\mu)-\sinh(\mu)(2\sin(\mu)+\mu\cos(\mu))+\\
&\quad \cosh(\mu)((\mu+\sin(2\mu))\sinh(\mu)-\mu\sin(\mu))))/(4\mu^2(\cos(\mu)\cosh(\mu)-1)^2)\\
M(1,3) &= (lm(3\sin(\mu)+\sinh(\mu)(\mu\sin(\mu)\cos(\mu)+3)-\cosh(\mu)(3\sin(\mu)\cos(\mu)+\\
&\quad \sinh(\mu)(\mu\sin(\mu)+3\cos(\mu)))))/(\mu(2-2\cos(\mu)\cosh(\mu))^2)\\
M(1,4) &= (l^2m(-\mu\sin(\mu)+6\cos(\mu)-2\mu\sin^2(\mu)\sinh(\mu)-2(\cos(2\mu)+3)\cosh(\mu)+\\
&\quad \sinh^2(\mu)(\mu\sin(\mu)+2\cos(\mu))+\cosh^2(\mu)(\mu\sin(\mu)+2\cos(\mu))))/\\
&\quad (8\mu^2(\cos(\mu)\cosh(\mu)-1)^2)\\
M(2,2) &= ((1/32+i/32)l^3m(-4\sin((1+i)\mu)+(1-i)\sin(2\mu)+\sin((2+2i)\mu)+\\
&\quad (-4-4i)\mu\cos((1+i)\mu)-(2-2i)\mu\cos(2\mu)+4\sinh((1+i)\mu)-(1-i)\sinh(2\mu)\\
&\quad -\sinh((2+2i)\mu)+(4+4i)\mu\cosh((1+i)\mu)+(2-2i)\mu\cosh(2\mu)))/\\
&\quad (\mu^3(\cos(\mu)\cosh(\mu)-1)^2)\\
M(2,3) &= -(l^2m(-\mu\sin(\mu)+6\cos(\mu)-2\mu\sin^2(\mu)\sinh(\mu)-2(\cos(2\mu)+3)\cosh(\mu)\\
&\quad +\sinh^2(\mu)(\mu\sin(\mu)+2\cos(\mu))+\cosh^2(\mu)(\mu\sin(\mu)+\\
&\quad 2\cos(\mu))))/(8\mu^2(\cos(\mu)\cosh(\mu)-1)^2)\\
M(2,4) &= (l^3m(\sin(\mu)+2\mu\cos(\mu)+\sinh(\mu)(\mu\sin(\mu)\cos(\mu)-1)+\\
&\quad \cosh(\mu)(-2\mu-\sin(\mu)\cos(\mu)+\sinh(\mu)(\mu\sin(\mu)+\cos(\mu)))))/\\
&\quad (4\mu^3(\cos(\mu)\cosh(\mu)-1)^2)\\
M(3,3) &= (lm(4\mu-(6-6i)\sin((1+i)\mu)+3\sin(2\mu)+(3/2-3i/2)\sin((2+2i)\mu)-\\
&\quad 4\mu\cos((1+i)\mu)+2\mu\cos(2\mu)-(6-6i)\sinh((1+i)\mu)+3\sinh(2\mu)+(\frac{3}{2}-\\
&\quad 3i/2)\sinh((2+2i)\mu)-4\mu\cosh((1+i)\mu)+2\mu\cosh(2\mu))/(4\mu(2-2\cos(\mu)\cosh(\mu))^2)\\
M(3,4) &= (l^2m(-\mu\sin(\mu)\cos(\mu)+\sinh(\mu)(2\sin(\mu)+\mu\cos(\mu))+\\
&\quad \cosh(\mu)(\mu\sin(\mu)-(\mu+\sin(2\mu))\sinh(\mu))))/(4\mu^2(\cos(\mu)\cosh(\mu)-1)^2)\\
M(4,4) &= -((1/32+i/32)l^3m(4\sin((1+i)\mu)-(1-i)\sin(2\mu)-\sin((2+2i)\mu)+\\
&\quad (4+4i)\mu\cos((1+i)\mu)+(2-2i)\mu\cos(2\mu)-4\sinh((1+i)\mu)+\\
&\quad (1-i)\sinh(2\mu)+\sinh((2+2i)\mu)-(4+4i)\mu\cosh((1+i)\mu)-\\
&\quad (2-2i)\mu\cosh(2\mu)))/(\mu^3(\cos(\mu)\cosh(\mu)-1)^2)
\end{aligned}
$$

A.3 Impedance matrix Z

$$
\begin{aligned}
Z(1,1) = {} & (i\mathrm{EI}\mu^4(-4\mu-(2-2i)\sin((1+i)\mu)+\sin(2\mu)+(1/2-i/2)\sin((2+2i)\mu)+\\
& 4\mu\cos((1+i)\mu)-2\mu\cos(2\mu)-(2-2i)\sinh((1+i)\mu)+\\
& \sinh(2\mu)+(1/2-i/2)\sinh((2+2i)\mu)+4\mu\cosh((1+i)\mu)-\\
& 2\mu\cosh(2\mu)))/(16l^3(\cos(\mu)\cosh(\mu)-1)^2)-(\mathrm{EI}\mu^3(-4\mu-\\
& (2-2i)\sin((1+i)\mu)+\sin(2\mu)+(1/2-i/2)\sin((2+2i)\mu)+4\mu\cos((1+i)\mu)-\\
& 2\mu\cos(2\mu)-(2-2i)\sinh((1+i)\mu)+\sinh(2\mu)+(1/2-i/2)\sinh((2+2i)\mu)+\\
& 4\mu\cosh((1+i)\mu)-2\mu\cosh(2\mu)))/(16l^3(\cos(\mu)\cosh(\mu)-1)^2)-\\
& (\mathrm{EI}\mu^3(4\mu-(6-6i)\sin((1+i)\mu)+3\sin(2\mu)+\\
& (1/2-i/2)\sin((2+2i)\mu)-4\mu\cos((1+i)\mu)+2\mu\cos(2\mu)-(6-6i)\sinh((1+i)\mu)+\\
& 3\sinh(2\mu)+(3/2-3i/2)\sinh((2+2i)\mu)-4\mu\cosh((1+i)\mu)+2\mu\cosh(2\mu)))/\\
& (4l^3(2-2\cos(\mu)\cosh(\mu))^2)\\
Z(1,2) = {} & -(i\mathrm{EI}\mu^3(\mu\sin(\mu)\cos(\mu)+\sinh(\mu)(2\sin(\mu)-\mu\cos(\mu))+\\
& \cosh(\mu)(\sinh(\mu)(\mu-2\sin(\mu)\cos(\mu))-\mu\sin(\mu))))/\\
& (4l^2(\cos(\mu)\cosh(\mu)-1)^2)+(\mathrm{EI}\mu^2(\mu\sin(\mu)\cos(\mu)+\\
& \sinh(\mu)(2\sin(\mu)-\mu\cos(\mu))+\cosh(\mu)(\sinh(\mu)(\mu-2\sin(\mu)\cos(\mu))-\\
& \mu\sin(\mu))))/(4l^2(\cos(\mu)\cosh(\mu)-1)^2)-\\
& (\mathrm{EI}\mu^2(\mu\sin(\mu)\cos(\mu)-\sinh(\mu)(2\sin(\mu)+\mu\cos(\mu))+\\
& \cosh(\mu)((\mu+\sin(2\mu))\sinh(\mu)-\mu\sin(\mu))))/(4l^2(\cos(\mu)\cosh(\mu)-1)^2)\\
Z(1,3) = {} & -(i\mathrm{EI}\mu^4(-\sin(\mu)+\sinh(\mu)(\mu\sin(\mu)\cos(\mu)-1)+\\
& \cosh(\mu)(\sin(\mu)\cos(\mu)+\sinh(\mu)(\cos(\mu)-\mu\sin(\mu)))))/\\
& (4l^3(\cos(\mu)\cosh(\mu)-1)^2)+(\mathrm{EI}\mu^3(-\sin(\mu)+\sinh(\mu)(\mu\sin(\mu)\cos(\mu)-1)+\\
& \cosh(\mu)(\sin(\mu)\cos(\mu)+\sinh(\mu)(\cos(\mu)-\mu\sin(\mu)))))/\\
& (4l^3(\cos(\mu)\cosh(\mu)-1)^2)-(\mathrm{EI}\mu^3(3\sin(\mu)+\sinh(\mu)(\mu\sin(\mu)\cos(\mu)+3)-\\
& \cosh(\mu)(3\sin(\mu)\cos(\mu)+\sinh(\mu)(\mu\sin(\mu)+3\cos(\mu)))))/\\
& (l^3(2-2\cos(\mu)\cosh(\mu))^2)\\
Z(1,4) = {} & (i\mathrm{EI}\mu^3(\mu\sin(\mu)+6\cos(\mu)+2\mu\sin^2(\mu)\sinh(\mu)-2(\cos(2\mu)+3)\cosh(\mu)\\
& +\sinh^2(\mu)(2\cos(\mu)-\mu\sin(\mu))+\cosh^2(\mu)(2\cos(\mu)-\\
& \mu\sin(\mu))))/(8l^2(\cos(\mu)\cosh(\mu)-1)^2)-(\mathrm{EI}\mu^2(\mu\sin(\mu)+\\
& 6\cos(\mu)+2\mu\sin^2(\mu)\sinh(\mu)-2(\cos(2\mu)+3)\cosh(\mu)+\\
& \sinh^2(\mu)(2\cos(\mu)-\mu\sin(\mu))+\cosh^2(\mu)(2\cos(\mu)-\mu\sin(\mu))))/(8l^2(\cos(\mu)\cosh(\mu)-1)^2)-\\
& (\mathrm{EI}\mu^2(-\mu\sin(\mu)+6\cos(\mu)-2\mu\sin^2(\mu)\sinh(\mu)-2(\cos(2\mu)+3)\cosh(\mu)+\\
& \sinh^2(\mu)(\mu\sin(\mu)+2\cos(\mu))+\cosh^2(\mu)(\mu\sin(\mu)+2\cos(\mu))))/(8l^2(\cos(\mu)\cosh(\mu)-1)^2
\end{aligned}
$$

$$
\begin{aligned}
Z(2,2) = {} & ((1/32 - i/32)\mathrm{EI}\mu^2(12\sin((1+i)\mu) - (3-3i)\sin(2\mu) - 3\sin((2+2i)\mu) + \\
& (-4-4i)\mu\cos((1+i)\mu) - (2-2i)\mu\cos(2\mu) - 12\sinh((1+i)\mu) + \\
& (3-3i)\sinh(2\mu) + 3\sinh((2+2i)\mu) + (4+4i)\mu\cosh((1+i)\mu) + \\
& (2-2i)\mu\cosh(2\mu)))/(l(\cos(\mu)\cosh(\mu)-1)^2) - ((1/32 + i/32)\mathrm{EI}\mu(-4\sin((1+i)\mu) + \\
& (1-i)\sin(2\mu) + \sin((2+2i)\mu) + (-4-4i)\mu\cos((1+i)\mu) - (2-2i)\mu\cos(2\mu) + \\
& 4\sinh((1+i)\mu) - (1-i)\sinh(2\mu) - \sinh((2+2i)\mu) + (4+4i)\mu\cosh((1+i)\mu) + \\
& (2-2i)\mu\cosh(2\mu)))/(l(\cos(\mu)\cosh(\mu)-1)^2) + \\
& ((1/32 + i/32)\mathrm{EI}\mu(12\sin((1+i)\mu) - (3-3i)\sin(2\mu) - 3\sin((2+2i)\mu) + \\
& (-4-4i)\mu\cos((1+i)\mu) - (2-2i)\mu\cos(2\mu) - 12\sinh((1+i)\mu) + (3-3i)\sinh(2\mu) + \\
& 3\sinh((2+2i)\mu) + (4+4i)\mu\cosh((1+i)\mu) + (2-2i)\mu\cosh(2\mu)))/ \\
& (l(\cos(\mu)\cosh(\mu)-1)^2)
\end{aligned}
$$

$$
\begin{aligned}
Z(2,3) = {} & -(i\mathrm{EI}\mu^3(\mu\sin(\mu) + 6\cos(\mu) + 2\mu\sin^2(\mu)\sinh(\mu) - 2(\cos(2\mu)+3)\cosh(\mu) + \\
& \sinh^2(\mu)(2\cos(\mu) - \mu\sin(\mu)) + \cosh^2(\mu)(2\cos(\mu) - \mu\sin(\mu))))/ \\
& (8l^2(\cos(\mu)\cosh(\mu)-1)^2) + (\mathrm{EI}\mu^2(\mu\sin(\mu) + 6\cos(\mu) + \\
& 2\mu\sin^2(\mu)\sinh(\mu) - 2(\cos(2\mu)+3)\cosh(\mu) + \\
& \sinh^2(\mu)(2\cos(\mu) - \mu\sin(\mu)) + \cosh^2(\mu)(2\cos(\mu) - \mu\sin(\mu))))/ \\
& (8l^2(\cos(\mu)\cosh(\mu)-1)^2) + (\mathrm{EI}\mu^2(-\mu\sin(\mu) + 6\cos(\mu) - \\
& 2\mu\sin^2(\mu)\sinh(\mu) - 2(\cos(2\mu)+3)\cosh(\mu) + \\
& \sinh^2(\mu)(\mu\sin(\mu) + 2\cos(\mu)) + \cosh^2(\mu)(\mu\sin(\mu) + 2\cos(\mu))))/ \\
& (8l^2(\cos(\mu)\cosh(\mu)-1)^2)
\end{aligned}
$$

$$
\begin{aligned}
Z(2,4) = {} & -(i\mathrm{EI}\mu^2(-3\sin(\mu) + 2\mu\cos(\mu) + \sinh(\mu)(\mu\sin(\mu)\cos(\mu)+3) + \cosh(\mu)(-2\mu + \\
& 3\sin(\mu)\cos(\mu) + \sinh(\mu)(\mu\sin(\mu) - 3\cos(\mu)))))/(4l(\cos(\mu)\cosh(\mu)-1)^2) + \\
& (\mathrm{EI}\mu(-3\sin(\mu) + 2\mu\cos(\mu) + \sinh(\mu)(\mu\sin(\mu)\cos(\mu)+3) + \\
& \cosh(\mu)(-2\mu + 3\sin(\mu)\cos(\mu) + \sinh(\mu)(\mu\sin(\mu) - 3\cos(\mu)))))/ \\
& (4l(\cos(\mu)\cosh(\mu)-1)^2) - (\mathrm{EI}\mu(\sin(\mu) + 2\mu\cos(\mu) + \\
& \sinh(\mu)(\mu\sin(\mu)\cos(\mu) - 1) + \cosh(\mu)(-2\mu - \sin(\mu)\cos(\mu) + \sinh(\mu)(\mu\sin(\mu) + \\
& \cos(\mu)))))/(4l(\cos(\mu)\cosh(\mu)-1)^2)
\end{aligned}
$$

$$
\begin{aligned}
Z(3,3) = {} & (i\mathrm{EI}\mu^4(-4\mu - (2-2i)\sin((1+i)\mu) + \\
& \sin(2\mu) + (1/2 - i/2)\sin((2+2i)\mu) + 4\mu\cos((1+i)\mu) - 2\mu\cos(2\mu) - \\
& (2-2i)\sinh((1+i)\mu) + \sinh(2\mu) + (1/2 - i/2)\sinh((2+2i)\mu) + \\
& 4\mu\cosh((1+i)\mu) - 2\mu\cosh(2\mu)))/(16l^3(\cos(\mu)\cosh(\mu)-1)^2) - \\
& (\mathrm{EI}\mu^3(-4\mu - (2-2i)\sin((1+i)\mu) + \sin(2\mu) + \\
& (1/2 - i/2)\sin((2+2i)\mu) + 4\mu\cos((1+i)\mu) - 2\mu\cos(2\mu) - (2-2i)\sinh((1+i)\mu) + \\
& \sinh(2\mu) + (1/2 - i/2)\sinh((2+2i)\mu) + 4\mu\cosh((1+i)\mu) - \\
& 2\mu\cosh(2\mu)))/(16l^3(\cos(\mu)\cosh(\mu)-1)^2) - (\mathrm{EI}\mu^3(4\mu - \\
& (6-6i)\sin((1+i)\mu) + 3\sin(2\mu) + (3/2 - 3i/2)\sin((2+2i)\mu) - \\
& 4\mu\cos((1+i)\mu) + 2\mu\cos(2\mu) - (6-6i)\sinh((1+i)\mu) + \\
& 3\sinh(2\mu) + (\frac{3}{2} - \frac{3i}{2})\sinh((2+2i)\mu) - 4\mu\cosh((1+i)\mu) + \\
& 2\mu\cosh(2\mu)))/(4l^3(2 - 2\cos(\mu)\cosh(\mu))^2)
\end{aligned}
$$

$$
\begin{aligned}
Z(3,4) = &-(i\mathrm{EI}\mu^3(-\mu\sin(\mu)\cos(\mu)+\sinh(\mu)(\mu\cos(\mu)- \\
&2\sin(\mu))+\cosh(\mu)(\mu\sin(\mu)+(\sin(2\mu)-\mu)\sinh(\mu))))/(4l^2(\cos(\mu)\cosh(\mu)-1)^2)+ \\
&(\mathrm{EI}\mu^2(-\mu\sin(\mu)\cos(\mu)+\sinh(\mu)(\mu\cos(\mu)-2\sin(\mu))+ \\
&\cosh(\mu)(\mu\sin(\mu)+(\sin(2\mu)-\mu)\sinh(\mu))))/(4l^2(\cos(\mu)\cosh(\mu)-1)^2)- \\
&(\mathrm{EI}\mu^2(-\mu\sin(\mu)\cos(\mu)+\sinh(\mu)(2\sin(\mu)+\mu\cos(\mu))+ \\
&\cosh(\mu)(\mu\sin(\mu)-(\mu+\sin(2\mu))\sinh(\mu))))(4l^2(\cos(\mu)\cosh(\mu)-1)^2) \\
Z(4,4) = &-(i\mathrm{EI}\mu^2((6+6i)\sin((1+i)\mu)-3\sin(2\mu)-(3/2+3i/2)\sin((2+2i)\mu)- \\
&4i\mu\cos((1+i)\mu)-2\mu\cos(2\mu)-(6+6i)\sinh((1+i)\mu)+ \\
&3\sinh(2\mu)+(3/2+3i/2)\sinh((2+2i)\mu)+4i\mu\cosh((1+i)\mu)+ \\
&2\mu\cosh(2\mu)))/(16l(\cos(\mu)\cosh(\mu)-1)^2)+ \\
&((1/32+i/32)\mathrm{EI}\mu(4\sin((1+i)\mu)-(1-i)\sin(2\mu)-\sin((2+2i)\mu)+ \\
&(4+4i)\mu\cos((1+i)\mu)+(2-2i)\mu\cos(2\mu)- \\
&4\sinh((1+i)\mu)+(1-i)\sinh(2\mu)+\sinh((2+2i)\mu)-(4+4i)\mu\cosh((1+i)\mu)- \\
&(2-2i)\mu\cosh(2\mu)))/(l(\cos(\mu)\cosh(\mu)-1)^2)+(\mathrm{EI}\mu((6+6i)\sin((1+i)\mu)- \\
&3\sin(2\mu)-(3/2+3i/2)\sin((2+2i)\mu)-4i\mu\cos((1+i)\mu)- \\
&2\mu\cos(2\mu)-(6+6i)\sinh((1+i)\mu)+3\sinh(2\mu)+ \\
&(3/2+3i/2)\sinh((2+2i)\mu)+4i\mu\cosh((1+i)\mu)+2\mu\cosh(2\mu)))/ \\
&(16l(\cos(\mu)\cosh(\mu)-1)^2)
\end{aligned}
$$

Appendix B

Linear model 2: M and K

B.1 Mass matrix M

$$
\begin{aligned}
M(1,1) = m + (&0.125 l \mathrm{mc}((-2.\cos(1.((l^4\mathrm{mc}\omega^2)/(\mathrm{EI}))^{0.25})\sin((\frac{l^4\mathrm{mc}\omega^2}{\mathrm{EI}})^{0.25}) + 2.\cos((\frac{l^4\mathrm{mc}\omega^2}{\mathrm{EI}})^{0.25})\\
&\sin(1.(\frac{l^4\mathrm{mc}\omega^2}{\mathrm{EI}})^{0.25}) + 2.\sin(2(\frac{l^4\mathrm{mc}\omega^2}{\mathrm{EI}})^{0.25}))\cosh^2(1.(\frac{l^4\mathrm{mc}\omega^2}{\mathrm{EI}})^{0.25}) + (-1.\sin(2.(\frac{l^4\mathrm{mc}\omega^2}{\mathrm{EI}})^{0.25})\\
&\cos(1.(\frac{l^4\mathrm{mc}\omega^2}{\mathrm{EI}})^{0.25}) - 4.(\frac{l^4\mathrm{mc}\omega^2}{\mathrm{EI}})^{0.25}\cos(1.(\frac{l^4\mathrm{mc}\omega^2}{\mathrm{EI}})^{0.25}) +\\
&1.\sin((\frac{l^4\mathrm{mc}\omega^2}{\mathrm{EI}})^{0.25}) + \cosh(2.(\frac{l^4\mathrm{mc}\omega^2}{\mathrm{EI}})^{0.25})(-2.\sin((\frac{l^4\mathrm{mc}\omega^2}{\mathrm{EI}})^{0.25}) -\\
&1.\sin(1.(\frac{l^4\mathrm{mc}\omega^2}{\mathrm{EI}})^{0.25})) + 1.\cos(2.(\frac{l^4\mathrm{mc}\omega^2}{\mathrm{EI}})^{0.25})\sin(1.(\frac{l^4\mathrm{mc}\omega^2}{\mathrm{EI}})^{0.25}) -\\
&3.\sin(1.(\frac{l^4\mathrm{mc}\omega^2}{\mathrm{EI}})^{0.25}) + \cos((\frac{l^4\mathrm{mc}\omega^2}{\mathrm{EI}})^{0.25})(2.\cos((\frac{l^4\mathrm{mc}\omega^2}{\mathrm{EI}})^{0.25}) +\\
&2.\cos(1.(\frac{l^4\mathrm{mc}\omega^2}{\mathrm{EI}})^{0.25}))\sinh(1.(\frac{l^4\mathrm{mc}\omega^2}{\mathrm{EI}})^{0.25}) - 1.\cos((\frac{l^4\mathrm{mc}\omega^2}{\mathrm{EI}})^{0.25})\\
&\sinh(2.(\frac{l^4\mathrm{mc}\omega^2}{\mathrm{EI}})^{0.25}) + 1.\sin((\frac{l^4\mathrm{mc}\omega^2}{\mathrm{EI}})^{0.25})\sinh(2.(\frac{l^4\mathrm{mc}\omega^2}{\mathrm{EI}})^{0.25}) - 1.\sin(1.(\frac{l^4\mathrm{mc}\omega^2}{\mathrm{EI}})^{0.25})\\
&\sinh(2.(\frac{l^4\mathrm{mc}\omega^2}{\mathrm{EI}})^{0.25}))\cosh(1.(\frac{l^4\mathrm{mc}\omega^2}{\mathrm{EI}})^{0.25}) + 4.\cos(1.(\frac{l^4\mathrm{mc}\omega^2}{\mathrm{EI}})^{0.25})\sin((\frac{l^4\mathrm{mc}\omega^2}{\mathrm{EI}})^{0.25})\\
&\sinh^2(1.(\frac{l^4\mathrm{mc}\omega^2}{\mathrm{EI}})^{0.25}) - 4.\cos((\frac{l^4\mathrm{mc}\omega^2}{\mathrm{EI}})^{0.25})\sin(1.(\frac{l^4\mathrm{mc}\omega^2}{\mathrm{EI}})^{0.25})\sinh^2(1.(\frac{l^4\mathrm{mc}\omega^2}{\mathrm{EI}})^{0.25}) + 1.\\
&(\frac{l^4\mathrm{mc}\omega^2}{\mathrm{EI}})^{0.25}\cos(2.(\frac{l^4\mathrm{mc}\omega^2}{\mathrm{EI}})^{0.25}) + 0.5\sin(2.(\frac{l^4\mathrm{mc}\omega^2}{\mathrm{EI}})^{0.25}) - 1.\cos((\frac{l^4\mathrm{mc}\omega^2}{\mathrm{EI}})^{0.25})\sinh(1.\\
&(\frac{l^4\mathrm{mc}\omega^2}{\mathrm{EI}})^{0.25}) - 1.\cos(1.(\frac{l^4\mathrm{mc}\omega^2}{\mathrm{EI}})^{0.25})\sinh(1.(\frac{l^4\mathrm{mc}\omega^2}{\mathrm{EI}})^{0.25}) - 3.\cos(1.(\frac{l^4\mathrm{mc}\omega^2}{\mathrm{EI}})^{0.25})\\
&\cos(2.(\frac{l^4\mathrm{mc}\omega^2}{\mathrm{EI}})^{0.25})\sinh(1.(\frac{l^4\mathrm{mc}\omega^2}{\mathrm{EI}})^{0.25}) - 3.\sin(1.(\frac{l^4\mathrm{mc}\omega^2}{\mathrm{EI}})^{0.25})\sin(2.(\frac{l^4\mathrm{mc}\omega^2}{\mathrm{EI}})^{0.25})\\
&\sinh(1.(\frac{l^4\mathrm{mc}\omega^2}{\mathrm{EI}})^{0.25}) + \cosh(2.(\frac{l^4\mathrm{mc}\omega^2}{\mathrm{EI}})^{0.25})(0.5\sin(2.(\frac{l^4\mathrm{mc}\omega^2}{\mathrm{EI}})^{0.25}) + (1.\cos((\frac{l^4\mathrm{mc}\omega^2}{\mathrm{EI}})^{0.25}) -\\
&1.\sin((\frac{l^4\mathrm{mc}\omega^2}{\mathrm{EI}})^{0.25}) + 1.\sin(1.(\frac{l^4\mathrm{mc}\omega^2}{\mathrm{EI}})^{0.25}))\sinh(1.(\frac{l^4\mathrm{mc}\omega^2}{\mathrm{EI}})^{0.25}) + 1.(\frac{l^4\mathrm{mc}\omega^2}{\mathrm{EI}})^{0.25}) -\\
&1.\sin^2((\frac{l^4\mathrm{mc}\omega^2}{\mathrm{EI}})^{0.25})\sinh(2.(\frac{l^4\mathrm{mc}\omega^2}{\mathrm{EI}})^{0.25}) + 0.5\cos(2.(\frac{l^4\mathrm{mc}\omega^2}{\mathrm{EI}})^{0.25})\sinh(2.(\frac{l^4\mathrm{mc}\omega^2}{\mathrm{EI}})^{0.25}) +\\
&1.\sin((\frac{l^4\mathrm{mc}\omega^2}{\mathrm{EI}})^{0.25})\sin(1.(\frac{l^4\mathrm{mc}\omega^2}{\mathrm{EI}})^{0.25})\sinh(2.(\frac{l^4\mathrm{mc}\omega^2}{\mathrm{EI}})^{0.25}) + 2.\sin((\frac{l^4\mathrm{mc}\omega^2}{\mathrm{EI}})^{0.25})\\
&\sinh(1.(\frac{l^4\mathrm{mc}\omega^2}{\mathrm{EI}})^{0.25})\sinh(2.(\frac{l^4\mathrm{mc}\omega^2}{\mathrm{EI}})^{0.25}) + 1.\sin(1.(\frac{l^4\mathrm{mc}\omega^2}{\mathrm{EI}})^{0.25})\sinh(1.(\frac{l^4\mathrm{mc}\omega^2}{\mathrm{EI}})^{0.25})\\
&\sinh(2.(\frac{l^4\mathrm{mc}\omega^2}{\mathrm{EI}})^{0.25}) + 0.5\sinh(2.(\frac{l^4\mathrm{mc}\omega^2}{\mathrm{EI}})^{0.25}) + 2.(\frac{l^4\mathrm{mc}\omega^2}{\mathrm{EI}})^{0.25}))/((\frac{l^4\mathrm{mc}\omega^2}{\mathrm{EI}})^{0.25}(\cos((\frac{l^4\mathrm{mc}\omega^2}{\mathrm{EI}})^{0.25})\\
&\cosh((\frac{l^4\mathrm{mc}\omega^2}{\mathrm{EI}})^{0.25}) - 1.)^2)
\end{aligned}
$$

$$
\begin{aligned}
M(1,2) = (&l\mathrm{mc}((-0.25l\cos^2(2.(\frac{l^4\mathrm{mc}\omega^2}{\mathrm{EI}})^{0.25}) + 0.25l\cosh(2.(\frac{l^4\mathrm{mc}\omega^2}{\mathrm{EI}})^{0.25})\\
&\cos(2.(\frac{l^4\mathrm{mc}\omega^2}{\mathrm{EI}})^{0.25}) - 1.l\sin(1.(\frac{l^4\mathrm{mc}\omega^2}{\mathrm{EI}})^{0.25})\\
&\sinh(1.(\frac{l^4\mathrm{mc}\omega^2}{\mathrm{EI}})^{0.25})\cos(2.(\frac{l^4\mathrm{mc}\omega^2}{\mathrm{EI}})^{0.25}) - 0.25l\sin^2(2.(\frac{l^4\mathrm{mc}\omega^2}{\mathrm{EI}})^{0.25})\\
&- 0.25l\sinh^2(2.(\frac{l^4\mathrm{mc}\omega^2}{\mathrm{EI}})^{0.25}) - 0.5l(\frac{l^4\mathrm{mc}\omega^2}{\mathrm{EI}})^{0.25}\\
&\sin(2.(\frac{l^4\mathrm{mc}\omega^2}{\mathrm{EI}})^{0.25}) + 1.l(\frac{l^4\mathrm{mc}\omega^2}{\mathrm{EI}})^{0.25}\cos(1.(\frac{l^4\mathrm{mc}\omega^2}{\mathrm{EI}})^{0.25})\\
&\sinh(1.(\frac{l^4\mathrm{mc}\omega^2}{\mathrm{EI}})^{0.25}) - 2.l\cos((\frac{l^4\mathrm{mc}\omega^2}{\mathrm{EI}})^{0.25})\cosh(1.(\frac{l^4\mathrm{mc}\omega^2}{\mathrm{EI}})^{0.25})\\
&\sin((\frac{l^4\mathrm{mc}\omega^2}{\mathrm{EI}})^{0.25})\sinh(1.(\frac{l^4\mathrm{mc}\omega^2}{\mathrm{EI}})^{0.25}) + 1.l\cos(1.(\frac{l^4\mathrm{mc}\omega^2}{\mathrm{EI}})^{0.25})\\
&\cosh(1.(\frac{l^4\mathrm{mc}\omega^2}{\mathrm{EI}})^{0.25})\sin((\frac{l^4\mathrm{mc}\omega^2}{\mathrm{EI}})^{0.25})\sinh(1.(\frac{l^4\mathrm{mc}\omega^2}{\mathrm{EI}})^{0.25}) -\\
&1.l\cos((\frac{l^4\mathrm{mc}\omega^2}{\mathrm{EI}})^{0.25})\cosh(1.(\frac{l^4\mathrm{mc}\omega^2}{\mathrm{EI}})^{0.25})\sin(1.(\frac{l^4\mathrm{mc}\omega^2}{\mathrm{EI}})^{0.25})\\
&\sinh(1.(\frac{l^4\mathrm{mc}\omega^2}{\mathrm{EI}})^{0.25}) + 1.l\cos(1.(\frac{l^4\mathrm{mc}\omega^2}{\mathrm{EI}})^{0.25})\sin(2.(\frac{l^4\mathrm{mc}\omega^2}{\mathrm{EI}})^{0.25})\\
&\sinh(1.(\frac{l^4\mathrm{mc}\omega^2}{\mathrm{EI}})^{0.25}) + l\cosh(2.(\frac{l^4\mathrm{mc}\omega^2}{\mathrm{EI}})^{0.25})(-0.25\cos(2.(\frac{l^4\mathrm{mc}\omega^2}{\mathrm{EI}})^{0.25}) +\\
&0.25\cosh(2.(\frac{l^4\mathrm{mc}\omega^2}{\mathrm{EI}})^{0.25}) + \cosh(1.(\frac{l^4\mathrm{mc}\omega^2}{\mathrm{EI}})^{0.25})(0.5\sin(1.(\frac{l^4\mathrm{mc}\omega^2}{\mathrm{EI}})^{0.25}) -\\
&0.5\sin((\frac{l^4\mathrm{mc}\omega^2}{\mathrm{EI}})^{0.25})) - 0.5\sin((\frac{l^4\mathrm{mc}\omega^2}{\mathrm{EI}})^{0.25})\sinh(1.(\frac{l^4\mathrm{mc}\omega^2}{\mathrm{EI}})^{0.25}) -\\
&0.5\sin(1.(\frac{l^4\mathrm{mc}\omega^2}{\mathrm{EI}})^{0.25})\sinh(1.(\frac{l^4\mathrm{mc}\omega^2}{\mathrm{EI}})^{0.25})) + \cosh(1.(\frac{l^4\mathrm{mc}\omega^2}{\mathrm{EI}})^{0.25})\\
&(0.5l\cos(1.(\frac{l^4\mathrm{mc}\omega^2}{\mathrm{EI}})^{0.25})\cos(2.(\frac{l^4\mathrm{mc}\omega^2}{\mathrm{EI}})^{0.25}) - 0.5l\cos((\frac{l^4\mathrm{mc}\omega^2}{\mathrm{EI}})^{0.25})\\
&\cosh(2.(\frac{l^4\mathrm{mc}\omega^2}{\mathrm{EI}})^{0.25}) + 1.l(\frac{l^4\mathrm{mc}\omega^2}{\mathrm{EI}})^{0.25}\sin(1.(\frac{l^4\mathrm{mc}\omega^2}{\mathrm{EI}})^{0.25}) + 0.5l\sin(1.(\frac{l^4\mathrm{mc}\omega^2}{\mathrm{EI}})^{0.25})\\
&\sin(2.(\frac{l^4\mathrm{mc}\omega^2}{\mathrm{EI}})^{0.25}) + (2.l\cos((\frac{l^4\mathrm{mc}\omega^2}{\mathrm{EI}})^{0.25})\sin(1.(\frac{l^4\mathrm{mc}\omega^2}{\mathrm{EI}})^{0.25}) -\\
&2.l\cos(1.(\frac{l^4\mathrm{mc}\omega^2}{\mathrm{EI}})^{0.25})\sin((\frac{l^4\mathrm{mc}\omega^2}{\mathrm{EI}})^{0.25}))\sinh(1.(\frac{l^4\mathrm{mc}\omega^2}{\mathrm{EI}})^{0.25}))\\
&+ 0.5l\cosh(1.(\frac{l^4\mathrm{mc}\omega^2}{\mathrm{EI}})^{0.25})\sin((\frac{l^4\mathrm{mc}\omega^2}{\mathrm{EI}})^{0.25})\sinh(2.(\frac{l^4\mathrm{mc}\omega^2}{\mathrm{EI}})^{0.25}) + 0.5l\cosh(1.(\frac{l^4\mathrm{mc}\omega^2}{\mathrm{EI}})^{0.25})\\
&\sin(1.(\frac{l^4\mathrm{mc}\omega^2}{\mathrm{EI}})^{0.25})\sinh(2.(\frac{l^4\mathrm{mc}\omega^2}{\mathrm{EI}})^{0.25}) + 0.5l\cos((\frac{l^4\mathrm{mc}\omega^2}{\mathrm{EI}})^{0.25})\\
&\sinh(1.(\frac{l^4\mathrm{mc}\omega^2}{\mathrm{EI}})^{0.25})\sinh(2.(\frac{l^4\mathrm{mc}\omega^2}{\mathrm{EI}})^{0.25}) + 0.5l\sin((\frac{l^4\mathrm{mc}\omega^2}{\mathrm{EI}})^{0.25})\\
&\sinh(1.(\frac{l^4\mathrm{mc}\omega^2}{\mathrm{EI}})^{0.25})\sinh(2.(\frac{l^4\mathrm{mc}\omega^2}{\mathrm{EI}})^{0.25}) - 0.5l\sin(1.(\frac{l^4\mathrm{mc}\omega^2}{\mathrm{EI}})^{0.25})\sinh(1.(\frac{l^4\mathrm{mc}\omega^2}{\mathrm{EI}})^{0.25})\\
&\sinh(2.(\frac{l^4\mathrm{mc}\omega^2}{\mathrm{EI}})^{0.25}) - 0.5l(\frac{l^4\mathrm{mc}\omega^2}{\mathrm{EI}})^{0.25}\sinh(2.(\frac{l^4\mathrm{mc}\omega^2}{\mathrm{EI}})^{0.25}))/\\
&((\frac{l^4\mathrm{mc}\omega^2}{\mathrm{EI}})^{0.25}) - ((-0.5l\cos((\frac{l^4\mathrm{mc}\omega^2}{\mathrm{EI}})^{0.25}) + 0.5l\\
&\cos(1.(\frac{l^4\mathrm{mc}\omega^2}{\mathrm{EI}})^{0.25}) + 0.)\cosh(1.(\frac{l^4\mathrm{mc}\omega^2}{\mathrm{EI}})^{0.25}) + 0.)
\end{aligned}
$$

$$
\begin{aligned}
M(2,2) = {} & me\mathrm{gd}^2 + \mathrm{Jg} + (l^2\mathrm{mc}((-1.l\cosh(1.(\frac{l^4\mathrm{mc}\omega^2}{\mathrm{EI}})^{0.25})\sinh(1.(\frac{l^4\mathrm{mc}\omega^2}{\mathrm{EI}})^{0.25}) \\
& \cos^2((\frac{l^4\mathrm{mc}\omega^2}{\mathrm{EI}})^{0.25}) - 2.l\sin(1.(\frac{l^4\mathrm{mc}\omega^2}{\mathrm{EI}})^{0.25})\sinh^2(1.(\frac{l^4\mathrm{mc}\omega^2}{\mathrm{EI}})^{0.25}) \\
& \cos((\frac{l^4\mathrm{mc}\omega^2}{\mathrm{EI}})^{0.25}) + 1.l\cos(1.(\frac{l^4\mathrm{mc}\omega^2}{\mathrm{EI}})^{0.25})\cosh(1.(\frac{l^4\mathrm{mc}\omega^2}{\mathrm{EI}})^{0.25}) \\
& \sinh(1.(\frac{l^4\mathrm{mc}\omega^2}{\mathrm{EI}})^{0.25})\cos((\frac{l^4\mathrm{mc}\omega^2}{\mathrm{EI}})^{0.25}) + 0.5l\cosh(2.(\frac{l^4\mathrm{mc}\omega^2}{\mathrm{EI}})^{0.25}) \\
& \sinh(1.(\frac{l^4\mathrm{mc}\omega^2}{\mathrm{EI}})^{0.25})\cos((\frac{l^4\mathrm{mc}\omega^2}{\mathrm{EI}})^{0.25}) + \\
& 2.l\cos(1.(\frac{l^4\mathrm{mc}\omega^2}{\mathrm{EI}})^{0.25})\sin((\frac{l^4\mathrm{mc}\omega^2}{\mathrm{EI}})^{0.25})\sinh^2(1.(\frac{l^4\mathrm{mc}\omega^2}{\mathrm{EI}})^{0.25}) - \\
& 0.5l(\frac{l^4\mathrm{mc}\omega^2}{\mathrm{EI}})^{0.25}\cos(2.(\frac{l^4\mathrm{mc}\omega^2}{\mathrm{EI}})^{0.25}) - 1.l\cosh(1.(\frac{l^4\mathrm{mc}\omega^2}{\mathrm{EI}})^{0.25}) \\
& \sin(1.(\frac{l^4\mathrm{mc}\omega^2}{\mathrm{EI}})^{0.25}) - 0.25l\sin(2.(\frac{l^4\mathrm{mc}\omega^2}{\mathrm{EI}})^{0.25}) - 0.25l\cosh(2.(\frac{l^4\mathrm{mc}\omega^2}{\mathrm{EI}})^{0.25}) \\
& \sin(2.(\frac{l^4\mathrm{mc}\omega^2}{\mathrm{EI}})^{0.25}) + 1.l\cosh(1.(\frac{l^4\mathrm{mc}\omega^2}{\mathrm{EI}})^{0.25})\sin^2((\frac{l^4\mathrm{mc}\omega^2}{\mathrm{EI}})^{0.25}) \\
& \sinh(1.(\frac{l^4\mathrm{mc}\omega^2}{\mathrm{EI}})^{0.25}) + 1.l\cos(1.(\frac{l^4\mathrm{mc}\omega^2}{\mathrm{EI}})^{0.25})\sinh(1.(\frac{l^4\mathrm{mc}\omega^2}{\mathrm{EI}})^{0.25}) + \\
& 0.5l\cos(1.(\frac{l^4\mathrm{mc}\omega^2}{\mathrm{EI}})^{0.25})\cos(2.(\frac{l^4\mathrm{mc}\omega^2}{\mathrm{EI}})^{0.25})\sinh(1.(\frac{l^4\mathrm{mc}\omega^2}{\mathrm{EI}})^{0.25}) + \\
& 1.l\cosh(1.(\frac{l^4\mathrm{mc}\omega^2}{\mathrm{EI}})^{0.25})\sin((\frac{l^4\mathrm{mc}\omega^2}{\mathrm{EI}})^{0.25})\sin(1.(\frac{l^4\mathrm{mc}\omega^2}{\mathrm{EI}})^{0.25}) \\
& \sinh(1.(\frac{l^4\mathrm{mc}\omega^2}{\mathrm{EI}})^{0.25}) - 2.l(\frac{l^4\mathrm{mc}\omega^2}{\mathrm{EI}})^{0.25}\sin(1.(\frac{l^4\mathrm{mc}\omega^2}{\mathrm{EI}})^{0.25}) \\
& \sinh(1.(\frac{l^4\mathrm{mc}\omega^2}{\mathrm{EI}})^{0.25}) + 0.5l\sin(1.(\frac{l^4\mathrm{mc}\omega^2}{\mathrm{EI}})^{0.25})\sin(2.(\frac{l^4\mathrm{mc}\omega^2}{\mathrm{EI}})^{0.25}) \\
& \sinh(1.(\frac{l^4\mathrm{mc}\omega^2}{\mathrm{EI}})^{0.25}) + 0.25l\sinh(2.(\frac{l^4\mathrm{mc}\omega^2}{\mathrm{EI}})^{0.25}) + 0.25l\cos(2.(\frac{l^4\mathrm{mc}\omega^2}{\mathrm{EI}})^{0.25}) \\
& \sinh(2.(\frac{l^4\mathrm{mc}\omega^2}{\mathrm{EI}})^{0.25}) - 0.25l\cosh(2.(\frac{l^4\mathrm{mc}\omega^2}{\mathrm{EI}})^{0.25})\sinh(2.(\frac{l^4\mathrm{mc}\omega^2}{\mathrm{EI}})^{0.25}) + \\
& 0.5l\cosh(1.(\frac{l^4\mathrm{mc}\omega^2}{\mathrm{EI}})^{0.25})\sin((\frac{l^4\mathrm{mc}\omega^2}{\mathrm{EI}})^{0.25})\sinh(2.(\frac{l^4\mathrm{mc}\omega^2}{\mathrm{EI}})^{0.25}) - \\
& 0.5l\cosh(1.(\frac{l^4\mathrm{mc}\omega^2}{\mathrm{EI}})^{0.25})\sin(1.(\frac{l^4\mathrm{mc}\omega^2}{\mathrm{EI}})^{0.25})\sinh(2.(\frac{l^4\mathrm{mc}\omega^2}{\mathrm{EI}})^{0.25}) + \\
& 0.5l\cos((\frac{l^4\mathrm{mc}\omega^2}{\mathrm{EI}})^{0.25})\sinh(1.(\frac{l^4\mathrm{mc}\omega^2}{\mathrm{EI}})^{0.25}) - 0.5l\cos(1.(\frac{l^4\mathrm{mc}\omega^2}{\mathrm{EI}})^{0.25}) \\
& \sinh(1.(\frac{l^4\mathrm{mc}\omega^2}{\mathrm{EI}})^{0.25}) \\
& (\cos((\frac{l^4\mathrm{mc}\omega^2}{\mathrm{EI}})^{0.25})\cosh((\frac{l^4\mathrm{mc}\omega^2}{\mathrm{EI}})^{0.25}) - 1)^2)
\end{aligned}
$$

B.2 Stiffness matrix K

$$
\begin{aligned}
K(1,1) = (&0.125 l \mathrm{mc}\omega^2((2.\cos(1.(\frac{l^4\mathrm{mc}\omega^2}{\mathrm{EI}})^{0.25})\sin((\frac{l^4\mathrm{mc}\omega^2}{\mathrm{EI}})^{0.25}) - 2.\cos((\frac{l^4\mathrm{mc}\omega^2}{\mathrm{EI}})^{0.25})\\
&\sin(1.(\frac{l^4\mathrm{mc}\omega^2}{\mathrm{EI}})^{0.25}) - 2.\sin(2(\frac{l^4\mathrm{mc}\omega^2}{\mathrm{EI}})^{0.25}))\cosh^2(1.(\frac{l^4\mathrm{mc}\omega^2}{\mathrm{EI}})^{0.25}) +\\
&(-1.\sin(2.(\frac{l^4\mathrm{mc}\omega^2}{\mathrm{EI}})^{0.25})\cos(1.(\frac{l^4\mathrm{mc}\omega^2}{\mathrm{EI}})^{0.25}) - 4.(\frac{l^4\mathrm{mc}\omega^2}{\mathrm{EI}})^{0.25}\\
&\cos(1.(\frac{l^4\mathrm{mc}\omega^2}{\mathrm{EI}})^{0.25}) + 1.\sin((\frac{l^4\mathrm{mc}\omega^2}{\mathrm{EI}})^{0.25}) + 1.\cos(2.(\frac{l^4\mathrm{mc}\omega^2}{\mathrm{EI}})^{0.25})\sin(1.(\frac{l^4\mathrm{mc}\omega^2}{\mathrm{EI}})^{0.25}) +\\
&1.\cosh(2.(\frac{l^4\mathrm{mc}\omega^2}{\mathrm{EI}})^{0.25})\sin(1.(\frac{l^4\mathrm{mc}\omega^2}{\mathrm{EI}})^{0.25}) + 1.\sin(1.(\frac{l^4\mathrm{mc}\omega^2}{\mathrm{EI}})^{0.25}) + \cos((\frac{l^4\mathrm{mc}\omega^2}{\mathrm{EI}})^{0.25})\\
&(-2.\cos((\frac{l^4\mathrm{mc}\omega^2}{\mathrm{EI}})^{0.25}) - 2.\cos(1.(\frac{l^4\mathrm{mc}\omega^2}{\mathrm{EI}})^{0.25}))\sinh(1.(\frac{l^4\mathrm{mc}\omega^2}{\mathrm{EI}})^{0.25}) -\\
&1.\cos((\frac{l^4\mathrm{mc}\omega^2}{\mathrm{EI}})^{0.25})\sinh(2.(\frac{l^4\mathrm{mc}\omega^2}{\mathrm{EI}})^{0.25}) - 1.\sin((\frac{l^4\mathrm{mc}\omega^2}{\mathrm{EI}})^{0.25})\sinh(2.(\frac{l^4\mathrm{mc}\omega^2}{\mathrm{EI}})^{0.25}) +\\
&1.\sin(1.(\frac{l^4\mathrm{mc}\omega^2}{\mathrm{EI}})^{0.25})\sinh(2.(\frac{l^4\mathrm{mc}\omega^2}{\mathrm{EI}})^{0.25}))\cosh(1.(\frac{l^4\mathrm{mc}\omega^2}{\mathrm{EI}})^{0.25}) -\\
&4.\cos(1.(\frac{l^4\mathrm{mc}\omega^2}{\mathrm{EI}})^{0.25})\sin((\frac{l^4\mathrm{mc}\omega^2}{\mathrm{EI}})^{0.25})\sinh^2(1.(\frac{l^4\mathrm{mc}\omega^2}{\mathrm{EI}})^{0.25}) +\\
&4.\cos((\frac{l^4\mathrm{mc}\omega^2}{\mathrm{EI}})^{0.25})\sin(1.(\frac{l^4\mathrm{mc}\omega^2}{\mathrm{EI}})^{0.25})\sinh^2(1.(\frac{l^4\mathrm{mc}\omega^2}{\mathrm{EI}})^{0.25}) +\\
&1.(\frac{l^4\mathrm{mc}\omega^2}{\mathrm{EI}})^{0.25}\cos(2.(\frac{l^4\mathrm{mc}\omega^2}{\mathrm{EI}})^{0.25}) + 0.5\sin(2.(\frac{l^4\mathrm{mc}\omega^2}{\mathrm{EI}})^{0.25}) - 1.\\
&\cos((\frac{l^4\mathrm{mc}\omega^2}{\mathrm{EI}})^{0.25})\sinh(1.(\frac{l^4\mathrm{mc}\omega^2}{\mathrm{EI}})^{0.25}) + 3.\cos(1.(\frac{l^4\mathrm{mc}\omega^2}{\mathrm{EI}})^{0.25})\\
&\sinh(1.(\frac{l^4\mathrm{mc}\omega^2}{\mathrm{EI}})^{0.25}) + 1.\cos(1.(\frac{l^4\mathrm{mc}\omega^2}{\mathrm{EI}})^{0.25})\cos(2.(\frac{l^4\mathrm{mc}\omega^2}{\mathrm{EI}})^{0.25})\\
&\sinh(1.(\frac{l^4\mathrm{mc}\omega^2}{\mathrm{EI}})^{0.25}) + 1.\sin(1.(\frac{l^4\mathrm{mc}\omega^2}{\mathrm{EI}})^{0.25})\sin(2.(\frac{l^4\mathrm{mc}\omega^2}{\mathrm{EI}})^{0.25})\\
&\sinh(1.(\frac{l^4\mathrm{mc}\omega^2}{\mathrm{EI}})^{0.25}) + \cosh(2.(\frac{l^4\mathrm{mc}\omega^2}{\mathrm{EI}})^{0.25})(0.5\sin(2.(\frac{l^4\mathrm{mc}\omega^2}{\mathrm{EI}})^{0.25}) + (1.\cos((\frac{l^4\mathrm{mc}\omega^2}{\mathrm{EI}})^{0.25}) +\\
&1.\sin((\frac{l^4\mathrm{mc}\omega^2}{\mathrm{EI}})^{0.25}) - 1.\sin(1.(\frac{l^4\mathrm{mc}\omega^2}{\mathrm{EI}})^{0.25}))\sinh(1.(\frac{l^4\mathrm{mc}\omega^2}{\mathrm{EI}})^{0.25}) + 1.(\frac{l^4\mathrm{mc}\omega^2}{\mathrm{EI}})^{0.25}) +\\
&1.\sin^2((\frac{l^4\mathrm{mc}\omega^2}{\mathrm{EI}})^{0.25})\sinh(2.(\frac{l^4\mathrm{mc}\omega^2}{\mathrm{EI}})^{0.25}) + 0.5\cos(2.(\frac{l^4\mathrm{mc}\omega^2}{\mathrm{EI}})^{0.25})\sinh(2.(\frac{l^4\mathrm{mc}\omega^2}{\mathrm{EI}})^{0.25}) -\\
&1.\sin((\frac{l^4\mathrm{mc}\omega^2}{\mathrm{EI}})^{0.25})\sin(1.(\frac{l^4\mathrm{mc}\omega^2}{\mathrm{EI}})^{0.25})\sinh(2.(\frac{l^4\mathrm{mc}\omega^2}{\mathrm{EI}})^{0.25}) -\\
&1.\sin(1.(\frac{l^4\mathrm{mc}\omega^2}{\mathrm{EI}})^{0.25})\sinh(1.(\frac{l^4\mathrm{mc}\omega^2}{\mathrm{EI}})^{0.25})\sinh(2.(\frac{l^4\mathrm{mc}\omega^2}{\mathrm{EI}})^{0.25}) +\\
&0.5\sinh(2.(\frac{l^4\mathrm{mc}\omega^2}{\mathrm{EI}})^{0.25}) + 2.(\frac{l^4\mathrm{mc}\omega^2}{\mathrm{EI}})^{0.25}))/((\frac{l^4\mathrm{mc}\omega^2}{\mathrm{EI}})^{0.25}\\
&(\cos((\frac{l^4\mathrm{mc}\omega^2}{\mathrm{EI}})^{0.25})\cosh((\frac{l^4\mathrm{mc}\omega^2}{\mathrm{EI}})^{0.25}) - 1.)^2)
\end{aligned}
$$

$$
\begin{aligned}
K(1,2) = (&0.25l\mathrm{mc}\omega^2(-0.25l\cos^2(2.(\frac{l^4\mathrm{mc}\omega^2}{\mathrm{EI}})^{0.25}) + 0.25l\cosh(2.(\frac{l^4\mathrm{mc}\omega^2}{\mathrm{EI}})^{0.25})\cos(2.(\frac{l^4\mathrm{mc}\omega^2}{\mathrm{EI}})^{0.25}) + \\
&1.l\sin(1.(\frac{l^4\mathrm{mc}\omega^2}{\mathrm{EI}})^{0.25})\sinh(1.(\frac{l^4\mathrm{mc}\omega^2}{\mathrm{EI}})^{0.25})\cos(2.(\frac{l^4\mathrm{mc}\omega^2}{\mathrm{EI}})^{0.25}) - \\
&0.25l\sin^2(2.(\frac{l^4\mathrm{mc}\omega^2}{\mathrm{EI}})^{0.25}) - 0.25l\sinh^2(2.(\frac{l^4\mathrm{mc}\omega^2}{\mathrm{EI}})^{0.25}) - 0.5l(\frac{l^4\mathrm{mc}\omega^2}{\mathrm{EI}})^{0.25} \\
&\sin(2.(\frac{l^4\mathrm{mc}\omega^2}{\mathrm{EI}})^{0.25}) + 1.l(\frac{l^4\mathrm{mc}\omega^2}{\mathrm{EI}})^{0.25}\cos(1.(\frac{l^4\mathrm{mc}\omega^2}{\mathrm{EI}})^{0.25}) \\
&\sinh(1.(\frac{l^4\mathrm{mc}\omega^2}{\mathrm{EI}})^{0.25}) + 2.l\cos((\frac{l^4\mathrm{mc}\omega^2}{\mathrm{EI}})^{0.25})\cosh(1.(\frac{l^4\mathrm{mc}\omega^2}{\mathrm{EI}})^{0.25}) \\
&\sin((\frac{l^4\mathrm{mc}\omega^2}{\mathrm{EI}})^{0.25})\sinh(1.(\frac{l^4\mathrm{mc}\omega^2}{\mathrm{EI}})^{0.25}) - 1.l\cos(1.(\frac{l^4\mathrm{mc}\omega^2}{\mathrm{EI}})^{0.25}) \\
&\cosh(1.(\frac{l^4\mathrm{mc}\omega^2}{\mathrm{EI}})^{0.25})\sin((\frac{l^4\mathrm{mc}\omega^2}{\mathrm{EI}})^{0.25})\sinh(1.(\frac{l^4\mathrm{mc}\omega^2}{\mathrm{EI}})^{0.25}) + \\
&1.l\cos((\frac{l^4\mathrm{mc}\omega^2}{\mathrm{EI}})^{0.25})\cosh(1.(\frac{l^4\mathrm{mc}\omega^2}{\mathrm{EI}})^{0.25})\sin(1.(\frac{l^4\mathrm{mc}\omega^2}{\mathrm{EI}})^{0.25}) \\
&\sinh(1.(\frac{l^4\mathrm{mc}\omega^2}{\mathrm{EI}})^{0.25}) - 1.l\cos(1.(\frac{l^4\mathrm{mc}\omega^2}{\mathrm{EI}})^{0.25})\sin(2.(\frac{l^4\mathrm{mc}\omega^2}{\mathrm{EI}})^{0.25}) \\
&\sinh(1.(\frac{l^4\mathrm{mc}\omega^2}{\mathrm{EI}})^{0.25}) + l\cosh(2.(\frac{l^4\mathrm{mc}\omega^2}{\mathrm{EI}})^{0.25})(-0.25\cos(2.(\frac{l^4\mathrm{mc}\omega^2}{\mathrm{EI}})^{0.25}) + \\
&0.25\cosh(2.(\frac{l^4\mathrm{mc}\omega^2}{\mathrm{EI}})^{0.25}) + \cosh(1.(\frac{l^4\mathrm{mc}\omega^2}{\mathrm{EI}})^{0.25})(0.5\sin((\frac{l^4\mathrm{mc}\omega^2}{\mathrm{EI}})^{0.25}) - 0.5\sin(1.(\frac{l^4\mathrm{mc}\omega^2}{\mathrm{EI}})^{0.25})) + \\
&0.5\sin((\frac{l^4\mathrm{mc}\omega^2}{\mathrm{EI}})^{0.25})\sinh(1.(\frac{l^4\mathrm{mc}\omega^2}{\mathrm{EI}})^{0.25}) + 0.5\sin(1.(\frac{l^4\mathrm{mc}\omega^2}{\mathrm{EI}})^{0.25}) \\
&\sinh(1.(\frac{l^4\mathrm{mc}\omega^2}{\mathrm{EI}})^{0.25})) + \cosh(1.(\frac{l^4\mathrm{mc}\omega^2}{\mathrm{EI}})^{0.25})(0.5l\cos(1.(\frac{l^4\mathrm{mc}\omega^2}{\mathrm{EI}})^{0.25}) \\
&\cos(2.(\frac{l^4\mathrm{mc}\omega^2}{\mathrm{EI}})^{0.25}) - 0.5l\cos((\frac{l^4\mathrm{mc}\omega^2}{\mathrm{EI}})^{0.25})\cosh(2.(\frac{l^4\mathrm{mc}\omega^2}{\mathrm{EI}})^{0.25}) + \\
&1.l(\frac{l^4\mathrm{mc}\omega^2}{\mathrm{EI}})^{0.25}\sin(1.(\frac{l^4\mathrm{mc}\omega^2}{\mathrm{EI}})^{0.25}) + 0.5l\sin(1.(\frac{l^4\mathrm{mc}\omega^2}{\mathrm{EI}})^{0.25}) \\
&\sin(2.(\frac{l^4\mathrm{mc}\omega^2}{\mathrm{EI}})^{0.25}) + (2.l\cos(1.(\frac{l^4\mathrm{mc}\omega^2}{\mathrm{EI}})^{0.25})\sin((\frac{l^4\mathrm{mc}\omega^2}{\mathrm{EI}})^{0.25}) - \\
&2.l\cos((\frac{l^4\mathrm{mc}\omega^2}{\mathrm{EI}})^{0.25})\sin(1.(\frac{l^4\mathrm{mc}\omega^2}{\mathrm{EI}})^{0.25}))\sinh(1.(\frac{l^4\mathrm{mc}\omega^2}{\mathrm{EI}})^{0.25})) - \\
&0.5l\cosh(1.(\frac{l^4\mathrm{mc}\omega^2}{\mathrm{EI}})^{0.25})\sin((\frac{l^4\mathrm{mc}\omega^2}{\mathrm{EI}})^{0.25})\sinh(2.(\frac{l^4\mathrm{mc}\omega^2}{\mathrm{EI}})^{0.25}) - \\
&0.5l\cosh(1.(\frac{l^4\mathrm{mc}\omega^2}{\mathrm{EI}})^{0.25})\sin(1.(\frac{l^4\mathrm{mc}\omega^2}{\mathrm{EI}})^{0.25})\sinh(2.(\frac{l^4\mathrm{mc}\omega^2}{\mathrm{EI}})^{0.25}) + \\
&0.5l\cos((\frac{l^4\mathrm{mc}\omega^2}{\mathrm{EI}})^{0.25})\sinh(1.(\frac{l^4\mathrm{mc}\omega^2}{\mathrm{EI}})^{0.25})\sinh(2.(\frac{l^4\mathrm{mc}\omega^2}{\mathrm{EI}})^{0.25}) \\
&- 0.5l\sin((\frac{l^4\mathrm{mc}\omega^2}{\mathrm{EI}})^{0.25})\sinh(1.(\frac{l^4\mathrm{mc}\omega^2}{\mathrm{EI}})^{0.25})\sinh(2.(\frac{l^4\mathrm{mc}\omega^2}{\mathrm{EI}})^{0.25}) + \\
&0.5l\sin(1.(\frac{l^4\mathrm{mc}\omega^2}{\mathrm{EI}})^{0.25})\sinh(1.(\frac{l^4\mathrm{mc}\omega^2}{\mathrm{EI}})^{0.25})\sinh(2.(\frac{l^4\mathrm{mc}\omega^2}{\mathrm{EI}})^{0.25}) - \\
&0.5l(\frac{l^4\mathrm{mc}\omega^2}{\mathrm{EI}})^{0.25}\sinh(2.(\frac{l^4\mathrm{mc}\omega^2}{\mathrm{EI}})^{0.25}))/((\frac{l^4\mathrm{mc}\omega^2}{\mathrm{EI}})^{0.25}) - \\
&((-0.5l\cos((\frac{l^4\mathrm{mc}\omega^2}{\mathrm{EI}})^{0.25}) + 0.5l\cos(1.(\frac{l^4\mathrm{mc}\omega^2}{\mathrm{EI}})^{0.25}) + 0.) \\
&\cosh(1.(\frac{l^4\mathrm{mc}\omega^2}{\mathrm{EI}})^{0.25}) + 0.)/((\frac{l^4\mathrm{mc}\omega^2}{\mathrm{EI}})^{0.25})))/((\frac{l^4\mathrm{mc}\omega^2}{\mathrm{EI}})^{0.25} \\
&(\cos((\frac{l^4\mathrm{mc}\omega^2}{\mathrm{EI}})^{0.25})\cosh((\frac{l^4\mathrm{mc}\omega^2}{\mathrm{EI}})^{0.25}) - 1)^2)
\end{aligned}
$$

$$
\begin{aligned}
K(2,2) = \mathrm{EI}(&\frac{l^4\mathrm{mc}\omega^2}{\mathrm{EI}})^{0.5}((1.l\cosh(1.(\frac{l^4\mathrm{mc}\omega^2}{\mathrm{EI}})^{0.25})\sinh(1.(\frac{l^4\mathrm{mc}\omega^2}{\mathrm{EI}})^{0.25})\\
&\cos^2((\frac{l^4\mathrm{mc}\omega^2}{\mathrm{EI}})^{0.25}) + 2.l\sin(1.(\frac{l^4\mathrm{mc}\omega^2}{\mathrm{EI}})^{0.25})\sinh^2(1.(\frac{l^4\mathrm{mc}\omega^2}{\mathrm{EI}})^{0.25})\\
&\sinh(1.(\frac{l^4\mathrm{mc}\omega^2}{\mathrm{EI}})^{0.25})\cos((\frac{l^4\mathrm{mc}\omega^2}{\mathrm{EI}})^{0.25}) - 2.l\cos(1.(\frac{l^4\mathrm{mc}\omega^2}{\mathrm{EI}})^{0.25})\\
&\sin((\frac{l^4\mathrm{mc}\omega^2}{\mathrm{EI}})^{0.25})\sinh^2(1.(\frac{l^4\mathrm{mc}\omega^2}{\mathrm{EI}})^{0.25}) - 0.5l(\frac{l^4\mathrm{mc}\omega^2}{\mathrm{EI}})^{0.25}\\
&\cos(2.(\frac{l^4\mathrm{mc}\omega^2}{\mathrm{EI}})^{0.25}) + 1.l\cosh(1.(\frac{l^4\mathrm{mc}\omega^2}{\mathrm{EI}})^{0.25})\sin(1.(\frac{l^4\mathrm{mc}\omega^2}{\mathrm{EI}})^{0.25}) -\\
&0.25l\sin(2.(\frac{l^4\mathrm{mc}\omega^2}{\mathrm{EI}})^{0.25}) - 0.25l\cosh(2.(\frac{l^4\mathrm{mc}\omega^2}{\mathrm{EI}})^{0.25})\sin(2.(\frac{l^4\mathrm{mc}\omega^2}{\mathrm{EI}})^{0.25}) -\\
&1.l\cosh(1.(\frac{l^4\mathrm{mc}\omega^2}{\mathrm{EI}})^{0.25})\sin^2((\frac{l^4\mathrm{mc}\omega^2}{\mathrm{EI}})^{0.25})\sinh(1.(\frac{l^4\mathrm{mc}\omega^2}{\mathrm{EI}})^{0.25}) -\\
&\cos(2.(\frac{l^4\mathrm{mc}\omega^2}{\mathrm{EI}})^{0.25})\sinh(1.(\frac{l^4\mathrm{mc}\omega^2}{\mathrm{EI}})^{0.25}) - 1.l\cosh(1.(\frac{l^4\mathrm{mc}\omega^2}{\mathrm{EI}})^{0.25})\\
&\sin((\frac{l^4\mathrm{mc}\omega^2}{\mathrm{EI}})^{0.25})\sin(1.(\frac{l^4\mathrm{mc}\omega^2}{\mathrm{EI}})^{0.25})\sinh(1.(\frac{l^4\mathrm{mc}\omega^2}{\mathrm{EI}})^{0.25}) -\\
&\sinh(2.(\frac{l^4\mathrm{mc}\omega^2}{\mathrm{EI}})^{0.25}) - 0.5l\cosh(1.(\frac{l^4\mathrm{mc}\omega^2}{\mathrm{EI}})^{0.25})\sin((\frac{l^4\mathrm{mc}\omega^2}{\mathrm{EI}})^{0.25})\\
&\sinh(2.(\frac{l^4\mathrm{mc}\omega^2}{\mathrm{EI}})^{0.25}) + 0.5l\cosh(1.(\frac{l^4\mathrm{mc}\omega^2}{\mathrm{EI}})^{0.25})\sin(1.(\frac{l^4\mathrm{mc}\omega^2}{\mathrm{EI}})^{0.25})\\
&\sinh(2.(\frac{l^4\mathrm{mc}\omega^2}{\mathrm{EI}})^{0.25}) - 1.l\sin((\frac{l^4\mathrm{mc}\omega^2}{\mathrm{EI}})^{0.25})\sinh(1.(\frac{l^4\mathrm{mc}\omega^2}{\mathrm{EI}})^{0.25})\\
&\sinh(2.(\frac{l^4\mathrm{mc}\omega^2}{\mathrm{EI}})^{0.25}) - 0.5l\sin(1.(\frac{l^4\mathrm{mc}\omega^2}{\mathrm{EI}})^{0.25})\sinh(1.(\frac{l^4\mathrm{mc}\omega^2}{\mathrm{EI}})^{0.25})\\
&\sinh(2.(\frac{l^4\mathrm{mc}\omega^2}{\mathrm{EI}})^{0.25}) + \cosh(2.(\frac{l^4\mathrm{mc}\omega^2}{\mathrm{EI}})^{0.25})(0.25\sinh(2.(\frac{l^4\mathrm{mc}\omega^2}{\mathrm{EI}})^{0.25})l +\\
&0.5(\frac{l^4\mathrm{mc}\omega^2}{\mathrm{EI}})^{0.25}l + \cosh(1.(\frac{l^4\mathrm{mc}\omega^2}{\mathrm{EI}})^{0.25})(0.5l\sin((\frac{l^4\mathrm{mc}\omega^2}{\mathrm{EI}})^{0.25}) +\\
&0.5l\sin(1.(\frac{l^4\mathrm{mc}\omega^2}{\mathrm{EI}})^{0.25})) + (0.5l\sin((\frac{l^4\mathrm{mc}\omega^2}{\mathrm{EI}})^{0.25}) - 0.5l\sin(1.(\frac{l^4\mathrm{mc}\omega^2}{\mathrm{EI}})^{0.25}))\\
&\sinh(1.(\frac{l^4\mathrm{mc}\omega^2}{\mathrm{EI}})^{0.25})) + l\cosh(1.(\frac{l^4\mathrm{mc}\omega^2}{\mathrm{EI}})^{0.25})(0.5\cosh(2.(\frac{l^4\mathrm{mc}\omega^2}{\mathrm{EI}})^{0.25})\\
&\sin((\frac{l^4\mathrm{mc}\omega^2}{\mathrm{EI}})^{0.25}) + 2.\sin(1.(\frac{l^4\mathrm{mc}\omega^2}{\mathrm{EI}})^{0.25})\sinh(1.(\frac{l^4\mathrm{mc}\omega^2}{\mathrm{EI}})^{0.25})\\
&\sin((\frac{l^4\mathrm{mc}\omega^2}{\mathrm{EI}})^{0.25}) + \cosh(1.(\frac{l^4\mathrm{mc}\omega^2}{\mathrm{EI}})^{0.25})(-1.\cos((\frac{l^4\mathrm{mc}\omega^2}{\mathrm{EI}})^{0.25})\\
&\sin((\frac{l^4\mathrm{mc}\omega^2}{\mathrm{EI}})^{0.25}) + 1.\cos(1.(\frac{l^4\mathrm{mc}\omega^2}{\mathrm{EI}})^{0.25})\sin((\frac{l^4\mathrm{mc}\omega^2}{\mathrm{EI}})^{0.25}) +\\
&\cos((\frac{l^4\mathrm{mc}\omega^2}{\mathrm{EI}})^{0.25})(-1.\sin((\frac{l^4\mathrm{mc}\omega^2}{\mathrm{EI}})^{0.25}) - 1.\sin(1.(\frac{l^4\mathrm{mc}\omega^2}{\mathrm{EI}})^{0.25}))) - 0.5\cos(2.(\frac{l^4\mathrm{mc}\omega^2}{\mathrm{EI}})^{0.25})\\
&\sin(1.(\frac{l^4\mathrm{mc}\omega^2}{\mathrm{EI}})^{0.25}) + 0.5\cos(1.(\frac{l^4\mathrm{mc}\omega^2}{\mathrm{EI}})^{0.25})\sin(2.(\frac{l^4\mathrm{mc}\omega^2}{\mathrm{EI}})^{0.25}) +\\
&2.\cos((\frac{l^4\mathrm{mc}\omega^2}{\mathrm{EI}})^{0.25})\cos(1.(\frac{l^4\mathrm{mc}\omega^2}{\mathrm{EI}})^{0.25})\sinh(1.(\frac{l^4\mathrm{mc}\omega^2}{\mathrm{EI}})^{0.25}) -\\
&0.5\cos((\frac{l^4\mathrm{mc}\omega^2}{\mathrm{EI}})^{0.25})\sinh(2.(\frac{l^4\mathrm{mc}\omega^2}{\mathrm{EI}})^{0.25})) + 0.)/((\frac{l^4\mathrm{mc}\omega^2}{\mathrm{EI}})^{0.25}) -\\
&(l\cosh(1.(\frac{l^4\mathrm{mc}\omega^2}{\mathrm{EI}})^{0.25})(0.5\sin((\frac{l^4\mathrm{mc}\omega^2}{\mathrm{EI}})^{0.25}) - 0.5\sin(1.(\frac{l^4\mathrm{mc}\omega^2}{\mathrm{EI}})^{0.25}) + 0.) +\\
&0.5l\cos((\frac{l^4\mathrm{mc}\omega^2}{\mathrm{EI}})^{0.25})\sinh(1.(\frac{l^4\mathrm{mc}\omega^2}{\mathrm{EI}})^{0.25}) - 0.5l\cos(1.(\frac{l^4\mathrm{mc}\omega^2}{\mathrm{EI}})^{0.25})\\
&\sinh(1.(\frac{l^4\mathrm{mc}\omega^2}{\mathrm{EI}})^{0.25}) + 0.)/((\frac{l^4\mathrm{mc}\omega^2}{\mathrm{EI}})^{0.25}))/(4l^2(\cos((\frac{l^4\mathrm{mc}\omega^2}{\mathrm{EI}})^{0.25})\\
&\cosh((\frac{l^4\mathrm{mc}\omega^2}{\mathrm{EI}})^{0.25}) - 1)^2)
\end{aligned}
$$

Bibliography

[1] N. Barbieri and R. Barbieri. "Dynamic Analysis of Stockbridge Damper". In: *Advances in Acoustics and Vibration* 2012 (2012).

[2] N. Barbieri and R. Barbieri. "Linear and Non-Linear Analysis of Stockbridge Damper". In: *Proc. of the 21st Brazilian Congress of Mechanical Engineering, Natal, RN, Brazil*. Ed. by Proceedings of COBEM. 2011.

[3] N. Barbieri et al. "Dynamical Analysis of Various Transmission Line Cables". In: *Proc of the X International Conference on Structural Dynamics , EURODYN 2017*. Ed. by Procedia Engineering 199. 2017, pp. 516–521.

[4] R. Barbieri et al. "Validation of a Mathematical Model of Stockbridge Damper". In: *Proc. of the 19th International Congress of Mechanical Engineering, Brasilia, DF*. Ed. by Proceedings of COBEM. 2007.

[5] O. Barry. "Finite Element Analysis of a Single Conductor with a Stockbridge Damper under Aeolian Vibration". MA thesis. Ryerson University, 2010.

[6] O. Barry et al. "Analytical and Experimental Investigation of Overhead Transmission Line Vibration". In: *Journal of Vibration and Control* 21 (2014), pp. 2825–2837.

[7] M. Buscemi. "Studio di un Sistema di Controllo Attivo per la Riduzione delle Vibrazioni nelle Linee Aeree di Trasmissione dell'Energia Elettrica". MA thesis. Politecnico di Milano, 2016.

[8] C.N. Canales et al. "Optimal Design of Stockbridge Dampers". In: *Ingenieria Mecanica Tecnologia y Desarollo* 2 (2008), pp. 193–199.

[9] A. Cardou. "Taut Helical Strength Bending Stiffness". In: *URL http://www.utfscience.deI/2006* (2006).

[10] A. Cardou and C. Jolicoeur. "Mechanical Models of Helical Strands". In: *Applied Mechanics Reviews* 50 (1997), pp. 1–14.

[11] F. Cheli and G. Diana. *Advanced Dynamics of Mechanical Systems*. Springer, 2015.

[12] CIGRE. *Modeling of Aeolian Vibrations of a Single Conductor Plus Damper - Assessment of Technology*. CIGRE WG B2.11 TF1. Electra Vol. 223, 2005.

[13] CIGRE. *State of the Art of Conductor Galloping*. Technical Brochure no. 322. CIGRE WG TF B2.11.06, 2007.

[14] R. Claren and G. Diana. “Mathematical Analysis of Transmission Line Vibration”. In: *IEEE Transactions on Power Apparatus and Systems* 88 (1969), pp. 1741–1771.

[15] J.P. Den Hartog. *Mechanical Vibrations*. Dover Publications, 1985.

[16] G. Diana and M. Falco. “On The Forces Transmitted to a Vibrating Cylinder by a Blowing Wind”. In: *Meccanica* 6 (1971), pp. 9–22.

[17] G. Diana et al. “Stockbridge-Type Damper Effectiveness Evaluation: Part I - Comparison Between Tests on Span and on the Shaker”. In: *IEEE Transactions on Power Delivery* 18 (2003), pp. 1462–1469.

[18] G. Diana et al. “Stockbridge-Type Damper Effectiveness Evaluation: Part II-The Influence of the Impedance Matrix Terms on the Energy Dissipated”. In: *IEEE Transactions on Power Delivery* 18 (2003), pp. 1470–1477.

[19] J.M.M. Dos Santos. “Modelling and Analysis of Wind-Excited Vibrations of Transmission Lines”. MA thesis. University of Porto, 2015.

[20] Electric Research Power Institute EPRI. *Transmission Line Reference Book: Wind-Induced Conductor Motion*. Palo Alto, 2006.

[21] M. Ervik et al. “Report on Aeolian Vibration”. In: *Electra* 124 (1986), pp. 40–77.

[22] F. Foti and L. Martinelli. “An Analytical Approach to Model the Hysteretic Bending Behavior of Spiral Strands”. In: *Applied Mathematical Modelling* 40 (2016), pp. 6451–6467.

[23] F. Foti and L. Martinelli. “Finite Element Modeling of Cable Galloping Vibrations. Part II: Application to an Iced Cable in 1:2 Multiple Internal Resonance”. In: *Journal of Vibration and Control* 24 (2016), pp. 1322–1340.

[24] F. Foti and L. Martinelli. “Hysteretic Behaviour of Stockbridge Dampers: Modelling and Parameter Identification”. In: *Mathematical Problems in Engineering* (2018).

[25] F. Foti and L. Martinelli. “Mechanical Modeling of Metallic Strands Subjected to Tension, Torsion and Bending”. In: *International Journal of Solids and Structures* 91 (2016), pp. 1–17.

[26] F. Foti et al. “A parametric Study on the Structural Damping of Suspended Cables”. In: *Proc. of the X International Conference on Structural Dynamics, EURODYN 2017*. Ed. by Procedia Engineering 199(2017). 2017, pp. 140–145.

[27] M. Geradin and D. Rixen. *Mechanical Vibrations: Theory and Application to Structural Dynamics*. 2nd edition. Wiley, 1997.

[28] P. Hagedorn. “On the Computation of Damped Wind-Excited Vibrations of Overhead Transmission Lines”. In: *Journal of Sound and Vibration* 83 (1982), pp. 253–271.

[29] P. Hagedorn. “Wind-Excited Vibrations of Transmission Lines: A Comparison of Different Mathematical Models”. In: *Mathematical Modelling* 8 (1987), pp. 352–358.

[30] P. Hagedorn and D. Sauter. "On the Hysteresis of wire cables in Stockbridge Dampers". In: *International Journal of Non-Linear Mechanics* 37 (2002), pp. 1453–1459.

[31] H. Kasap. "Investigation of Stockbridge Dampers for Vibration Control of Overhead Transmission Lines". MA thesis. Middle East Technical University, 2012.

[32] S. Langlois and F. Legeron. "Prediction of Aeolian Vibration on Transmission-Line Conductors Using a Nonlinear Time Hystory Model - Part I: Damper Model". In: *IEEE Transactions on Power Delivery* 29 (2014), pp. 1168–1175.

[33] S. Langlois and F. Legeron. "Prediction of Aeolian Vibration on Transmission-Line Conductors Using a Nonlinear Time Hystory Model - Part II: Conductor and Damper Model". In: *IEEE Transactions on Power Delivery* 29 (2014), pp. 1176–1183.

[34] J.H. Lienhard. "Synopsis of Lift, Drag and Vortex Frequency Data for Rigid Circular Cylinders". In: *Technical Extension Service* (1966).

[35] J.L. Lilien. *Power Line Aeolian Vibrations*. Tech. rep. Universite de Liege, Department of Electronics, Electricity and Computer Sciences, 2013.

[36] M.L. Lu. "The Effect of Turbulence on the Wind Power Imparted to a Vibrating Conductor". In: *XI Conference Wind Engineering*. Ed. by Wind Science and Engineering. 2003, pp. 2125–2132.

[37] M.L. Lu and J.K. Chan. "An Efficient Algorithm for Aeolian Vibration of Single Conductor with Multiple Dampers". In: *IEEE Transactions on Power Delivery* 22 (2007), pp. 1822–1829.

[38] M.L. Lu and J.K. Chan. "Rational Design Equations for the Aeolian Vibration of Overhead Power Lines". In: *Power and Energy Society General Meeting*. Ed. by IEEE. 2015.

[39] X. Luo et al. "Nonlinear Numerical Model with Contact for Stockbridge Vibration Damper and Experimental Validation". In: *Journal of Vibration and Control* 22 (2014), pp. 1217–1227.

[40] M. Markiewicz. "Optimum Dynamic Characteristics of Stockbridge Dampers for Dead-End Spans". In: *Journal of Sound and Vibration* 188 (1995), pp. 243–256.

[41] A.R. McCulloch et al. "Ten Years of Progress with Self-Damping Conductor". In: *IEEE Transactions on Power Apparatus and Systems* PAS-99 (1980), pp. 998–1011.

[42] S. Meynen et al. "On the Numerical Simulation of Vortex-Induced Vibrations of Oscillating Conductors". In: *Journal of Fluids and Structures* 21 (2005), pp. 41–48.

[43] O. Nigol et al. "Aeolian Vibration of Single Conductors and Its Control". In: *IEEE Transactions on Power Apparatus and Systems* PAS-104 (1985), pp. 3245–3254.

[44] D.U. Noiseux. "Similarity Laws of the Internal Damping of Stranded Cables in Transverse Vibrations". In: *IEEE Transactions on Power Delivery* 7 (1992), pp. 1574–1581.

[45] A.S. Richardson. “Performance Requirements for Vibration Dampers”. In: *Electric Power Systems Research* 36 (1996), pp. 21–28.

[46] D. Sauter. “Modeling the Dynamic Characteristics of Slack Wire Cables in Stockbridge Dampers”. MA thesis. Technischen Universitat Darmstadt, 2003.

[47] K. Spak et al. “Cable Modeling and Internal Damping Developments”. In: *Applied Mechanics Reviews* 65 (2013), pp. 1–18.

[48] G.H. Stockbridge. “Overcoming Vibrations in Transmission Cables”. In: *Electrical World* 86 (1925), pp. 1304–1305.

[49] J. Vecchiarelli. “Aeolian Vibration of a Conductor with a Stockbridge-Type Damper”. PhD thesis. University of Toronto, 1997.

[50] J. Vecchiarelli et al. “Computational Analysis of Aeolian Conductor Vibration with a Stockbridge-Type Damper”. In: *Journal of Fluids and Structures* 14 (2000), pp. 489–509.

[51] H. Wagner et al. “Dynamics of Stockbridge dampers”. In: *Journal of Sound and Vibration* 30 (1973), pp. 207–220.

[52] H. Wolf et al. “Numerical Aspects of Determination of Natural Frequencies of a Power Transmission Line Cable equipped With In-Line Fittings”. In: *Engineering Structures* 160 (2018), pp. 510–518.